A Micromechanical Study of Undrained Granular Media Using Fluid-coupled Discrete Numerical Simulations

By

Wei Zhang

A thesis

presented to the University of Waterloo

in fulfilment of the

thesis requirement for the degree of

Doctor of Philosophy

in

Civil Engineering

Waterloo, Ontario, Canada

Examining Committee Membership

The following served on the Examining Committee for this thesis. The decision of the Examining Committee is by majority vote.

External Examiner	DR. PEIJUN GUO Professor
Supervisor	DR. LEO ROTHENBURG Professor
Internal Member	DR. GIOVANNI CASCANTE Professor
Internal Member	DR. DIPANJAN BASU Associate Professor
Internal-external Member	DR. CAROLYN REN Professor

Author's declaration

I hereby declare that I am the sole author of this thesis. This is a true copy of the thesis, including any required final revisions, as accepted by my examiners.

I understand that my thesis may be made electronically available to the public

Abstract

Engineering behavior of saturated granular materials under rapid loading as during earthquakes is reasonably well explored empirically. Presently, theoretical models developed within concepts of classical soil mechanics are generally adequate for engineering design. Nevertheless, even such basic soil mechanics questions, for example, as the influence of soil gradation on the stability of hydraulically placed fills can be hotly debated in engineering offices. This is due to lack of a well-developed physical framework for understanding soil behavior at a particle level, specifically in undrained conditions.

The main objective of the present study is to explore micromechanics of undrained behavior of granular media using numerical simulations in which motions of discrete particles are coupled with pore fluid movements caused by deformations of individual pores. The latter are modeled as forming an interconnected network. The rate of fluid transfer between pores is considered proportional to pressure differential between pores so that macroscopically the system follows the Darcy's Law. The fluid is considered elastic in response to pore volume change. It is demonstrated that this type particle-fluid coupling results in macroscopic Biot-Terzaghi poroelastic behavior when the system of intergranular contacts is fixed and the contact force vs interparticle displacement relationship is linear. In the case of unbound granular assemblies, when the mechanical behavior under shear deformations involves creation and disintegration of intergranular contacts, the key modeling challenge addressed in this thesis is development of a robust algorithm that tracks modifications of the pore space preserving fluid mass balance. This substantially extends the range of applications for the simulation methodology developed by Dr. R. Olivera at the University of Waterloo in 2004.

The developed algorithm is based on identification of sub-volumes in the assembly containing pore groups with one-to-one mapping into uniquely identified sub-volumes in the configuration that existed at the previous computational step. These related sub-volumes contain pores that coalesced due to contact disintegration or where larger pores became subdivided into smaller pores due to creation of contacts. The subdivision of space into related sub-volumes makes it possible to accurately maintain fluid mass balance to practically any strain level as the assembly undergoes through dramatic microstructural changes. Numerical simulations of granular samples under axial loading and constant lateral stress carried out at different void ratio and consolidation stress qualitatively resemble the mechanical response of granular soils in conventional laboratory testing, including static liquefaction of loose samples. This comparison demonstrates that the developed simulation methodology reasonably reflects physical processes in undrained granular media.

As an application of the developed simulation methodology the thesis presents a study of the effects of granular soil permeability on undrained behavior. In this particular study the base material is taken as a

loose granular assembly of medium to fine particles where permeability was varied by changing the rate of fluid transfer from pore to pore. This physically reflects addition of fine particles into pores to impede flow (without taking into account the effect of fines on interparticle interactions). Simulations demonstrate that restricting fluid transfer from pore to pore results in increased undrained strength. Similar results were obtained in a published laboratory study that concluded that addition of fines to a granular material can prevent static liquefaction. The present study confirms this conclusion. The mechanism of this phenomenon is discussed in the thesis based on examination of the way permeability indirectly influences distributions of intergranular forces.

In addition to conventional stress-strain characterization of mechanical behavior, results of all simulations are examined in terms of micromechanical descriptors that characterize changes in the number of intergranular contacts with strain, their spatial anisotropy and average contact forces. Although all micromechanical descriptors in drained and undrained conditions evolve to some asymptotic values at large shear strain, only in the case of drained deformations the same asymptotic state is reached at the same mean stress level irrespective of the initial state of packing. This mean stress-dependent "critical state" corresponds to specific values of void ratio and average coordination number induced in the course of shear deformations. Evolution of simulated granular assemblies towards the same state is not observed in undrained conditions although steady state is always reached. Envelopes of asymptotic states as function of mean stress identified for simulated samples with different initial void ratio, the so-called critical and steady state lines, are somewhat different in cases of drained and undrained deformations, as far as void ratio and coordination numbers are concerned. There appears to be no distinction in values of induced asymptotic anisotropy in drained and undrained conditions. This topic requires further studies and various avenues for further research in this area are identified in the concluding chapter of the thesis.

Acknowledgements

I would like to express my sincere gratitude to my advisor Prof. Leo Rothenburg for his support and guidance over the course of my PhD journey. I would like to thank you wholeheartedly for your patience over the years, you have been a tremendous mentor and teacher through your everyday examples both inside and outside of the classroom. The kindness you have shown me has transformed my life. I could not have imagined having a better advisor and role model.

I would also like to extend my appreciation to my teacher and friend, Prof. Tim Topper. Thank you for your always encouraging and supporting words throughout the years. Your many advises has been invaluable to me.

Special thanks to Prof. Giovanni Cascante, Prof. Dipanjan Basu and the Civil and Environmental Engineering Faculty for their continuous guidance and support over the years. Extended thanks to my committee members, Prof. Peijun Guo and Prof. Carolyn Ren for their valuable advises.

Heartfelt thanks to all my friends at the University of Waterloo for all the wonderful memories that we have shared. I am particularly thankful to my colleagues in the Geotechnical group for all the good and difficult experiences shared during these years.

Dedication

To my parents for their unconditional love and support.

Table of Contents

List of Figures

List of Tables

List of Symbols

A	area
$\ddot{\theta}$	angular acceleration of a particle
f_o^c	average contact force over all contacts in an assembly
l_0^c	average contact vector length
γ	average coordination number
R	average dimeter of a particle
F	axial load
ε_a	axial strain
f_i^β	boundary force
B_f	bulk modulus of the fluid
Δu	change or pore pressure
c_v	coefficient of consolidation
m_v	contact density
$f_i^c(\theta)$	contact force
n^c	contact normal
$S(\theta)$	contact normal distribution function
k_n	contact stiffness in normal direction
k_t	contact stiffness in tangential direction
$l_j^c(\theta)$	contact vector
CSR	critical stress ratio
ρ	density
q	deviator stress in 2D ($q = (\sigma_1 - \sigma_2)/2$)
e_c	eccentricity of a particle
u_e	excess pore pressure
b_n	fourth order coefficient of contact normal anisotropy
θ_b	fourth order principal direction of contact normal anisotropy
D_m	global damping act on mass
D_I	global damping act on moment of inertia
c_m	global damping coefficient act on mass

c_I	global damping coefficient act on moment of inertia
F_1	horizontal load
k	hydraulic conductivity
i	hydraulic gradient
ΔF_n	increment of contact force in normal direction
ΔF_t	increment of contact force in tangential direction
e_0	initial void ratio
μ	inter-particle friction coefficient
K	intrinsic permeability
δ_{ij}	Kronecker's delta
r_i^{β}	location vector
σ_{ij}^{β}	macroscopic stress tensor on the boundary
p'	mean effective stress $(p' = (\sigma_1' + \sigma_2')/2)$
$sin\varphi$	mobilized friction angle
I	moment of inertia of a particle
D_n	normal contact damping
c_n	normal contact damping coefficient
$f_n^c(\theta)$	normal contact force
Δn	normal displacement
v_n	normal relative density
M_g	number of contacts fall within each group
n_f	number of floaters
N	number of particles
M	number of physical contacts
d	pipe diameter
ν	Poisson's ratio
u	pore water pressure
QSS	quasi-steady state
D_r	relative density
v_R	relative velocity

a_n second order coefficient of contact normal anisotropy

a_f second order coefficient of the average normal contact force anisotropy

a_t second order coefficient of the average tangential contact force anisotropy

θ_a second order principal direction of contact normal anisotropy

θ_n second order principal direction of normal contact force anisotropy

θ_t second order principal direction of tangential contact force anisotropy

ε_t shear strain

I_s state index

ψ state parameter

SSL steady state line

$\dot{\varepsilon}_{ij}$ strain rate at the boundary

σ_{ij} stress tensor

D_s tangential contact damping

c_s tangential contact damping coefficient

$f_t^c(\theta)$ tangential contact force

Δt tangential displacement

v_t tangential relative density

t time

T_v time factor

$\ddot{x}$ translational acceleration of a particle

C_u uniformity coefficient

$\bar{\mu}$ viscosity of the fluid

F_2 vertical load

e void ratio

e_{ss} void ratio at steady state

V volume

Q volumetric flow rate

E Young's modulus

Chapter 1 Introduction

1.1 General background

The micromechanical study of undrained behavior of granular media in this thesis is motivated by a persistent need to understand mechanisms and conditions when mechanical behavior of sand is drastically altered under cyclic loading as during earthquakes.

Cyclic and static liquefaction failure

Large scale deformation and liquefaction of saturated sand in an undrained condition under monotonic or cyclic loading (i.e. during earthquakes) has led to many failures throughout the history of civil construction. The striking case of collapsed and settled buildings (Fig. 1.1) in Kawagishi-cho of Niigata, Japan, due to an earthquake in 1964 is probably one of the most representative and striking liquefaction failures induced by cyclic loading. It drew attention and resulted in extensive research on the mechanism of liquefaction, although at that time the name "liquefaction" had not been introduced yet. In 1971, an earthquake induced liquefaction destroyed the upstream slope of the lower San Fernando Dam (see Figure 1.2) in California, USA. Unlike the Niigata liquefaction failure that happened during the cyclic shaking of an earthquake, the lower San Fernando Dam liquefaction failure occurred soon after an earthquake ceased. So some researchers consider the mechanism of the lower San Fernando Dam liquefaction to be static although the induced pore pressure rise was triggered by an earthquake (Seed, Lee, Idriss, & Makdisi, 1975). Indeed, an earthquake can cause liquefaction either statically or dynamically. The static liquefaction failures during construction, which were related to hydraulic fill placement in the Fort Peck Dam, USA, in 1938 and in Nerlerk in the Beaufort Sea, Canada, in 1983 are two typical cases of the static type of liquefaction.

Figure 1.1 Liquefaction caused by the earthquake on buildings in Niigata, 1964
(http://en.wikipedia.org/wiki/Soil_liquefaction#/media/File:Liquefaction_at_Niigata.JPG)

Figure 1.2 The upstream slide after liquefaction failure of Lower San Fernando dam (http://research.engineering.ucdavis.edu/gpa/wp-content/uploads/sites/43/2015/02/Slide-after-drawdown.jpg)

What is liquefaction?

These aforementioned construction failures were all induced by sand liquefaction, which is "a phenomenon wherein a mass of soil loses a large percentage of its shear resistance, when subjected to undrained monotonic, cyclic or shock loading, and flows in a manner resembling a liquid until the shear stresses acting on the mass are as low as the reduced shear resistance" (Castro and Poulos, 1977). This is the definition of liquefaction given by Castro and Poulos in 1977, which was proposed 57 years after Hazen's description of the liquefaction mechanism from the Calaveras Dam failure in California in 1920 (Hazen, 1920). A similar concept that is usually compared to liquefaction but is fundamentally different is cyclic mobility, which refers to "the progressive softening of saturated soil when subjected to cyclic loading at a constant void ratio. The softening is accompanied by a high pore pressure, increasing cyclic deformation, and in some cases, permanent deformation, but it does not lead to a loss in shear strength nor continuous deformation, both of which are essential aspects of liquefaction" (Castro et al., 1982). According to Castro (1975), liquefaction only exists in a loose sand state, however, cyclic mobility can happen in both loose and dense states of sand. Figs. 1.3 and 1.4 shows conceptual plots of liquefaction and cyclic mobility, respectively. Figure 1.3 illustrates the conceptual stress-strain responses of the soil in an undrained condition that triggers traditional liquefaction, where (a) is from a monotonic load test and (b) is from a cyclic load test. It is noted in this figure that both monotonic and cyclic loading can lead to a suddenly rapid

decrease of the deviator stress associated with large deformations. Fig. 1.4 conceptually depicts the axial load and axial strain variations of cyclic mobility. It is shown in the figure that no reduction of shear resistance is revealed, although the axial strain increases. This research will only deal the former phenomenon, traditional liquefaction.

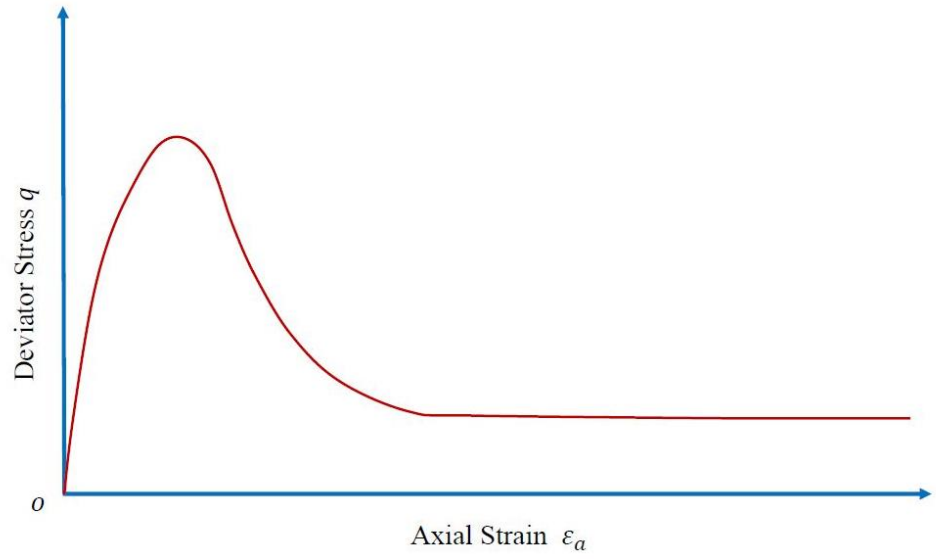

(a)

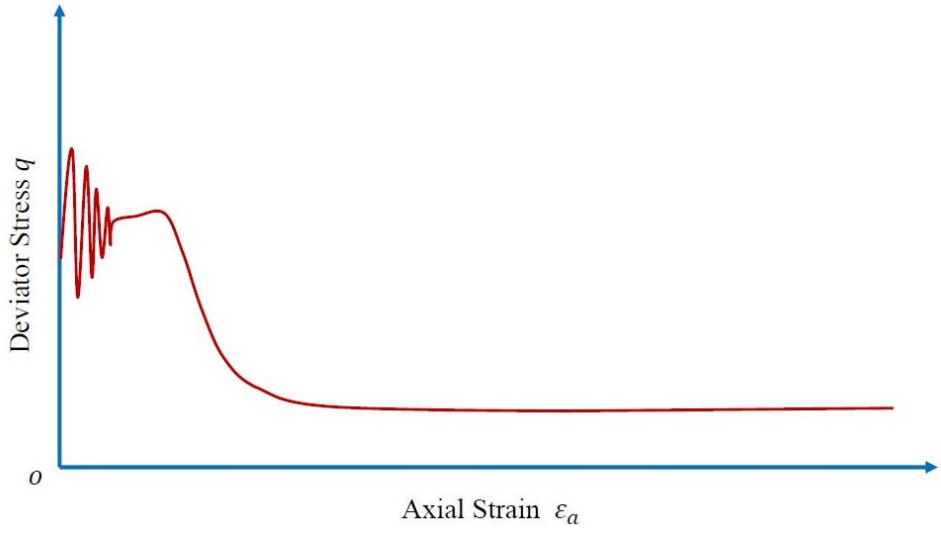

(b)

Figure 1.3 Conceptual stress-strain relationships for samples triggered liquefaction under (a) monotonic load (b) cyclic load

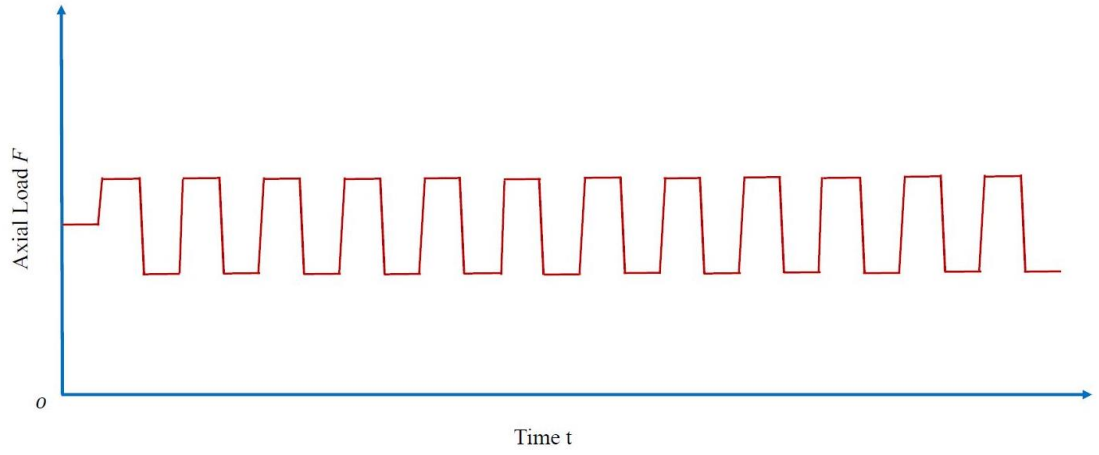

(a)

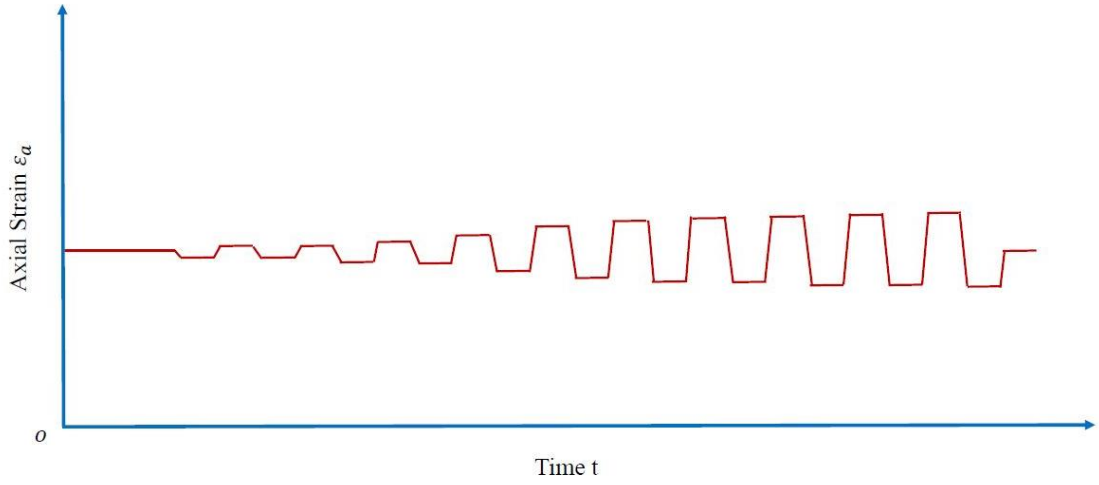

(b)

Figure 1.4 Conceptual representation of cyclic mobility with time (a) axial load variations (b) axial strain responses

Liquefaction potential evaluation

With respect to the evaluation of the liquefaction potential, Ishihara in 1993 suggested two main features of an analysis of a seismically-induced liquefaction, which are the onset condition that is governed by cyclic strength and the post-seismic stability analysis that is controlled by residual strength. With respect to the residual strength study alone, evidence from many laboratory monotonic and cyclic shear tests indicates that cyclic loading and monotonic loading can both result in a consistent residual strength (Castro, 1969). Hence, the residual strength controls liquefaction susceptibility. The fundamental idea of the well-known liquefaction potential evaluation proposed by Poulos and Castro in 1985 was that liquefaction susceptibility

depends on the soil's initial state relative to the steady state line in a state diagram. They believe the undrained steady state strength is only a function of void ratio and the soil itself. Therefore, the major task of liquefaction potential evaluating the of a soil structure such as a foundation, dam, embankment or hydraulic sand fills is to select an appropriate and representative undrained residual strength, which can be obtained by careful laboratory monotonic undrained triaxial testing.

Why a micromechanical study?

Since the well-recognized dominant reason for liquefaction is the loss of contact between soil particles due to the generation of excess pore pressure, an understanding of sand behavior from a particle perspective in an undrained condition is necessary. In addition, among the factors that influence the laboratory testing to determine the undrained residual strength and the undrained response of a soil (i.e. void ratio, confining stress, and initial fabric etc.), the initial fabric is a critical one. This is evident from the experience that different sample preparation methods (i.e. moist tamping and air pluviation) can lead to different results even though the void ratio and confining stress are the same (Benahmed et al., 2015; Ishihara, 1993; Mulilis et al., 1977; Tatsuoka et al., 1986). Hence, it is essential to perform a study on the particulate micromechanics of sand media to reveal the intrinsic fabric and contact force properties of sand during liquefaction. However, laboratory testing of soil mechanical properties at the particulate level is very complex and in most case not attainable. Therefore, a numerical modelling technique has been adopted instead by most researchers conducting micromechanical studies on soil. This research will conduct micromechanical studies using a numerical modelling technique.

1.2 Statement of the problem

Micromechanical study of undrained granular behaviors and liquefaction

A study of the undrained behavior of granular media as an important component of a liquefaction evaluation has been conducted by many researchers (Castro, 1969; Castro, 1975; Poulos et al., 1985). Among them, micromechanical studies of the undrained behavior of granular media are unusual because of its complexity, however, it is necessary since the notion that liquefaction is induced by the loss of contact resulting from a rapid pore pressure generation is well recognized. Due to the lack of a method to perform microscopic undrained testing, numerical simulation has been employed for most micromechanics research on granular material. To simulate undrained response and liquefaction microscopically, an essential component is the analysis of soil particle and fluid flow interactions. The simplified constant volume method cannot achieve this objective since it only simulates the behavior of a soil in an undrained condition by preserving the volume of the sample without any real computation of pore pressure and soil particle interactions. Hence, a comprehensive fluid-coupled DEM should be employed instead for the micromechanical simulation of

soil undrained response and liquefaction. Research that treated the fluid as a continuum coupled with the particles neglected the non-uniform pore pressure distribution in the micro-pores in the assembly, and hence, is not a comprehensive fluid-coupled DEM. As indicated by Iwashita and Oda (1999), to successfully conduct a fluid-coupled DEM simulation, at least four problems regarding pore pressure computation should be solved, which are the pore volume change due to particle movements, the excess pore pressure resulted from the pore volume change, the excess pore pressure forces exerted on particles, and the dissipation of excess pore pressure. The idea of computing each pore's individual pressure was initially proposed by Hakuno and Tarumi (1988) and extended later by Nakase et al. (1999), and Olivera (2004). Although the fluid-coupled DEM model proposed by Olivera (2004) successfully depicts the undrained behavior of relative loose to dense granular assemblies for small to medium strain ranges, it fails to capture the phenomenon of liquefaction, because it does not allow the computation of pore pressures when rapid changes in pore structure due to creation and disintegration of inter-granular contacts occurs. Following his fluid-coupled DEM idea, this research will further develop a pore identification scheme, which keeps track of "pore groups" where some voids may coalesce due to contact disintegration and other voids may be subdivided into parts due to contact creation. It will help with handling the extremely complex modifications of pore space when both coalescence and subdivision of voids affecting a group of voids take place simultaneously. Using this "pore groups" idea, a comprehensive fluid-coupled DEM analysis of undrained soil behavior will be carried out and the micromechanical mechanism of liquefaction will be studied with the aim of extracting information on the particle scale and applying it to understanding the associated mechanical behaviors.

Permeability effect on liquefaction susceptibility

Permeability as an important indicator of the pores media's potential for fluid flow is frequently accessed in the geotechnical engineering related design process such as slope stability analysis, foundation design, and dam or embankment design. This is due to the closely relationship between permeability and pore pressure build up and dissipation rate, which has a strong impact on the safety and stability of geotechnical engineering constructions. Hence, it is necessary to examine the permeability effect when studying the undrained behavior of granular media. With regards to its effect on liquefaction, studies from both laboratory testing and numerical simulations of soil subjected to cyclic loading were conducted in the past two decades by many researchers, most of which indicate that soil with a higher permeability tends to be less susceptible to liquefaction (Dewoolkar et al., 1999; Yang and Elgamal, 2002). Much less attention has been paid to the effect of permeability on the static liquefaction of a sample subjected to monotonic loading. Some representative studies are for example, the study of undrained behaviors of liquefiable soil with different percentages of fine components performed by many researchers (Evans and Zhou, 1995; Lade and

Yamamuro, 1997; Law and Ling, 1992; Pitman et al., 1994; Yamamuro and Lade, 1997), which indirectly indicated the permeability influence on the liquefaction potential of sand. Another representative simulation study conducted by Yang and Elgamal in 2002 showed that with identical mechanical soil properties in a model, a sample with a low permeability displayed a much larger shear resistance compared to the one with a higher permeability due to the negative pore pressure generation. However, their study of permeability effect is under drained simple shear condition which is not sufficient to depict permeability effect in an undrained condition. Since the effect of permeability on a soil subjected to cyclic loading has been shown to be very significant in tests and simulations, its influence should be equally extended to monotonic loading due to similar mechanisms of pore pressure generation and dissipation. Thus, a comprehensive study of the permeability effect on the undrained behavior of granular media under monotonic loading, especially on its liquefaction susceptibility is essential to understanding the phenomenon of liquefaction. In this research, a numerical study of the permeability effect on granular media is conducted by directly assigning different representations of permeability of a liquefiable granular assembly and exploring their effect on the liquefaction susceptibility. Meanwhile, to develop a comprehensive permeability study, a micromechanical analysis will be conducted, which aims at demonstrating the mechanisms by which permeability affects the undrained behavior of liquefiable granular media.

Consistency of the critical state line and the steady state line

From the literature, we see that much of the research on the residual shear strength during liquefaction is based on the hypothesis that the limiting state of sand reached during undrained liquefaction is the same *critical state* whose characteristics are well-established in soil mechanics from studies of drained deformation (Been et al., 1991; Sladen et al., 1985; Verdugo and Ishihara, 1996). The view of liquefaction as a critical state phenomenon has an important practical benefit in that we can use the extensively-studied drained characteristics of sands to predict behavior in undrained conditions and, consequently, liquefaction. In particular, the unified view makes it possible to establish the in-situ liquefaction potential of a sand deposit from common drained penetration testing. With the *critical void ratio* as a function of *mean effective stress* having the same characteristics for both drained and undrained behavior, liquefaction is viewed as the reaching of a critical state due to pore pressure generation that causes a related reduction in the mean effective stress until it reaches the critical value.

The relationship between the critical void ratio and the mean effective stress is considered to be an intrinsic property of a granular material characterizing the state reached in the course of large shear deformations. Referred to as “critical state line” because of its linear shape in void ratio – log of mean effective stress coordinates, most studies of liquefaction consider it to also be an envelope of states reached in the course of large strain deformations when sand liquefies and essentially flows at a *steady rate* as a fluid (Been et

al., 1991; Sladen et al., 1985; Verdugo and Ishihara, 1996). Other studies suggest that the states reached during steady liquefaction flow are distinct and although characterized by a similar envelope of limiting states, refer to it as a "steady state line" (Castro, 1969; Alarcon-Guzman and Leonards, 1988; Alarcon-Guzman et al., 1988). This is to emphasize the physical distinctions between the limiting states of drained and undrained processes. Therefore, it is necessary to examine the physical legitimacy of treating liquefaction as a critical state phenomenon so that the critical state line and steady state line are the same. Or on the other hand whether the physical processes during drained and undrained deformation are distinctly different and the critical state line and the steady state line require different representations. To conduct an in-depth investigation of the intrinsic properties of a limiting state for sand in both drained and undrained conditions, a detailed micromechanics study of granular material to reveal the microstructural differences between the drained transition to a critical state and the undrained transition to steady state flow is essential. Therefore, this study is aimed at examining the fabric, anisotropy and contact force characteristics for sand under critical and steady state flow conditions, and describing the macroscopic behavior of sand in these cases. Both drained and undrained simulation tests will be conducted to large strains. A comparison will be made between the steady state line and the critical state line to see whether they are microscopically identical or not.

1.3 Objectives and approach of study

The primary objective of this research was to numerically study the undrained behaviors of granular media from a micromechanical framework and explain their associated macroscopic behaviors in an undrained condition. Liquefaction as a particular undrained behavior, its mechanisms and characteristics will be studied for granular material in an undrained condition. Both microscopic and macroscopic studies will be performed to depict the underlying causes of the phenomenon of liquefaction. Some factors such as the void ratio, confining stresses, and permeability that affect the undrained behavior of liquefiable granular media will also be studied from a micromechanics point of view to reveal the reason for their effects. Besides, the consistency of the critical state line and the steady state line in liquefaction evaluation related researches, will be studied using both macroscopic and microscopic concepts. The specific approach of the study is as follows:

1. Further develop the fluid-coupled DEM scheme that was first proposed by Olivera in 2004 by extending its capability to handle rapid changes in pore structure due to the creation and disintegration of inter-granular contacts. This will also improve the method's effectiveness in computing the pore pressure variations when extremely complex modifications of pore space involving both coalescence and

subdivision of voids is taking place. This usually affects a group of voids simultaneously and frequently appears during the initiation of liquefaction at large strains.

2. Compare the behavior of improved fluid-coupled DEM model with the behavior of a poro-elastic configuration by conducting pore pressure equalization test and pore pressure dissipation test. Compare the pore pressure dissipation test results with those obtained from Terzaghi's classical one-dimensional consolidation theory.

3. Perform two-dimensional undrained biaxial compression simulations on granular assemblies with different initial void ratios and confining stresses. Extract data from the simulations and conduct mechanics and micromechanics analyses. Focus on fabric, anisotropy, and contact forces variations when studying the micromechanical properties of the assemblies and interpreting the associated macroscopic behavior exhibited during deformations.

4. Compare the above simulated results with those from the laboratory tests to evaluate the effectiveness of the simulation. Also, a comparison of the undrained behavior obtained using the fluid-coupled DEM approach with that from the behavior indicated by the frequently applied constant volume method will be made, aiming at illustrating the deficiency of the constant volume method due to its failure to compute the pore pressure effect on the particles.

5. Conduct a study of the effect of permeability on the liquefaction susceptibility of a liquefiable assembly. Perform undrained biaxial compression simulations on the given assembly with different descriptions of permeability. And study the permeability effect on undrained behavior of the liquefiable assemblies from both macroscopic and microscopic perspectives.

6. Perform both drained and undrained biaxial compression simulations on a series of granular assemblies with different initial void ratios and confining stresses subjected to a large strain. Extract the data for the void ratio, the average coordination number, and the mean effective stresses at chosen ultimate state points. Develop relationships of void ratio versus mean effective stress and average coordination number versus mean effective stress using the data at the ultimate states for both drained and undrained simulations. Compare and study the consistency of the two groups of relationships.

1.4 Organization of the thesis

This thesis is organized as follows:

Chapter 1 introduces some well-known liquefaction failures in civil construction history and then proposes a definition of liquefaction and stresses the importance of a micromechanical study. Following a statement of the problem that exists so far, a micromechanical study on undrained behavior of granular media is

proposed. It then, presents the objectives and approaches of a numerical micromechanical study proposed for this thesis. Finally, it lists an outline and organization of this thesis and explains the significance of its findings.

Chapter 2 summaries a literature review of both continuum mechanics based and micromechanics based concepts and properties of sand. Particularly, the undrained behavior and properties of sand obtained from the traditional soil mechanics and a brief explanation of some micromechanics concepts and theories are introduced to provide a better understanding of the results in later chapters. A history of the development of DEM and fluid-coupled DEM is introduced. Different understandings of the consistency and differences between critical and steady state lines and studies of permeability impacts on liquefaction are reviewed and discussed.

Chapter 3 illustrates in detail the methodology of the adopted Distinct Element Method (DEM), and the proposed further developed fluid-coupled DEM scheme. As main components of the DEM, the force displacement law, the equation of motion, damping effects, and a critical time step are introduced with an application to elliptical particles. For fluid flow effect, a systematic process from pore identification to individual microscopic pore pressure calculations and their coupling with DEM are presented. In addition, an explanation of the servo control boundary conditions implemented in the simulation, and the adopted representations of the macroscopic average stress, strain and pore pressure are also shown in this chapter. Finally, the "pore groups" idea and some of the fluid-coupled DEM implementation details are enumerated, and a comparison of improved model's behavior with the behavior of a poro-elastic configuration is presented.

Chapter 4 presents results of the undrained biaxial compression simulations using the proposed further developed fluid-coupled DEM for granular assemblies with different initial conditions (void ratio and confining stress). A particular floating particle removal technique is presented that creates samples with different initial void ratios for simulations. With the data extracted from the simulations, analyses based on both classical soil mechanics and micromechanics are conducted, which interpret the macroscopic undrained behaviors of the granular assemblies through micromechanical concepts and descriptors. A comparison of the simulated results with physical data taken from laboratory tests found in the literature is made to show the practicality of the simulation. At the end of the chapter, a comparison of the undrained behaviors obtained by using the proposed further developed fluid-coupled DEM with that from the constant volume method is performed and studied to examine the differences between the two methods.

Chapter 5 shows a study of the effect of permeability on liquefaction susceptibility by using improved fluid-coupled DEM with various permeability representations. Five simulations are conducted on exactly the

same liquefiable assembly but with different permeability representations. Both soil mechanics and micromechanical analysis are performed to study the impact of permeability on the liquefaction susceptibility. The simulated results are then compared with those of laboratory undrained tests of sand with different percentages of fine components taken from the literature to show the consistency.

Chapter 6 presents a study of the consistency between the critical state line and the steady state line from the perspective of both classical soil mechanics and micromechanics. A series of drained simulations and some undrained simulations in addition to those already presented in Chapter 4 are conducted in this chapter to construct the critical state line and steady state line. The consistency of the two lines is studied in terms of both void ratio and average coordination number versus the mean effective stress, the former of which is also compared with that from the physical data found in the literature.

Chapter 7 highlights the conclusions of this thesis and proposes some work and some recommendations for the future.

1.5 Significance of the research

In this research, a further developed version of the fluid-coupled DEM model that was first developed by Olivera in 2004 is proposed by introducing the idea of "pore groups". Using this idea, the difficulty of effectively computing the pore pressure effect on particles during the rapid changes in pore structure due to creation and disintegration of inter-granular contacts is overcome. This occurs, during the formation of liquefaction, when extremely complex modification of pore space occurs when both coalescence and subdivision of voids is taking place affecting a group of voids simultaneously. Using this method, the "pore groups" are kept track of when some voids coalesce due to contact disintegration and other voids are subdivided into parts due to contact creation, hence, allowing the micromechanical undrained behavior of a granular media to be simulated. Due to the effectiveness in capturing the microscopic pore pressure effects on the particles in the assembly, the formation mechanism of the liquefaction phenomenon is interpreted through the micromechanical descriptors. This contributes to a comprehensive understanding of liquefaction. In addition, through a comparison between the further developed fluid-coupled DEM in this research and the frequently used constant volume method, the deficiencies of the latter are explained.

A micromechanical study of the effect of permeability on the liquefaction susceptibility of a granular media subjected to a monotonic loading conducted in this research, describes the micromechanical mechanisms controlling the influence of permeability on liquefiable assemblies. The permeability effect depicted in the simulation provides insights into the practical evaluation of liquefaction potential.

A micromechanical study of the ultimate states of granular media in drained and undrained conditions, the critical state and the steady state was conducted. The different opinions regarding the consistency of the

critical state line and steady state line in past research were clarified using micromechanical descriptors. The comparison of the two ultimate state lines contributes to the fundamental justification for treating liquefaction as a critical state phenomenon and using the much better-studied drained characteristics of sands to predict behavior in the undrained and liquefaction conditions. It also contributes to the characterization of the parameters controlling liquefaction.

Chapter 2 Literature Review

2.1 General

This chapter presents a literature review of both continuum mechanics based and micromechanics based concepts in studies of granular material, and reviews the engineering properties of sand in both drained and undrained conditions. Particularly, the undrained behavior and properties of sand obtained from the traditional soil mechanics and a brief explanation of some micromechanics concepts and theories are introduced for a better understanding of the results in later chapters. Section 2.2 introduces a history of the development of DEM and fluid-coupled DEM. Section 2.3 gives an introduction to some typical undrained behaviors and studies of granular soil based on classical soil mechanics. A description of micromechanics based concepts and theories related to this research is presented in section 2.4.

2.2 Evolution of micromechanical studies on granular media

The micromechanical study of granular media started since the middle of the twentieth century, and experienced four phases, which are a qualitative study, a quantitative study, a numerical DEM study, and a fluid-coupled DEM study. The first three phases are only related to behavior of dry granular media at a particle level and do not involve fluid flow. In the following, the evolution of micromechanical studies on granular media will be introduced in terms of these four phases.

2.2.1 Qualitative micromechanical study of granular media

Initial studies of the micromechanics of discrete assemblies started with using the metal rods by Schneebeli (1956) and later the optically sensitive material by Dantu (1957) to simulate a two-dimensional discrete system. The forces were transmitted through the chains of particles in a preferred direction was discovered from using the optically sensitive material, which announced the importance of the study of microstructure, fabric anisotropy and the internal force interaction mechanism of granular media.

Among the earliest studies of fabric anisotropy, the studies of the contact frequency distribution in the form of a rosette by Biarez and Wiendieck (1963) showed that contact anisotropy and the applied load direction are almost coincident. In 1969, De Josselin De Jong and Verruijt conducted a biaxial compression test using photo-elastic discs to extract microscopic information from discrete granular models (De Josselin De Jong and Verruijt, 1969). Figure 2.1(a) explains the test settings ($F_2 > F_1$), and the induced contacts in the vertical and horizontal directions are shown in Figure 2.1(b) and (c), respectively. Conspicuously, more contacts are exhibited in the vertical direction than in the horizontal direction, which is in accordance with a higher load F_2 being applied vertically than the load F_1 in the horizontal direction. The difference between the number of contacts in the two directions indicates the production of an anisotropy. Inspired by the above work, Oda and Konishi (1974a), (1974b) performed biaxial compression tests and simple shear tests using

photo-elastic cylinders to examine contact normal directions and contact force distribution characteristics. The contact normal directions and contact force distributions they extracted from the isochromatics confirmed Dantu's conclusion that loads are transmitted through chains of particles and perpendicular to the contact planes (Oda and Konishi, 1974a, b). In addition to the above studies on the anisotropy and internal force transmission, the average coordination number as a crucial micromechanical descriptor was also studied and demonstrated that it is highly correlated with the void ratio (porosity) and the relative density of a material (Smith et al., 1929; Field, 1963; Athanasiou-Grivas and Harr, 1980).

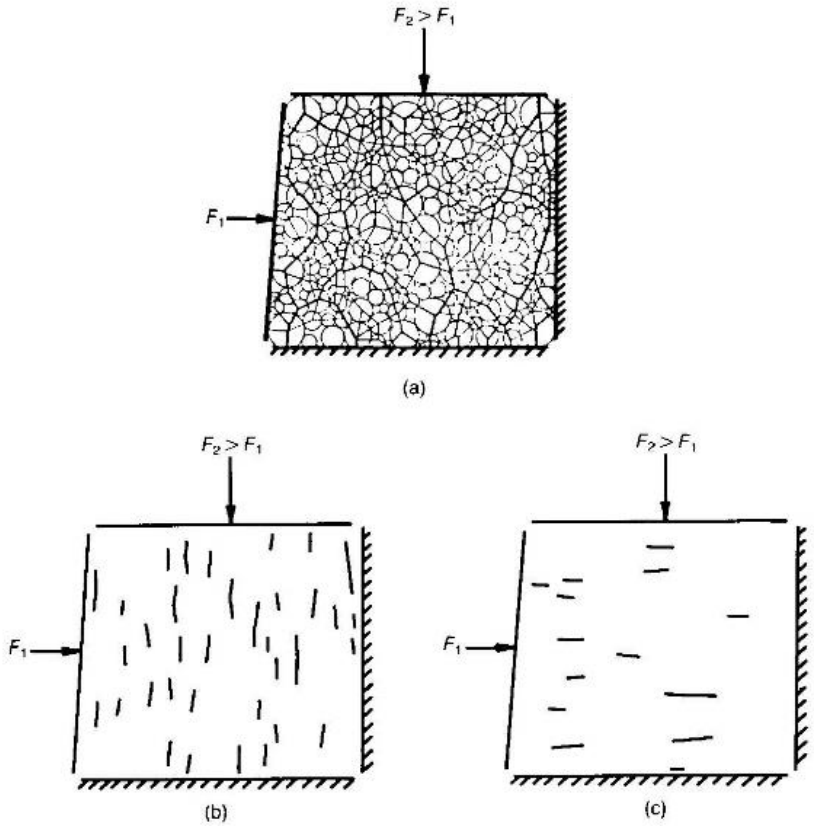

Figure 2.1 Biaxial compression test on a photo-elastic disc assembly (a) contact force distribution; (b) contacts in vertical direction; (c) contacts in horizontal direction (after De Josselin De Jong and Verruijt, 1969)

2.2.2 Quantitative micromechanical study and numerical simulation of granular media

The quantitative study of the micromechanical properties of granular materials started with the study of the average stress tensor (Hill, 1963; Weber, 1966; Drescher et al., 1972;Landau and Lifshitz, 1980) and the distribution of particle contact orientations (Biarez and Wiendieck 1963; Horne, 1965; Konishi, 1978) for a large homogeneous discrete assembly. Both two and three dimensional models using photo elastic materials were adopted for extracting microscopic information. In 1980, a stress-force-fabric relationship

was proposed by Rothenburg (1980) (see equation (2.26)), which incorporated the macroscopic stress, the contact forces and the associated anisotropic descriptors. A detailed description of the quantitative study of micromechanics on granular materials has been included in section 2.3.

The micromechanical study of granular media developed rapidly in the late of 1970's due to the availability of the computer facilities. Numerical methods were developed to simulate particle movement and load transmission, which were favored than the other methods for the easiness of extracting the micromechanical details at each step during a test. In 1978, the Distinct Element Method (DEM) was developed (Strack and Cundall, 1978) to simulate a two-dimensional granular system under a simple shear mode. This method is a modified version of the Distinct Block Method (DBM) proposed by Cundall (1971), which was applied to simulate forces between discrete blocks of rock mass. The FORTRAN program BALL was constructed to apply the DEM model to a granular media in order to produce a numerical analogue of the published laboratory tests done by De Josselin De Jong and Verruijt (1969), and Oda and Konishi (1974a). Following the above pioneering work, Bathurst in 1985 implemented a highly modified version of BALL, named DISC, to simulate a two-dimensional biaxial compression test (Bathurst, 1985; Rothenburg and Bathurst, 1989; Rothenburg and Bathurst, 1991; Bathurst and Rothenburg, 1988; Bathurst and Rothenburg, 1990), the stress-force-fabric relationship (2.26) was verified by these numerical simulations.

2.2.3 Numerical simulation of undrained granular media

The undrained simulation applying the Discrete Element Method was first mentioned by Cundall and Strack in 1979 (Cundall and Strack, 1979), but the pore pressure effect during an undrained test was not proposed until Hakuno and Tarumi (1988). In their work, the fluid was regarded as an elastic material, and the excess pore pressure was induced by the volume change of the system. Extending this idea, Nakase et al. (1999) used square elements instead of pores to calculate pore pressure changes in terms of the total volume change based on the displacement of neighbouring cells. Since there is a pressure discrepancy across cells, fluid will flow from a high pressure to a low pressure region, which in turn induces forces that are transmitted to the particles. Also extending the idea of Hakuno and Tarumi (1988), Thallak (1991) proposed a 2-D flow-coupled discrete model of a disc assembly to simulate hydraulic fracturing in a granular media with a single phase fluid flow in 1991. The flow channels were assigned by connecting the nodes inside the pores, and the volumetric flow rates were computed using the Hagen-Poiseuille equation. A modified version of Thallak's model was proposed by Olivera in 2004 to simulate undrained behaviors of granular material of elliptical particles. The main idea of Olivera's model is adopted in this research to simulate undrained behaviors of the granular material.

2.2.4 Fluid-coupled DEM versus constant volume method

Research on the numerical simulation of soil liquefaction or undrained responses mainly follows two methods, which are constant volume DEM modelling and fluid-coupled DEM modelling. The former imposes the constraint of constant volume for the target undrained simulation domain under the assumption that both soil particles and water have a low compressibility (Olivera, 2004; El Shamy and Zeghal, 2005; Hakuno and Tarumi, 1988; Nakase et al., 1999; Okada and Ochiai, 2007; Shafipour and Soroush, 2008; Thallak, 1991; Zeghal and El Shamy, 2004). The constant volume constraint is implemented by applying a compress strain rate in vertical direction and an equal tensile strain rate in the horizontal direction for two-dimensional biaxial modelling. This method avoids complicated calculations for the soil and fluid interaction, but cannot depict the real characteristics of microscopic pore pressure variations and the micromechanical mechanisms of liquefaction. By contrast, the latter one, the fluid-coupled DEM can achieve this goal, although the computation is much more complicated than constant volume DEM modelling (Olivera, 2004; El Shamy and Zeghal, 2005; Hakuno and Tarumi, 1988; Nakase et al., 1999; Okada and Ochiai, 2007; Shafipour and Soroush, 2008; Thallak, 1991; Zeghal and El Shamy, 2004). The fluid-coupled DEM method can be used to model the fluid phase and solid particle phase separately and simultaneously, so that the effects of the fluid phase are incorporated into modelling of the solid particle phase to implement the overall action into a motion calculation for the next cycle. Because the force from fluid flow through the porous media system is simulated and applied to the particles, this method can demonstrate the interactions between the fluid and soil particles and reveal the underlying characteristics of soil undrained response and the fundamental cause of liquefaction. The widely adopted fluid simulation components for fluid-coupled DEM are continuum based modelling by applying finite element or finite difference methods (Shafipour and Soroush, 2008; Zeghal and El Shamy, 2004) and microscopic based modelling achieved by computing of each one of the pore pressure's variations (Olivera, 2004; Hakuno and Tarumi, 1988). To conduct a comprehensive micromechanical study, this research will adopt the latter one, to study the effects of each individual pore pressure and model the dynamic interactions between the fluid flow and soil particles.

2.3 Undrained behaviors and studies of granular soil based on classical soil mechanics

2.3.1 Undrained behavior of granular soil under monotonic shearing

The undrained behavior of soil under monotonic shearing may be understood by examining the stress-strain response on the q-ε_t plane, the pore pressure variation on u-ε_t plane, the stress path on q-p' plane, and the state diagram on e-p' plane as shown conceptually as Figure 2.2. From Castro (1969), there are typically three types of stress-strain responses (Fig. 2.2a) with their associated pore pressure generation (Figure 2.2b)

and stress paths (Figure 2.2c) that can be predicted for a typical undrained monotonic loading test depend on the location of the soil's initial state (e and p') on the state diagram (Fig.2.2 d).

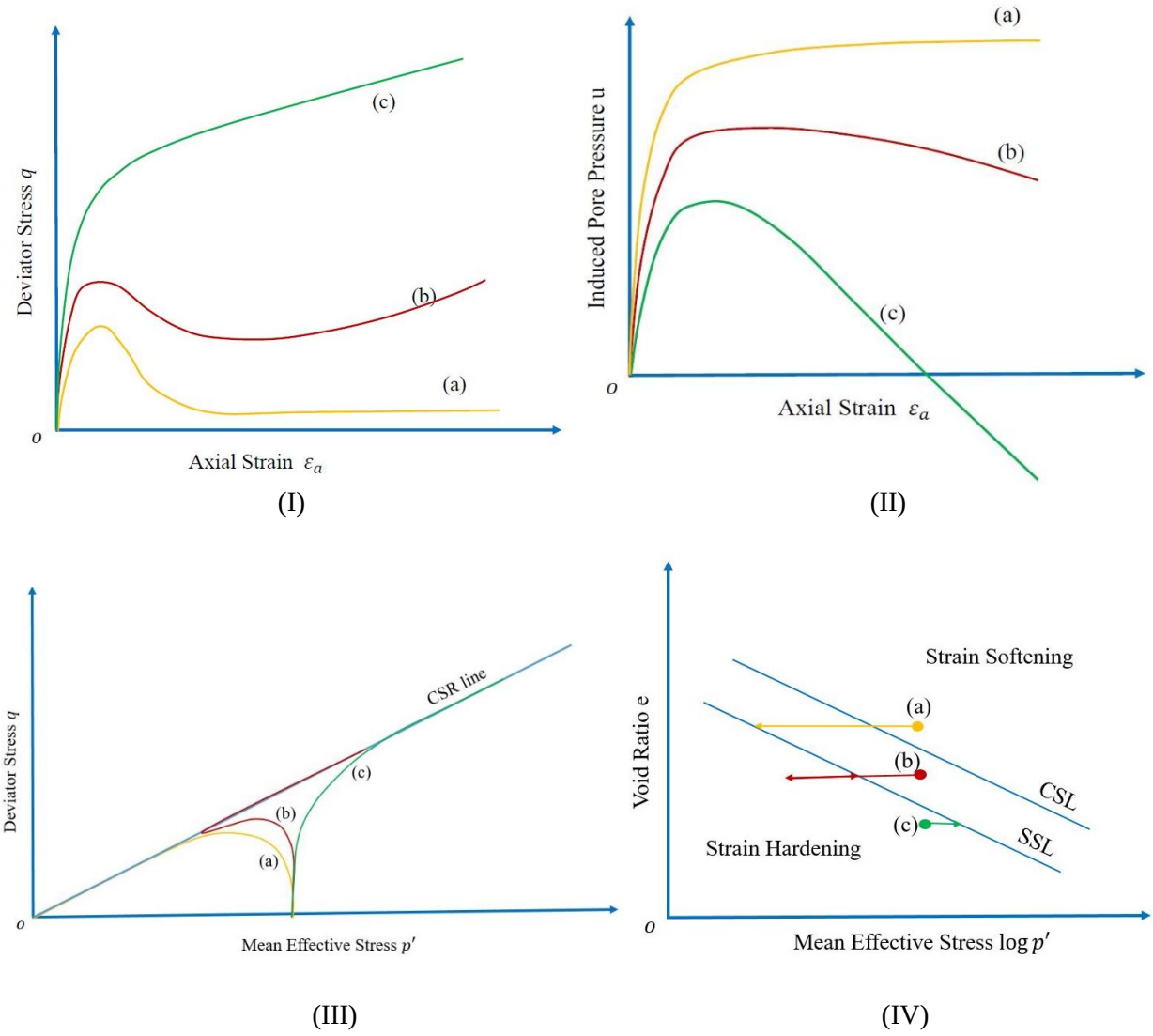

Figure 2.2 Conceptual undrained behavior of sand from monotonic shearing tests

Test (a) depicts a traditional strain softening response, which happens when the initial state of a soil sample is above the critical state line on state diagram (Figure 2.2d). This type of response usually occurs when the samples are very loose. It can be seen in Figure 2.2a that at the beginning of the test, the deviator stress increases rapidly and attains its peak value at a low axial strain. Meanwhile, the associated pore pressure (Figure 2.2b) also increases rapidly and reaches large value at the strain where the deviator stress hits its peak value. After that, the deviator stress starts to drop until a low value and stays at the low value (the residual strength) with increasing axial strain. In this phase, the pore pressure still increases a bit but quite slowly until it finally attains and maintains an almost constant peak value, which indicates the occurrence

of a steady state. The stress path of test (a) displayed in Fig. 2.2c also indicates a strain softening response, which tends to converge with a single point on the critical stress ratio line indicating the arrival of steady state deformation. Sladen et al. (1985) denotes a line connecting the convergence point and the peak deviator stress as a collapse surface, which distinguishes stable undrained behavior from unstable undrained behaviors. A similar idea called "flow liquefaction line" proposed by Lade and Pradel (1990) also presents the boundary between stable and unstable responses but connected the peak deviator stress point with the origin point on a q-p' plane, indicating no residual strength at the end of liquefaction.

Test (b) in the figure displays a classical strain softening-hardening type of response. From Castro (1969), this type of response usually occurs when the initial state of the soil sample falls between the CSL (critical state line) and SSL (steady state line) indicated in Figure 2.2d. A characteristic of this strain softening-hardening type of response is, that after reaching the maximum deviator stress at a relatively low strain, the shear resistance first declines to the minimum strength then remains at an almost constant value with continued shearing for a while and afterwards rises mildly. During the shear resistance variations, the pore pressure initially increases rapidly but at a lower rate than in test (a). When the deviator stress reaches its maximum value, the corresponding pore water pressure usually has attained over 80% of its ultimate value. Continued shearing raises the pore pressure to its maximum value. Afterwards, when the deviator stress increases again, the pore pressure reduces accordingly indicating the tendency to dilation. Distinctively, the particular stress-strain and the pore pressure response of test (b) corresponds to the tendency to change from volume contraction to volume dilation. The stage in which an intermediate minimum shear strength combines with a maximum pore water pressure was named quasi-steady state, by Alarcon-Guzman et al. (1988). This phenomenon has been described by numerous researchers (Ishihara, 1993; Ishihara et al., 1975; Konrad, 1990a,b; Mohamad and Dobry, 1986; Vaid et al., 1990). The minimum strength is important in a practical sense because it may be less than the residual strength. Sometimes "quasi-steady state" is also named as "limited liquefaction" alternatively that proposed by Alarcon-Guzman et al. (1988), Been et al. (1991), Castro (1969), and Ishihara et al. (1975). A concept very similar to quasi-steady state is the phase transformation proposed by Ishihara et al. (1975), and Ishihara (1993), which was also used to describe the tendency to temporary transition from contraction to dilation. For most cases, the above two terms may be used interchangeable, however, phase transformation is a more extensive concept, which is not necessarily associated with a temporary drop in shear stress. Some research indicates that the quasi-steady state depends on a soil's condition during consolidation and initial shear (Ishihara, 1993; Verdugo and Ishihara, 1996). Kramer and Seed (1988) indicated limited liquefaction should also be considered as a type of liquefaction because of the danger induced by the large deformations. Although the quasi-steady state makes the undrained response very special, some research suggests that the quasi-steady state is the same as the steady state. Castro (1969) indicates that a steady state line and a quasi-steady state line merge in a state diagram.

Ishihara (1993) postulates that the phase transformation merges with the steady state for very loose samples, because of the never become apparent dilative tendency. He also pointed out that the internal friction angle at the quasi-steady state and at the steady state are the same. The stress path of test (b) shown in Fig.2.2c visually displays the phenomenon of phase transformation in terms of an "elbow" when it crosses the steady state line. Further increases follow the CSR line by continue shearing.

Test (c) reveals a general strain hardening type of behavior, which usually happens when the initial state of the sample is below the steady state line (i.e. a dilative sample). It is shown in Figure 2.2a and b, both stress and pore pressure increase rapidly at the beginning of the test, and subsequently, pore water pressure reaches a maximum and then gradually reduces until the test terminates. On the contrary, in this process, the deviator stress continuously increases until the end of test. For load controlled testing, the test would terminate abruptly. However, for strain rate control, pore pressure might continue reducing until a constantly negative value is achieved, and the tendency to dilation would continue until the steady state deformation is reached. Reflected from the stress path, an "elbow" also exhibits in this strain hardening type of response when it crosses the CSR line, and will continue rising along the CSR line upon further shearing (see Figure 2.2 (c)).

2.3.2 Critical state and steady state

Critical state and steady state are similar concepts in soil mechanics, both of which are applied to define the ultimate state of a soil under shearing. Their difference lies in that the former occurs in a drained condition while the latter is usually associated with an undrained condition. From the definition, a critical state describes the ultimate state of a soil under drained shearing, in which it exhibits a constant stress, shear resistance, and void ratio (Roscoe et al., 1958). The prototype of the critical state is the "critical void ratio" or the "critical density" that was proposed by Casagrande (1940). This idea is quite similar to that of a critical state but with the focus on an unique void ratio or relative density that remains unaltered at the ultimate state instead of an overall condition the sand experiences. Figure 2.3 shows the critical void ratio obtained in a drained direct shear test that was conducted by Casagrande and Watson in 1938. The figure indicates that both loose and dense samples merge to a unique critical void ratio at the end of the tests. Based on the critical void ratio, Roscoe et al. (1958) postulated during drained shearing, a loose sand sample will contract, while if it is dense it will dilate. Both loose and dense samples of the sand will attain and maintain the same ultimate state the "critical state". Continuing with Roscoe's idea, critical state soil mechanics is developed as a sub-branch of soil mechanics started in Cambridge, UK. Both the Granta-gravel model and the Cam Clay model were proposed based on the theory of plasticity and the idea of critical state (Schofield and Wroth, 1968).

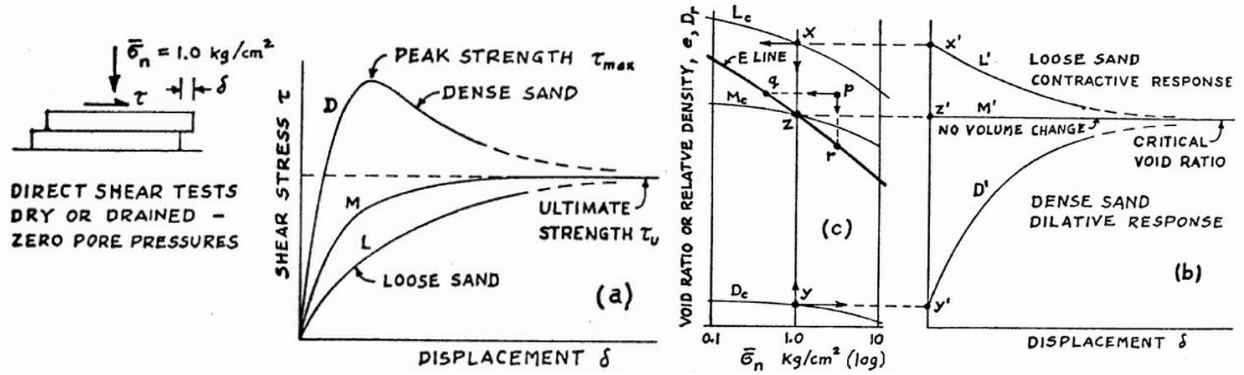

Figure 2.3 Concept of the critical void ratio (after Casagrande and Watson, 1938; Casagrande, 1976)

Corresponding to the critical state, the steady state is the ultimate state for undrained shearing when "constant volume, normal and shear stresses, and velocity" are achieved (Poulos, 1981). For the liquefiable soils, the steady state only appears after flow liquefaction is initiated (Poulos, 1981). Some researchers believe that a "flow structure" exists when steady state deformation occurs (Poulos, 1981; Poulos et al., 1985), however, only limited hypothesis descriptions of the imagined "flow structure" have been proposed, no quantitative demonstrations have been reported within the scope of the author's knowledge. Figure 2.4 and Figure 2.5 depict the steady state deformation in both monotonically and cyclically loaded anisotropically consolidated undrained triaxial tests that were conducted by Castro (1969). The figures indicate that both monotonic and cyclic loads can trigger liquefaction in undrained condition. The deviator stress dropped rapidly after the initiation of liquefaction and thereafter remained at a very low value with increasing axial strain which announced the formation of steady state.

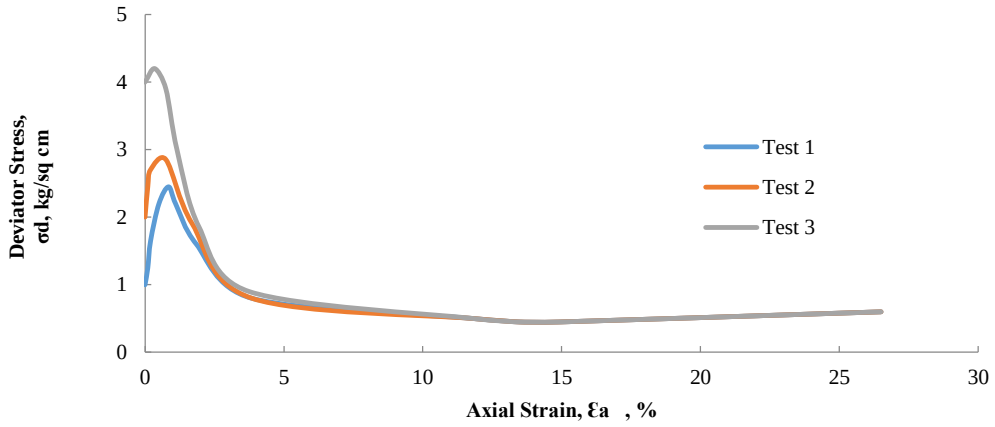

Figure 2.4 Steady state formation from three monotonically loaded, anisotropically consolidated triaxial tests (replot from Castro, 1969)

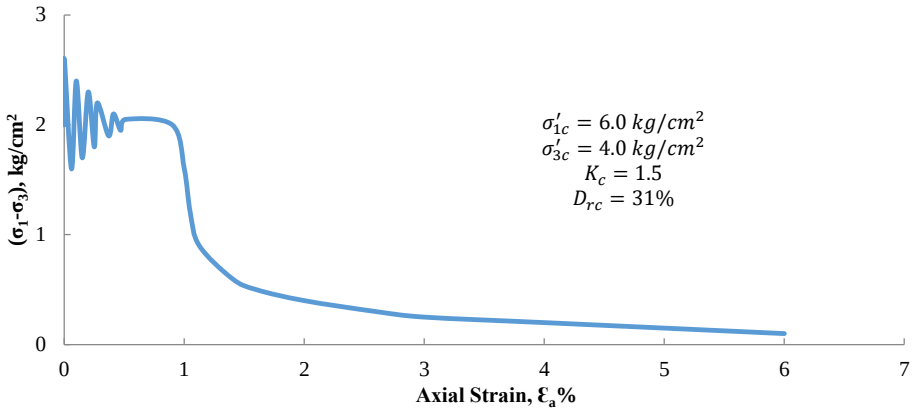

Figure 2.5 Steady state formation from a cyclically loaded, anisotropically consolidated triaxial test (replot from Castro, 1978)

2.3.3 Dispute regarding the consistency of the critical state line and the steady state line

As already introduced in Fig. 2.2, from Castro (1969), a granular soil's behavior can be predicted based on its initial state referenced to the CSL and SSL on the state diagram. Hence, Castro (1969) believes the two lines are different, which prompted comparisons between the critical state line and the steady state line. In his thesis, a series of drained and undrained triaxial tests were conducted under load control, the critical state line constructed from drained tests and the steady state line constructed from undrained tests were obtained and compared. The result of the comparison is shown as Fig. 2.6, it can be seen from the figure that the critical state line e_S and the steady state line e_F varied greatly, e_F lies to the left and below e_S. These two lines are both referenced to the initial condition of a given type of soil, consist of the locus of points that represents the condition of ultimate deformation under shearing. Each type of soil has unique critical and steady state lines, even though the initial anisotropy of the soil sample being tested may be different (Jafarian et al., 2013). It is indicated by Been and Jefferies (1985), and Jefferies and Been (2006) that as a reference criterion, the two lines encompass all the soil property information such as compressibility, grain character, and steady state friction angle (Been and Jefferies, 1985; Jefferies and Been, 2006).

The dispute regarding the consistency of the critical state line and the steady state line has continued ever since Castro reported a discrepancy between the two lines. In 1981, Poulos (1981) presented a definition of steady state deformation, and postulated that a "flow structure" arises at the steady state. He pointed out that a steady state can exist in any drained condition as long as the "flow structure" appears, but did not mention the steady state line is unique under different drainage conditions. However, Poulos et al. (1988) indicated that a unique steady state line exists for a "narrowly graded, fine and angular quartz sand that is the tailing from tar-sand operations." Consistent with Poulos et al., other researchers Been et al. (1991), Sladen et al. (1985), and Verdugo and Ishihara (1996) all believe in the coincidence of the critical state line

and the steady state line. Contrary opinions voiced by Alarcon and Leonards (1988), Alarcon-Guzman et al. (1988), and Castro (1969) state that the drained and undrained steady state lines are different, it is the pore water pressure induced by the sudden soil structure collapse that results in the discrepancy between the two lines (Alarcon-Guzman et al., 1988). Also, Konrad (1990a), (1990b) reported a non-uniqueness of the steady state line, both upper and lower limits of the steady state line were proposed based on laboratory tests. A coincidence of the steady state line and the critical state line was not supported by the research conducted by Konrad, because even the steady state line itself was not unique in his results.

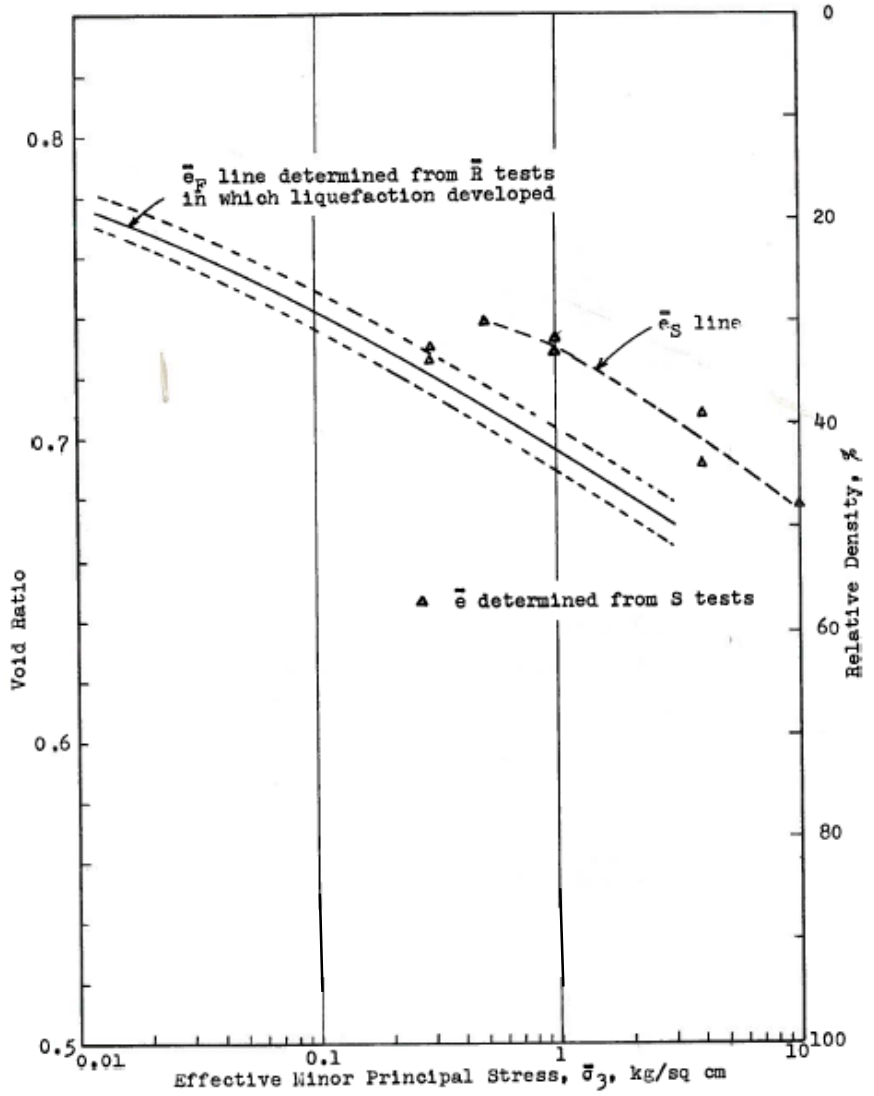

Figure 2.6 Comparison of the critical state line e_S and the steady state line e_F (Castro, 1969)

2.3.4 State parameter and state index

It is recognized that the stress-strain response of a soil under shearing depends on its initial void ratio and confining stress, which can be altered by an applied action. With different confining stresses, a soil can

behave quite differently even though having the same initial void ratio. Studies have shown that it is the combination of void ratio and confining stress that controls the deformation of a soil (Bolton, 1986; Rowe, 1962; Roscoe and Poorooshasb, 1963). These authors postulate that the distance between the void ratio at initial state and the void ratio at steady state controls soil behavior, which is the prototype of the concept of a "state parameter". However, it was not until in 1985 that this distance was named as "state parameter" by Been and Jefferies (1985). Since then, the void ratio and the confining stress have been unified as a one parameter to predict a soil's behavior under shearing.

The meaning of the state parameter ψ can be explained with the help of Figure 2.7, it is the vertical distance from the current void ratio of the soil to the void ratio of the critical state at the same mean effective stress. From the studies of Been and Jefferies (1985), and Jefferies and Been (2006), soils with the same state parameter behave similarly in both drained and undrained conditions. The peak undrained shear stress, the pore pressure parameter, the angle of the shearing resistance, the cone penetration resistance, and the dilation rate are all highly related to the state parameter (Been and Jefferies, 1985; Jefferies and Been, 2006).

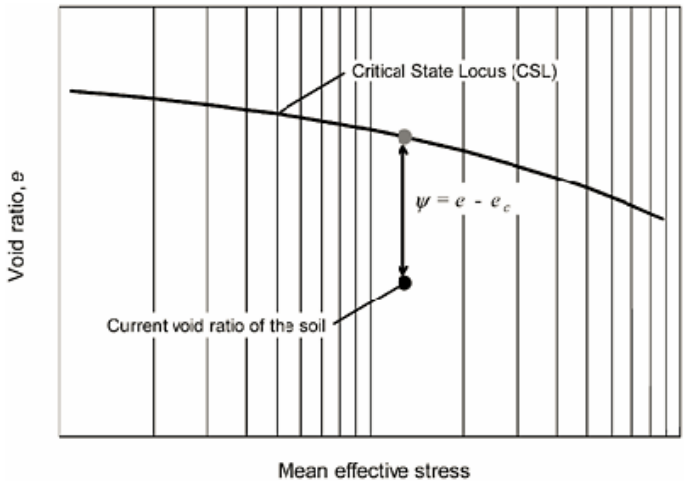

Figure 2.7 Concept of the state parameter (Jefferies and Been, 2006).

Following the idea of the state parameter from Been and Jefferies (1985), Konrad (1990a), (1990b) proposed a modified state parameter, which has the form of equation (2.1):

$$\Psi_i = e_c - e_{UF} \tag{2.1}$$

Where e_c is the void ratio after consolidation and e_{UF} denotes the void ratio at the upper limit of the steady state line. Konrad's idea came from the fact that the steady state points scattered significantly in the laboratory testing he conducted. He concluded based on the test results he obtained that the steady state line is not unique, but that upper and lower limits of the steady state line exist. The modified state parameter

that proposed by Konrad applies the void ratio at the upper limit of the steady state line instead of at the unique steady state line proposed in prior research.

In 1993, Ishihara proposed a state index given the reason that a state parameter is less tenable for soils at a low confining stress and a high void ratio. He pointed out that sand behavior becomes very sensitive when the void ratio is large, therefore, instead of using the void ratio at the steady state, Ishihara proposed using the void ratio at the quasi-steady state as a reference. The advantage of this modification lies in that it considers the sand behavior in the medium strain range, and hence is well suited to determining the minimum strength in a practical problem. The definition of the state index I_s is given by equation (2.2).

$$I_s = \frac{e_0 - e}{e_0 - e_s} \tag{2.2}$$

where e_0 is the threshold void ratio at which the residual strength becomes zero and e_s is the void ratio at the quasi-steady state for a given confining stress. Since the state index I_s takes care of the medium strain range, it has practical meaning. However, the limitation of the state index lies in the non-uniqueness of the QSS line, which usually depends on the initial fabric of the sand. Thus, the sample preparation method has to be indicated when using the state index in a practical problem. On the contrary, the state parameter applies the void ratio at the critical state, which is determined uniquely without relating to the initial fabric.

2.3.5 Influence of sample preparation methods

It is introduced above that the initial state of a soil, specifically the void ratio and confining stress, controls a soil's behavior to a significant extent, i.e. the steady state line is constructed on the e-p' plane. However, some research (Mulilis et al., 1977; Tatsuoka et al., 1986; Ishihara, 1993) reveal that soil samples formed with the same relative density but using different methods may exhibit distinct differences in resistance to liquefaction even under the same confining stress. In laboratory testing, the two frequently used methods for sample preparation are the moist tamping and the air pluviation. The former may be assumed to reproduce loose windblown deposits with subsequent flooding, while the latter may represent the formation of end-tipping with subsequent flooding. Figure 2.8 depicts the influence of sample preparation on the cyclic stress ratio of sand reported by Mulilis et al. in 1977. Both moist tamping and air pluviation were adopted as the sample preparation methods. It is shown in the figure that the cyclic stress ratio varies significantly between the two sample preparation methods even though the relative density and confining stress are the same for both samples. The distinct responses may be induced by different fabric structures created during samples preparation. Figure 2.9 is reported by Benahmed et al. (2015), which demonstrates the influence of sample preparation on the stress-strain response and the effective stress paths of a typical soil. Again, both air pluviation and moist tamping methods are adopted to prepare soil samples with the

same relative density. However, it is indicated from the figure that in undrained loading, moist tamping leads to soil strain softening while air pluviation induces strain hardening. The corresponding effective stress path plots go completely opposite directions. Therefore, it may be concluded that void ratio or relative density is not enough to combine with the confining stress to determine the potential of a soil's instability in an undrained condition. Some soil strcture characteristics should also be included in order to explain soil's behavior under undrained shearing.

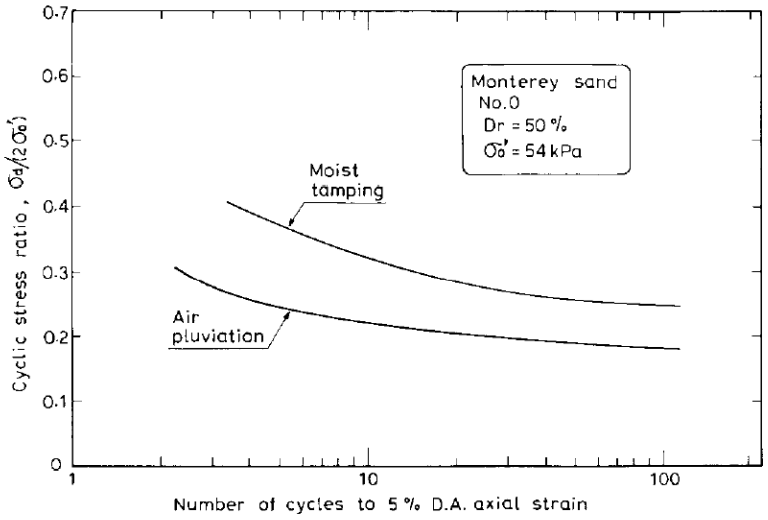

Figure 2.8 Influence of different sample preparations on sand's cyclic shear strength (Mulilis et al., 1977)

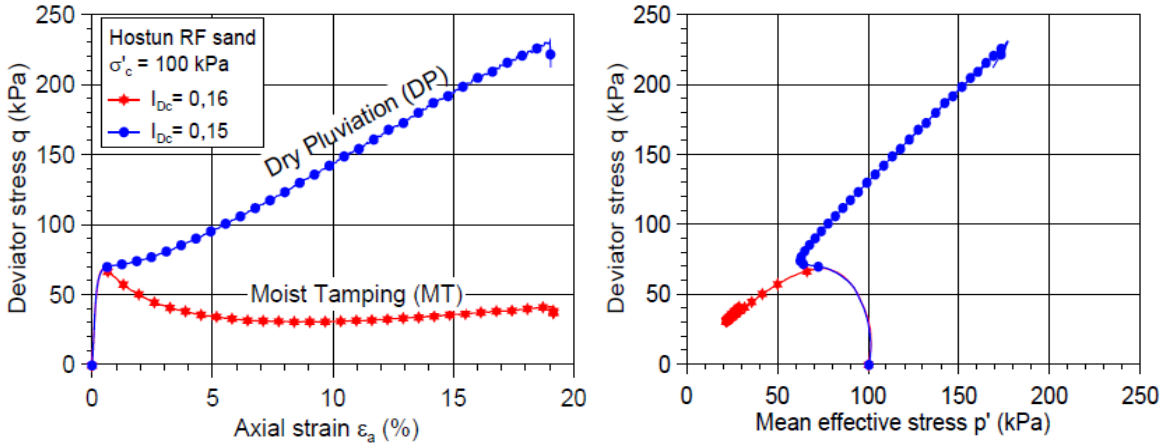

Figure 2.9 Effects of sample preparation on stress-strain responses (left) and mean effective stress paths (right) (Benahmed et al., 2015)

Explanations regarding why the two sample preparation methods can induce completely different responses were proposed by N. Benahmed et al. in 2015 using electron microscope observations. It is shown as Figure 2.10 that microphotographs of Hostun sand from electron microscope observation reveal totally different

structures for the two methods. The moist tamping method produces an aggregates and macropores structure while dry pluviation generates a regular single-grained packing. It may be that the "metastable" macropores structure that the moist tamping method produces resulted in an instability leading to liquefaction, because of the tendency to a higher volume contraction would create a larger pore pressure and thereby a lower effective stress. However, this might only be the case for relatively loose samples since research from Ishihara (1993) indicates that the isotropic consolidation line for a sand in the densest state is unique from different preparation methods (Ishihara, 1993).

Figure 2.10 Microphotographs showing aggregates and macropores structure, and regular single-grained packing structure (Benahmed et al., 2015)

2.3.6 Permeability effect on liquefaction susceptibility

Studies about the permeability effect on liquefaction susceptibility haven been conducted in the past two decades by many researchers from both laboratory testing and numerical simulations. Among them, most studies of permeability impacts on the excess pore pressure generation and dissipation properties are mainly focused on simulating the cyclic load occurring during an earthquake by using the centrifuge or shaking table methods. For example, the level ground seismic centrifuge test conducted by Dewoolkar et al. in 1999 that used both water saturated soil and metolose (very viscous fluid) saturated soil to highlight the permeability effect, indicated that a lower permeability was achieved by dissolving powdered methylcellulose in water to induce a much higher excess pore pressure generation rate and a much lower dissipation rate than those obtained for water alone (Dewoolkar et al., 1999). The addition of metolose resulted in the occurrence of liquefaction, which did not happen in the comparable water saturated soil due to an associated higher permeability. Similar to the results from laboratory testing, numerical simulations of the permeability effect on liquefaction potential of sand subjected to cyclic loading conducted by other

researchers also demonstrated that soil with a higher permeability tends to be less susceptible to liquefaction (Yang and Elgamal, 2002).

The effect of monotonic loading on static liquefaction was also examined in both laboratory and simulation studies although fewer studies were conducted than for cyclic loading. For example, studies on the liquefaction susceptibility of granular soil with different percentages of fine components are one of the representative studies that indirectly indicated permeability effect. Different permeabilities than that of a clean granular soil were examined by many researchers (Pitman et al., 1994; Lade and Yamamuro, 1997; Yamamuro and Lade, 1997; Law and Ling, 1992; Evans and Zhou, 1995), although these research did not concentrate on an analysis of the effect of permeability but rather on the influence of fine grained soils on liquefaction behavior and their contact mechanism on changing the undrained behavior. With respect to numerical study aspect, the numerical simulations of a drained monotonic simple shear test on a single element conducted by Yang and Elgamal (2002) showed that with identical mechanical soil properties in a model, a sample with a low permeability displayed a much larger shear resistance compared to the one with a higher permeability due to the negative pore pressure generation. However, the simulation is under drained condition, thus, the permeability effect on the liquefaction susceptibility is not really depicted. Due to the lack of attention to the effect of permeability on granular sand triggered liquefaction, this research will perform an extensive study of the effect of permeability from both macroscopic and microscopic perspectives, and explain the mechanism by which it affects the liquefaction susceptibility.

2.4 Micromechanics based concepts and theories

2.4.1 Descriptors of fabric and microstructure of granular media

In order to apply a micromechanical analysis to a study of the undrained behavior of granular media, some terminology that is exclusively used in micromechanics on a particle scale need to be introduced. In contrast to the concepts of overall or average properties, such as void ratio e and relative density D_r, which are used to indicate the average density of a given granular media on a macroscopic scale, concepts in micromechanics such as an average coordination number γ and contact density m_V are the two corresponding fundamental parameters used to represent the contact between neighbouring particles and the degree of particle packing intensity. By definition, the average coordination number γ is the average number of neighboring particles that each particle is in contact with in an assembly (how many of contacts each particle has). It can be calculated by using two times the number of physical contacts M (because each physical contacts contributes two contacts in an overall scale) divided by the total number of particles N in any given assembly as equation (2.4):

$$\gamma = \frac{M}{N} \tag{2.4}$$

Similarly, the contact density m_v is the number of contacts M per unit volume V in a three-dimensional system or per unit area A in a two-dimensional plane, and can be represented as:

$$m_v = \frac{M}{V} = \frac{\gamma \mathrm{N}}{V} \tag{2.5}$$

Average coordination number γ and the contact density m_v are related and both are terms used to quantitatively depict the intensity and denseness of particle packing, they are essential to the understanding of soils at a microstructural level. In addition, average coordination number is highly correlated with the void ratio (Athanasiou-Grivas and Harr, 1980; Smith et al., 1929). Since void ratio e is a fundamental parameter in describing soil behavior which various essential concepts in soil mechanics such as the state parameter are based on, therefore, the coordination number should be treated as an equally crucial variable that indicates a granular material's behavior. In a given granular system, the average coordination number can to some extent indicate the stability of the system. The higher the average coordination number, the more stable a system is. Dense packing assemblies generally have high average coordination numbers. The minimum value of the average coordination number for a two-dimensional equilibrium system is 3 from a consideration of static equilibrium for each particle.

In the case of concepts with respect to each individual particle, a sense of how the contacts between particles orientate or distribute spatially may be need to be introduced. Figure 2.11 presents the concept of contact normal, contact vectors, and contact forces given by Bathurst (1988). As illustrated on the figure, the contact vector l^c is the length between a particle's mass center and its contact point with another particle (Rothenburg and Selvadurai, 1981). A similar concept that describes how two particles in contact with each other are oriented is the 'branch length' used by Satake (1978). But branch length gives no indication on the shape of a particle, which is different from the contact vector. Also indicated in Figure 2.11 is the contact force and the contact normal direction. Basically, the contact force f^c is the inter-particle force between contacting particles named A and B in the figure, and the contact normal n^c is the unit vector orthogonal to the contact tangent line, which is tangent to both of the contacting particles and traverses the contact point. For particles with a round shape, the contact vector would be identical to the particle radius, and the contact normal orientation is parallel to the line that connects the contacting disc centers (Bathurst and Rothenburg, 1988).

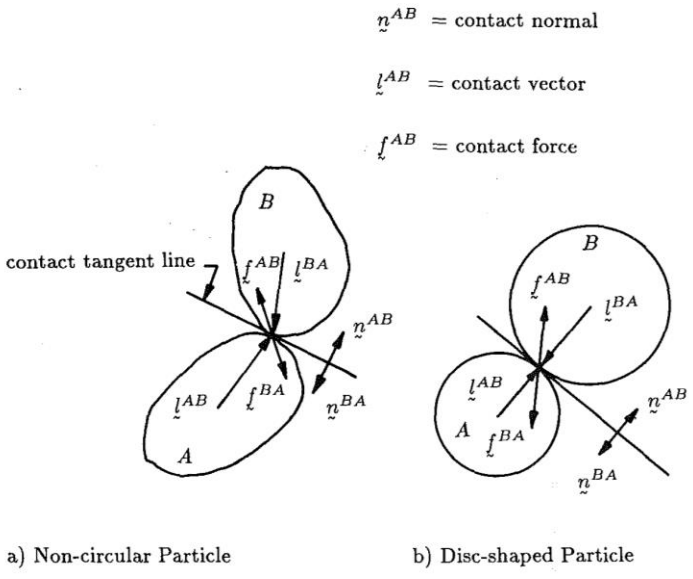

Figure 2.11 Concept of contact normals, contact vectors, and contact forces (Bathurst and Rothenburg, 1988)

2.4.2 Contact normal distribution

To study the anisotropy characteristic of a granular system, it is necessary to understand how the particulate contacts variate in space, because generally anisotropy is created when the number contacts in one direction is greater than the others during external loading. This may be achieved by examining the number or proportion of contacts that rest in each interval given that the whole plane 2π is divided into continuous groups in the sense that each group has an orientation between θ and $\theta + \Delta\theta$. Then the contact normal distribution can be introduced as a function that is applied to describe the anisotropy characteristic in terms of a polar histogram. For example, if the overall quantity of contacts M in the assembly is divided into polar groups, each one of which has an orientation between θ and $\theta + \Delta\theta$, then the number of contacts in each group or interval can be described intuitively by equation (2.6) (Horne, 1965):

$$\Delta M = MS(\theta)\Delta\theta \tag{2.6}$$

where $S(\theta)$ represents the contact normal distribution function. Since contacts within group θ and $\theta + \pi$ coincide, this symmetric property lead to the fact that the contact normal distribution function $S(\theta)$ should equals $S(\theta + \pi)$. In addition, if we take the integral of $S(\theta)$ from 0 to 2π, it yields one (see equation 2.7). For an isotropic granular system, the value of $S(\theta)$ is $1/2\pi$.

$$\int_0^{2\pi} S(\theta)d\theta = 1 \tag{2.7}$$

Since a Fourier series can be broadly used to describe a continuous periodic function, and inspired by the physical test results of fabric changes from Konishi (1978), Rothenburg (1980) suggested the following Fourier series approximation of S(θ) for a two-dimensional disc assembly:

$$\mathrm{S}(\theta) = \frac{1}{2\pi}\{1 + a_n cos2(\theta - \theta_a) + b_n cos4(\theta - \theta_b) + \cdots\} \tag{2.8}$$

where a_n and b_n are the second and fourth order coefficients of contact normal anisotropy, θ_a and θ_b are the second and fourth order principal directions of contact normal anisotropy. a_n and b_n indicate the intensity of the contact normals in the principal directions of contact normal anisotropy, usually higher values of a_n and b_n represent higher levels of anisotropy. Odd terms are cancelled out because of the symmetric property of function S(θ). Demonstrations of shape of the function S(θ) and the associated anisotropy parameters a_n, b_n, θ_a and θ_b for both initial and critical states are depicted as Fig. 2.12 (a) and (b). Both of the two polar histogram distributions are from a biaxial compression simulation of a 10000 particle sample - 36 intervals in total are grouped from the whole plane 2π. The smooth red solid line in the figure is obtained by the fourth order approximation of equation (2.8). It is seen in this figure that S(θ) with a fourth order truncation approximates the contact normal distribution well. However, it can be imagined that an increasing number of particles and total interval groups should contribute to a smoother contact normal distribution, which should be closer to the Fourier series approximation as given by equation (2.8).

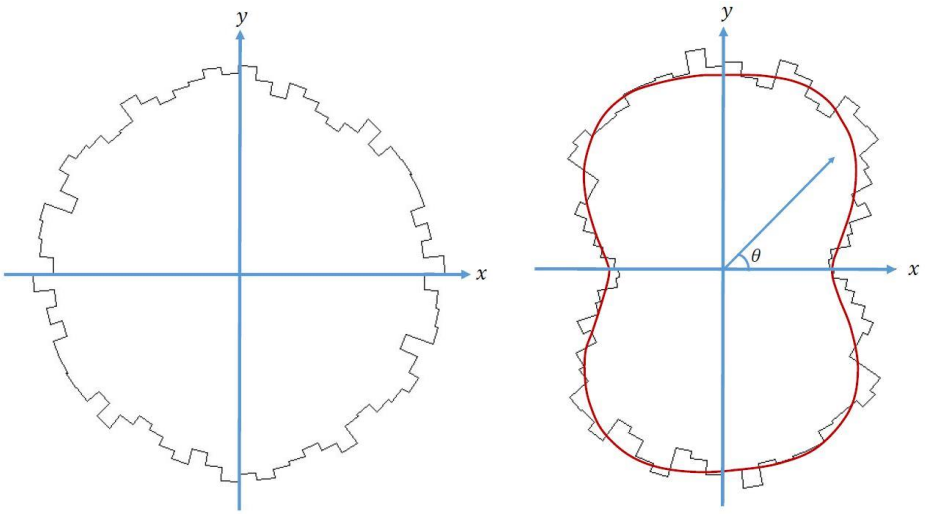

(a) (b)

Figure 2.12: Contact normal distributions and their approximation by a continuous function S(θ): (a) initial state; (b) critical state

2.4.3 Contact force distribution

Since the contact force $f_i^c(\theta)$ between any two contacting particles is a vector, it can be converted into the summation of two perpendicular vector components in a plane Cartesian coordinate system: the normal contact force vector f_n^c and the tangential contact force vector f_t^c. Each one of them can be associated with a directional unit vector in a polar coordinate system $n = (cos\theta, sin\theta)$ and $t = (-sin\theta, cos\theta)$ to indicate the corresponding force component orientation. So the contact force $f_i^c(\theta)$ can be rewritten as:

$$f_i^c(\theta) = f_n^c(\theta)n + f_t^c(\theta)t \qquad i,j = 1,2 \tag{2.9}$$

Both normal and tangential contact forces can be statistically counted in a manner analogous to the contact normal distribution function. Again, divide the plane 2π into groups in a continuous pattern, each one of the groups lies in the interval between θ and $\theta + \pi$, thus the numbers of normal contact forces and tangential contact forces that fall within each group would exhibit certain types of distribution in a plane. Since each pair of normal contact forces possesses the same magnitude but totally opposite orientation, analogous to the contact normal distribution, the normal contact force distribution can also be approximated by a Fourier series. A truncated representation of a normal contact force $f_n^c(\theta)$ with an even term is shown in equation (2.10) (Rothenburg, 1980). Only even terms are reserved for the same reason as for the contact normal distribution: normal contact forces that fall in the interval of θ and $\theta + \pi$ coincide.

$$f_n^c(\theta) = f_0^c\{1 + a_f cos2(\theta - \theta_n)\} \tag{2.10}$$

where f_0^c is the average contact force in an assembly, a_f is a second-order coefficient of the average normal contact force anisotropy, θ_n is the second-order principal direction of normal contact force anisotropy. a_f indicates the extent of the normal contact forces that fall into the direction θ_n throughout the assembly.

A similar action can be applied to obtain the tangential contact force distribution $f_t^c(\theta)$, which can also be approximated by a truncated Fourier series as given by equation (2.11), but with odd terms (Rothenburg, 1980):

$$f_t^c(\theta) = -f_0^c\{a_t sin2(\theta - \theta_t)\} \tag{2.11}$$

where a_t is a second-order coefficient of the average tangential contact force anisotropy, θ_t is the second-order principal direction of tangential contact force anisotropy. Equation (2.11) is satisfied when θ_t is equivalent to θ_a, otherwise a parameter α_w should be introduced to counter balance the difference between θ_t and θ_a. A demonstration of the measured normal and tangential contact force distributions for the initial and critical states from a 10000 particle biaxial compression simulation with 36 group orientations fitted with equation (2.10) and (2.11) is shown in Figs. 2.13 and 2.14, respectively. A better fit may be expected

if an assembly with a larger number of particles along with more group intervals is introduced, although from the graphs the Fourier series approximations are already fit with the simulation results well.

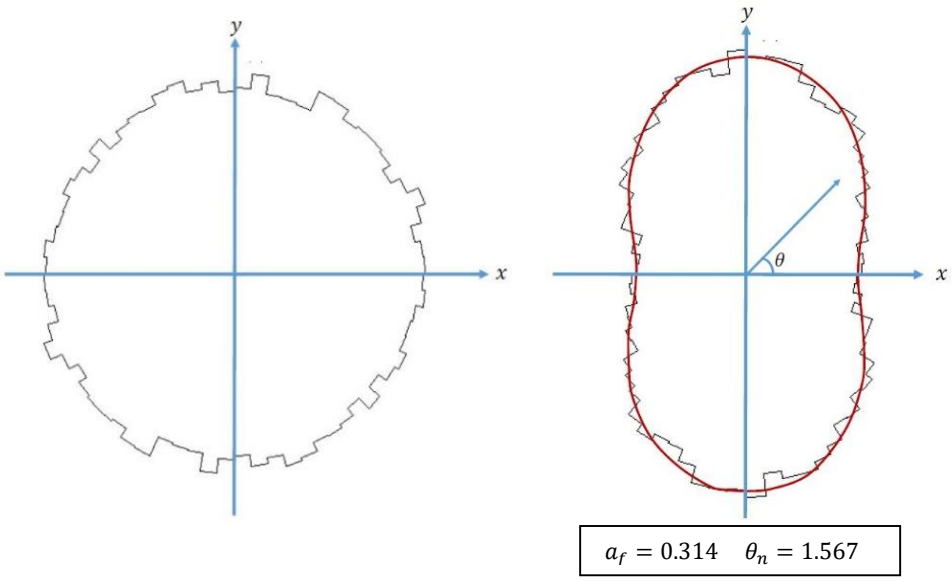

(a) (b)

Figure 2.13 Average normal contact forces and their approximation by a continuous function: (a) initial state; (b) critical state

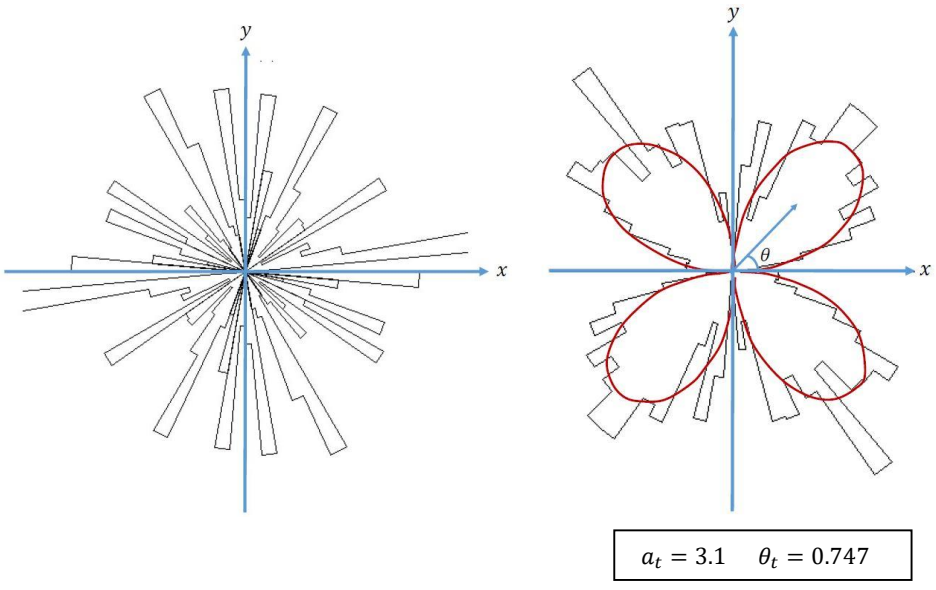

(a) (b)

Figure 2.14 Average tangential contact forces and their approximation by a continuous function: (a) initial state; (b) critical state

2.4.4 Average stress tensor from microstructure representation

Previous studies of the stress tensor in a granular assembly indicate that considering the tractions on the boundary segments and following Cauchy's theorem and the Gauss-Green theorem, a macroscopic stress tensor σ_{ij} may be introduced to describe the tractions on the boundary, which has the form of:

$$\sigma_{ij} = \frac{1}{V}\sum_{\beta \in S} f_i^{\beta}\, r_j^{\beta} \tag{2.12}$$

where f_i^{β} is the boundary force, and r_j^{β} is the location vector that corresponds to that force (Landau and Lifshitz, 1980; Drescher and De Josselin De Jong, 1972; Strack and Cundall, 1978). In addition, from static equilibrium, considering all contact forces and the associated position vector for each particle, Rothenburg (1980) proposed that in an overall sense, boundary forces and internal contact forces are related through the boundary force position vector and contact vector as:

$$\sum_{\beta \in S} f_i^{\beta}\, r_j^{\beta} = \sum_{c \in S} f_i^{c}\, l_j^{c} \tag{2.13}$$

where f_i^{c} is the internal contact forces between contacting particles and l_j^{c} is the contact vector from each contact. Thus, combining equations (2.12) and (2.13), the macroscopic average stress tensor may be represented by the volume average of internal contact forces and their associated contact vector lengths as follows:

$$\sigma_{ij} = \frac{1}{V}\sum_{c \in V} f_i^{c} l_j^{c} \quad i,j = 1,2,3 \tag{2.14}$$

The same form of above representation was also reported by Weber (1966), Hill (1963) and Dantu (1968). The second order stress tensor σ_{ij} is considered to possess the same properties as in continuum mechanics and will be treated the same, although this would be strictly true only for an assembly containing an infinite number of particles. Nevertheless, it may be a reasonable assumption when an assembly is large.

Although the macroscopic average stress tensor on the boundary can be described by using the volume average of a summation of contact forces and contact vectors, it is indeed very difficult to compute each one of the contact forces and contact vectors. Some average values of contact forces and contact vectors may be instead adopted as follows as proposed by Rothenburg (1980), and Mehrabadi et al. (1982). Considering the collection of all the contact forces in an assembly into θ_g groups, each one of which possesses an orientation between θ and $\theta + \Delta\theta$. Then the number of contacts that fall within each group M_g can be approximated by:

$$M_g = MS(\theta)\Delta\theta \tag{2.15}$$

Averaging $f_i^c(\theta)$ and $l_j^c(\theta)$ for each group, the group average $\overline{f_i^c(\theta)l_j^c(\theta)}$ may be treated as a representative value for the following computation given that $f_i^c(\theta)$ and $l_j^c(\theta)$ are not dependent on each other, and the average stress tensor can thus be modified correspondingly as:

$$\sigma_{ij} = \frac{1}{V}\sum_{\theta_g} \overline{f_i^c(\theta)l_j^c(\theta)}\, MS(\theta)\Delta\theta \qquad i,j = 1,2 \tag{2.16}$$

For an granular assembly with an infinite number of particles and volume, an integral expression can be applied to approximate the summation of all group values, which is:

$$\sigma_{ij} = m_v \int_0^{2\pi} \overline{f_i^c(\theta)l_j^c(\theta)} S(\theta)\mathrm{d}\theta \qquad i,j = 1,2 \tag{2.17}$$

where m_v is the contact density, which is given by equation (2.5). Splitting the average contact force for each group into normal and tangential contact force components with the associated directional unit vectors as given in equation (2.9), the stress tensor can be presented as:

$$\sigma_{ij} = m_v \int_0^{2\pi} \overline{[f_n^c(\theta)n + f_t^c(\theta)t]l_j^c(\theta)} S(\theta)\mathrm{d}\theta \qquad i,j = 1,2 \tag{2.18}$$

For a granular disc system with an equal diameter d_0, Rothenburg (1980) proposed that the average stress tensor σ_{ij} can be further simplified as:

$$\sigma_{ij} = \frac{m_v d_0}{2} \int_0^{2\pi} \{\overline{f_n^c}(\theta)n_i n_j + \overline{f_t^c}(\theta)t_i n_j\} S(\theta)\mathrm{d}\theta \tag{2.19}$$

If instead, a representative average contact vector length l_0^c is assumed for the assembly:

$$l_j^c(\theta) = l_0^c n_j \tag{2.20}$$

then equation (2.18) can be simplified to (Rothenburg, 1980; Rothenburg and Bathurst, 1989):

$$\sigma_{ij} = m_v l_0^c \int_0^{2\pi} \{\overline{f_n^c}(\theta)n_i n_j + \overline{f_t^c}(\theta)t_i n_j\} S(\theta)\mathrm{d}\theta \qquad i,j = 1,2 \tag{2.21}$$

Therefore, for a granular disc system with equal diameters d_0, Rothenburg (1980) proposed that the average stress tensor σ_{ij} can be written as:

$$\sigma_{ij} = \frac{m_v d_0}{2} \int_0^{2\pi} \{\overline{f_n^c}(\theta)n_i^c n_j^c + \overline{f_t^c}(\theta)t_i^c n_j^c\} S(\theta)\mathrm{d}\theta \tag{2.22}$$

2.4.5 Stress-force-fabric relationship

From the derivation in section 2.3.4, the average stress tensor of a granular assembly can be represented by using normal and tangential contact forces associated with the microstructure descriptors as shown by equation (2.21). Applying the Fourier series approximation for the contact normal anisotropy distribution and the normal and tangential contact force distributions as given by equations (2.8), (2.10) and (2.11), σ_{11}, σ_{22}, and σ_{12} can be computed. Assuming all orientations of anisotropy are the same, $\theta_0 = \theta_a = \theta_n = \theta_t$, then the stress tensor invariants σ_n and σ_t can be presented accordingly as follows (Rothenburg and Bathurst, 1989):

$$\sigma_n = \frac{\sigma_{11} + \sigma_{22}}{2} = \frac{m_v l_0^c f_0^c}{2}\left(1 + \frac{a_n a_f}{2}\right) \tag{2.23}$$

$$\sigma_t = \sqrt{\left[(\frac{\sigma_{11} - \sigma_{22}}{2})^2 + {\sigma_{12}}^2\right]} = \frac{m_v l_0^c f_0^c}{4}\left(a_n + a_f + a_t\right) \tag{2.24}$$

So the sine of the mobilized friction angle φ can be written as the ratio between the above two stress invariant tensors as:

$$sin\varphi = \frac{\sigma_t}{\sigma_n} = \frac{\frac{1}{2}(a_n + a_f + a_t)}{1 + \frac{1}{2}a_n a_f} \tag{2.25}$$

When the product of a_n and a_f is small, (both of them are less than 0.5 typically), the term $a_n a_f/2$ can be neglected. Therefore, the above equation can be simplified as:

$$sin\varphi = \frac{1}{2}\left(a_n + a_f + a_t\right) \tag{2.26}$$

Equation (2.26) is the stress-force-fabric relationship that was proposed by Rothenburg (1980) and verified using DEM numerical simulation by Rothenburg and Bathurst (1989). This relationship relates the mobilized friction angle with the anisotropy parameters a_n, a_f, a_t, irrespective of particle size and shape, which indicates the shear capacity of a granular system depends on the three anisotropy parameters from contact normal, and normal and tangential contact forces.

Chapter 3 Methodology

3.1 General

This chapter presents in detail the methodology adopted in this research. The numerical computations performed in this research employ two main components, which are the Discrete Element Method (DEM), and the fluid-coupled DEM algorithm. The DEM method adopted in this research is presented in section 3.2, it follows closely that used the study conducted by Bathurst, 1985. This method can be applied alone to simulate a biaxial compression test in a drained condition. Section 3.3 illustrates the fluid-coupled DEM scheme employed in this thesis, which is further developed based on the model proposed by Olivera (2004). This further developed algorithm will be applied to simulate a biaxial compression test of granular assemblies in an undrained condition. Sections 3.4 and 3.5 summarize the boundary control and calculation cycles implemented in the simulation, respectively. And a representation of the calculation of macroscopic average stress, strain, and pore pressure applied in this research is shown in section 3.6. In section 3.7, some implementation details of the fluid-coupled DEM code is illustrated, especially, the "pore groups" idea which aims at dealing the difficulty of effectively computing the pore pressure during the rapid changes in pore structure due to creation and disintegration of inter-granular contacts is proposed. It is followed by a comparison with behavior of poroelastic configuration in section 3.8.

3.2 Discrete element method

The discrete element method (DEM) which was first proposed by Cundall and Strack (1978), applies an explicit numerical scheme to demonstrate the mechanical behaviors of assemblies of particles on a granular basis according to Newton's Second Law (Strack and Cundall, 1978). Fig. 3.1 is a flow chart describing typical calculation cycles of the DEM. The method incorporates two main components in each computational cycle: the force-displacement calculation for each contact between immediate neighbor particles, and a motion calculation for each particle using a vectorial summation of all the contact forces applied to it. The former is based on application of the force-displacement law to the contact overlap (should be small relative to the particle size) between each pair of contacting particles. A vectorial sum of all the contact forces that work on each particle then gives the resultant force which is used to calculate the motion. The motion is obtained using Newton's second law on a particle to particle basis. Once the motion is determined, a new displacement and a new contact overlap for each particle are obtained and used in a new cycle of calculations. The computations are a dynamic process in which the initial movement of the boundary particles of the assembly is propagated inwards throughout the whole particle system. The time step applied for each cycle of calculation should be small enough to guarantee that the disturbances at each step affect only the neighboring particles that the particle being considered is contacting with. To maintain the equilibrium of the whole dynamic granular system in each time-step, a damping effect is introduced.

Also, the velocities and accelerations from the motion calculation are assumed to be constant within each time-step.

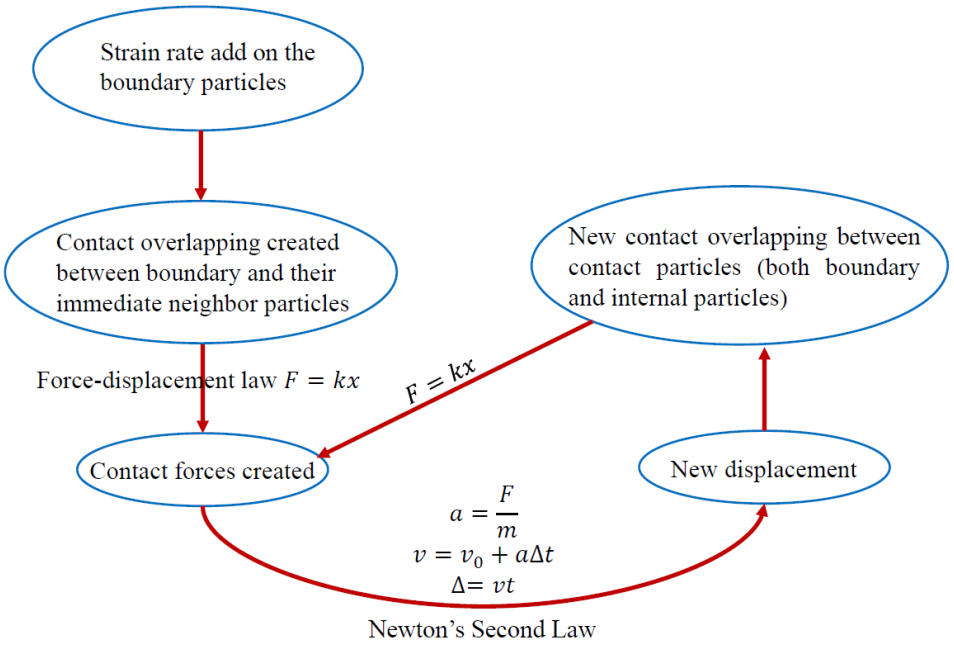

Figure 3.1 Flow chart of discrete element method

3.2.1 Force-displacement law

A force-displacement law is employed to compute the contact forces between any two immediately contacting particles. The following explanations of the force-displacement law employ an elliptical geometry as shown in Fig. 3.2, which is equally applicable for disc particles.

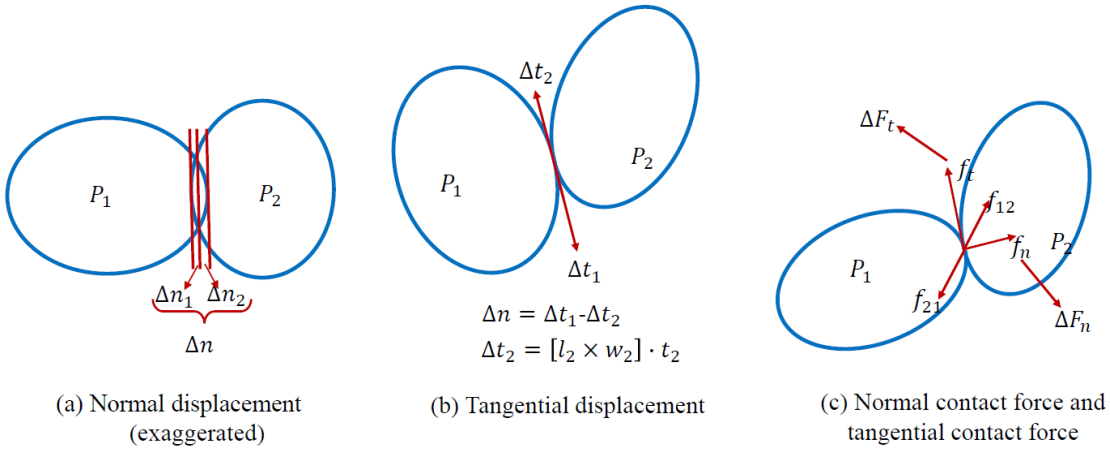

Figure 3.2 Concept of normal and tangential displacements and contact forces of ellipse particles

The basic form of the force-displacement law in the normal and tangential directions at each contact between any two contacting particles is the product of the particle stiffness and the associated displacement as described by equations (3.1) and (3.2):

$$\Delta F_n = k_n \Delta n \tag{3.1}$$

$$\Delta F_s = k_s \Delta t \tag{3.2}$$

where ΔF_n and ΔF_s are the increments of a contact force in the normal and tangential directions (see Fig. 3.2 c), k_n and k_s are the contact stiffnesses in the normal and tangential directions, and Δn and Δt are the displacements in the normal and tangential directions respectively (see Fig.3.2 a and b). In terms of the explicit numerical scheme, at the end of each time step, the displacements in the normal and tangential directions at each particle center has the following forms:

$$(F_n)_{N+1} = (F_n)_N + (\Delta F_n)_N = (F_n)_N + k_n(\Delta_n)_{N+\frac{1}{2}} \tag{3.3}$$

$$(F_s)_{N+1} = (F_s)_N + (\Delta F_s)_N = (F_s)_N + k_s(\Delta_t)_{N+\frac{1}{2}} \tag{3.4}$$

To compute the normal and tangential displacement component Δ_n and Δ_t at each contact, the associated relative velocity components v_n and v_t are integrated. Introducing n_i and t_i as the unit vectors $n_i = \{cos\theta, sin\theta\}$, $t_i = \{-sin\theta, cos\theta\}$, where t_i is obtained from rotating n_i through 90 degrees, then the relative velocity v_R between any two particles such as P1 and P2 in Figure 3.2 can be expressed as:

$$v_R = \left(\dot{x}_i^B - \dot{x}_i^A\right) - \left(\dot{\theta}^A|l_c^A| + \dot{\theta}^B|l_c^B|\right)t_i^c \tag{3.5}$$

Projecting v_R onto the unit vectors n_i and t_i respectively gives the relative velocities in the normal and tangential directions as:

$$v_n = v_R n_i = \left(\dot{x}_i^B - \dot{x}_i^A\right)n_i - \left(\dot{\theta}^A|l_c^A| + \dot{\theta}^B|l_c^B|\right)t_i n_i = \left(\dot{x}_i^B - \dot{x}_i^A\right)n_i \tag{3.6}$$

$$v_t = v_R t_i = \left(\dot{x}_i^B - \dot{x}_i^A\right)t_i - \left(\dot{\theta}^A|l_c^A| + \dot{\theta}^B|l_c^B|\right)t_i t_i = \left(\dot{x}_i^B - \dot{x}_i^A\right)t_i - \left(\dot{\theta}^A|l_c^A| + \dot{\theta}^B|l_c^B|\right) \tag{3.7}$$

Thus, in terms of each time step Δt, the normal and tangential displacement components Δ_n and Δ_t at each contact can be obtained as the integrals of v_n and v_t:

$$(\Delta_n)_{N+\frac{1}{2}} = [(\dot{x}_i^B - \dot{x}_i^A)_{N+\frac{1}{2}}]n_i \Delta t \qquad i = 1, 2 \tag{3.8}$$

$$(\Delta_s)_{N+\frac{1}{2}} = \{[\left(\dot{x}_i^B - \dot{x}_i^A\right)_{N+\frac{1}{2}}]t_i - \left(\dot{\theta}^A|l_c^A| + \dot{\theta}^B|l_c^B|\right)_{N+\frac{1}{2}}\}\Delta t \qquad i = 1, 2 \tag{3.9}$$

where l_c^A and l_c^B are contact vectors, which describe the distance between centroid of a particle and the midpoint of the contact penetration as indicated as Fig. 2.11. Therefore, combining the stiffness and relative displacement in the normal and tangential directions for each contact by the above equations (3.8) and (3.9), yields the force-displacement equations (3.3) and (3.4). Vectorially summing up all the contact forces for each particle, the contact force at the end of each step is given by.

$$(F_i)_{N+1}^k = \sum_{n=1}^{n_k} [(F_n)_{N+1} n_i + (F_s)_{N+1} t_i] \qquad i = 1, 2 \tag{3.10}$$

The corresponding moment of each particle is:

$$(M)_{N+1}^k = \left| l^k \right| \sum_{n=1}^{n_k} [(F_s)_{N+1}] \tag{3.11}$$

When calculating the tangential contact force at each contact, Coulomb's friction law is adopted as a criterion to determine if the contact particles slip with respect to each other. This only happens when the tangential contact force is equal or greater than the product of the coefficient of the friction and the normal contact force:

$$F_{smax} = \mu F_n = tan\phi_\mu \tag{3.12}$$

Where ϕ_μ is the smaller of the interparticle friction angles of the two particles in contact. If the calculated tangential contact force F_s is greater than F_{smax}, then F_s should be set as the value of F_{smax} preserving the sign of F_s.

3.2.2 Equations of motion

The above force-displacement relationship is used to compute the contact forces at each contact, and then a vectorial summation of the contact forces for each particle is obtained for the following motion calculation. According to Newton's Second Law, the force and moment are related to the acceleration and moment of inertia via equations (3.13) and (3.14):

$$(F_i)_N = m(\ddot{x}_\iota)_N \qquad i = 1, 2 \tag{3.13}$$

$$(M)_N = I(\ddot{\theta})_N \tag{3.14}$$

where m is the mass of a particle, I is the particle's moment of inertia, F and M are the net force and moment at the center of an elliptical particle, $\ddot{x}_\iota$ and $\ddot{\theta}$ are the two acceleration components, and N represents the step number. Based on the central difference scheme, the velocity components at the center

of each particle can be related to the force and moment through an integration of the acceleration and moment of inertia as follows:

$$(\dot{x}_i)_{N+\frac{1}{2}} = (\dot{x}_i)_{N-\frac{1}{2}} + (\ddot{x}_\iota)_N \Delta t = (\dot{x}_i)_{N-\frac{1}{2}} + \frac{(F_i)_N \Delta t}{m} \qquad \text{i} = 1,2 \qquad (3.15)$$

$$(\dot{\theta})_{N+\frac{1}{2}} = (\dot{\theta})_{N-\frac{1}{2}} + (\ddot{\theta})_N \Delta t = (\dot{\theta})_{N-\frac{1}{2}} + \frac{(M)_N \Delta t}{I} \qquad (3.16)$$

where Δt is the time increment. Hence, from the above two velocity components, the two displacement components can be obtained from a further integration. The updated particle center location at the end of each step is obtained as:

$$(x_i)_{N+1} = (x_i)_N + \left[(\dot{x}_i)_{N+\frac{1}{2}}\right] \Delta t \qquad i = 1,2 \qquad (3.17)$$

$$(\theta)_{N+1} = (\theta)_N + \left[(\dot{\theta})_{N+\frac{1}{2}}\right] \Delta t \qquad (3.18)$$

Therefore, from the above updated center location at the end of each time step Δt, the updated relative displacement between any two contact particles is computed, leading to a new cycle of computation using equations (3.3) and (3.4) (see Fig. 3.1).

3.2.3 Damping

To maintain the static equilibrium of the granular system throughout the dynamic propagation movement during simulation, damping should be incorporated to dissipate the kinetic energy (Bathurst, 1985). From Strack and Cundall (1978), two types of damping can be employed in the DEM computations: friction damping and viscous damping. The former is applied only during the occurrence of sliding, which reduces the inter-particle tangential contact force and displacement through friction. The latter can be further divided into contact damping and global damping as illustrated as Fig. 3.3. Both contact damping (D_n and D_s) and global damping (D_m and D_I) can be represented by dashpots. As their names indicate, contact damping (D_n and D_s) occurs at each contact point and global damping (D_m and D_I) operates on the whole particle. The specific functions used to describe each one of them are explained in the following:

Contact damping (D_n and D_s) is associated with the relative velocities in normal and tangential directions, c_n and c_s are adopted as the contact damping coefficients, which are related to the contact stiffness k_n and k_s in the normal and tangential directions through a coefficient of proportionality β. Equations (3.19) and (3.20) describe how c_n and c_s affect the relative velocities.

$$(D_n)_N = c_n\left[\left(\left(\dot{x}_i^B - \dot{x}_i^A\right)_{N-\frac{1}{2}}\right)n_i\right] \tag{3.19}$$

$$(D_s)_N = c_s\left[\left(\left(\dot{x}_i^B - \dot{x}_i^A\right)_{N-\frac{1}{2}}\right)t_i - \left(\dot{\theta}^A|l_A^c| + \dot{\theta}^B|l_B^c|\right)_{N-\frac{1}{2}}\right] \qquad i = 1,2 \tag{3.20}$$

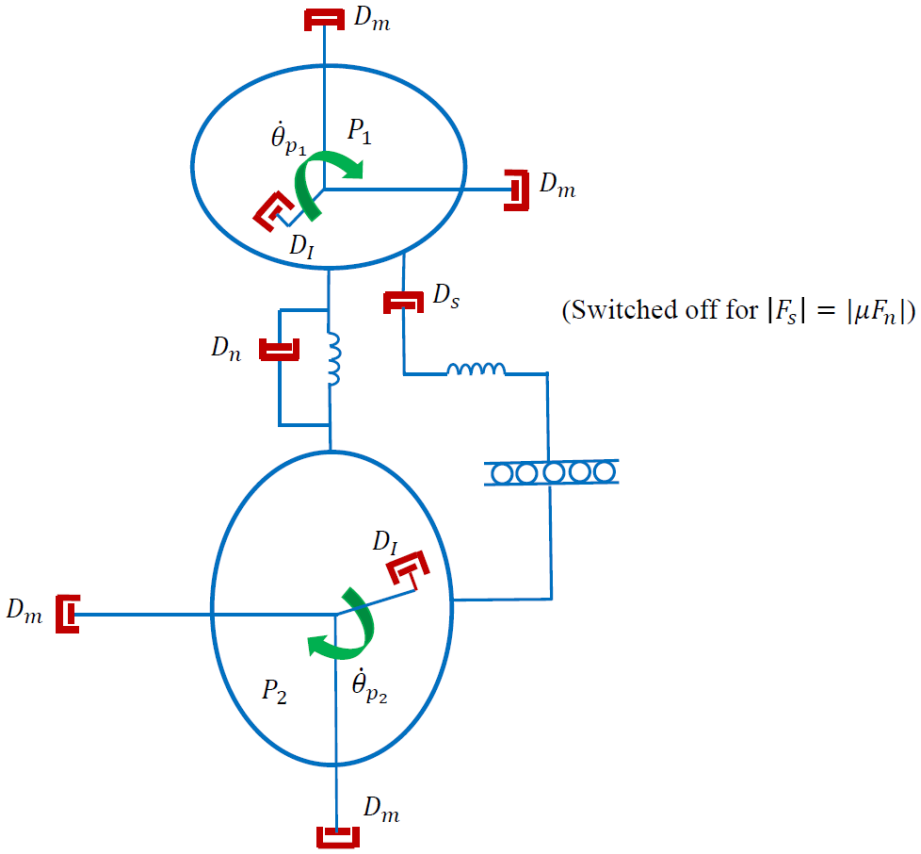

Figure 3.3 Friction damping, contact damping, and global damping

Once the above damping forces D_n and D_s are obtained, they are expressed as D_i and incorporated into the force component to participate the camputation. Thus, in terms of relative velocity, equation (3.15) is updated as:

$$\dot{x}_{i_{N+\frac{1}{2}}} = \dot{x}_{i_{N-\frac{1}{2}}} + \left[\left(\frac{F_i + D_i}{m}\right)_N\right]\Delta t \qquad i = 1,2 \tag{3.21}$$

The corresponding anguler velocity component can also be updated accordingly to take the contact damping forces into consideration. See equation (3.22)

$$\dot{\theta}_{i_{N+\frac{1}{2}}} = \dot{\theta}_{i_{N-\frac{1}{2}}} + \left[\left(\frac{M_i}{I}\right)_N\right]\Delta t \qquad i = 1,2 \tag{3.22}$$

The above equations have a half-time step error in the determation of the contact damping values $(D_n)_N$ and $(D_s)_N$, which is considered to be negligible (Strack and Cundall, 1978).

The second type of viscous damping adopted, the global damping (D_m and D_I), helps to connect each particle to a fixed reference. It acts on the velocity of each particle during the motion computation via the coefficients c_m and c_I, which are related to the mass and moment of inertia in the following manner:

$$c_m = \alpha m \tag{3.23}$$

$$c_I = \omega \alpha I \tag{3.24}$$

where both α and ω are coefficients of proportionality, ω is applied to amplify the effect of α in the rotational component. Hence, incorporating the effects of both contact and global damping into each particle's motion equation, the force and moment equations (3.13) and (3.14) can be rewritten as:

$$m(\ddot{x}_i)_N = (F_i + D_i)_N - c_m(\dot{x}_i)_N \qquad i = 1, 2 \tag{3.25}$$

$$I(\ddot{\theta})_N = (M_n)_N - c_I(\dot{\theta})_N \tag{3.26}$$

Applying a central difference scheme into the calculation of velocity and acceleration, the velocity and acceleration can be written as:

$$(\dot{x}_i)_N = \frac{1}{2}\left((\dot{x}_i)_{N+\frac{1}{2}} + (\dot{x}_i)_{N-\frac{1}{2}}\right) \qquad i = 1, 2 \tag{3.27}$$

$$(\dot{\theta})_N = \frac{1}{2}\left((\dot{\theta})_{N+\frac{1}{2}} + (\dot{\theta})_{N-\frac{1}{2}}\right) \tag{3.28}$$

and:

$$(\ddot{x}_i)_N = \frac{(\dot{x}_i)_{N+\frac{1}{2}} - (\dot{x}_i)_{N-\frac{1}{2}}}{\Delta t} \qquad i = 1, 2 \tag{3.29}$$

$$(\ddot{\theta})_N = \frac{(\dot{\theta})_{N+\frac{1}{2}} - (\dot{\theta})_{N-\frac{1}{2}}}{\Delta t} \tag{3.30}$$

Therefore, the updated equation of motion formulae with the viscous damping effects incorporated takes the following form:

$$(\dot{x}_i)_{N+\frac{1}{2}} = \frac{(\dot{x}_i)_{N-\frac{1}{2}}\left(1 - \frac{\alpha \Delta t}{2}\right) + (F_i + D_i)_N \Delta t/m}{1 + \frac{\alpha \Delta t}{2}} \qquad i = 1, 2 \tag{3.31}$$

$$\left(\dot{\theta}\right)_{N+\frac{1}{2}} = \frac{\left(\dot{\theta}\right)_{N-\frac{1}{2}}\left(1-\frac{\alpha\Delta t}{2}\right)+(M)_N\Delta t/m}{1+\frac{\alpha\Delta t}{2}} \tag{3.32}$$

3.2.4 Critical time step

To maintain the calculations constantly stable and the granular system in static equilibrium, the time step adopted should to be small enough. This may be achieved by setting the time step as a suitable fraction of the critical time step. From Cundall and Strack (1979), the critical time step can be found by considering a mass connected to ground through a spring with a single degree-of-freedom. So the critical time step can be determined as follows:

$$\Delta t_c = \Delta t = 2FRAC\sqrt{\frac{m_{min}}{k_{max}}} \tag{3.33}$$

where k_{max} is the larger of the values of the normal or shear contact stiffness, m_{min} is the lowest particle mass in the assembly, and FRAC is a constant that indicates the number of springs that act on each particle. From Strack and Cundall (1978), FRAC can be assigned as value of 0.1 to maintain computational stability.

3.3 Fluid-coupled DEM

3.3.1 Pore pressure generation and fluid-particle interaction

In an undrained condition, with an applied external load on a granular material, a pore water pressure is generated and which reduces the effective stress between particles. This will in turn influence the overall behavior of the solid particles macroscopically and microscopically. In order to simulate the process of pore pressure generation of individual pores, according to Hakuno et al. (1988), Hakuno (1995), Thallak (1991), and Olivera (2004), the fluid in each pore can be assumed to be an elastic material with zero shear modulus. Hence, a change of the pore pressure can be represented by assigning a bulk modulus that acts on the volumetric strain. Therefore, the two major tasks involved in the study of pore pressure generation are the identification of the pores and the determination of the rate of volume change.

Pore identification

To calculate the average pore pressure of a granular assembly in an undrained condition following the idea proposed by Hakuno et al. (1988), Hakuno (1995), Thallak (1991), and Olivera (2004), it is crucial to compute the individual pore pressure within each pore. So the first step is to identify the pores within the granular system. Fig. 3.4 shows a subset of a granular assembly that includes a series of pores named A to N surrounded by elliptical particles. In this figure, it can be seen that these pores are formed by the contacts among particles. So an algorithm for the identification the pores in an assembly can be implemented by

searching the contacts that can constitute a closed circuit. The method of pore identification of this study follows the idea that proposed by Thallak (1991), Dullien (1991), and Olivera (2004). Basically, this method is based on searching for and storing the contacts that belong to each particle in a group. Then, the contacts in each group are sorted in order of the contact normal orientation from 0 to 2π. The construction of a closed circuit can be demonstrated by referring to pore L in Fig. 3.4. For example, the construction starts from particle a shown in the figure, the contacts belonging to particle a in the order of contact normal orientation from 0 to 2π are particles b, c, and d, respectively. So particle b is found and stored as the second particle that constitutes a closed circuit. Now the contact searching is switched to start from particle b. Particle b is in contact with particle e, a, f, g in the same order of contact normal orientation from 0 to 2π. Once the contact searching finds particle a, previous particle e should be taken as the third particle that constitutes the closed circuit and is then stored in the same array as particles a and b. Now contact searching is switched to particle e, which is in contact with particles i, h, and b. Following the same pattern, particle h can be found and stored in the closed circuit array. Then the contact searching is switched to particle h, and particle c can be found and stored into the closed circuit array following the same method. At last, the contact searching is switched to particle c, and particles h, j, and a are found. Once particle a is found, the searching for this close circuit is completed since the searching starts from particle a. So pore L is identified. The same process can be applied to form other closed circuits, allowing the pores in the granular system to be identified and stored in an array.

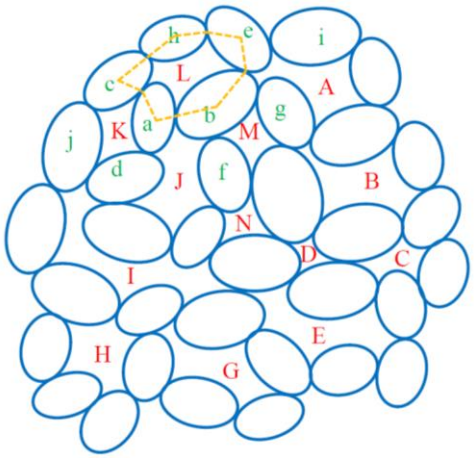

Figure 3.4 Subset of a granular assembly showing pore identification

Individual pore pressure calculations

To microscopically compute the pore pressure in the assembly using an idea proposed by Hakuno et al. (1988), Hakuno (1995), Thallak (1991), and Olivera (2004), it is necessary to know how the individual pore pressures vary. The voids may be treated as being 100% saturated and full of fluid. The fluid is regarded as

being a pure elastic medium that possesses a certain elastic modulus. Then the volume change of a particular pore in an assembly will be equal to the fluid volume change, and the pore pressure variation Δu_i can be related to the volumetric strain of a particular pore by the bulk modulus B_f in the following form:

$$\Delta u_i = B_f \frac{\Delta V_i}{V_i} \tag{3.34}$$

where V_i is the original volume of pore i, ΔV_i is the change of volume of pore i, and B_f is the bulk modulus of the fluid. In terms of a two-dimensional assembly, the change of area of pore i, ΔA_i, and the original area of pore i, A_i, should be applied instead of ΔV_i and V_i.

As for the volume change (area change in terms of a two-dimensional assembly) in any time step for a pore surrounded by a group of particles, precise calculations should be conducted to determine the volumetric strain and hence obtain the pore pressure of the pore. The area change calculation for a two-dimensional assembly case can be explained by referring to Figure 3.5. It is illustrated in the figure that a pore is formed by a group of five elliptical particles contact with each other. The penetrations shown in the figure are exaggerated for clarity of the explanation. A polygon can be constructed by connecting each ellipse's centroid point to the two corresponding inner intersection points to the pore shown as point *m* and *n* in the picture. So the area of the void is given by the subtraction from the polygon's area of the sum of the sector areas indicated by shaded areas in the figure.

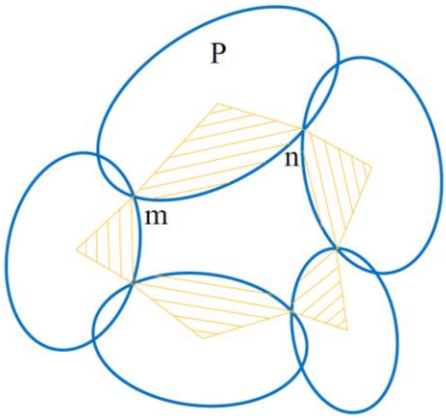

Figure 3.5 Polygon formation for pore volume computation

With respect to the computation of each shaded sector area, a method of area normalization can be implemented to simplify the whole shaded sector area computation to the use of one algorithm. The calculation is based on a coordinate transformation for each particle to make the x abscissa along the major axis of the ellipse and the particle center located at the origin. An example of this idea is shown in Fig. 3.6, where particle P is taken from the particle group constituting the pore shown in Fig. 3.5. So the normalized

sector area that enclosed by the x abscissa and any contact length vector, i.e. $\overrightarrow{om}$ or $\overrightarrow{on}$ shown in this figure can be computed as:

$$A_n = R^2 \frac{1-e_c^2}{2}\left\{arctan\left[\frac{1+e_c}{1-e_c}tan(\alpha)\right]\right\} \qquad 0 \leq \alpha < \frac{\pi}{2} \qquad (3.35)$$

where α is the angle that is measured from the major axis of the elliptical particle to a given contact length vector. Therefore, the shaded sector area shown in the figure is the difference between the sector area from x abscissa to a contact length vector $\overrightarrow{on}$ (corresponding to angle α_2) and the sector area from the x abscissa to the contact length vector $\overrightarrow{om}$ (corresponding to angle α_1).

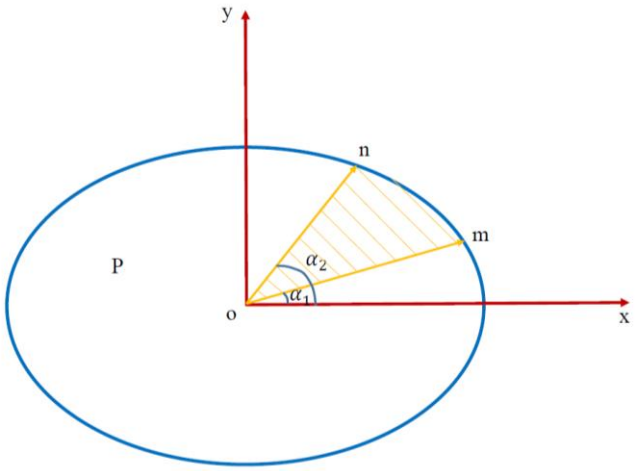

Figure 3.6 Normalized sector for area calculation

3.3.2 Transient pore pressure calculations

Soil is a porous media, the fluid inside the pores can flow through the pores in a saturated soil and generate a transient excess pore pressure. To simulate fluid flow through a porous media, a flow network in an undrained assembly can be constructed by connecting the gravity centers of the polygons that are formed by connecting the centres of contacting particles (Olivera, 2004). Fig. 3.7 a shows an example of a subset flow network of an undrained granular assembly. The polygons encircling the pores are described by yellow broken lines, while the red double lines represent the fluid network. Each red double line segment can be treated as a cylindrical conduit that connects the immediately neighbouring pores, as magnified in Fig. 3.7b. When a pore pressure difference exists between immediate neighbouring pores (pore I, II, and III), a transient fluid flow is induced through the connecting conduit. The magnitude of the flow rate q can be related to the conduit diameter d and length L (see Fig. 3.7b) based on the Hagen-Poiseuille theory, which has the following form:

$$q = \frac{\pi d^4}{128\bar{\mu}} \frac{(u_1 - u_2)}{L} \tag{3.36}$$

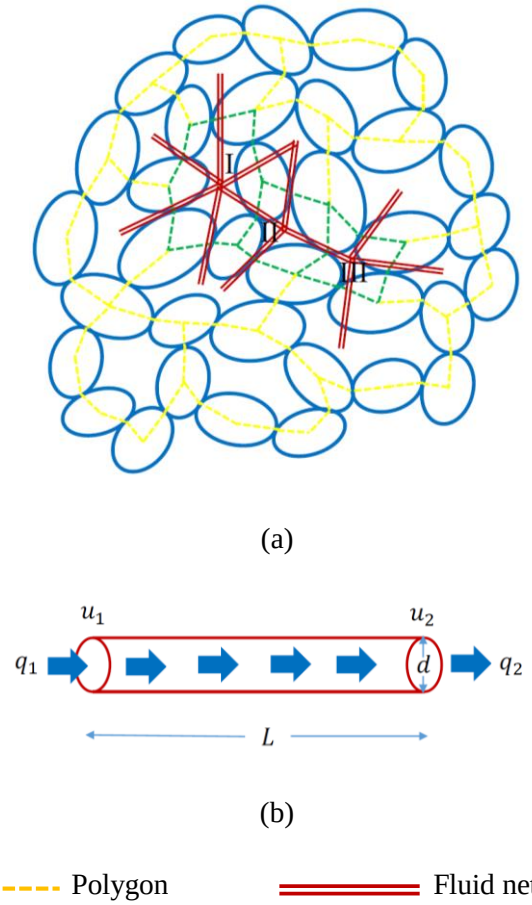

Figure 3.7 Fluid flow network construction for a subset of a granular assembly

To obtain the transient excess pore pressure of each pore, from equation (3.34), the change of the volume for each pore should be known. For a fully saturated assembly, within one time increment, the total volume change of fluid inside any pore i is the summation of the pure pore volume change from particle movement and the amount of input or output flow volume as determined with the help of equation (3.36). Thus, for a fully saturated assembly that encompasses *N* pores, the total volume change of the pore *i* is:

$$\Delta V_i = \Delta V_i^p + \sum_{j=1}^{n} \Delta q_j \Delta t \qquad i = 1, \dots, N \tag{3.37}$$

where ΔV_i^p is the change of the pore volume from particle movement, Δq is the vectorial sum of the input and output volumes of fluid from all n conduits of pore i, and Δt is time increment. Substituting equation (3.36) into (3.37) gives:

$$\Delta V_i = \Delta V_i^p + \sum_{j=1}^{n} \frac{\pi d^4}{128\bar{\mu}} \frac{(u_i - u_j)}{L} \Delta t \qquad i = 1, \dots, N \qquad (3.38)$$

If we introduce k_j as expressed by equation (3.39) to make the above equation concise, then an updated form of above equation is obtained as equation (3.40):

$$k_j = \frac{\pi d_j^4}{128\bar{\mu} L_j} \qquad (3.39)$$

$$\Delta V_i = \Delta V_i^\beta + \sum_{j=1}^{n} k_j (u_i - u_j) \Delta t \qquad i = 1, \dots, N \qquad (3.40)$$

Combining equations (3.40) and (3.34), the following ordinary differential equation that describes the transient pore pressure variation with time is:

$$\frac{du_i}{dt} = \left\{ \frac{dV_i^p}{dt} - \sum_{j=1}^{n} k_j (u_i - u_j) \right\} \frac{B_f}{V_i} \qquad i = 1, \dots, N \quad (3.41)$$

Therefore, the pore pressure for each void can be obtained by solving the above ordinary differential equation with the first term on the right hand side $\frac{dV_i^p}{dt}$ directly computed from the pore area change before and after each time step for a two-dimensional case.

3.3.3 Fluid-coupled DEM system

The transient excess pore pressure of each pore calculated based on Equation (3.41) in the previous section can now be coupled with DEM through the particle's motion equation. Specifically, each pore pressure force can be transformed into horizontal and vertical force components that can be added onto surrounding particle's center. An explanation of the force components of each particle converted from the neighbouring pore pressure are shown schematically in Figure 3.8. The figure 3.8a shows a particle P surrounded by three pores with pore pressures $u_1, u_2,$ and u_3, respectively. Figure 3.8b shows a normalization of particle P by coordinate transformation in the manner that orients the elliptical particle's major axis with the x axis and fixes the particle centroid at the origin. After normalization of the major axis as indicated by Figure 3.8b, the horizontal and vertical force components for each pore u_i can be represented as:

$$F_x^i = u_i (b_x - a_x) \Delta \qquad (3.42)$$

$$F_y^i = u_i (a_y - b_y) \Delta \qquad (3.43)$$

where Δ is the thickness of the particle, u_i is he pore pressure in pore i, and a and b are the intersection points that can be determined as follows. The polygon that encircles each void is constructed in a counter clockwise manner. It is determined by the first intersection point encountered that forms a polygon which starts from particle whose center is a, and whose second contact point is b. Fig. 3.8 parts c, d, and e illustrates points a and b for the three pores, respectively.

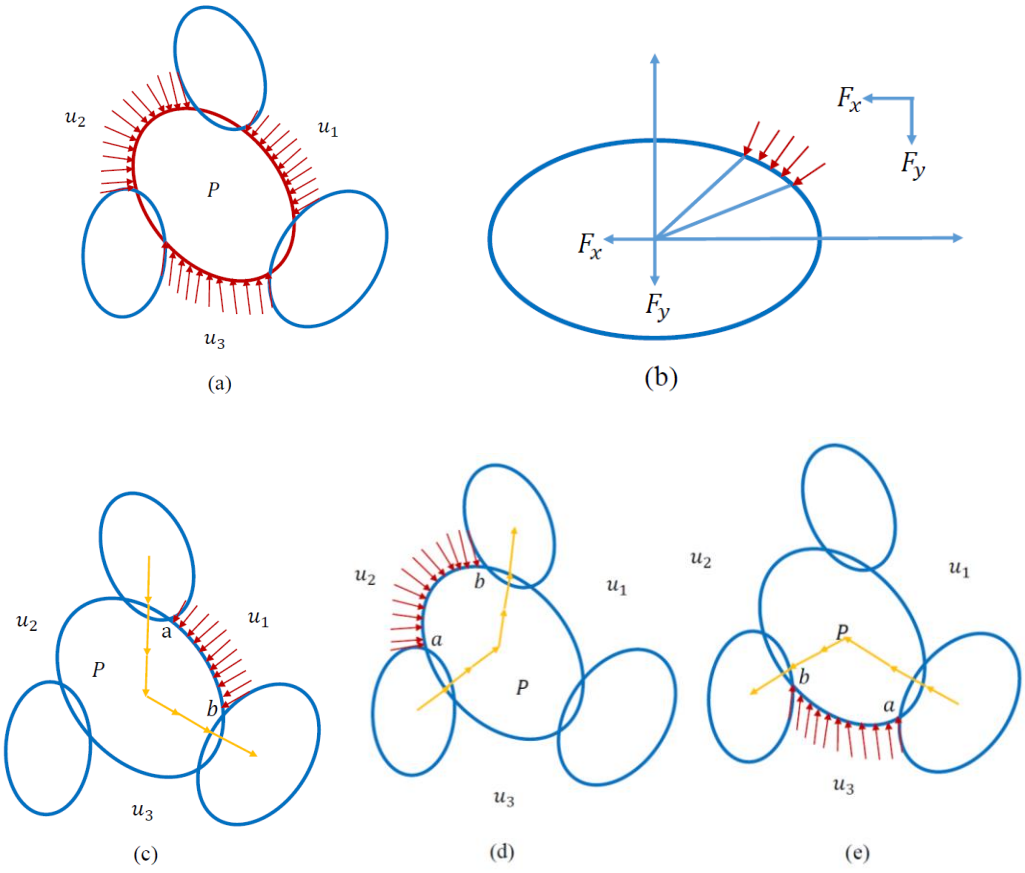

Figure 3.8 Forces converted from nearby pore pressure

In the manner described above, horizontal and vertical forces derived from the pore pressure of each particle's immediate neighbouring pores can be obtained. Synthesizing the forces from all immediate neighbour pores for each particle gives the equation (3.45). The derived pressure forces are then incorporated into motion calculations, therefore, the fluid effect and the DEM of particles are coupled to describe the particles mechanical behavior under an undrained condition.

$$(F_i)^u = \sum_{n=1}^{n_p} F_i^n \qquad i = 1,2 \qquad (3.45)$$

3.4 Boundary control

To simulate the increasing load on a granular media, a servo-controlled scheme is used to control an assembly's boundary. Three servo-control modes are employed in this research to simulate loading effects on an assembly's boundary: strain rate controlled boundary, stress controlled boundary and biaxial compression testing.

Strain rate controlled boundary (Mode 2-Constant boundary strain rate test)

The strain rate controlled boundary, which is named as Mode 2 in the program, applies a constant strain rate $\dot{\epsilon}_{ij}^{\beta}$ to the midpoint of each boundary particle x_j^{β}. So the induced velocity for each boundary particle $\dot{x}_i^{\beta}$ can be obtained through the product of strain rate and the length connecting the boundary particle midpoint location x_j^{β} and the center of the assembly x_j^{c} in the manner as following:

$$\dot{x}_i^{\beta} = \dot{\epsilon}_{ij}^{\beta}\left(x_j^{\beta} - x_j^{c}\right) \tag{3.46}$$

where x_j^{β} is the midpoint location of each boundary particle at the beginning of the calculation. The strain rate controlled boundary is applied in the research to prepare granular assembly samples with a prescribed initial stress, which is analogous to an isotropic consolidation process. The strain rate controlled boundary is also used to perform constant volume method testing, which preserves the total volume of an assembly and simulates the case of instant pore pressure dissipation. The strain rates applied on the horizontal and vertical boundaries when conducting constant volume method simulation are set as:

$$\dot{\epsilon}_{11}^{\beta} = -\dot{\epsilon}_{22}^{\beta} \tag{3.47}$$

Stress controlled boundary (Mode 1-Constant stress test)

A stress controlled boundary is named as Mode 1 in the program. As the name "stress controlled" indicates, this mode is designed by setting the value of the stress on the boundary. This target stress is achieved by using a strain controlled servo-mechanism. Specifically, a boundary stress σ_{ij}^{β} is prescribed at the start of the test, afterwards, the calculated value of the stress σ_{ij} of the assembly from each cycle is compared with the prescribed boundary stress σ_{ij}^{β}. Based on their difference, the applied velocity of each boundary particle is modified using the following equation:

$$\dot{x}_i^{\beta} = \frac{g(\sigma_{ij}^{\beta} - \sigma_{ij})(x_j^{\beta} - x_j^{c}))}{\sigma_{ij}^{b}} \tag{3.48}$$

where g is the servo gain parameter. This mode of boundary control is applied in this research to achieve an equilibrium of the particles in a granular assembly before performing shear testing. It is a critical step in producing an isotropic sample. It is also used to prepare samples with different confining stresses.

Constant σ_{11} Test (Mode 3-Biaxial Compression test)

The constant σ_{11} test is called Mode 3 in the program. As the name implies, this mode keeps the stress component σ_{11} constant. This boundary control is achieved by keeping the stress in the horizontal direction σ_{11} constant using Mode 1, and at the same time applying a strain rate $\dot{\epsilon}_{22}^{\beta}$ in the vertical direction, which is analogous to a biaxial compression test. The stress component σ_{11} is kept constant by using the stress-controlled mode (mode 1), but only the calculated stress component σ_{11} from each cycle is compared with the prescribed boundary stress σ_{11}^{β}. The strain rate $\dot{\epsilon}_{22}^{\beta}$ in the vertical direction is achieved in the same manner as using equation (3.46). Accordingly, the velocity of each boundary particle is updated in each cycle. For an undrained testing, the velocity of each boundary particle can be computed using equation (3.49):

$$\dot{x}_i^{\beta} = \frac{g(\sigma_{ij}^{b} - (\sigma_{ij}' + \bar{u}\delta_{ij})(x_j^{\beta} - x_j^{c}))}{\sigma_{ij}^{b}} \tag{3.49}$$

where $\bar{u}$ is the average pore pressure. This type of boundary control is used to simulate drained and undrained biaxial compression testing in this research.

3.5 Calculation cycles

Based on all the above explanations of how the Fluid-coupled DEM is achieved, and the associated boundary control scheme, a calculation cycle flow chart can be established as shown in Figure 3.9. In this figure, the left column is the DEM computation portion and the right column demonstrates the pore pressure generation and its effect on granular particles.

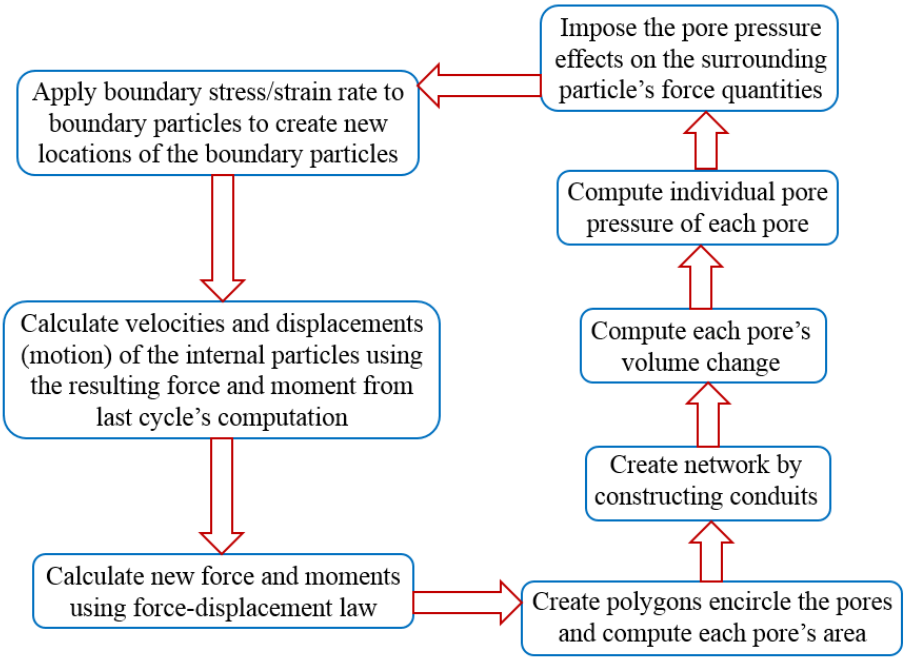

Figure 3.9 Flow chart of fluid-coupled DEM compupation

3.6 Representation of macroscopic average stress, strain and pore pressure

When exploring the undrained characteristics of a granular media using the micromechanics method, it is critical to obtain macroscopic representations of the average stress, strain and pore pressures through micromechanical descriptors. As indicated by equation (2.14) from chapter 2, the macroscopic average stress tensor σ_{ij} can be expressed in terms of the volume average (area average in a two-dimensional case) of the product summation of each inter-particle contact force f_i^c and the associated contact vector l_j^c. This research adopts this average stress tensor representation, which is rewritten for a two-dimensional case as equation (3.50).

$$\sigma_{ij} = \frac{1}{A}\sum_{c\in A} f_i^c l_j^c \quad i,j = 1,2 \tag{3.50}$$

The average strain tensor ε_{ij} computed for each cycle follows the modified two-dimensional equation that was proposed by Cundall et al. in 1979, which is shown as equation (3.51)

$$\varepsilon_{ij} = \frac{1}{A}\sum_{\beta=1}^{n}\left[\frac{1}{2}\left(\Delta x_j^{\beta} + \Delta x_j^{\beta+1}\right) e_i S^{\beta}\right] \qquad i,j = 1,2 \tag{3.51}$$

where A is the total area of the assembly, S^{β} is the line that connects the neighbouring boundary particles, β indicates the boundary particles serial numbers in sequence from 1 to n, Δx_j^{β} is the displacement of the boundary particle β, and e_i is the unit vector that is orthogonal to the boundary line segment S^{β}.

The macroscopic average pore pressure representation follows the idea proposed by Olivera in 2004. The volume (area in a two-dimensional case) is adopted as the weight to perform a weighted average calculation of the pore pressure for each pore. This is because when calculating each individual pore pressure (see equation 3.34), the change of each pore area was combined with the assigned bulk modulus B_f. Therefore, the macroscopic average of the pore pressure can be represented as:

$$\bar{u} = \frac{\sum \Delta u_i A_i}{\sum A_i} \tag{3.52}$$

3.7 Fluid-coupled DEM code implementation details

3.7.1 Evolution of the void system

In an effort to simulate an undrained granular system response under loading using the aforementioned fluid-coupled DEM, a crucial step is to identify the voids in the system and recognize how their areas evolve throughout the test. Then each pore pressure is determined using the pore pressure computation method of equation (3.41). And the transformed forces from each pore's pressure can be applied to its encircled particles to achieve fluid-coupled DEM. However, each pore's area is changing constantly. In an undrained simulation, with an applied boundary load, the pore structure changes rapidly due to the creation and disintegration of inter-granular contacts. For example, voids in the system of pores may keep the same encircling particles when none of the contacts constituting the void is lost. Or the void may change when any pair of immediately neighboring particles constituting the encircled particles lose their connection, or any particle in the void constituting group connects with a new neighboring particle in the same group. More common is an extremely complex modification of pore space when both coalescence and subdivision of voids is taking place affecting a group of voids simultaneously. Hence, to handle the rapid changes in pore structure and accurately compute pore area change from the subsequence of two cycles, an idea of "pore group" may be applied. This idea keeps track of "pore groups" where some voids may coalesce due to contact disintegration or some voids are subdivided into parts due to contact creation, therefore, forms a robust pore identification mechanism.

An explanation of how a group of voids evolves in a pores system will be given with the help of Figure 3.10. Figure 3.10 (a) shows one type of pore group evolution in a granular system in an undrained condition under loading, and Figure 3.10 (b) presents an simplified example of complicated pore group evolution scenario. During a step cycle during testing, the left of Figure 3.10 (a) shows three individual pores (I, II

and III) being formed by sixteen particles named sequentially from No. 1 to 16. During particle movement, in the following time step, contacts in this three pore system change, either by being lost or by new contacts being created. On the right hand side of Fig. 3.10 (a) which exhibits a case of a typical void formation. Specifically, the contact between particles 3 and 4 breaks, which results in the formation of pore IV as indicated on the right of Fig. 3.10 (a). Thus, when computing the volumetric strain of pore IV, the area of pore IV should be compared to the area summation of pores I and II in the previous step. Meanwhile, with the forming of pore IV in the pore system, a new contact is created between particles 6 and 14, thereby forming two separated pores V and VI. In this case, the area summation of the pores V and VI should be compared with the area of pore III when calculating the volumetric strain of pores V and VI. They share the same value of pore pressure in this case.

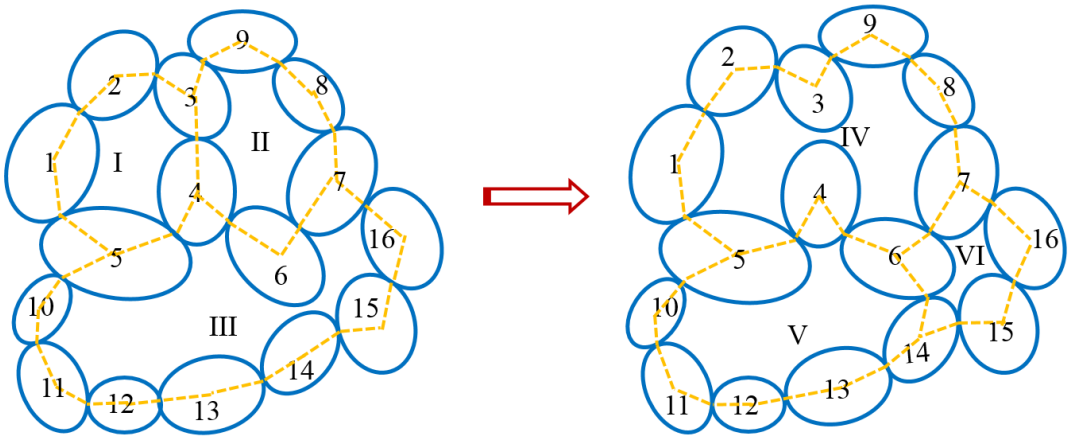

(a)

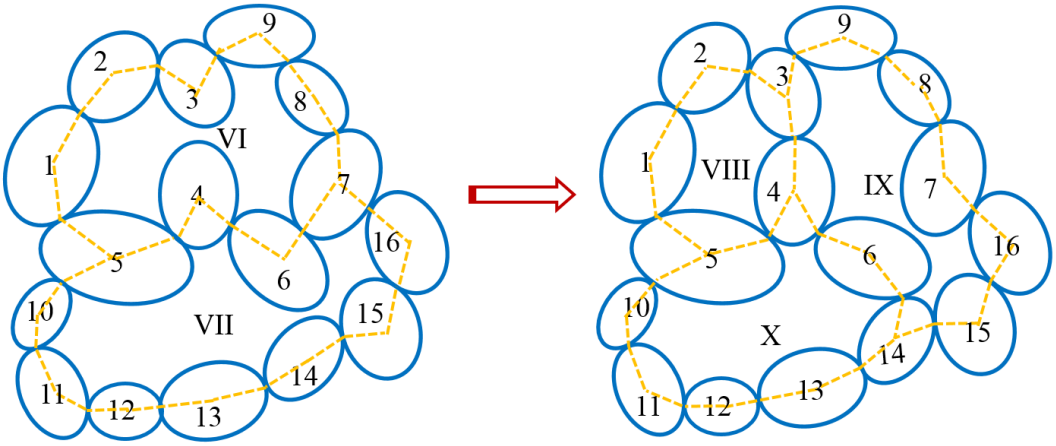

(b)

Figure 3.10 Example of pores evolution

A simplified example of more complicated pore group evolution scenario is shown in Figure 3.10 (b). In this case, two pores (VI and VII) are formed originally by the same sixteen particles already named sequentially from No. 1 to 16 in the previous section in a given step cycle during testing (see left of Fig. 3.10 (b)). Again, through the action of particle movement, in the following time step, contacts in this two pore system may change, either by being lost or by new contacts being created. A simplified complicated case of void formation that may appear is exhibited on the right of Fig. 3.10 (b). Specifically, a new contact between particles 3 and 4 is created, thereby forming a new pore VIII. Meanwhile, the contact between particles 6 and 7 breaks, and a new contact between particles 6 and 14 is created, which results in the formation of pores IX and X as indicated on the right of Fig. 3.10 (b). Thus, when computing the volumetric strain of pores VIII, IX, and X, the area of these three pores should be grouped together and compared to the area summation of pores VI and VII in the previous step. Pores VIII, IX, and X share the same value of pore pressure when computing the corresponding transformed forces exerted on the particles.

3.7.2 Local liquefaction

In addition to the above pores changes due to contact creation and disintegration, during an undrained simulation, with the particle movement and pore area variation, a situation of "local liquefaction" as shown as Fig. 3.11 may appear repeatedly, especially when the granular assembly is very loose. It is seen in Figure 3.11 (a) that in a given time step, three pores i, ii and iii are formed in the pore system which are separated by particles 1, 2, 3, and 4 respectively. In the following time step, movement of particles 1 to 4, causes pore iv to be formed by particles 1, 2, and 3, which is inside pore v. This creates local liquefaction in pore v. When calculating the change of pore areas in this case, pores iv and v should be seen as one group in comparing their area summation with the area of the group made up of pores i, ii and iii from the previous step. Furthermore, since pore iv is completely inside pore v, it can be seen as floating in pore v, so that when performing the pore pressure force transformation onto the particles, the overall pressure forces applied to particles 1, 2, and 3 should all be zero, the same as particle 4. In other words, the area of the groups iv and v should be the area of v after subtracting the areas of particles 1 to 4. When it comes to the next cycle, the possible cases of the void evolutions of pore groups iv and v may be as shown as Figure 3.11c or d. For the case exhibited in Figure 3.11c, pores vi and vii constitute one group whose area should be compared with the combined area of groups iv and v when computing the volumetric strain. In this case particles 2 and 3 are no longer floating inside the pore. However, for the case shown in Figure 3.11d, the pore iv breaks, which creates pore viii whose area should be compared to the area from the previous group of pores iv and v to calculate the area change. Particles 1 to 4 are still floating inside the pore viii, so the overall transformed pressure force attributed to them is zero.

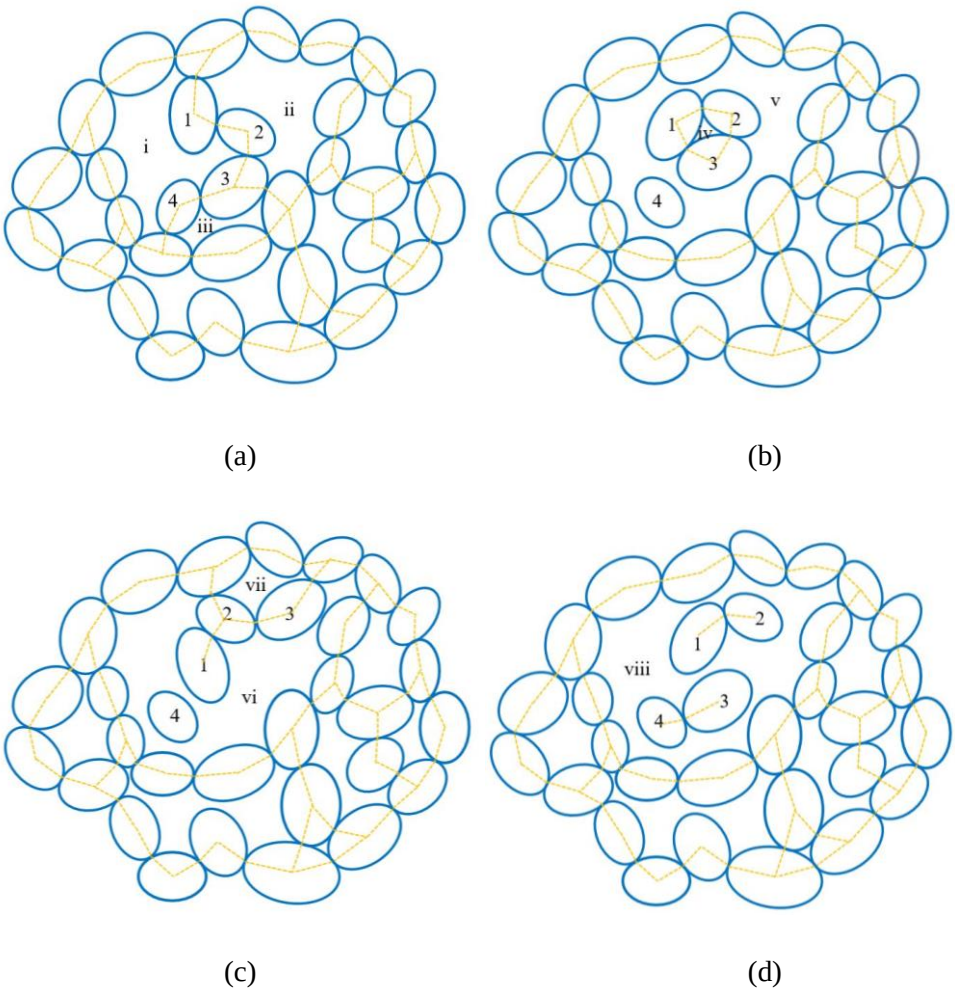

Figure 3.11 Local liquefaction formation and pores evolution

3.8 Comparison of fluid-coupled DEM model with behavior of a poroelastic configuration

In order to compare the proposed fluid-coupled DEM model with the behavior of a poroelastic configuration, two simulations targeted at testing the pore pressure dissipation in the system of pores were conducted: a pore pressure dissipation test and a pore pressure equalization test. For ease of testing, a rectangular assembly with 10000 disc particles were prepared to perform the comparison. Fig. 3.12 shows the schematic rectangular assembly, and Fig. 3.13 shows the grain size distribution of the disc particles in the assembly.

In the two tests, a particular scheme of fixing all particle centers to their coordinates is applied, so that particles cannot move and the voids in the assembly can be considered to be small reservoirs that are connected to each other through the applied conduit pipes which have already been shown in section 3.3.2. Since there is no volume change of each pore from particle movement in this case, the volume change is

only due to the fluid flowing through the conduit pipes that results from the pore pressure gradient between the neighboring pores. Therefore, the two tests allow the effectiveness of the fluid flow scheme to be tested. The diameter of the conduit pipes applied in this section is 80 um.

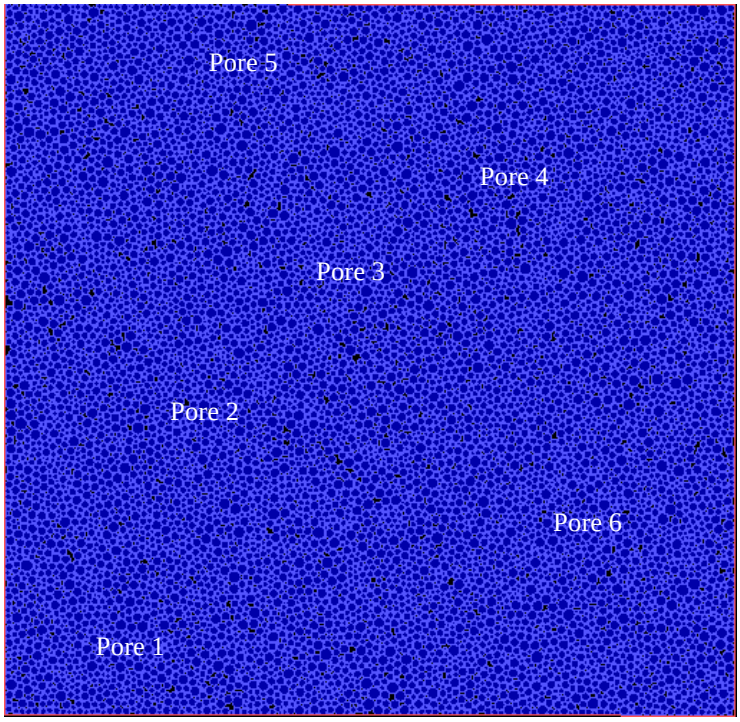

Figure 3.12 Rectangular assembly of 10000 disc particles

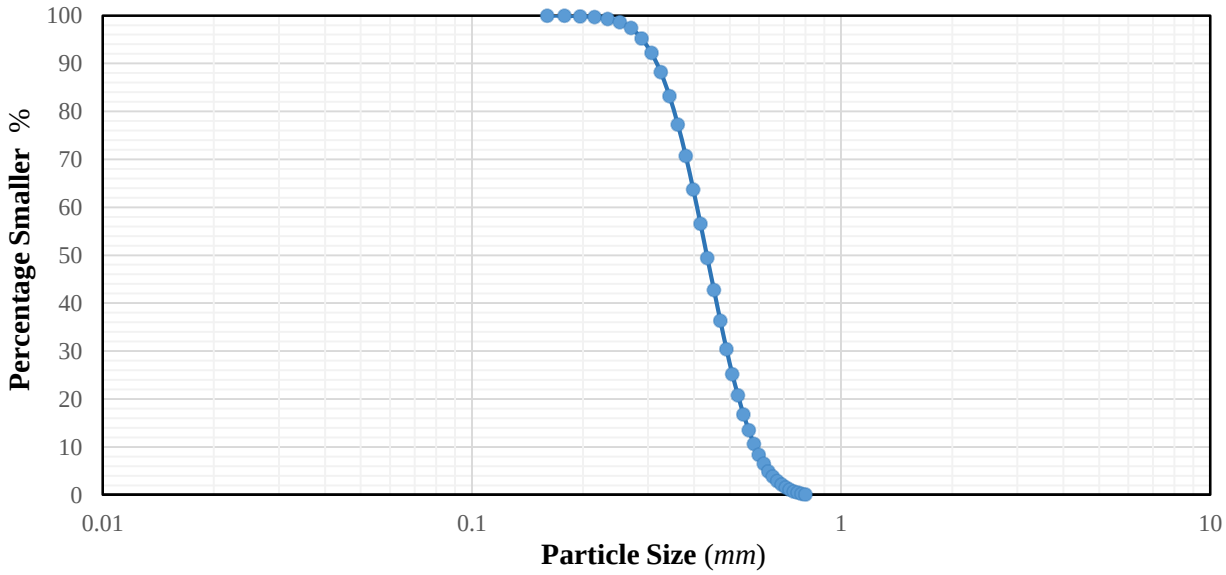

Figure 3.13 Grain size distribution of the particles in the rectangular assembly

3.8.1 Pore pressure dissipation simulation

The comparison of the proposed fluid-coupled DEM model with behavior of a poroelastic configuration can be performed by simulating the excess pore pressure variations during a consolidation process and comparing the results with that from the classical Terzaghi's theory of one-dimensional of consolidation. The simulation of the process of consolidation is achieved by initially setting a pore pressure of 50 kPa for all the pores in the rectangular assembly shown in Fig. 3.12 at the beginning of the test. Once the test starts, the pore pressures of the pores at the top and bottom boundaries are set to zero instantly. Since the particles are not allowed to move, pore pressure dissipation can only occur from the middle layer of the assembly to the top and bottom boundaries due to the pressure gradient. This process resembles a one-dimensional consolidation process with two-way drainage paths.

Equation (3.53) shows the partial differential equation that describes the one-dimensional consolidation process that was proposed by Terzaghi (Terzaghi, 1951). The analytical solution to this equation for a two way paths drainage case starting from uniform pressure distribution is shown as equation (3.54).

$$\frac{\partial u_e}{\partial t} = c_v \frac{\partial^2 u_e}{\partial z^2} \tag{3.53}$$

$$u_e = \sum_{m=0}^{m=\infty} \frac{2u_i}{M}\left(sin\frac{Mz}{d}\right)\exp(-M^2 T_v) \tag{3.54}$$

where u_e is the excess pore pressure, c_v is the coefficient of consolidation, M and T_v are two parameters having the representation shown as equations (3.55) and (3.56).

$$M = \frac{\pi}{2}(2m+1) \tag{3.55}$$

$$T_v = \frac{c_v t}{d^2} \tag{3.56}$$

Fig. 3.14 shows a comparison of the simulated pore pressure variations at different height of the assembly with that obtained from the analytical solution of the Terzaghi's one-dimensional consolidation theory at selected cycles during the progress of the test. The horizontal axis is the pore pressure and the vertical axis represents the vertical height of the assembly. The simulated pore pressure value of each pore is plotted with respect to the vertical coordinate of the pore's center of gravity which is represented by color blue. The black lines in the figure represent the theoretical excess pore pressure values at different heights of the assembly computed by using equation (3.54). From the comparison, it can be seen that, the simulated results perfectly match the analytical solution at all the selected cycles. Therefore, the behavior of the proposed fluid-coupled DEM model is very close to that of the poroelastic configuration.

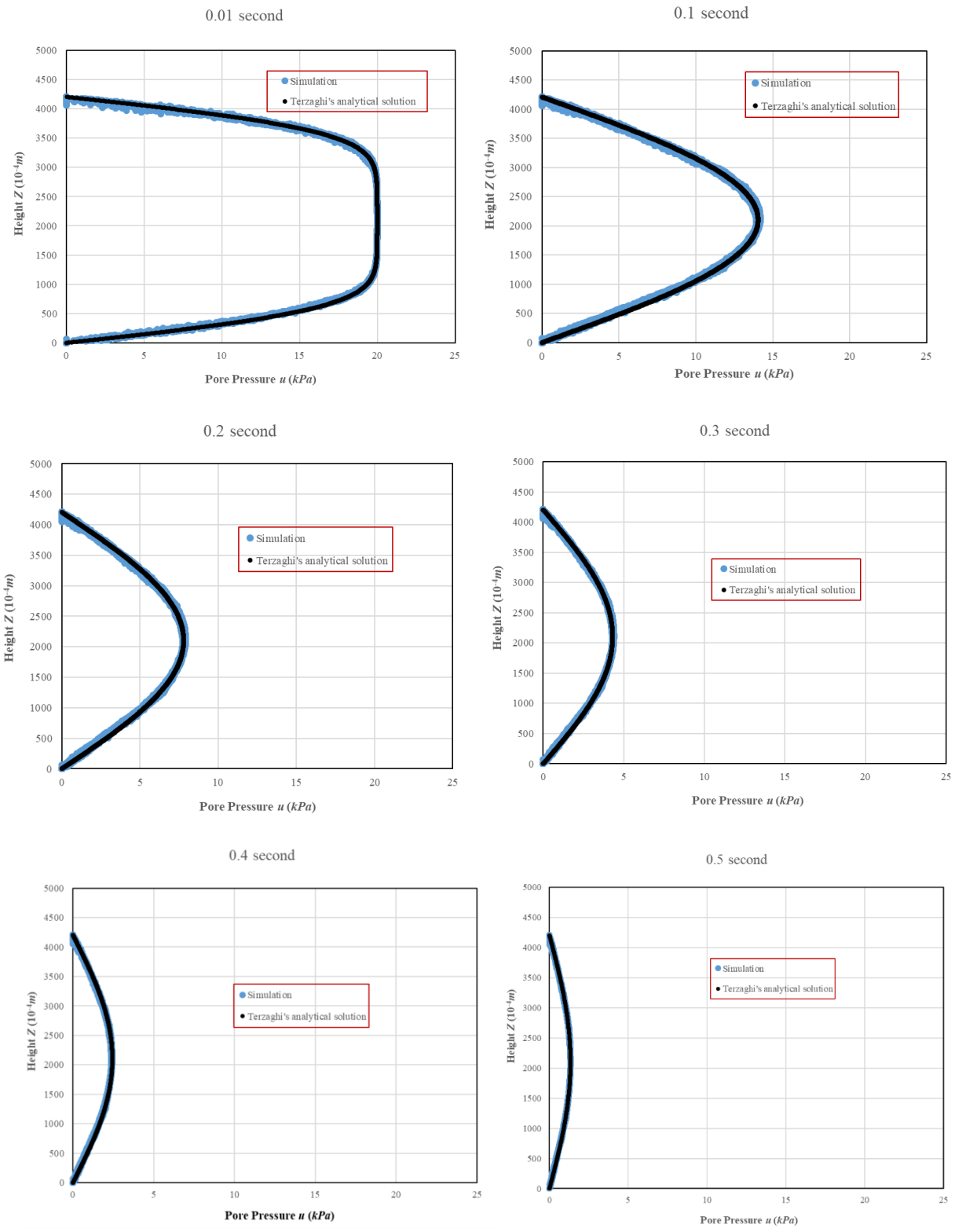

Figure 3.14 Comparison of the pore pressure dissipation from the proposed scheme with that from Terzaghi's one-dimensional consolidation theory

3.8.2 Pore pressure equalization simulation

With the above background that all the particles are restrained from moving, and fluid can only flow through the pores through the connecting conduit pipes, a test aimed at examining the equalization process of the pore pressures from pores in different locations in the assembly is also conducted. Different pore pressure values from 0 to 50 kPa are first assigned randomly to the pores in the assembly at the beginning of the test. Subsequently, the fluid in the assembly is allowed to flow freely without applying any external load for a certain time period. After this period, the pore pressure variations with time factor T_v for some randomly selected pores are examined and see if they all converge to a single value. Theoretically, it should take an unlimited time for all the pore pressures to become equal.

Results of the pore pressure variations during the simulation for six pores selected randomly in different regions in the assembly is shown as Fig. 3.15. It can be seen from the figure that although the initial assigned pore pressures of the six pores are very different, after about time factor T_v equals to 0.8, they all merge together. The pore pressure changes of all the six pores are rapidest at the begging of the test. Gradually, all the rates of change slowed down and approached zero at the end of the test when all six plots merged together with almost the same pore pressure of 25 kPa.

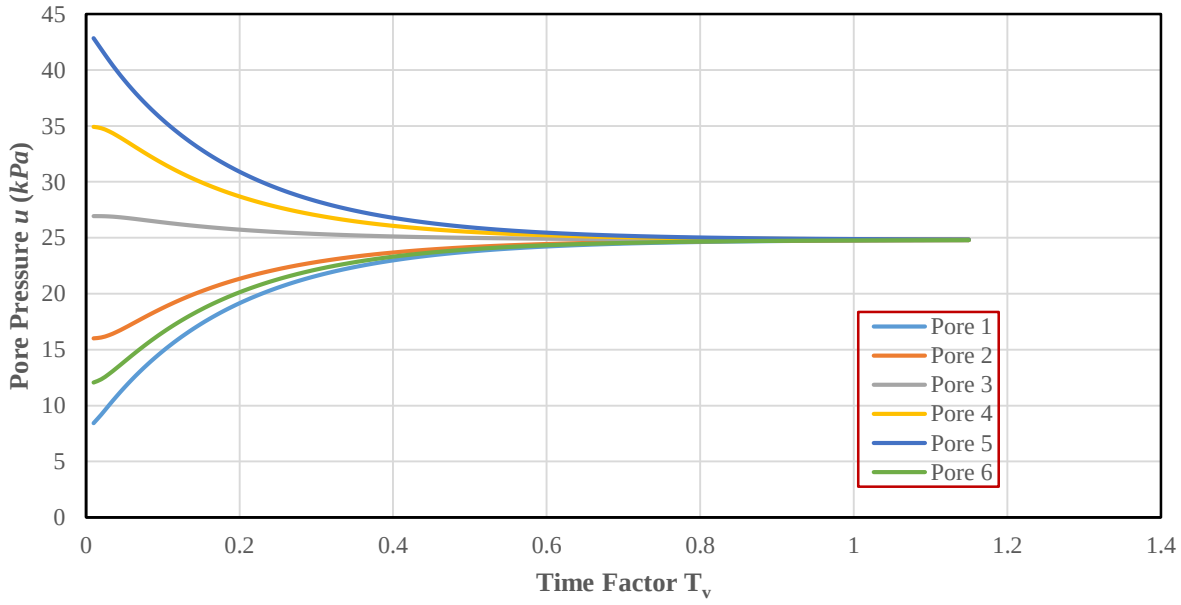

Figure 3.15 Pore pressure equalization process from 6 pores in different locations with different initial pore pressures.

3.8.3 Selection of the diameter of the conduit pipes

To correctly simulate the undrained behavior of a granular media using the proposed further developed fluid-coupled DEM, a reasonable estimate of the value of the diameter *d* of the assumed conduit pipe (Fig.

3.7) is necessary to correctly simulate the transient excess pore pressure dissipation among the connected pores. A determination of the diameter *d* for the conduit pipes can be achieved by conducting some tests of fluid flow through the rectangular assembly shown in Fig. 3.12 and employing the Darcy's law as follows.

First of all, a vertical pressure gradient *i* can be assigned at the top and bottom boundaries of the rectangular assembly to generate a fluid flow through the network of conduits in the assembly. Subsequently, we bring the flow network system to a steady state in which the pressure gradient is uniformly distributed inside the assembly. In this state, the total amount of the fluid that flows into the assembly at the top boundary due to the pressure gradient should be the same as the amount of fluid that flows out of the assembly at the bottom boundary. Next, we compute the volumetric flow rate of the fluid flow into the assembly in the vertical direction, which is the summation of the volumetric flow rates of all the pipes on the top boundary of the assembly. According to the Hagen-Poiseuille's equation (3.36), the total volumetric flow rate into the vertical direction of the assembly is:

$$Q_{in} = \sum_{n=1}^{m} q_n \tag{3.57}$$

Since Darcy's Law indicates that the volumetric flow rate can be computed by using the relationship shown in equation (3.58), where *k* is the coefficient of permeability, and *A* is the cross sectional area. Thus by combining equations (3.57) and (3.58), the coefficient of permeability *k* can be written as equation (3.59).

$$Q_{in} = kiA \tag{3.58}$$

$$k = \frac{Q_{in}}{iA} = \frac{\sum_{n=1}^{m} q_n}{iA} \tag{3.59}$$

Now a relationship between the coefficient of permeability *k* and the conduit diameter *d* can be obtained by repeating the test taking various diameter values for the conduit pipes. Fig. 3.16 shows calculated results for the coefficient of permeability *k* plotted versus the conduit diameter *d*. It can be seen from the figure that *k* increases rapidly with a small increase in *d*. It is worthy of note that the relationship between *k* and *d* shown in Fig. 3.16 is exclusive to the network constructed in this research.

Based on Fig. 3.16, an appropriate value of the conduit diameter can be selected considering the grain size distribution shown in Fig. 3.13. From Fig. 3.13, it can be seen that the average diameter of the grains (D_{50}) in the assembly is about 0.44 mm, which falls in the range of fine to medium sand. Since the typical value of coefficient of permeability for coarse sand is between 1.0 and 0.01 cm/s, and for fine sand it is between 0.01 to 0.001 cm/s (Das & Sivakugan, 2016), therefore, based on Fig. 3.16, for the adopted fine to medium

size particles, the conduit diameter is selected as 80 μm, which will be used in the undrained simulations in Chapter 4.

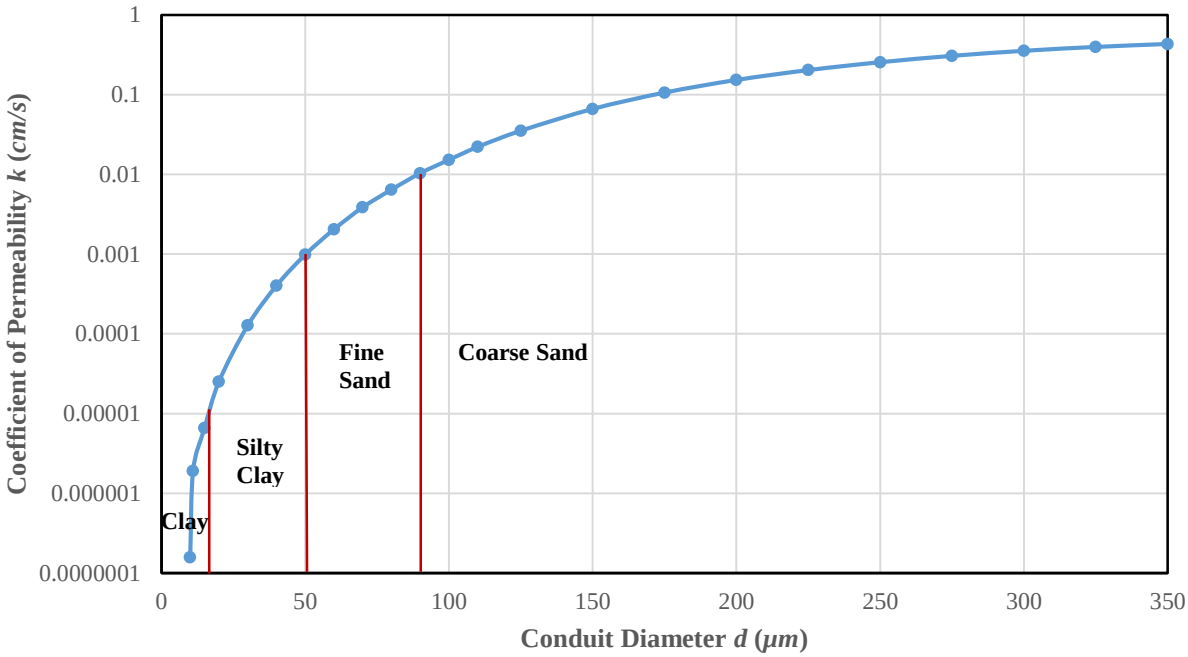

Figure 3.16 Relationship between coefficient of permeability *k* and conduit diameter *d*

Chapter 4 Simulations of Undrained Behaviors of Granular Media

4.1 General background

This chapter presents the results of the undrained simulations of assemblies of disc particles under different initial states using the proposed further developed fluid-coupled DEM. It is targeted at studying the macroscopic and microscopic characteristics of a granular media when it is subjected to undrained shearing. Based on the classic soil mechanics, a series of simulations are performed on assemblies with a variety of initial void ratios and confining stresses. To evaluate the feasibility and practicality of the proposed further developed fluid-coupled DEM in describing the undrained monotonic compression process of granular media, results from simulations are compared with those from laboratory monotonic undrained triaxial compression tests reported in the literature. In addition, a comparative study of a constant volume simulation is conducted to compare its response with that of the proposed further developed fluid-coupled DEM model. The aim is to study the macroscopic and microscopic responses influenced by pore pressure that are not captured by the constant volume method.

The characteristics of the assembly and flow network of conduit pipes along with the simulation test parameters are presented in Section 4.2. The undrained biaxial compression simulations using the further developed fluid-coupled DEM under different initial void ratios and confining stresses are presented in Section 4.3. Section 4.4 presents some results for the undrained responses of sand under different initial conditions for laboratory monotonic triaxial compression tests obtained from the literature. These results are qualitatively compared with the simulated results of Section 4.3 to show the consistency of the further developed fluid-coupled DEM and the laboratory methods. A comparison between the undrained simulation results from the proposed further developed fluid-coupled DEM and those from the constant volume method is shown in Section 4.5.

4.2 Characteristics of the assembly and flow network

4.2.1 Physical characteristics and properties of the granular system

Internal particles

The simulations in this chapter are conducted on assemblies of discs, each one of which contains about 10000 particles. The reason for choosing discs instead of ellipses is that round particles are more prone to show the phenomenon of liquefaction (Yang and Wei, 2012; Keramatikerman and Chegenizadeh, 2017; Ashmawy et al., 2003). Hence, in order to better demonstrate the micromechanical characteristics of liquefaction and thereby obtain a full picture of undrained behavior of granular media, disc particles are employed to perform the undrained simulations. The grain size distribution of the disc particles in the

assemblies adopted in this chapter follows that given in Fig. 3.13. So the grain sizes of the particles are uniform and in the fine to medium sand range. The physical properties of the disc particles such as Young's modulus, Poisson's ratio, inter-particle friction coefficient, and density come from quartzite (Franklin and Dusseault, 1991), and are listed as Table 4.1.

Table 4.1 Properties of the particles

Property	Symbol	Value
Young's modulus	E	80 *Gpa*
Poisson's ratio	υ	0.25
Inter-particle friction coefficient	μ	0.5
Density	ρ	2.65 g/cm^3

Boundary setting

It is known that there is a stress concentration at a corner on a boundary when simulations of granular media use rectangular boundaries (Olivera, 2004). To avoid this problem, the assemblies in this research adopt a circular boundary, which is constituted of 278 continuous and closed lines. Each one of the lines is seen as an elliptical particle with the same properties as the internal particles but having an eccentricity of one. Since the internal discs can also be seen as elliptical particles with an eccentricity of zero, the computations for the whole assembly can be performed by using an unified algorithm applied to the ellipse particles. Besides, the issue of membrane penetration that is frequently encountered in undrained laboratory testing is avoided in the proposed scheme.

4.2.2 Characteristics and properties of the flow system

The construction of the fluid flow system has been introduced in Chapter 3. Since the dynamic effect of the fluid flow through the porous media is simulated by using conduit pipes as illustrated in Figure 3.7, values of the dimensions of the conduit pipes need to be assigned. The length of each conduit pipe varies, according to the distance between the mass centers of neighbouring pores. The diameters of the pipes are assumed to be the same, and their value is assigned as 80 μm based on the analysis performed in section 3.8.3. Other than dimensions of the conduit pipes, physical properties of the fluid such as the viscosity and the bulk modulus are taken as those of water at 20°. The specific values are listed as Table 4.2.

Table 4.2 Properties of the fluid system

Property	Symbol	Value
Pipe diameter	d	80 μm
Viscosity (water at 20°)	$\bar{\mu}$	$1\times10^{-3}\,Pa{\cdot}s$
Fluid bulk modulus (water)	B_f	2.0 GPa

4.2.3 Generation of the assembly

To display a full picture of undrained behaviors, both dense and loose samples are necessary. And to create a sample that can trigger the phenomenon of liquefaction, a very high void ratio is critical. Among the most frequently used methods of sample preparation in laboratory undrained testing, it is the technique of moist tamping that can create a soil structure that induces liquefaction while other methods may only induce a limited liquefaction or even strain hardening, even for the same initial states. A sample of soil structure that was formed by moist tamping can be observed in the microphotographs that are presented in Figure 2.10. The aggregates and macropores are the most conspicuous characteristics of this type of structure that differ from the regular particle packing structure that is formed by air pluviation. Such particle structures having a variety of aggregates and macropores are generated numerically in this study.

The generation of the assemblies with different initial void ratios can be achieved by a combined process of expanding and shrinking the particle diameters repeatedly a few times, and then removing a certain amount of the particles that have no contact with any neighbour particles, which are termed floaters in this thesis, from the pores. The process of repeating the expansion and shrinking of the particle diameters is analogous to compaction, so the aggregates can be formed while maintaining equilibrium. By removing the floaters from the granular system, macropores can be formed without influencing the equilibrium of the whole system. The specific steps of the sample generation are as follows:

1. Create an initial assembly, then increase the boundary stress to the target level uniformly in both x and y directions by using mode 2 that was introduced in section 3.4. Both loading and relaxation are applied alternately resulting in a homogeneous assembly system.

2. Increase all internal particle diameters by 5%, which will produce large contact forces inside the assembly.

3. Alternate between loading and relaxation using mode 2 under the target boundary stress value, until equilibrium is achieved again.

4. Decrease the diameter of all particles to the original value, which will induce the loss of some contacts and the formation of some floaters within the assembly.

5. Bring the assembly to the target boundary stress value again using mode 2, until the whole system achieves an equilibrium condition.

6. Repeat the steps from 2 to 5 several times, so that the assembly can form many floaters inside the pores.

7. Remove different amounts of floaters from the system to create samples with different initial void ratios.

4.3 Undrained biaxial compression simulation tests

4.3.1 Effect of initial void ratio

4.3.1.1 Summary of the test program

To examine the influence of the initial void ratio on the undrained response of the granular assembly, a group of four samples, A, B, C, and D are prepared with different initial void ratios (see Figure 4.1). The different values of initial void ratio for the samples were achieved by controlling the number of floaters in the assembly while maintaining the condition that the main structures of all four samples were similar. The initial number of floaters of the four samples (from A to D) are 215, 705, 1245, and 1380, respectively. They are obtained by removing different amounts of floaters from the pores of the initial sample. Sample A is obtained by removing all the floaters in the assembly, sample B is obtained by removing two floaters per void, sample C is obtained by removing one floater per void, and sample D is the original sample without removing any of the floaters. After removing the different amount of floaters, all four assemblies are brought into an equilibrium state again, during which process the number of floaters in all the samples varied a bit. The above floater removal approach creates samples with a range of initial void ratios and helps the samples to exhibit a full picture of undrained behavior. Besides, the samples with different initial void ratios obtained by removing different number of floaters can help us study of how the number of floaters affects the undrained behavior of the granular assembly. The specific initial physical properties of each sample are shown as Table 4.3.

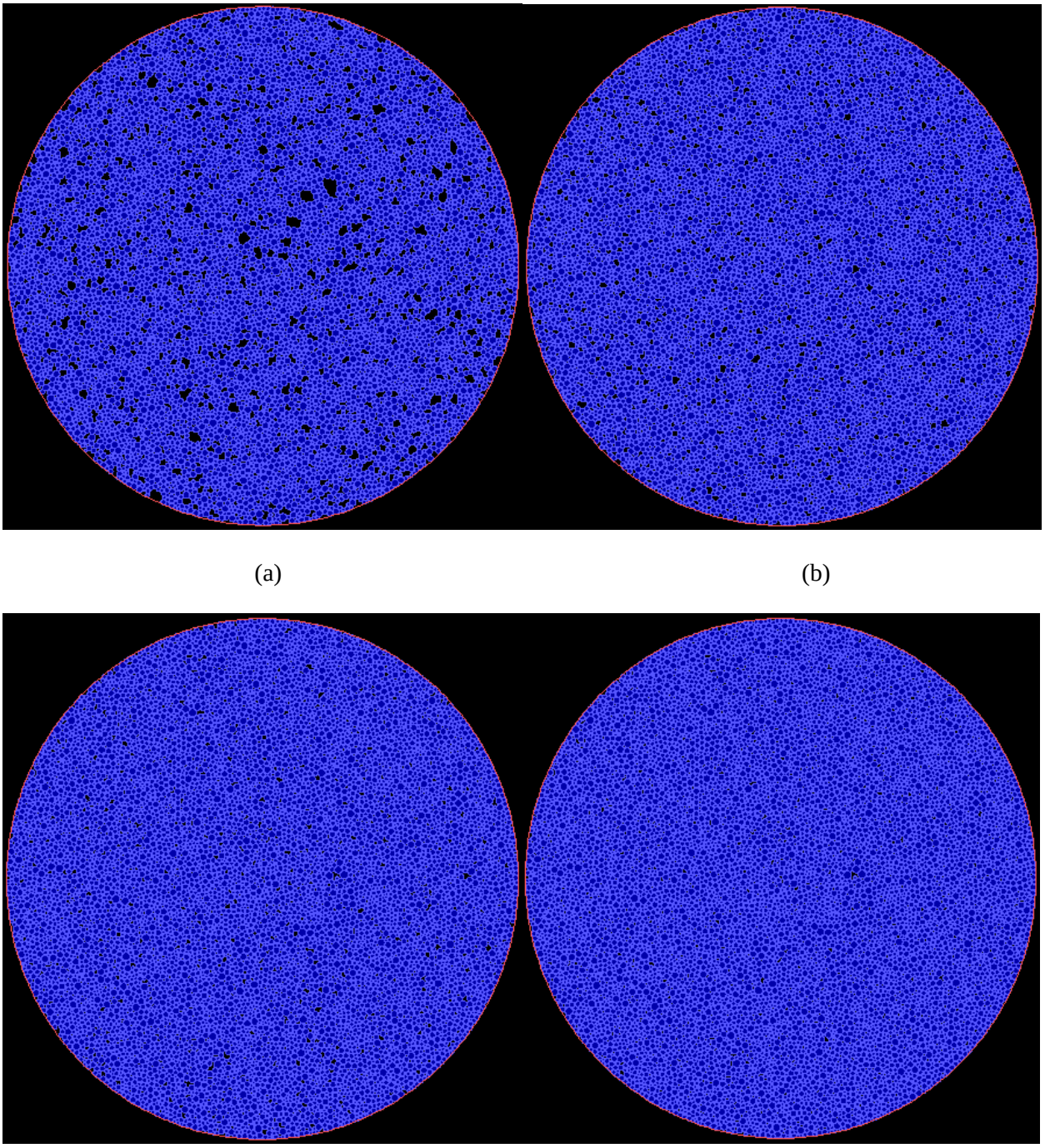

(a) (b)

(c) (d)

Figure 4.1 Initial granular assemblies with different void ratios (different number of floaters) before undrained shearing: (a) Sample A, (b) Sample B, (c) Sample C, (d) Sample D

The undrained biaxial compression simulations for all the four samples are conducted using mode 3 introduced in section 3.4, which maintains the average stress σ_{11} constant, and meanwhile, increases the average stress σ_{22} by applying a constant strain rate $\dot{\epsilon}_{22}^{\beta}$ (at the boundary). The confining stresses for all

four tests are set as 100 kPa. The associated undrained simulation test parameters such as the damping coefficient, time step, and the value of vertical strain rate employed in this section are listed in Table 4.4.

Table 4.3 Summary of initial physical properties of the tests

Test	**Sample**	**Number of floaters** (n_f)	**Initial average coordination number** (γ)	**Void ratio** (e)	**Confining stress (*kPa*)** (σ_1)
A	**A**	215	3.2045	0.3636	100
B	**B**	705	3.2246	0.2970	100
C	**C**	1245	3.2493	0.2383	100
D	**D**	1380	3.2669	0.2181	100

Table 4.4 Parameters for the undrained testing

Property	**Symbol**	**Value**
Global damping	α	0.76×10^{5} /sec
Contact damping	β	0.0 sec
Rotational damping	ω	1.0
Time step	Δt	5.28×10^{-7} sec
Vertical strain rate	$\dot{\varepsilon_{22}}$	1.0×10^{-2} /sec

4.3.1.2 Mechanical results from the simulation

Some mechanical results from the four undrained biaxial compression simulations with different initial void ratios A, B, C, and D are shown as Figs. 4.2 to 4.4, respectively. Figure 4.2 is the stress-strain response of the four samples under shearing, Figure 4.3 shows the pore pressure variations throughout the testing, and Figure 4.4 presents the stress paths of the four undrained tests. All four samples are sheared to 10% strain where a steady state is reached in samples A, B, and C. Only sample D still shows the tendency to dilation at the end of the simulation. In general, the behavior of the four tests that can be divided into two groups. Both samples A and B exhibited strain softening and developed liquefaction, while samples C and D displayed strain hardening. The specific characteristics of the undrained behavior for each test are illustrated as follows.

Test A

Sample A exhibits a very traditional strain softening type of response, and liquefaction is achieved, which typically occurs in a very loose sample. It is shown in Fig. 4.2 that the shear stress of sample A increases

rapidly during initial shearing until it reaches a peak strength of 19 kPa at about 0.3% shear strain. With continued shearing the shear stress decreased from this peak to 2.5 kPa at about 1.2% strain. Meanwhile, the corresponding pore pressure shown in Figure 4.3 increases rapidly at an almost constant rate from the beginning to about 1.2% strain, its value attains 99% of the confining stress. Subsequent shearing did not alter the shear stress much, there was only a small little reduction of the shear stress until the end of the test, indicating the achievement of a steady state condition. The residual strength obtained for this test is about 0.71 kPa. The corresponding pore pressure also did not change much, it only increases very slowly to a maximum value of 100 kPa, and then almost maintains that value until the end of the test. The stress path of test A presented in Figure 4.4 is consistent with the stress-strain curve and pore pressure variations in Figs. 4.2 and 4.3. While the shear stress increases to its peak value and there is an initial rapid pore pressure generation, the stress path starts from point (100, 0) then goes up and at the same time turns to the left in the figure because of the increasing shear stress and decreasing mean effective stress. The peak strength appears when the mean effective stress equals to 85 kPa. Continued shearing after the peak strength leads to the stress path going downwards and further to the left towards the origin due to the continuous softening of the sample and increasing pore pressure. At a large strain, the stress path maintains 0.71 kPa of shear stress and 1.6 kPa of mean effective stress until the end of the test, which is in a good agreement with the residual strength and the maximum pore pressure shown in Figs. 4.2 and 4.3.

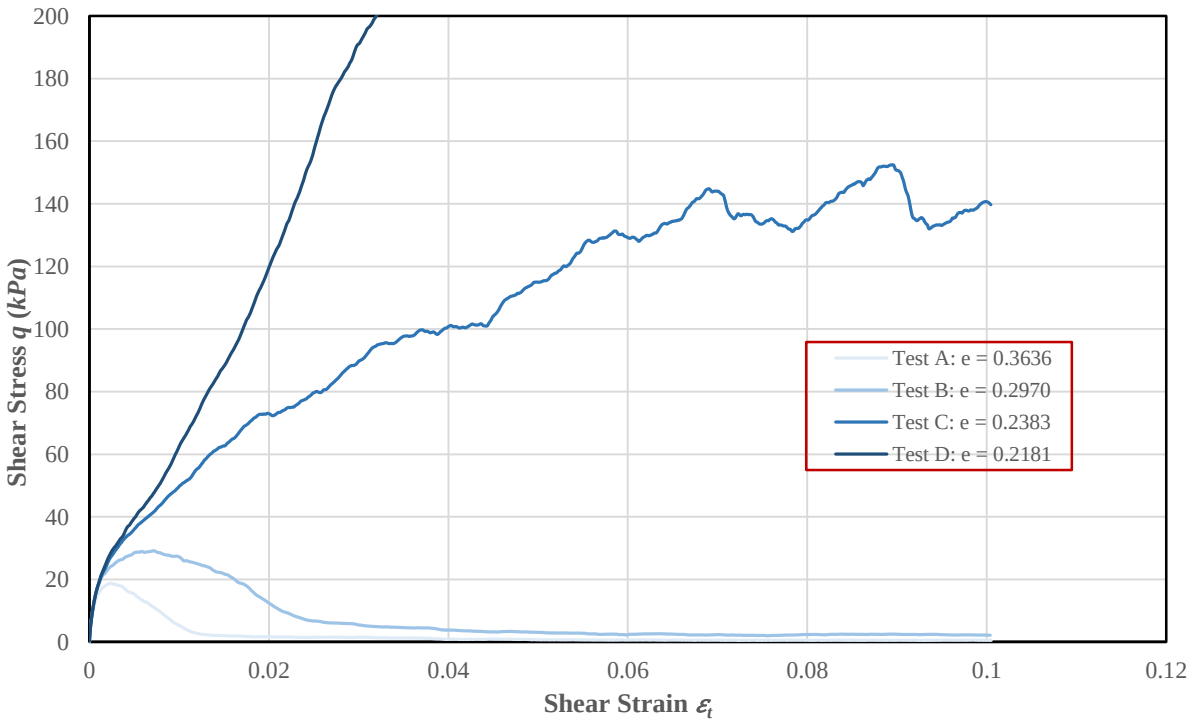

Figure 4.2 Stress-strain responses for assemblies with different void ratios

Test B

Similar to the behavior of test A, test B also triggered liquefaction, but with a higher peak strength and residual strength, as shown by the stress-strain response in Figure 4.2 and the stress path in Figure 4.4. During the initial shearing of test B, the shear stress increases rapidly at a rate of which is higher than that of test A. Along with the initial rapid increase of the shear stress, the pore pressure built up rapidly. Subsequently, the rate of the shear stress increase gradually reduces, and a peak strength of 29.1 kPa occurs at 0.74% strain, which is higher than that of test A. The pore pressure generation rate also reduces with the arrival of the peak strength. Afterwards, the shear stress decreases after reaching its peak value until reaching a value of 6.8 kPa at about 2.4% strain. The rate of decrease is lower than that of test A during strain softening. The pore pressure continued growing at first at a high rate and then gradually slowed down until about 2.4% strain it reached 91% of the confining stress value. The following shearing did not alter the shear stress and pore pressure much. There were small reductions in the shear stress and increases in the pore pressure until 5% strain, where the shear stress and pore pressure both achieved and maintained constant values indicating the achievement of a steady state. The residual strength of sample B is a bit higher than that of sample A, and the maximum pore pressure of sample B is a bit lower than that of sample A. In accordance with the stress-strain response and pore pressure variations, the stress path of test B also reveals the process of strain softening. As seen in Figure 4.4 the stress path of test B behaves very similarly to that of test A. It also goes upwards and to the left during initial shearing but with a higher peak strength and residual strength compared to test A. Therefore, sample B has a lower potential for strain softening and liquefaction than sample A.

Test C

Very different from tests A and B, test C exhibits a strain hardening response under a condition of undrained shearing. As shown in Figure 4.2 the shear stress increases from the beginning to the steady state condition, at different rates for each strain level. The rate of shear stress increase from the initiation of shearing until 0.3% strain is higher than that of test A and B at this stage. It gradually reduces until 0.3% strain, where the corresponding pore pressure reaches its peak value of 25 kPa. Subsequently, the shear stress continued increasing almost at a constant rate until 1.9% strain, while the pore pressure gradually decreased to the value of zero. From 1.9% to 3.7% strain, the shear stress further increases but at a bit lower rate than in the former stage. The corresponding pore pressure further decreases to a negative value, which indicates the microstructure tends to change from contraction to dilation. Continue shearing induces the further increase of shear stress with decreasing rate, until about 8.5% strain, the increase of shear stress almost terminated and stayed at a value of 140 kPa, and the pore pressure also stopped reducing and maintained a value of -70 kPa, indicating the arrival of a steady state condition. The stress path of test C, shows a completely

different response than that of tests A and B. From the start of the test, the shear stress increases with a small decrease of the mean effective stress due to the initial positive pore pressure generation. Afterwards, at a shear stress between 30 and 40 kPa only, corresponding to the strain at which the peak pore pressure is reached, the mean effective stress stops reducing and starts to increase due to the reduction of the pore pressure. Continued shearing causes both shear stress and mean effective stress to increase further with a constant slope until the end of the test. The corresponding decreasing pore pressure and rising shear stress indicate the occurrence of strain hardening. At the end of the test, the stress path terminated at a shear stress of 140 kPa with a mean effective stress of 240 kPa, which agrees with the residual shear strength and pore pressure shown in Figs. 4.2 and 4.3.

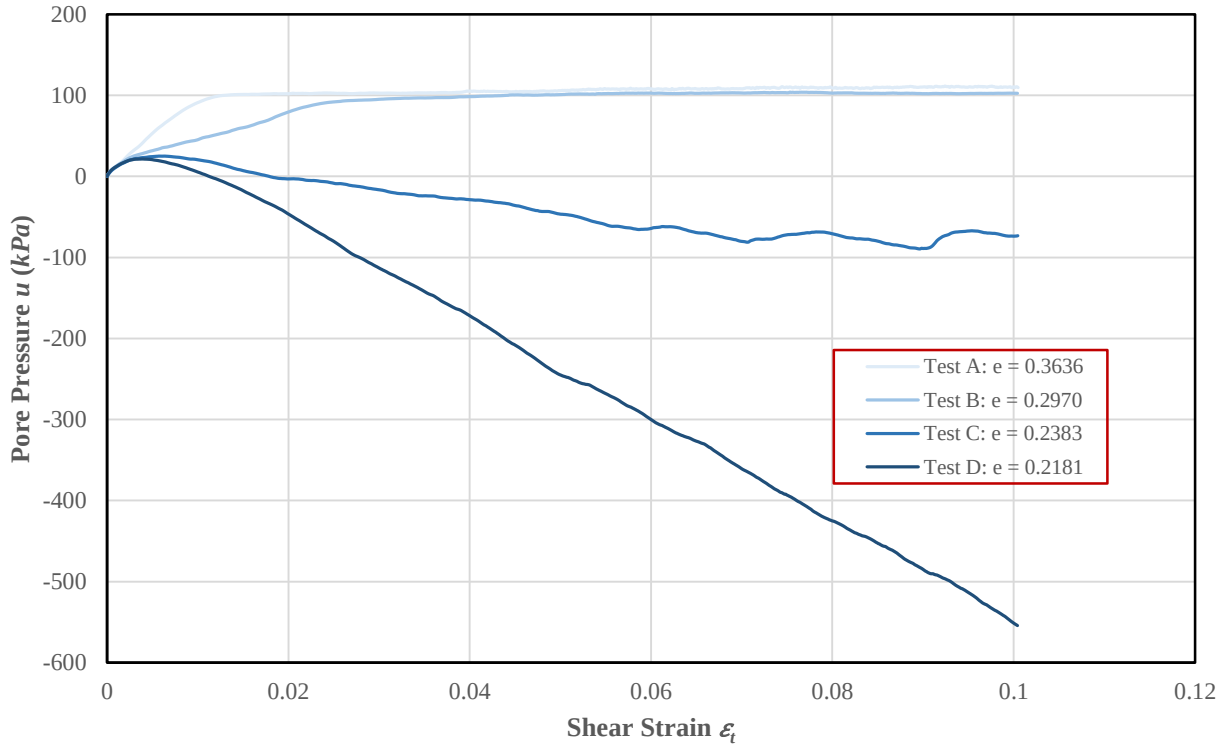

Figure 4.3 Pore pressure variations for assemblies with different void ratios

Test D

Test D also exhibits a strain hardening response but with a much higher shear strength at large strains than that of test C. The overall behavior of test D is quite similar to that of test C except that it did not achieve the steady state at the end of test. It is seen in Figure 4.2 that the shear stress of sample D increases at the highest rate among the four tests from initial shearing until 0.3% strain, where the increasing rate decreases. The corresponding pore pressure increased from zero to a peak value of 20 kPa during this initial shearing. After 0.3% strain, strain hardening initiated with almost constant rate of shear stress increase until the end of the test, and the pore pressure decreases at a constant rate from its peak value until the end of the test.

The pore pressure enters into the negative zone at 1.1% strain, which indicates the tendency to dilation. The stress path of test D is very close to that of test C, initially, it also goes up and to the left due to the generation of a positive pore pressure. Subsequently, it keeps going up but turns to the right and forms an "elbow", which corresponds to the point at which the pore pressure drops from its peak value. With further shearing the stress path increases to the right with a nearly constant slope, which is in good agreement with the decrease of pore pressure into the negative region and a steadily increasing shear stress. It is worth noting that at the point where the shear stress value equals 62 kPa and the mean effective stress equals 125 kPa, the stress path of test D merges with that of test C, indicating that the same critical stress ratio is achieved for both samples.

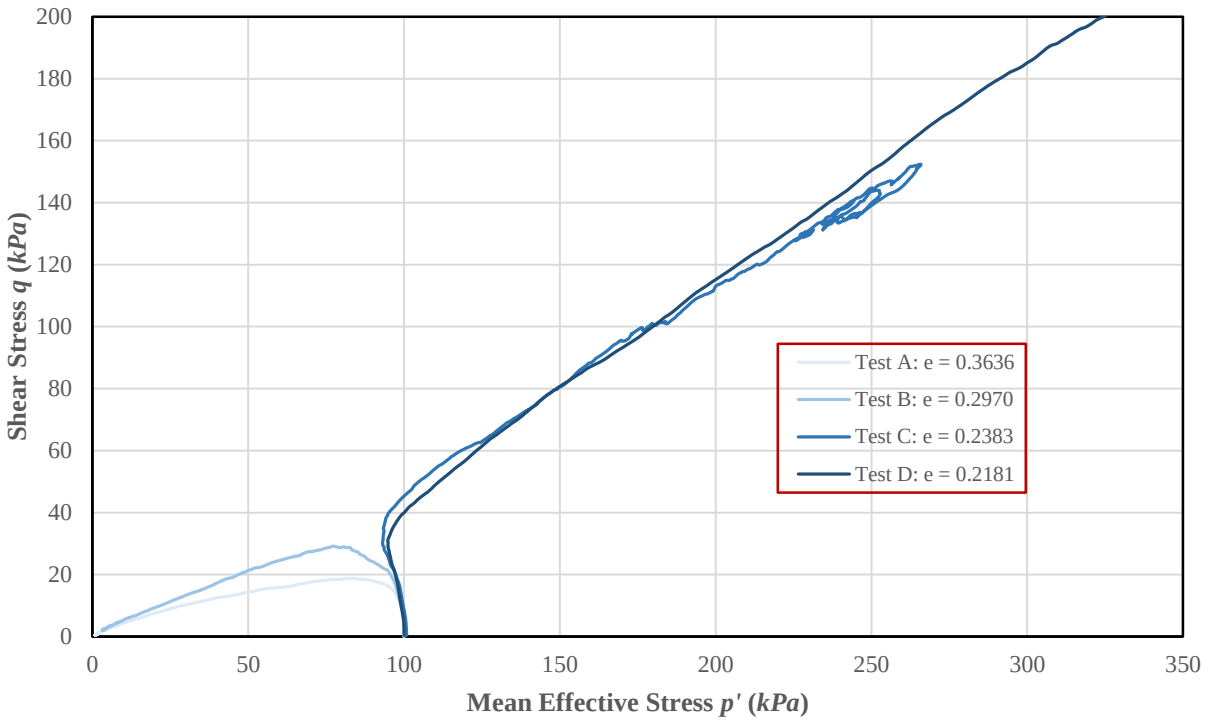

Figure 4.4 Stress paths for assemblies with different void ratios

Comments

Based on the three undrained mechanical features exhibited from Figure 4.2 to Figure 4.4, it can be seen that the four undrained tests displayed two different types of behaviors, strain softening and strain hardening. Since the four samples possess the same confining stress but different initial void ratios, it can be concluded that the void ratio controls the assembly behavior to a large extent. Basically, the lower void ratio of the assembly, the more stable the behavior of the assembly will be. Comparing the responses of the four undrained tests shown from Figs. 4.2 to 4.4, it can be seen that as void ratio decreases, the initial peak strength becomes much greater, and the strength at large strains also increases to different degrees. In

addition, as the void ratio decreases, the pore pressure at all stages decreases. As an indication of the shear stress and pore pressure variations, the stress path changes from turning left (strain softening) to turning right (strain hardening) with a decrease of the void ratio.

4.3.1.3 Micromechanical behaviors from the simulation

Figs. 4.5 to 4.8 presents the responses of descriptors that describe the micromechanical properties of the assembly (the average coordination number γ, the number of floaters n_f, the contact normal anisotropy parameter a_n, and the normal contact force anisotropy parameter a_f). Based on the responses of these descriptors throughout simulations, the corresponding mechanical undrained behaviors of each test can be understood. The specific micromechanical characteristics of each test are illustrated as follows.

Test A

It is shown as Figure 4.5 that from the beginning of shearing to 0.3% strain, the average coordination number γ decreased a bit, while the number of floaters n_f, the contact normal anisotropy parameter a_n and the normal contact force anisotropy parameter a_f shown in Figs. 4.6 to 4.8 all increased rapidly, which indicates contact creation mainly occurs vertically while contact disintegration is primarily in the horizontal direction. This corresponds to the initial rapid shear stress increase to the peak value and fast pore pressure generation stage shown in Figs. 4.2 and 4.3. From 0.3% to 1.2% strain, the rate of decrease of γ increases especially after 0.7% strain, and the rate of increase of both n_f and a_n does not vary much, while the rate of increase of a_f decreases a bit. These responses indicate the occurrence of an increasing number of contact losses in the vertical direction along with a large number of contact losses in the horizontal direction. This corresponds to the main portion of the strain softening and rapid pore pressure generation seen in Figure 4.2 and Figure 4.3. From 1.2% to 6% strain, γ further decreases but at a decreasing rate, n_f keeps on increasing at high rate, a_n increases at a decreasing rate, while a_f slowly reduced. These responses suggest that a large number of contacts disintegrate in both directions, and the sample is totally liquefied. From 6% and 8% strain, a_n decreases to some degree, while the other three descriptors do not change, which indicates that with the progress of liquefaction, more and more contacts are lost in the vertical direction. From about 8% strain, a steady state is achieved, and all four descriptors remain at almost constant values until the end of the test.

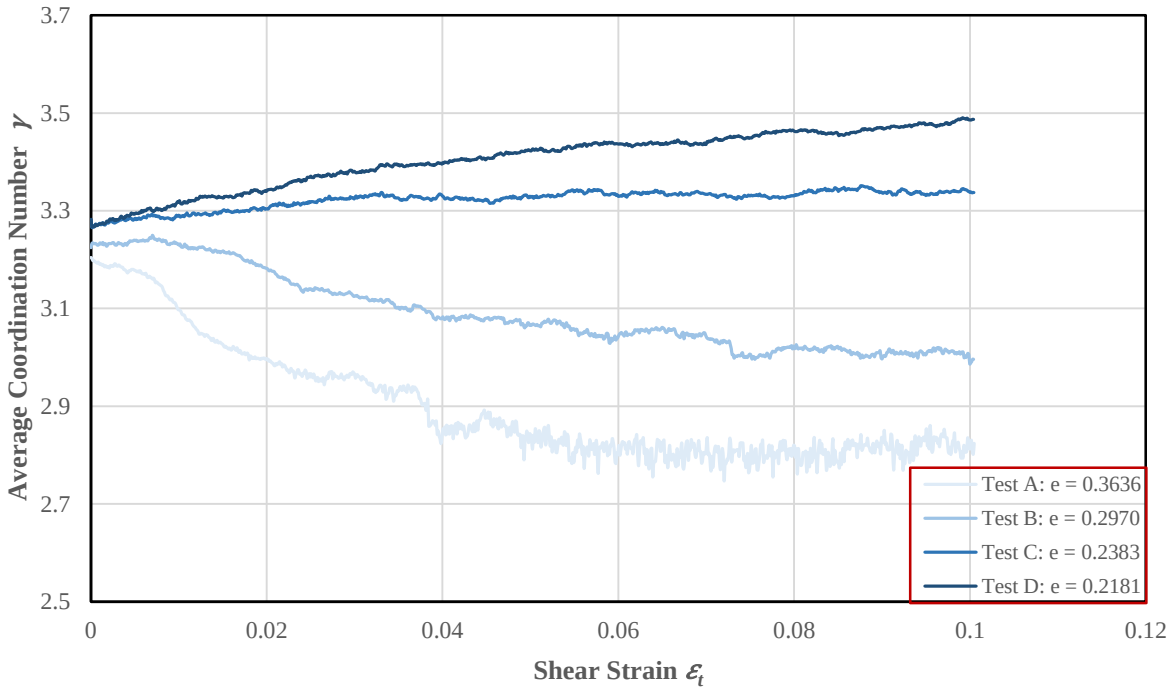

Figure 4.5 Average coordination number γ variations of assemblies with different void ratios

Test B

The overall micromechanical responses of sample B is similar to that of sample A. From the beginning of shearing to about 0.65% strain, the average coordination number γ depicted from Fig. 4.5 maintains an almost constant value, while the number of floaters n_f as shown in Fig. 4.6 decreased a bit at a constant rate. However, the associated contact normal anisotropy parameter a_n and the normal contact force anisotropy parameter a_f shown in Fig. 4.7 and Fig. 4.8 increased rapidly, at higher rates than those of test A in this phase. This response indicates that at this stage, the contact creation is mainly in the vertical direction and contact loss occurs in the horizontal direction. The slow decrease in the number of floaters n_f is the result of a fast contact creation with the help of floaters in the vertical direction. Thus, there is an associated increase of the shear stress as seen in Fig. 4.2. The subsequent shearing resulted in a strain softening of the sample, which in terms of the micromechanical descriptors results in a rapid reduction of γ, a bit lower rate of increase of a_n and a_f compared to the previous stage, and a slow increase of n_f. Hence, an increasing number of contacts are lost in the vertical direction along with a fast disintegration of horizontal contacts. From 2.4% to 7.3% strain, sample B entered into a liquefaction phase, γ drops further but at a lower rate than in the previous stage, while a_n, a_f and n_f all increase slowly indicating the contact disintegration occurs in both directions. Continued shearing after 7.3% strain did not further alter the values

of the four micromechanical descriptors, all of which maintained almost constant values, therefore, a steady state prevailed until the end of the test.

Test C

The micromechanical behavior of test C is very different from that of tests A and B. The initial shearing leads to a slow growth of γ and a dramatic reduction of the number of floaters n_f. The associated a_n and a_f values both increase faster than those of test A and B in this stage. This response demonstrates a large number of contacts are created vertically with the help of floaters in the pores and only a small number of contacts disintegrate horizontally. This response is most distinct from the beginning of the test to 0.5% strain. Afterwards, the microstructure tends to change from contraction to dilation as seen in Fig. 4.3. Until 8.5% strain, strain hardening manifests itself, where γ, a_n and a_f all steadily increase and n_f steadily reduces. Contact creation is predominant in this stage, and in both directions along with the generation of negative pore pressure exhibited in Fig. 4.3. After 8.5% strain, all the four descriptors maintain almost constant values which agrees with the unchanged shear strength seen in Fig. 4.2 and constant pore pressure in Fig. 4.3, so the granular system have reached a steady state.

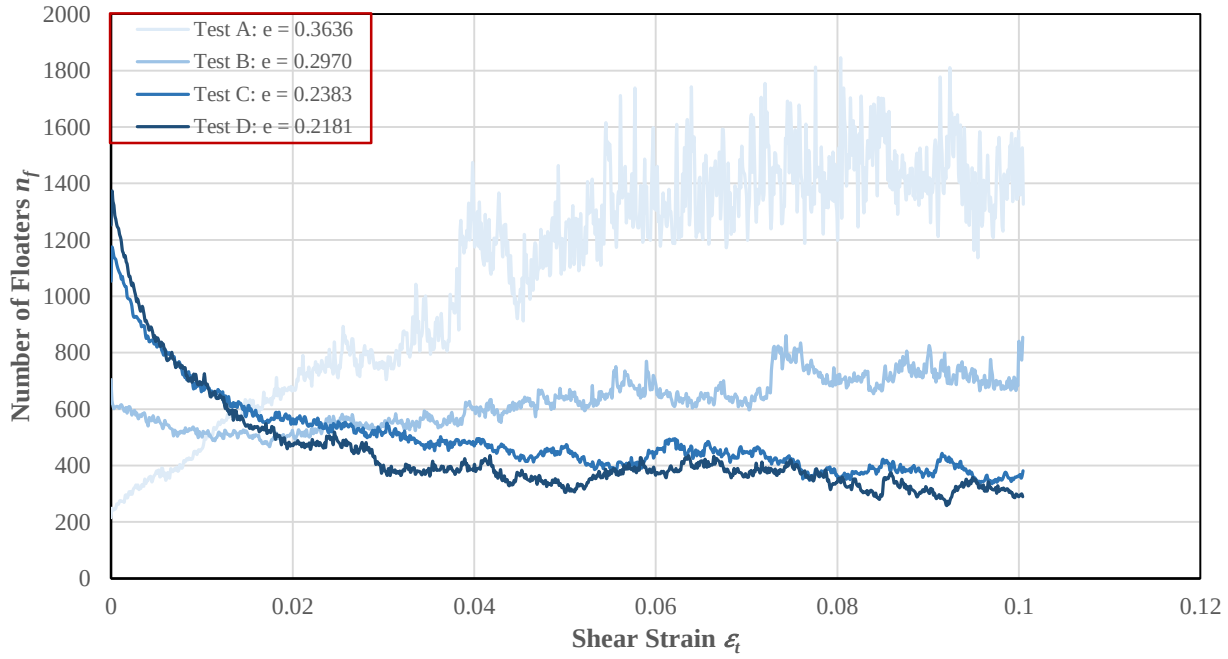

Figure 4.6 Number of floaters n_f variations for assemblies with different void ratios

Test D

The micromechanical response of test D is quite similar to that of test C, but shows more prominent characteristics, which is consistent with the associated mechanical behaviors. The initial shearing from the beginning to about 0.4% strain has a rapid increase in shear stress, while the associated pore pressure rises

to its peak value. In this stage, the changing rates of all descriptors for sample D shown in Figs. 4.5 to 4.8 are very close to those of test C in this stage. Hence, similarly to the micromechanical behavior of test C, contact creation in the vertical direction is predominant in this stage with the help of the floaters inside the pores. After 0.4% strain, the granular assembly starts to show the tendency to dilation. Manifested in Figs. 4.7 and 4.8 is the continuous rising of a_n and a_f at a decreasing rate. The rate of reduction of floater numbers n_f also become lower, but γ still keeps increasing at the same rate. This response demonstrates that in this stage, contact creation is predominant in the granular assembly, and that it occurs in both directions, which matches the mechanical behavior of a continuous reduction of the pore pressure and the tendency to dilation of the system. By the end of simulation, γ still continue increases, although the other three descriptors stop varying much. This means the construction of contacts in both directions continues due to the tendency to dilation until the end of simulation, which is in accordance with the non-stop increase of the shear stress at the end of simulation shown in Fig. 4.2. It can be expected if shearing of sample D is continued to an even larger strain it will reach the steady state and all the four descriptors will stop changing and stay at constant values like sample C.

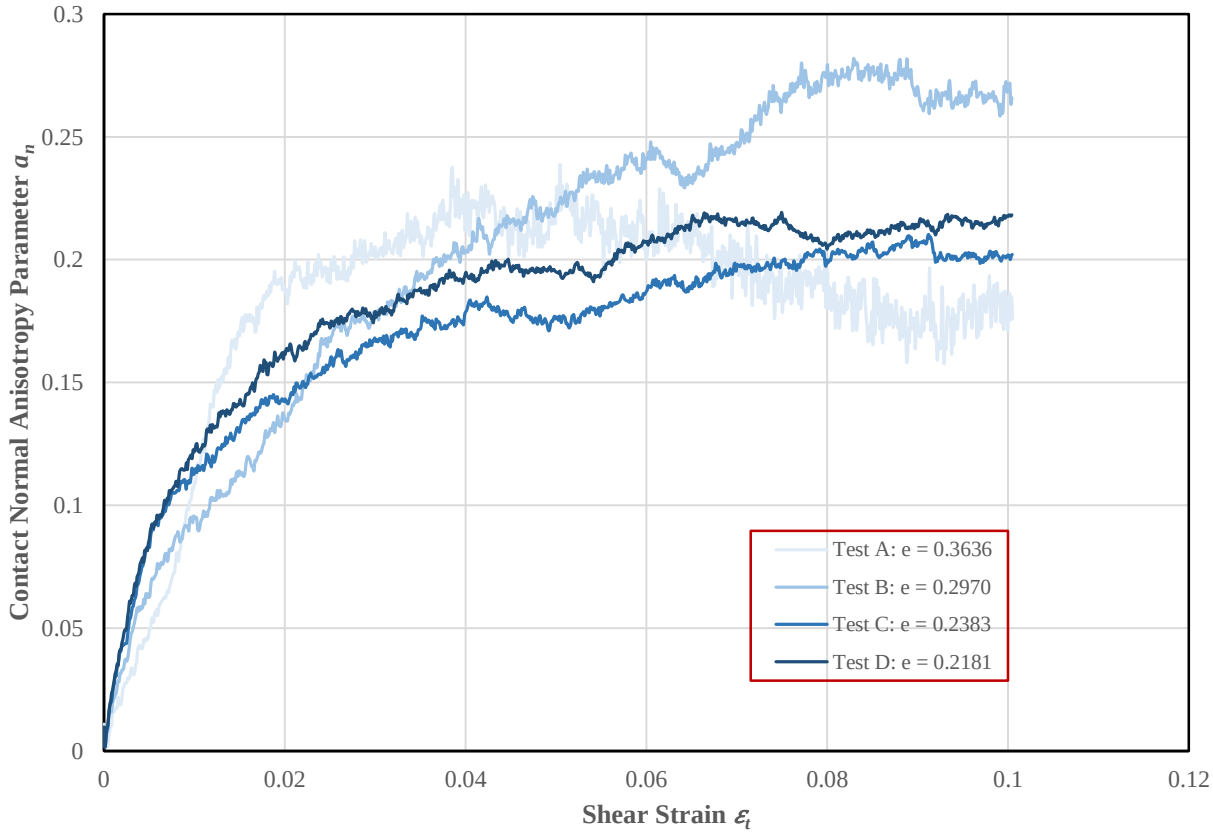

Figure 4.7 Contact normal anisotropy parameter a_n for assemblies with different void ratios

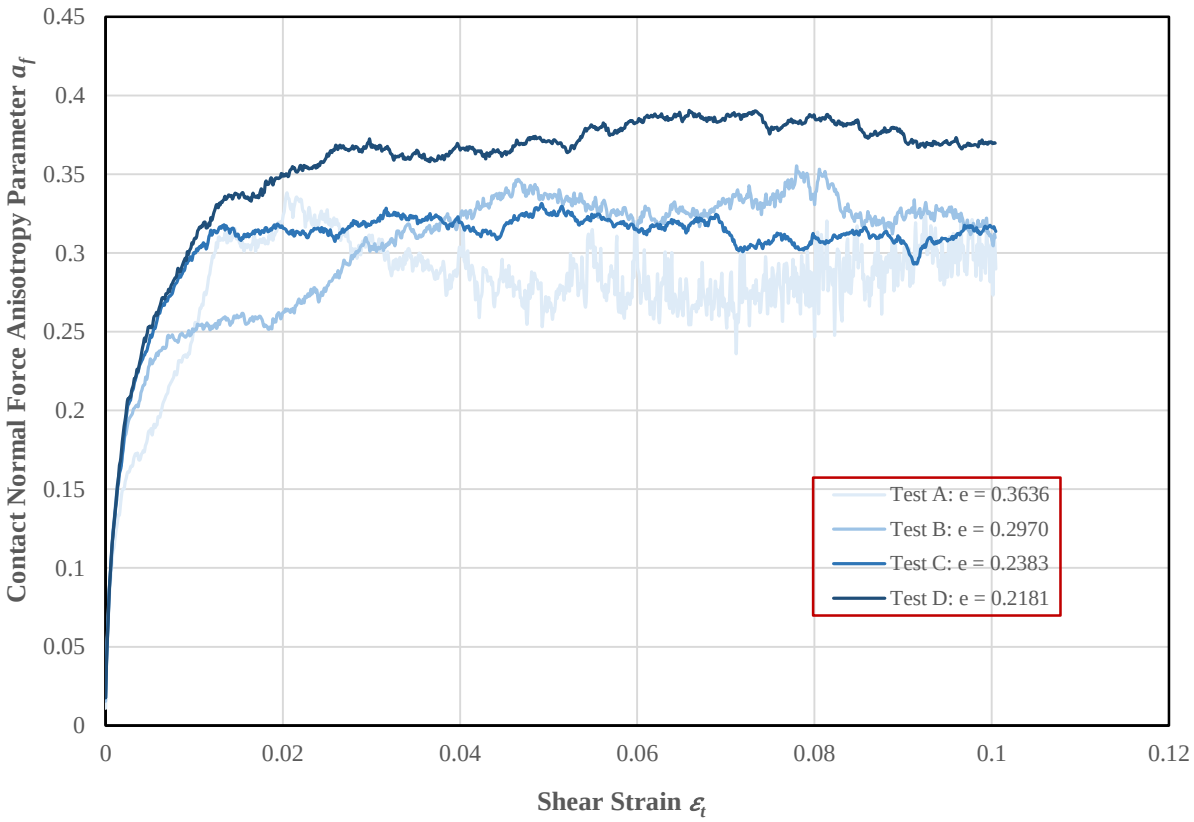

Figure 4.8 Normal contact force anisotropy parameter a_f for assemblies with different void ratios

Comments

Based on the above analysis of the micromechanical descriptors response along with the shearing, it can be seen that in addition to the void ratio of the assemblies, the number of floaters n_f affects the undrained behavior of the granular system. Upon the initial shearing of all the four tests, contact creation is mainly vertically due to the increase of the vertical load and contact disintegration is mainly horizontally. The subsequent shearing would be expected to create more contacts in the vertical direction to support the increasing load, however, it turns out the other way around as the growth of the pore pressure in tests A and B. An increasing number of vertical contact lost occurred in tests A and B so they softened, and, A which had fewer floaters n_f in its pores softened earlier than B. On the contrary, the greater number of floaters n_f inside the pores of samples C and D supported the increasing vertical load by satisfying the need for vertical contacts. Hence, C and D hardened, and less pore pressure was generated while creating the contacts vertically. With more pore pressures generated in samples A and B, a large number of vertical contacts disintegrated along with the fast horizontal contact lost, so the strain softening progressed and the associated number of floaters n_f increased accordingly. During the hardening of C and D, the large number of contacts created in the vertical direction induces the microstructure tendency to dilation. Thus, the pore pressure

continuously dropped and more contact creation occurred in both directions until the arrival of the steady state shown in test C, which did not exhibit in test D until the end of simulation. Therefore, besides the impact of void ratio, for the adopted assemblies, it is the number of floaters n_f that affects the behavior of the undrained granular assembly.

4.3.2 Effects of confining stress

4.3.2.1 Summary of the test program

To examine the influence of the confining stress on the undrained response of the granular assembly, a group of three samples (E, F, and G) were prepared in addition to sample B that has already shown in section 4.3.1. Samples E, F, and G have close void ratios but different values of confining stresses from 200 kPa to 400 kPa in intervals of 100 kPa. They were prepared based on sample B, but varied by increasing the confining stress of sample B to different levels from 200 kPa to 400 kPa first, then bringing them into the equilibrium state for testing. Some physical properties for each sample in this group are shown as Table 4.5.

Table 4.5 Summary of initial physical properties of the tests

Test	Sample	Number of floaters (n_f)	Initial average coordination number (γ)	Void ratio (e)	Confining stress (kPa) (σ_1)
B	**B**	705	3.2246	0.2970	100
E	**E**	309	3.3079	0.2955	200
F	**F**	267	3.3440	0.2941	300
G	**G**	238	3.3729	0.2929	400

Similar to the simulations present in section 4.3.1, the undrained biaxial compression simulations for all the four samples are conducted using mode 3 introduced in section 3.4, which maintains the average stress σ_{11} constant, and meanwhile, increases the average stress σ_{22} by applying a constant strain rate $\dot{\epsilon}_{22}^{\beta}$ (at the boundary). The associated simulation parameters for undrained biaxial compression testing in this section also follow the values presented in Table 4.4.

4.3.2.2 Mechanical results from the simulation

Some mechanical responses from the simulation for the four undrained biaxial compression tests with similar void ratio but different confining stresses B, E, F, and G are shown as Figs. 4.9 to 4.11, respectively.

All four samples were sheared to about 10% strain, where all had achieved steady states. Figure 4.9 gives the stress-strain responses under shearing, Figure 4.10 shows the pore pressure variations throughout the testing, and Figure 4.11 presents the stress paths for the four undrained tests. Overall, the behaviors seen in the graphs of the four tests are very similar, all of them exhibit strain softening and liquefaction. From B to G, the peak shear strength and maximum pore pressure both become higher with greater confining stresses. The stress paths of all four samples merge at the same critical stress ratio line after the occurrence of the peak shear strength. Since the responses of the four samples are very similar, and specific behavior of sample B has been interpreted in section 4.3.1, here the interpretation of the undrained behavior of the four samples will only focus on comparing their responses influenced by the confining stresses.

Stress-strain Responses

The stress-strain curves shown in Fig. 4.9 indicate that all four samples show the strain softening type of response. They all liquefied after the initiation of the strain softening, and the steady states were achieved at large strains. The residual strengths for all four samples are very low, which means all four granular assemblies lost most of their strength by the time they reached the steady state. The values of the residual strength for the four tests are very close, increasing from B to G. These are the similarities of the four tests, nevertheless, there are indeed some discrepancies among them. It can be seen from Fig. 4.9, that the most conspicuous characteristic of the responses is that as the value of the confining stress increase from B to G, the peak shear strength becomes higher, but the duration of the peak strength becomes shorter. In addition, the strains it took to complete strain softening becomes greater from B to G. Thus, the confining stress affects the peak shear strength and the extent of strength reduction significantly.

Pore Pressure Variations

The pore pressure variations of the four tests presented in Fig. 4.10 agree with the above stress-strain responses. Specifically, all four tests exhibit a very high pore pressure build up rate at the initial sharing. From B to G, the initial pore pressure built up rate increases in sequence, which is consistent with the sequence of initial shear stress growth rate illustrated in Fig. 4.9. Subsequently, the pore pressure increase rates for all four samples are gradually reduced while the shear stress climb to their peak value and then initiate strain softening. From B to G, the duration of this reduction in the rate of pore pressure increase decreases. A similar trend is shown in the sequence of the peak shear strength durations shown in Fig. 4.9. Afterwards, the rate of pore pressure increase for all four tests increased again as strain softening continued. Near the end of strain softening the pore pressure increase slowed down, as it approached 98% of each confining stress. The maximum pore pressure achieved at the end of the tests increase from B to G, in the same sequence as the peak shear strengths of Fig. 4.9. Therefore, the confining stress has a strong impact

on the initial pore pressure build up rate and the maximum pore pressure value at the steady state, both of which increase with increasing confining stress.

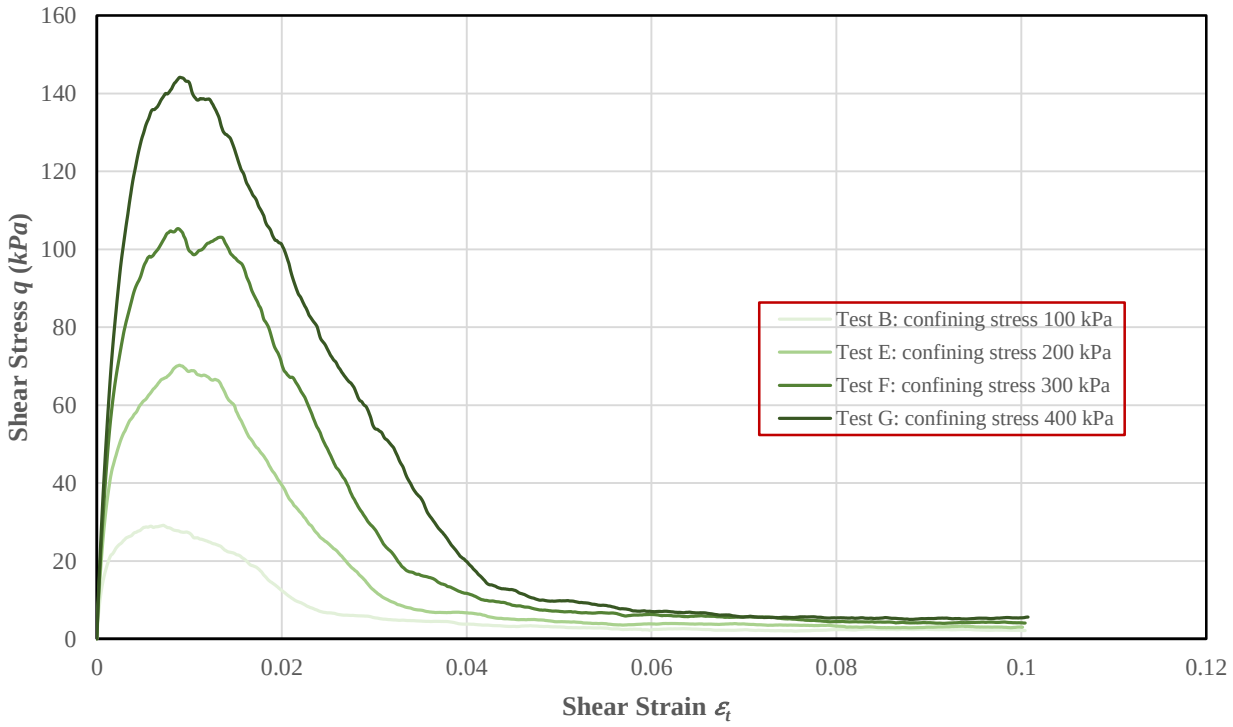

Figure 4.9 Stress-strain responses for assemblies with different confining stresses

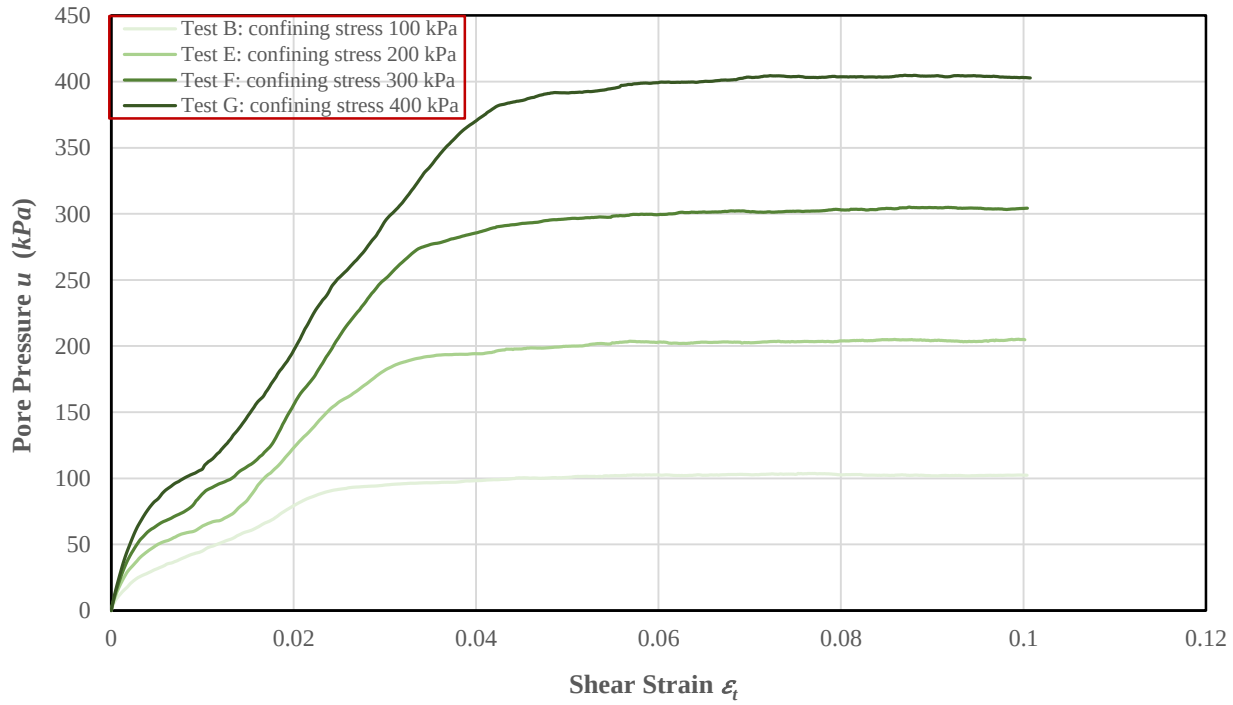

Figure 4.10 Pore pressure variations for assemblies with different confining stresses

Stress Paths

The stress path plots for the four tests presented in Fig. 4.11 are consistent with the stress-strain responses shown in Fig. 4.9 and the pore pressure variations given in Fig. 4.10. Although started with different points from 100 kPa to 400 kPa in the horizontal axis, the shear stress of all four tests all initially increase to the peak value with the decrease of mean effective stress, which then start to reduce with further reduction of the mean effective stresses following almost the same slope. It can be seen from Fig. 4.11 that the process of the shear stress increases to the peak and the following initiation of the strain softening are less rounded from B to G. This is in accordance with the sequence of the duration of the peak shear strength and the duration of the pore pressure increasing rate reduction. Until the steady state, all the four stress paths stop variating and in the sequence of less close to the origin point from B to G following the critical stress ratio line. From the above illustration of the stress path variations of the four tests, it can be seen that the confining stress affects the stress path to a large extent, mainly in the initial starting point and the peak shear strength value.

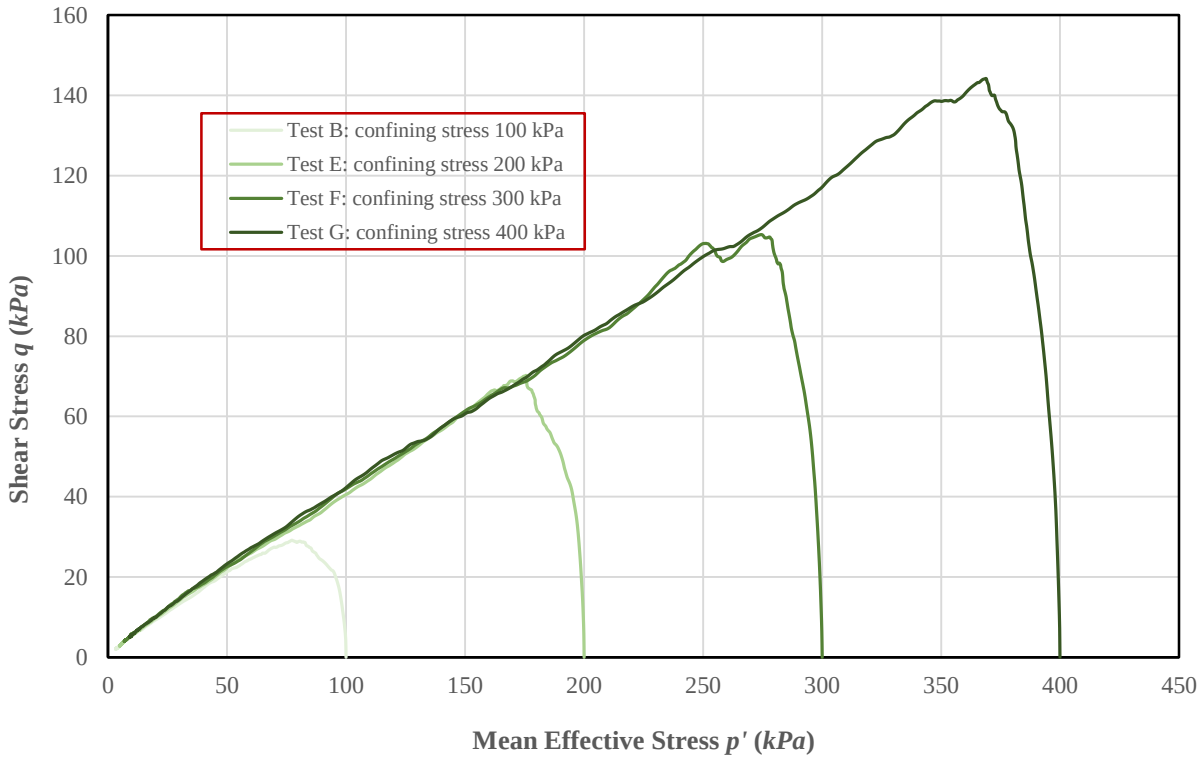

Figure 4.11 Stress paths for assemblies with different confining stresses

Comments

In general, the three mechanical response results exhibited in Figs. 4.9 to 4.11 demonstrate that although the undrained behaviors of the four samples are quite similar in terms of the overall pattern, the confining

stress affects the undrained behavior significantly, especially on the peak shear strength value and the pore pressure build up rate. The specific reasons that the confining stress has a strong impact on the undrained behavior of the granular system and in particular the different durations of the peak shear strength are considered from the point of view of micromechanics in the following section.

4.3.2.3 Micromechanical behaviors from the simulation

Figs. 4.12 to 4.15 shows the micromechanical descriptors (the average coordination number γ, the number of floaters n_f, the contact normal anisotropy parameter a_n, and the normal contact force anisotropy parameter a_f) responses of the four samples under undrained shearing. The overall undrained micromechanical behaviors of the four tests are quite similar and can be divided into three stages that are associated with the corresponding stress-strain responses.

First Stage

The first stage lasts from the beginning of the tests until the peak shear strength is reached – see Fig. 4.9. In this stage, the average coordination numbers γ for samples E, F, and G shown in Fig. 4.12 all slowly decreased while only that of sample B γ shows a small increase. From samples E to G, the rate decrease of γ increases slightly. The corresponding contact normal anisotropy parameter a_n and the normal contact force anisotropy parameter a_f in this stage both increase rapidly for all four tests, which indicates that contact creation mainly occurs vertically while contact integration mainly occurs horizontally. From B to G, the rate of increase of both a_n and a_f reduces a bit, which means that more contact is lost vertically in samples F and G that in samples B and E. This is related to the increasing rate of the initial pore pressure build up from B to G, which is also indicated from the fact that the number of floaters for all four tests in this stage drop with different degrees after the first instant change upon the shearing. Since the initial pore pressure build up rate increases from B to G, the decreasing rate of the number of floaters n_f become less accordingly due to the less connections of the floating particles with neighbour particles in the vertical direction from high pore pressure.

Second Stage

The second stage lasts from the peak shear strength to the end of strain softening for each test. In this stage γ continues to decrease for all four tests coincident with the development of the strain softening. The rates decrease of γ for the four tests are similar and in all cases, higher than in the previous stage indicating a drastic softening in this stage. When the strain softening nears its end, all four γ values stop their rapid decrease. The contact normal anisotropy parameter a_n in this stage still increases for all four tests, but at a much lower rate than in the former stage. The normal contact force anisotropy parameter a_f in this stage

decreases temporarily, then increases slowly. From the responses of γ, a_n, and a_f, it can be concluded that less net contact creation occurs vertically. From B to G the increasing rate of a_n and a_f decreases in sequence, which can be attributed to the reason that the contact lost happened in both directions are more drastic in sample F and G than in samples B and E in this stage. This is consistent with the higher strain softening rate in samples F and G compared to samples B and E shown in Fig. 4.9. The number of floaters in this stage for all four tests switches from decreasing to increasing, although the decrease lasted longer in samples B and E than in samples F and G because a lower pore pressure generation rate has less effect on contact creation due to the connection of floaters in the vertical direction. Correspondingly, the peak shear strength in Fig. 4.9 lasted much shorter in samples F and G than samples B and E, which is because of the relatively higher pore pressure build up rate prevented the vertical contact construction through connecting with the floaters. Afterwards, the number of floaters n_f in all samples increase but with a rate that decreases from B to G, which agrees with the decreasing rate of increase of a_n in this stage.

Third Stage

The third stage lasts from the end of the strain softening to the steady state at the end of the test. In this stage, γ further decreases but at a very much low rate than in the previous two stages for all four tests until the achievement of a constant coordination number at a large strain. The terminal values of γ for all four tests are similar with a small discrepancy, which is in consistent with the associated residual strengths of Fig. 4.9. The number of floaters n_f and the contact number anisotropy parameter a_n in this stage both increase slowly until reaching a constant value, which announced the arrival of the steady state. The values of all parameters at the steady state are close with a bit difference, which agrees with their close values in residual strength.

Comments

From the above interpretations of the micromechanical responses for the four tests in the three stages, it can be concluded that the micromechanical responses shown by the descriptors are in a good agreement with the mechanical undrained behaviors. The confining stress affects both mechanical and micromechanical responses greatly. The influence on the mechanical behavior mainly manifests itself with the association of the peak shear strength and the pore pressure build up rate. With respect to the micromechanical responses, the confining stress controls the rate of change of the four micromechanical descriptors in the course of reaching their steady state.

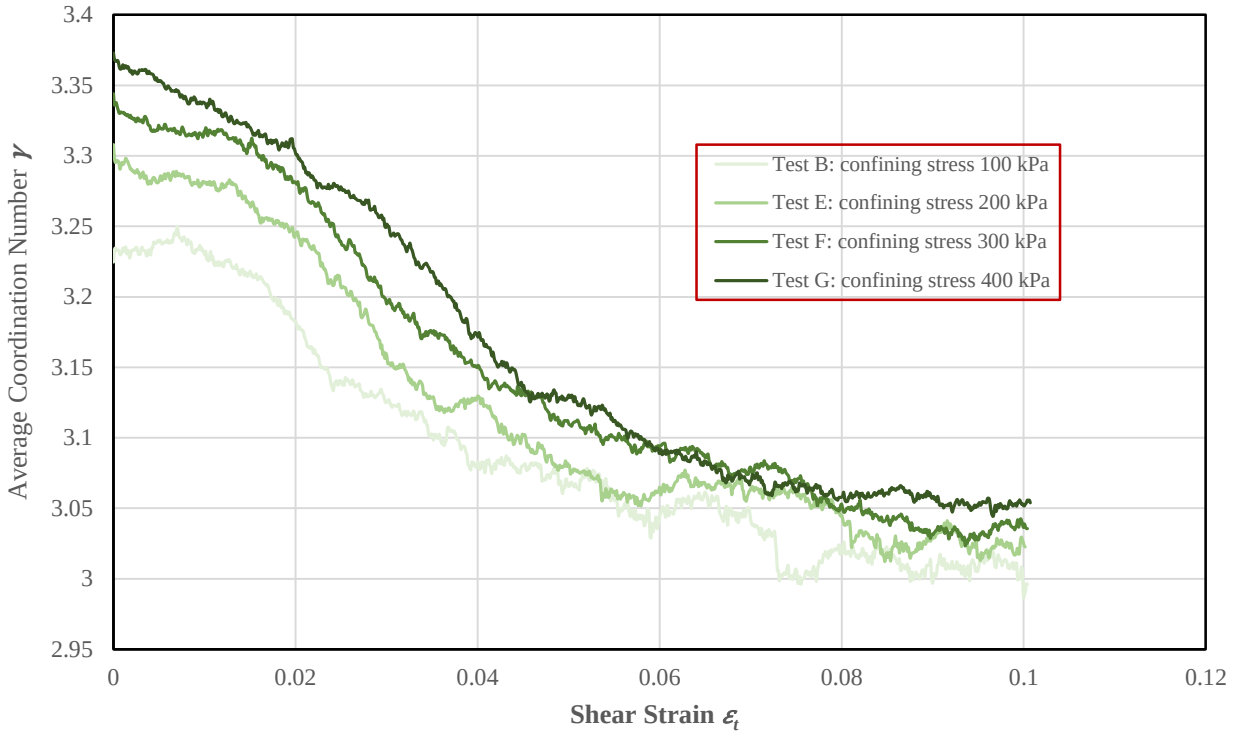

Figure 4.12 Average coordination number γ variations for assemblies with different confining stresses

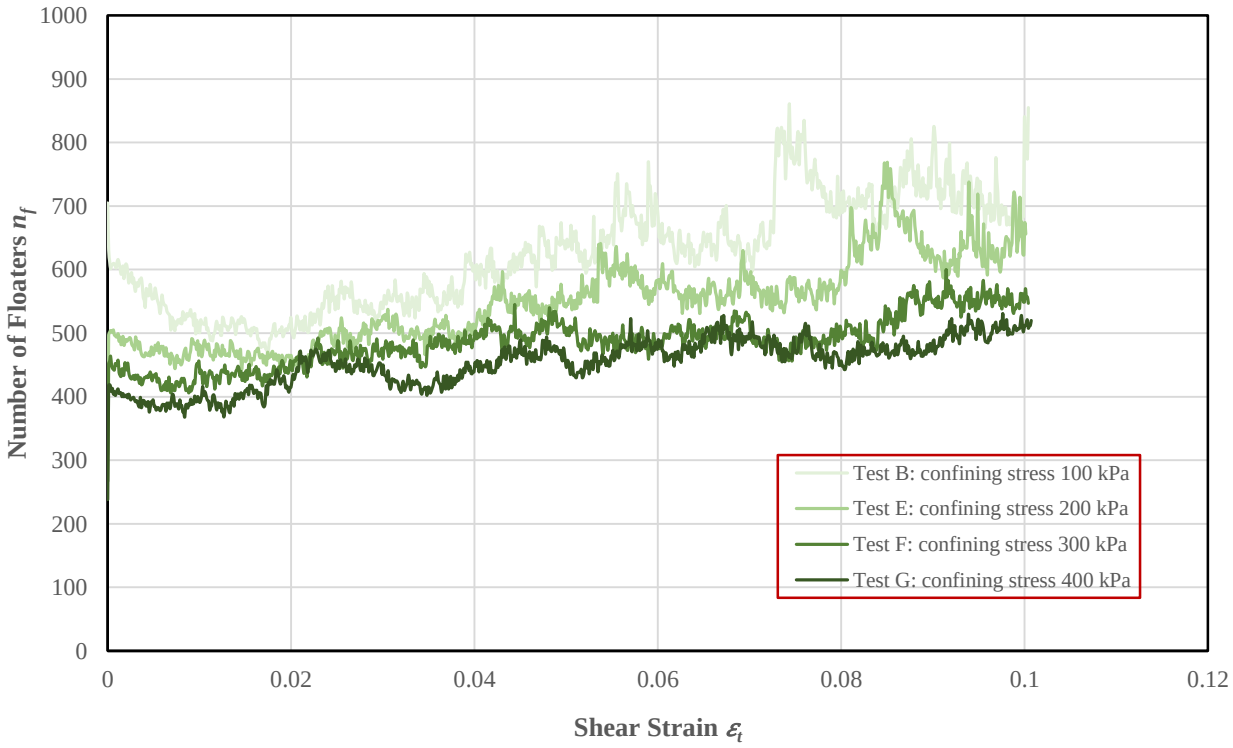

Figure 4.13 Number of floaters n_f variations for assemblies with different confining stresses

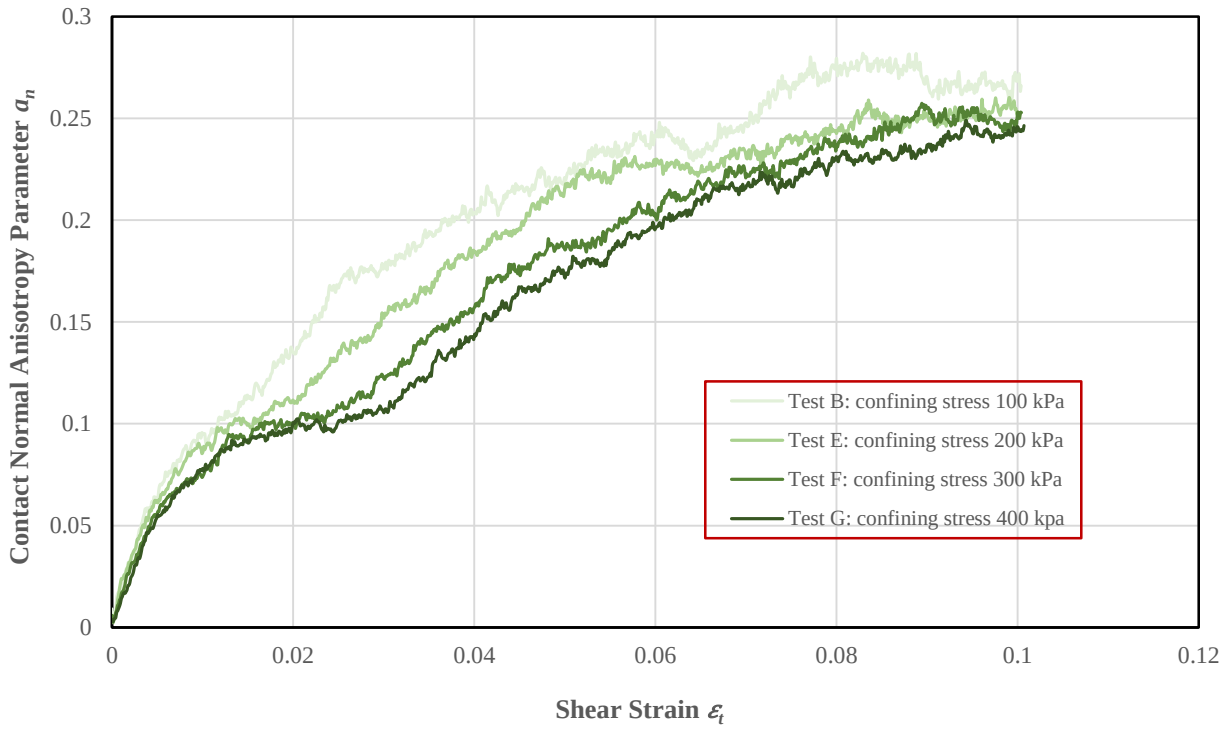

Figure 4.14 Contact normal anisotropy parameter a_n for assemblies with different confining stresses

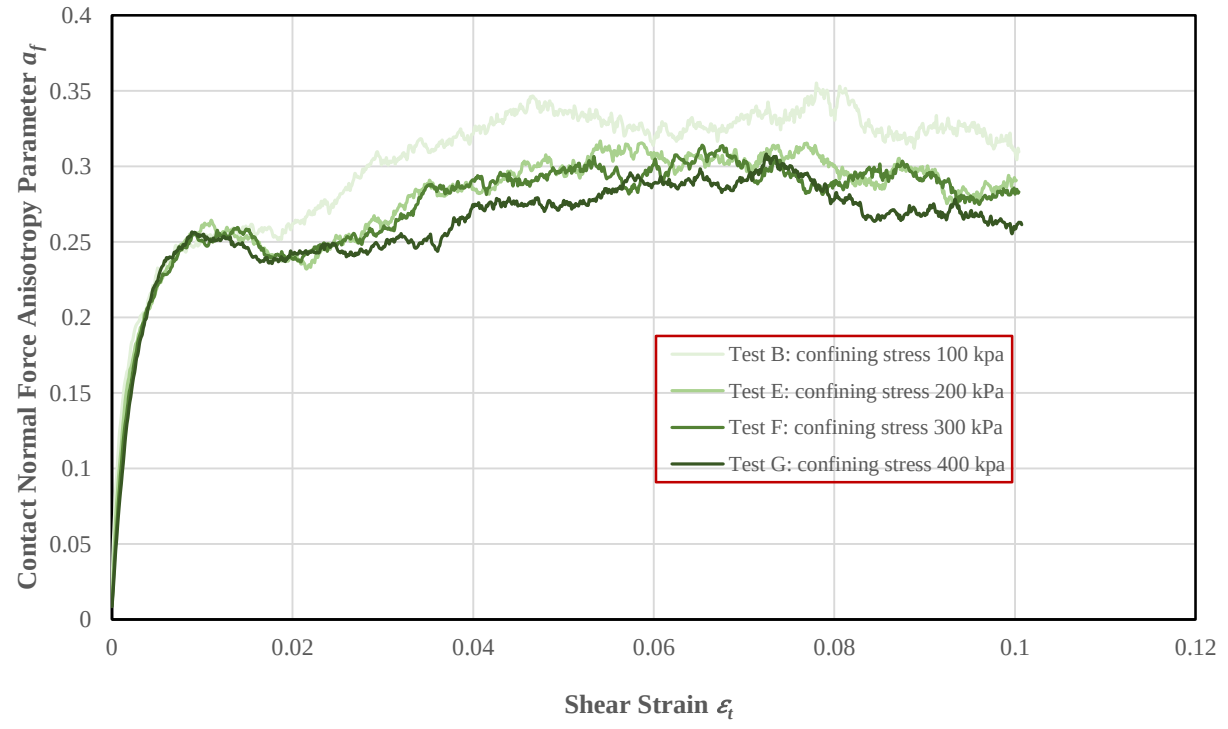

Figure 4.15 Normal contact force anisotropy parameter a_f for assemblies with different confining stresses

4.4 Comparison of simulated results with laboratory test results

4.4.1 Introduction

In this section, a comparison is made between simulated results from section 4.3 and results from undrained monotonic triaxial tests selected from the literature. The comparison of the simulated results and laboratory test results is made in terms of the effect of initial void ratio and confining stress as presented in section 4.3. The selected laboratory test results that were employed to perform the comparison are from undrained monotonic triaxial tests on Alaskan 140-5 sand, which were reported by Jefferies and Been in 2006 (Jefferies and Been, 2006). (Supporting data can be downloaded from http://www.golder.com/liq.) The Alaskan 140-5 sand is a fine sand with 5% of fines passing a No. 200 sieve. Its D_{50} is 140μm, its maximum and minimum void ratios are 0.856 and 0.565 respectively, and its specific gravity is 2.7. These physical properties of the Alaskan 140-5 sand are close to the properties we assigned to the assemblies when doing the simulations. In addition, all the selected results of Alaskan 140-5 sand were obtained by using samples prepared by a moist tamping technique, which creates a structure of aggregates and macropores that is similar to the structure of the assemblies developed in this research. Therefore, the results of Alaskan 140-5 sand are selected for the comparison. A specific comparison of the results obtained using the two methods for different void ratios and various confining stresses are as follows.

4.4.2 Comparison of the results from varying the void ratio

Figs. 4.16 to 4.18 presents a group of results from undrained monotonic triaxial testing of the Alaskan 140-5 sand, which were sheared under a confining stress of 200 kPa. The three samples in this series of tests have different initial void ratios of 0.872, 0.785, and 0.715 respectively. All of them were sheared to a large strain of over 15%. It can be seen from Fig. 4.16 that the stress-strain curves from the three tests display two types of undrained behavior. The one with the highest void ratio of 0.872 exhibits strain softening while the other two tests both show the strain hardening. Their associated pore pressure variations shown in Fig. 4.17 confirm this response pattern. The sample with a void ratio of 0.872 developed very high pore pressures that are close to its confining stress at a large strain, while the other two samples both induce negative pore pressures after reaching an intermediate strain indicating that the tendency to dilation was triggered due to the low void ratio. Consistent with Figs. 4.16 and 4.17, the stress paths shown in Fig. 4.18 also exhibit the same response. Only the stress path of the sample with a void ratio of 0.872 turns to the left towards the origin after passing the peak strength due to a continuous generation of positive pore pressure, which indicates the occurrence of liquefaction. While the stress paths of the other two tests both turn to right with the increase of shear stress following almost the same slope demonstrating the occurrence of strained hardening.

The above undrained behaviors of the Alaskan 140-5 sand are very similar to those of the undrained simulations shown in Figs. 4.2 to 4.4, although the undrained tests of the Alaskan 140-5 sand were conducted under a confining stress of 200 kPa while the simulated results were performed under a 100 kPa as the confining stress. Both of the two groups of results reveal the same behavior in that there is a higher potential for liquefaction when the samples are loose, while the tendency to strain harden and dilate will be displayed if the sample is dense. The only difference between the two groups of undrained behaviors is that compared to the simulated results, all the Alaskan 140-5 sand showed a higher strength at comparable levels of shear strain. In addition to the effect of confining stresses, the disc particles that were employed in the simulation may contribute to this difference, since the studies reported by Li (2013), Li et al. (2013), and Matsushima and Chang (2011) indicate a higher degree of roundness of particles usually results in a lower resistance. Other than these, the two groups of test results are very close to each other and show very similar responses of granular media under undrained shearing.

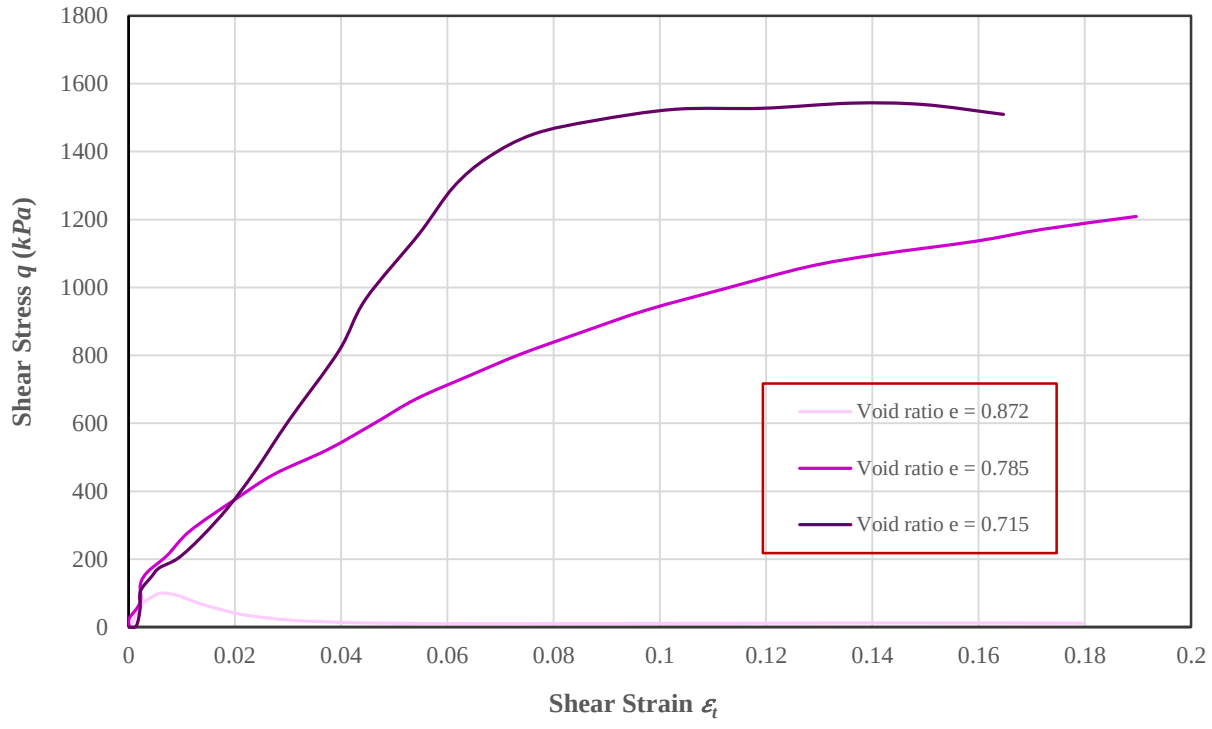

Figure 4.16 Stress-strain responses for Alaskan 140-5 sand with different void ratios (http://www.golder.com/liq)

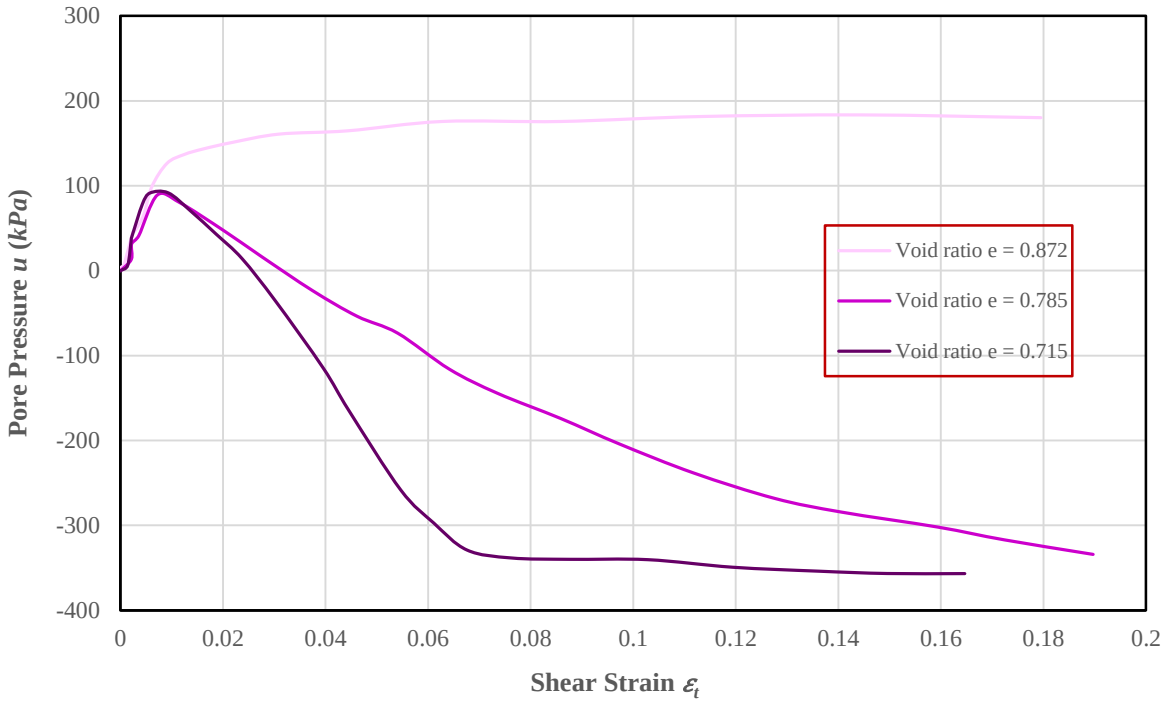

Figure 4.17 Pore pressure variations for Alaskan 140-5 sand with different void ratios (http://www.golder.com/liq)

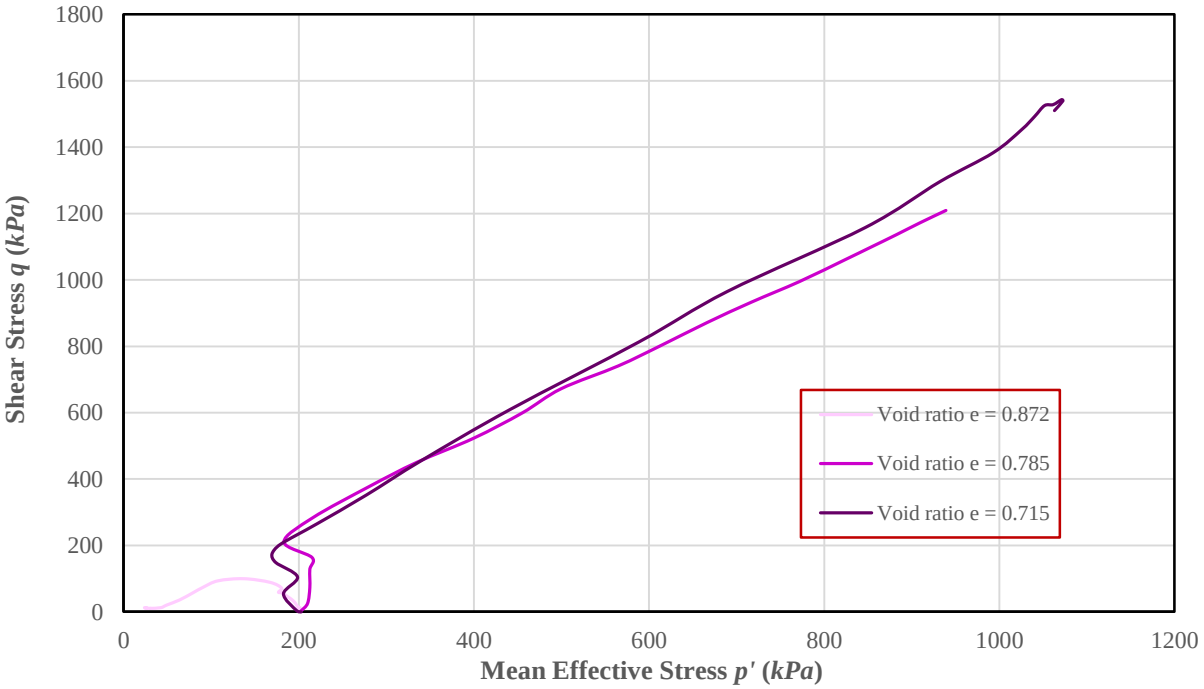

Figure 4.18 Stress paths for Alaskan 140-5 sand with different void ratios (http://www.golder.com/liq)

4.4.3 Comparison of the results for varying confining stresses

Figs. 4.19 to 4.21 shows a series of four undrained test responses of the Alaskan 140-5 sand with close void ratios but were sheared under different confining stresses varying from about 100 kPa to 400 kPa. The four samples have void ratios of 0.881, 0.872, 0.924, and 0.857 respectively for the sequence corresponding to 100 to 400 kPa pressure. All of them are sheared to a large strain of about 17% that triggered liquefaction. It can be seen from Fig. 4.19 that the stress-strain curves of the four tests all display a strain softening type of undrained behavior. From the test with the lowest confining stress to the one with the highest confining stress, the peak strength increases and the strain softening duration lasts longer. At large strains, all the four residual strengths are quite close to each other. Consistent with Fig. 4.19, the pore pressure variations in the four tests of Fig. 4.20 agree with their stress-strain responses. They all display a very high pore pressure build up rate during initial shearing, which gradually slow down and approach maximum values at large strains that are close to their confining stresses representing the initiation of the strain softening and the occurrence of liquefaction. The stress paths shown in Fig. 4.21 are in accordance with the stress-strain and pore pressure variations shown in Fig. 4.19 and Fig. 4.20. They started with different initial confining stress from about 100 kPa to 400 kPa, and the shear stress of all four tests all initially increase to their peak value with the decrease of mean effective stress, which then start to reduce with a reduction of the mean effective stresses following similar slopes. At the steady state, all the four stress paths terminated at low residual strengths and low mean effective stresses, which is in accordance with the residual strengths and maximum pore pressures shown in Figs. 4.19 and 4.20.

The above undrained behaviors of the Alaskan 140-5 sand sheared under different confining stresses are very similar to those of the simulated results shown in Figs. 4.9 to 4.11. Only at large strains, the residual strengths from the simulations are closer to each other than the undrained tests of Alaskan 140-5 sand, since the initial void ratios of the four assemblies for the simulations are very close to each other while the initial void ratios of the four Alaskan 140-5 sand samples have larger differences. Also the duration of corresponding peak strength exhibited by the two groups of tests are different, which can also be shown from the temporarily slow increase of the pore pressure generation rate and the associated relatively straight stress path at the intermediate strain range of the simulated results. All these responses can be attributed to the fact that there are many floaters in the assemblies that were adopted for simulation. Except for these two main differences, the undrained behaviors of simulations and experiments are very close to each other, all of them exhibit significant strain softening and liquefaction, and show that a higher peak strength is achieved when the associated confining stress is higher. In terms of the pore pressure variation, both exhibit the same pattern of a higher initial pore pressure build up rate and a much higher maximum pore pressure with a higher confining stress. Therefore, on the whole, the results of simulations and experiments are very

close to each other and show very similar responses of granular media under undrained shearing with different confining stresses.

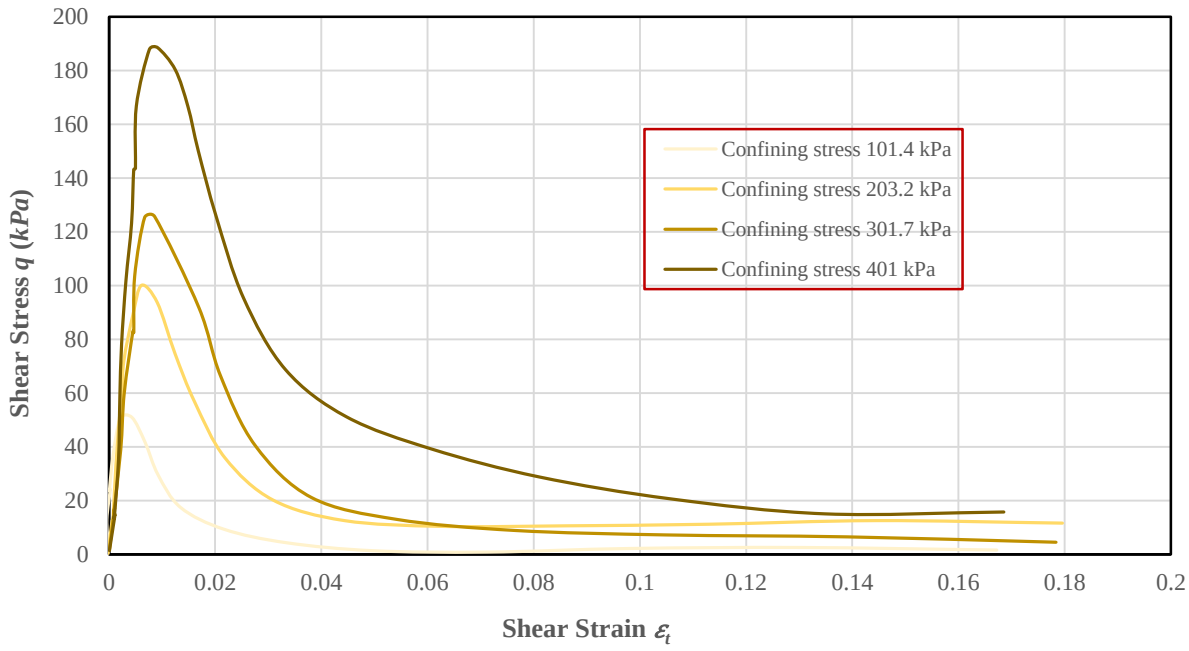

Figure 4.19 Stress-strain responses for Alaskan 140-5 sand with different confining stresses (http://www.golder.com/liq)

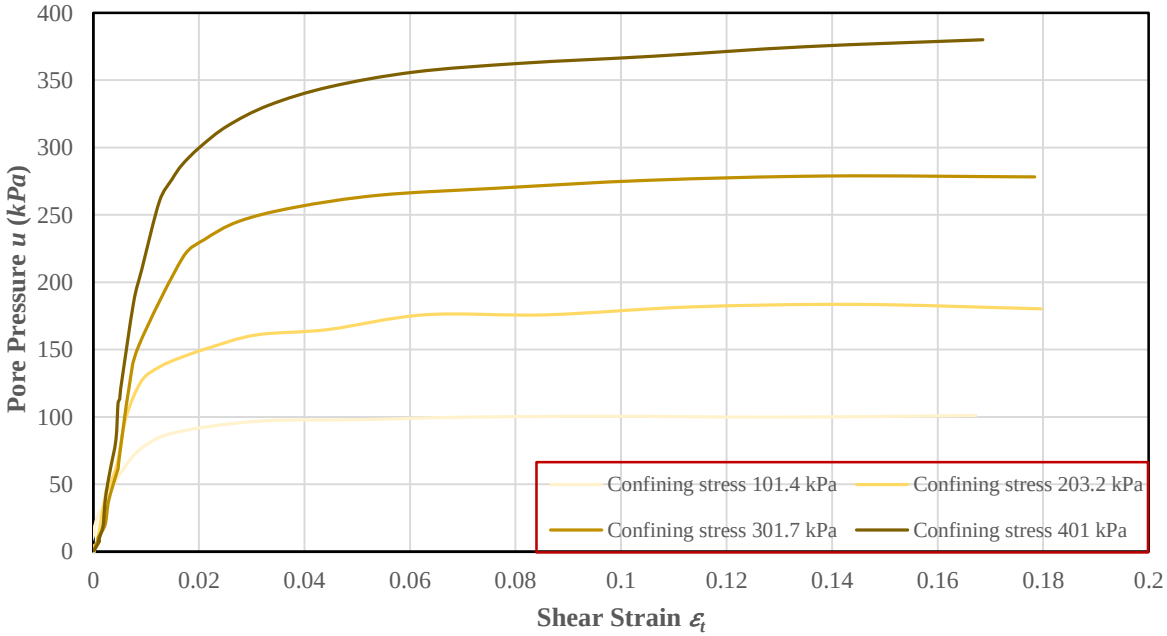

Figure 4.20 Pore pressure variations for Alaskan 140-5 sand with different confining stresses (http://www.golder.com/liq)

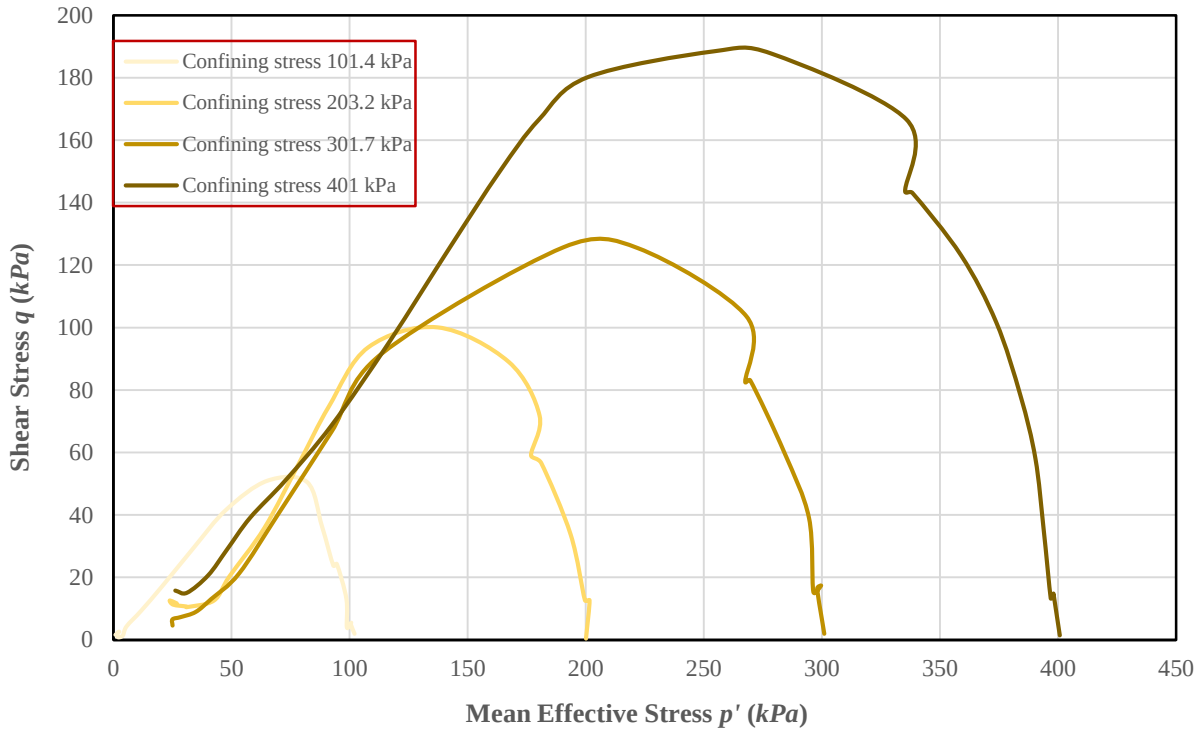

Figure 4.21 Stress paths for Alaskan 140-5 sand with different confining stresses (http://www.golder.com/liq)

Comparison of the peak shear strengths

Since the above two groups of tests both show the pattern that with a higher confining stress, the peak strength also becomes higher, a study of how the peak shear strength from the undrained test is influenced by the confining stress is performed by selecting the four peak shear strength values from Fig. 4.9 in section 4.3.2 and plotting them versus their associated confining stresses as shown in Fig. 4.22. It can be seen from the figure that all four peak shear strength points yield a linear trend line having a slope of 0.38 with a R squared value of 0.99. Hence, the peak shear strength and the confining stress are linearly correlated for the undrained simulations conducted using the proposed further developed fluid-coupled DEM model.

A comparison is made of the above peak shear strength versus confining stress plot from undrained simulations with that obtained from the undrained tests of Alaskan 140-5 sand (Figs. 4.19 to 4.21) and four additional results from laboratory undrained monotonic triaxial compression tests. These additional laboratory test results are also taken from Jefferies and Been (2006). (Supporting data can be downloaded from http://www.golder.com/liq.) Fig. 4.23 shows the comparison of the six plots and their associated trend lines and R squared values. It can be seen in the figure that all six plots present very high linear correlations between the maximum shear strength and the associated confining stress, since all R squared values are

very close to 1. Furthermore, the slope of all five plots from the laboratory testing are about 0.5 to 0.7, which is reasonably close to the slope of 0.4 obtained from the proposed simulations. The differences in slope among the six plots may be due to the fact that the grain size distribution and the particle shapes vary, for example, some of the samples are sub-rounded while the others are sub-angular while the simulated results are obtained using the perfect round discs. Therefore, different slopes in the trend lines exhibit, however, the pattern of the relationship between the maximum shear strength and the confining stress is clearly linear.

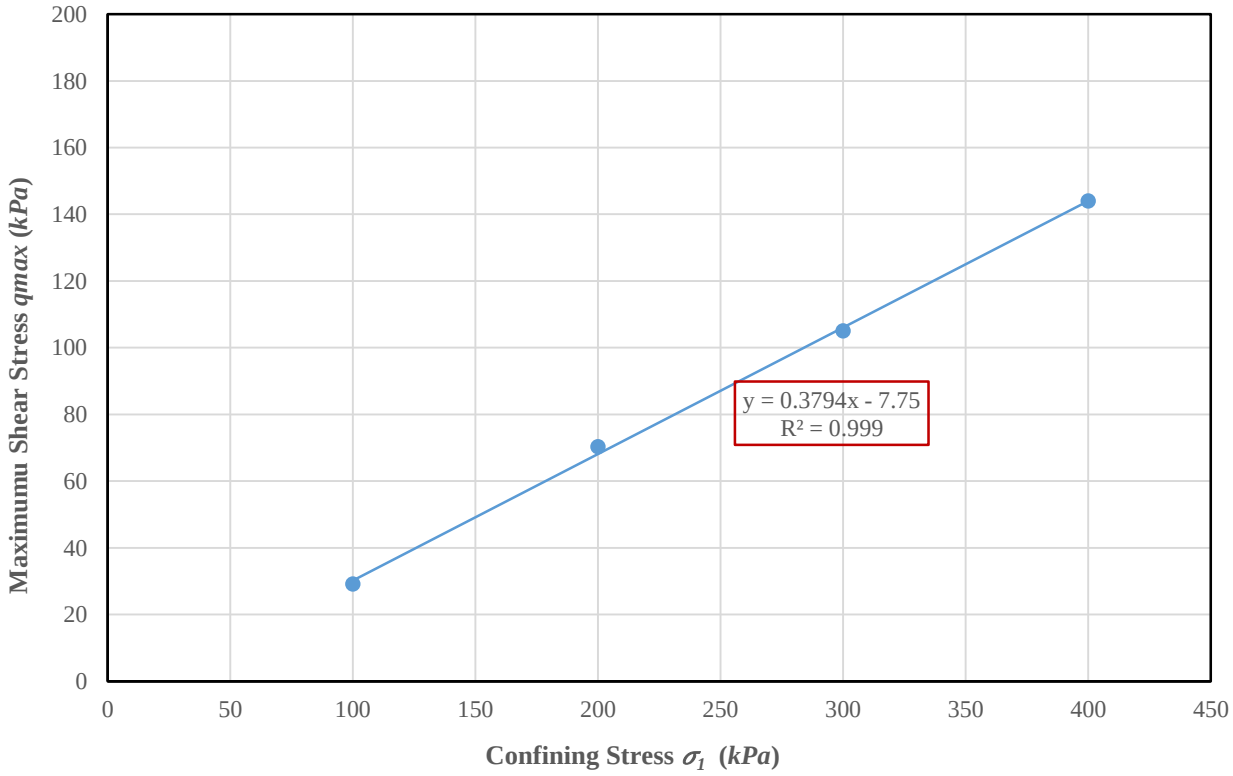

Figure 4.22 Relationship between the peak shear strength and the confining stress from the undrained fluid-coupled DEM simulation

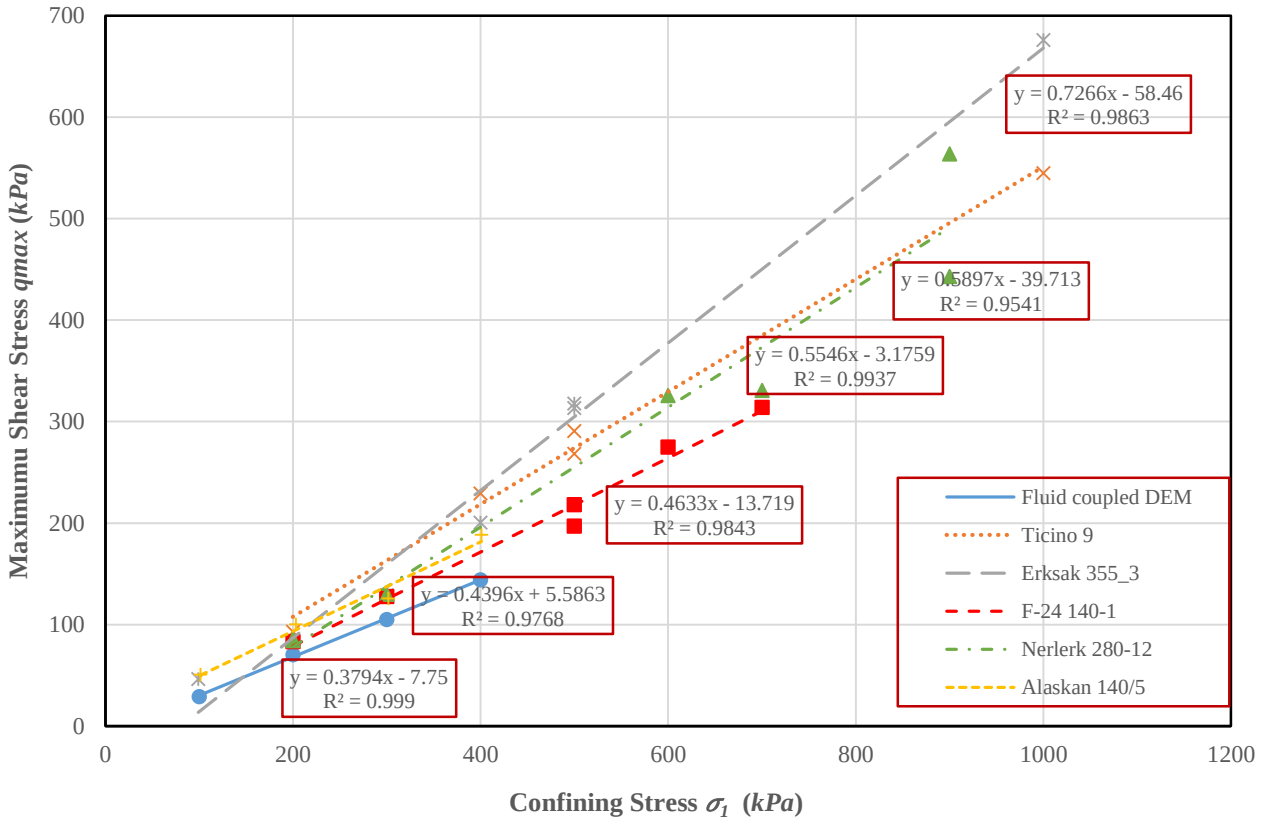

Figure 4.23 Comparison of the relationship between the peak shear strength and the confining stress for different type of soils (http://www.golder.com/liq)

4.5 Comparison of results from fluid-coupled DEM with those of the constant volume method

4.5.1 Introduction

We noted in Chapter 1 that the DEM simulation of a granular system in an undrained condition usually uses either the fluid-coupled DEM, or the constant volume method. The fluid-coupled DEM considers the interactions between the granular particles and the fluid flow when modelling the undrained behavior, while the constant volume method only preserves the volume of the sample assuming both particle and water have a very low compressibility. The disadvantage of the fluid-coupled DEM is that the calculations for interaction between the particles and the fluid are very complicated, so the computational time is very large. The constant volume method saves time but lacks a calculation of the pore pressure effect, hence, the validity of its results is questionable. Therefore, it is worthwhile to compare the undrained behaviors obtained from the aforementioned two methods to determine which one is more feasible.

In this section, both mechanical and micromechanical results of undrained simulations obtained from the further developed fluid-coupled DEM model are compared with those that come from using the constant

volume method. The preservation of the volume is achieved by setting the constant strain rates $\dot{\epsilon}_{11}^{\beta}$ and $\dot{\epsilon}_{22}^{\beta}$ at the boundary to equal values but of opposite signs using mode 2 that was introduced in section 3.4. To conduct a comprehensive comparison, exactly the same samples (A, B, C, and D) and confining stress (100 kPa) presented in Table 4.3 were selected to perform the constant volume method modelling. The parameters used for the constant volume method simulations also follow the values given in Table 4.4.

4.5.2 Comparison of the results

4.5.2.1 Comparison of the mechanical responses

A comparison of the mechanical responses from using the further developed fluid-coupled DEM and the constant volume method for samples A to D introduced in section 4.3.1 is presented in Figs. 4.24 and 4.25. Fig. 4.24 shows a comparison of the stress-strain responses of the two methods, and Fig. 4.25 compares the stress paths obtained from using the two methods. Because no values of pore pressure variations are produced by the constant volume method, a comparison of the mechanical responses is restricted to the stress-strain curve and the stress path plot. For ease of comparison, the results for samples A and B, both of which show a strain softening type of response, are plotted together and presented in Fig. 4.24a and Fig. 4.25a, while the results for samples C and D, both of which exhibited strain hardening, are combined and shown in Fig. 4.24b and Fig. 4.25b.

Stress-strain response

It can be seen from Fig 4.24a that for samples A and B, the peak strength obtained from the fluid-coupled DEM is higher than that from using the constant volume method, although they occur at the same strain level. After the initiation of strain softening, the residual strengths at large strains from the fluid-coupled DEM method are lower than those from the constant volume method. A similar pattern also appears for sample C, which can be seen from Fig 4.24b. The initial shear stress of sample C from the fluid-coupled DEM method is a bit higher than that from the constant volume method, subsequently, during strain hardening, the shear stress obtained from the fluid-coupled DEM increases at a lower rate than that given

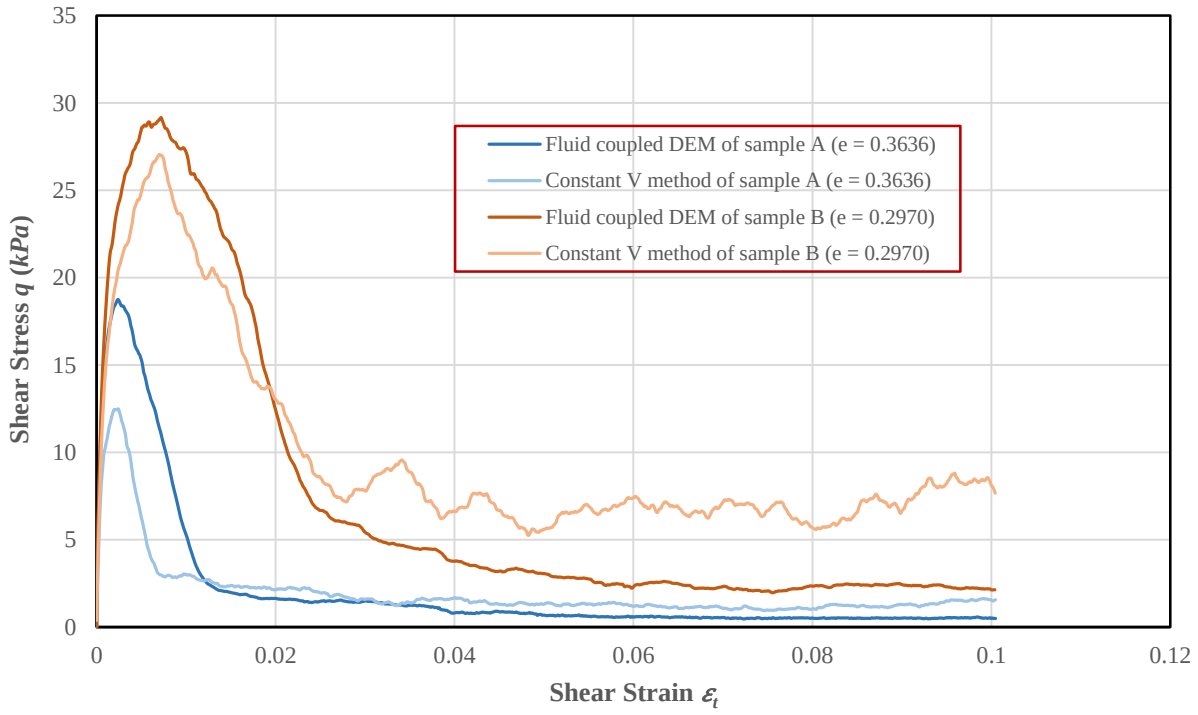

(a)

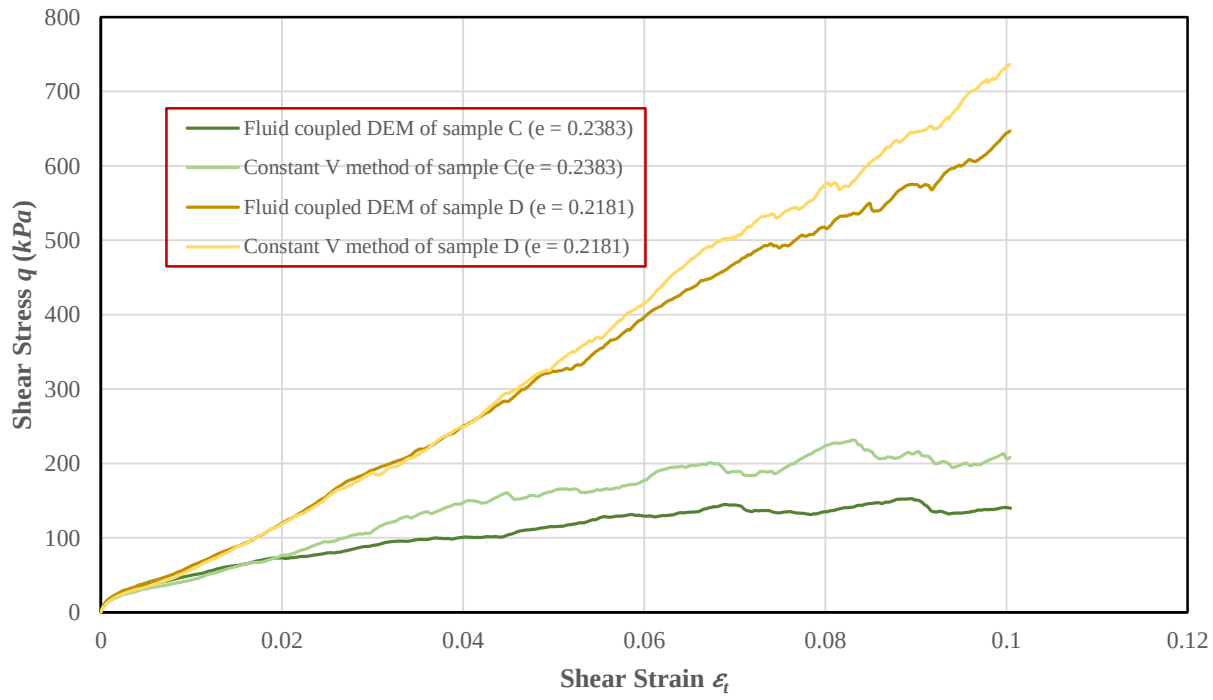

(b)

Figure 4.24 Comparison of stress-strain responses between using fluid-coupled DEM and using constant volume method

by the constant volume method and it gradually fall to a value below that of the plot from the constant volume method at 2% strain and last for the end of simulation. Unlike the results from the former three samples, the stress-strain responses given by the two methods for sample D fall close to each other until about 5% strain, then the shear stress from the constant volume method becomes higher than that from the fluid-coupled DEM until the end of the simulations. It is conspicuous that the discrepancy of the initial peak strength values between the two methods decreased from A to C and almost disappeared for sample D. However, at large strains, the two methods result in different stress-strain behavior for all four tests.

Stress Path

In comparing of the stress paths obtained from the two methods, it can be seen from Fig. 4.25a that the samples A and B, the stress paths obtained from the fluid-coupled DEM are above those from the constant volume method. In addition, they also terminated at lower residual strengths and mean effective stresses than the stress paths given by the constant volume method. For samples C and D, the difference between the stress paths given by the two methods is much less than that from samples A and B. The stress path from the constant volume method shows a bit lower shear stress and mean effective stress values at the "elbow" compared to those obtained using the fluid-coupled DEM. After passing the "elbow", all plots almost merge together with the increase of mean effective stress and shear stress

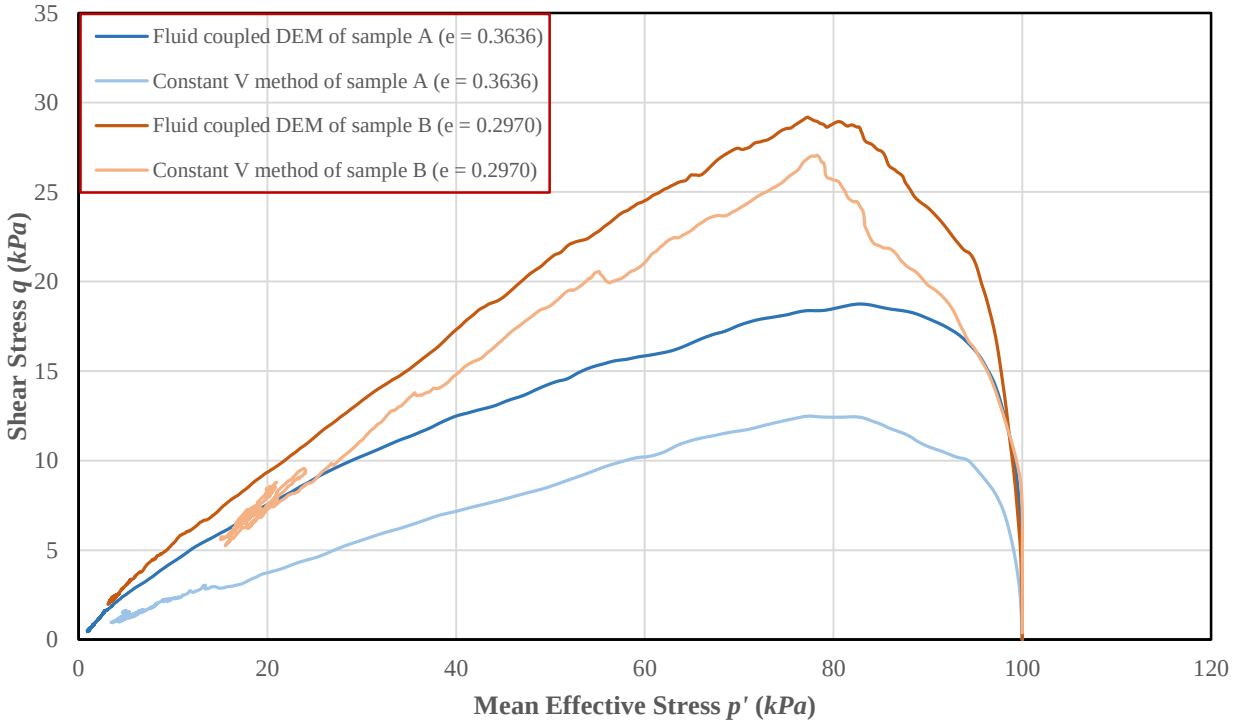

(a)

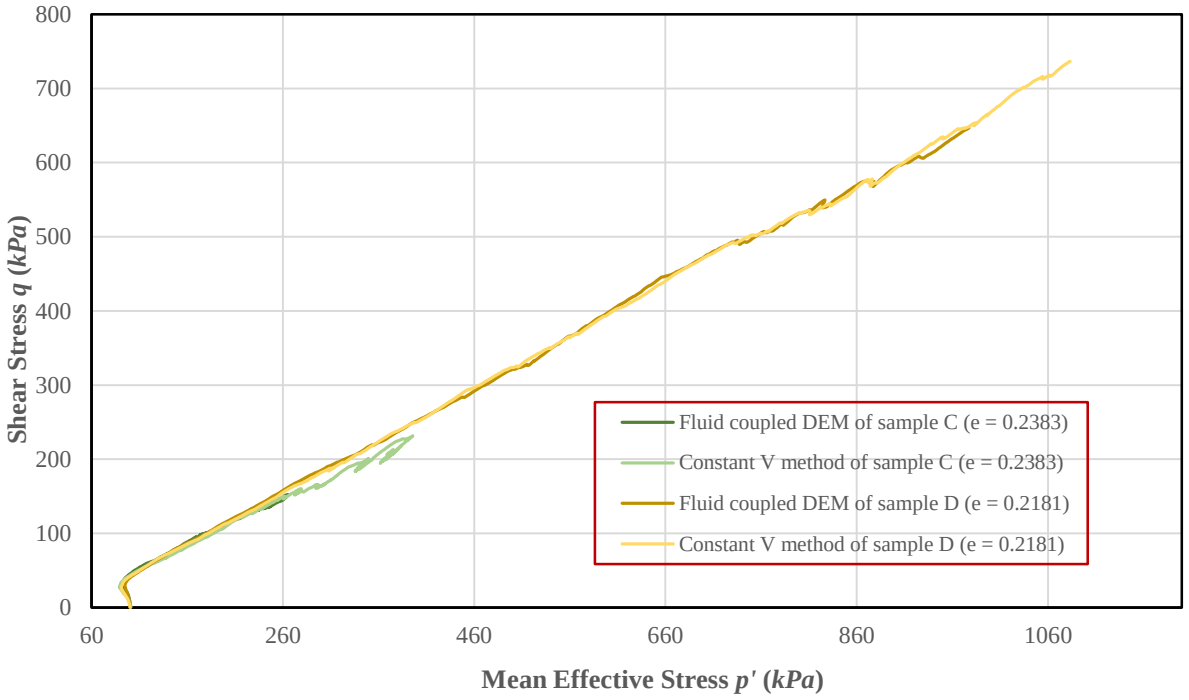

(b)

Figure 4.25 Comparison of the stress paths between using fluid-coupled DEM and using constant volume method

until at about a mean effective stress of 250 kPa, the stress path obtained from constant volume method of test C diverge a bit from the other three plots. Above all, the stress path obtained by using the fluid-coupled DEM situated above the stress path from using the constant volume method for samples A and B. While for samples C and D, the stress paths from using the two methods almost merge together, although they terminate at different points. From samples A to D the discrepancy of the initial peak strength obtained from using the two methods become less and less, however, the discrepancy of the mean effective stress where the steady state is achieved for the two methods becomes greater and greater.

4.5.2.2 Comparison of the micromechanical responses

Comparisons of the micromechanical responses given by the fluid-coupled DEM and constant volume method for samples A to D are shown in Figs. 4.26 to 4.29. Variations of the four micromechanical descriptors, which are the average coordination number γ, the number of floaters n_f, the contact normal anisotropy parameter a_n, and the normal contact force anisotropy parameter a_f are presented for both methods. As in the previous section, each descriptor depicted in Figs. 4.26 to 4.29 is studied by separating the four samples into two groups, where samples A and B are grouped together and samples C and D are shown together.

Average coordination number γ

Fig. 4.26 shows the variations of the average coordination number γ under shearing using the two methods. It can be seen from the figure that for samples A, B, and C, values of γ obtained by using the fluid-coupled DEM all fall below those taken from the constant volume method. This pattern is conspicuous at strains greater than 1%. Besides, from samples A to C, the difference in the values of γ from the two methods reduced for values of the strain range greater than 1%. The results for sample D given by the two methods do not show much difference until almost the end of simulation. The two plots merge at the beginning of the tests and remain together throughout the tests. The huge difference in the values of γ obtained from two methods for the loose samples A and B is attributed to the fact that the induced pore pressure helped break the contacts in the horizontal direction at an early stage of shearing and later helped break the contacts in the vertical direction. This pore pressure effect can also explain the large difference in the values of the contact normal anisotropy parameter a_n obtained by using the two methods for the loose samples A and B shown in Fig. 4.28. The results of γ for the loose sample obtained by using the constant volume method does not exhibit this phenomenon since there is no pore pressure computation involved, therefore, the values of γ do not deviate much from the critical value which is typically obtained from the drained testing. The pore pressure effect on γ reduces when the sample become less loose since there less positive pore pressure is generated, and the induced contact disintegration becomes less drastic. When the sample is dense enough, the pore pressure effect on γ under shearing almost disappears because although the granular system tends to dilate, both negative pore pressure and preserved volume value help to suppress the tendency to dilation by constructing contacts in both directions. Therefore, the impact of pore pressure on γ is only pronounced in a very loose sample like sample A.

Number of floaters n_f

Fig. 4.27 presents the number of floaters n_f variations of the four samples computed from the two methods. The comparison for samples A and B is shown in Fig. 4.27a, and the comparison for samples C and D is shown in Fig. 4.27b. Similar to the differences in γ, the number of floaters n_f also exhibited different degrees of discrepancy among the four samples using the two methods. It is shown in Fig. 4.27 that the number of floaters n_f computed from the two methods is quite similar at the initiation of shearing, (only sample B shows a small difference). After the initial shearing stage, all number of floaters computed from the fluid-coupled DEM for the four samples become higher than those of the constant volume method until the end of the test. In addition, as we move from samples A to D, the difference in the floater numbers between two methods reduces. Although the number of floaters n_f obtained by using the fluid-coupled DEM are higher than those from using the constant volume method for all the four samples, the reasons are

different. For samples A and B, the higher number of floaters n_f are produced because of the high positive pore pressure value at intermediate and large strains. Since the positive pore pressures are very high in samples A and B, they break the contacts between particles in both vertical and horizontal directions, thus, creating a higher number of floaters. For samples C and D, a higher number of floaters from using the fluid-coupled DEM at intermediate and large strain occurs because of the microstructure tendency changes from contraction to dilation. Hence, the negative pore pressure takes part of the responsibility for resisting the external load, and the number of floaters is higher than given by the constant volume method. This interpretation can be justified by the fact that the strain at which the number of floaters n_f given by the two methods deviated from each other, for samples C and D is the strain at which the pore pressures stop increasing and start to decrease in Fig. 4.3. This deviation of the two methods for sample C gradually disappeared after the assembly enter into the steady state where the tendency to dilation terminates. Based on the above analysis of the variations in the number of floaters n_f, it can be concluded that the pore pressure affects the number of floaters n_f significantly.

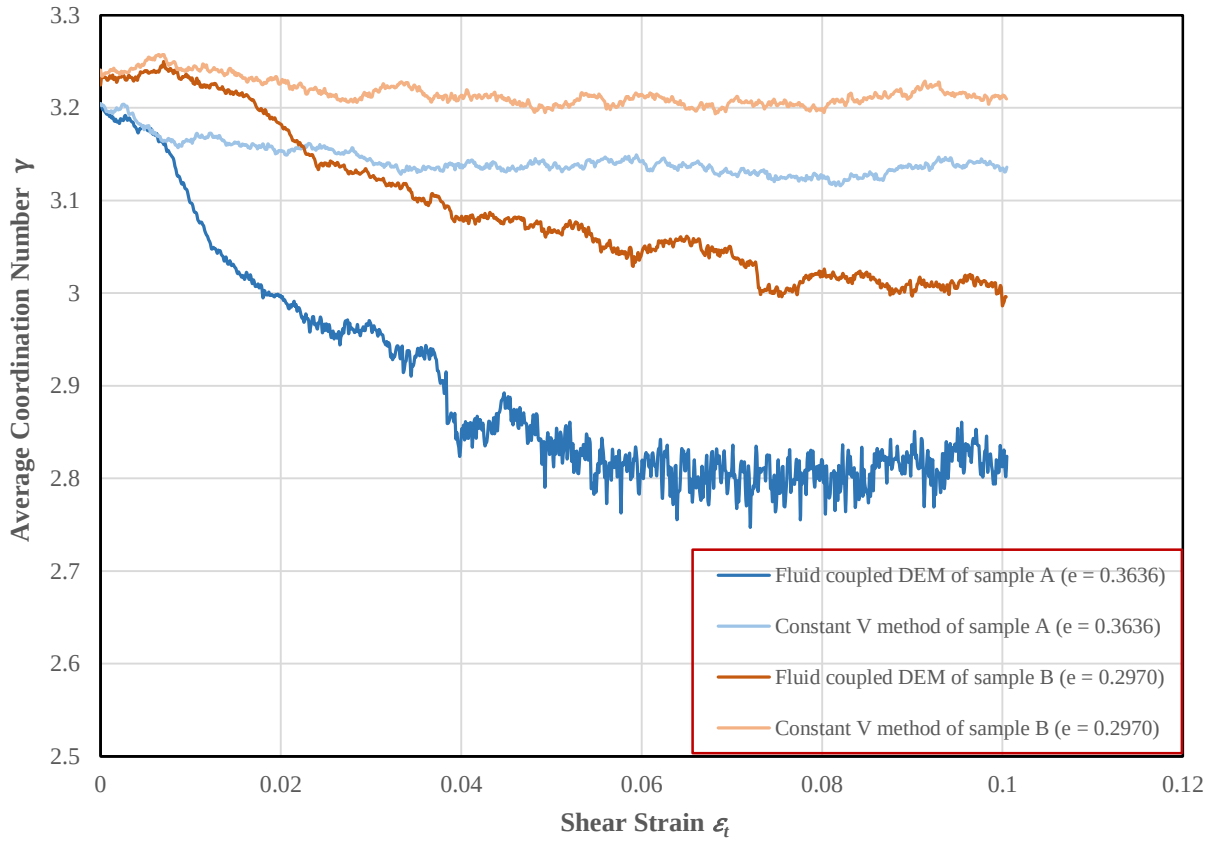

(a)

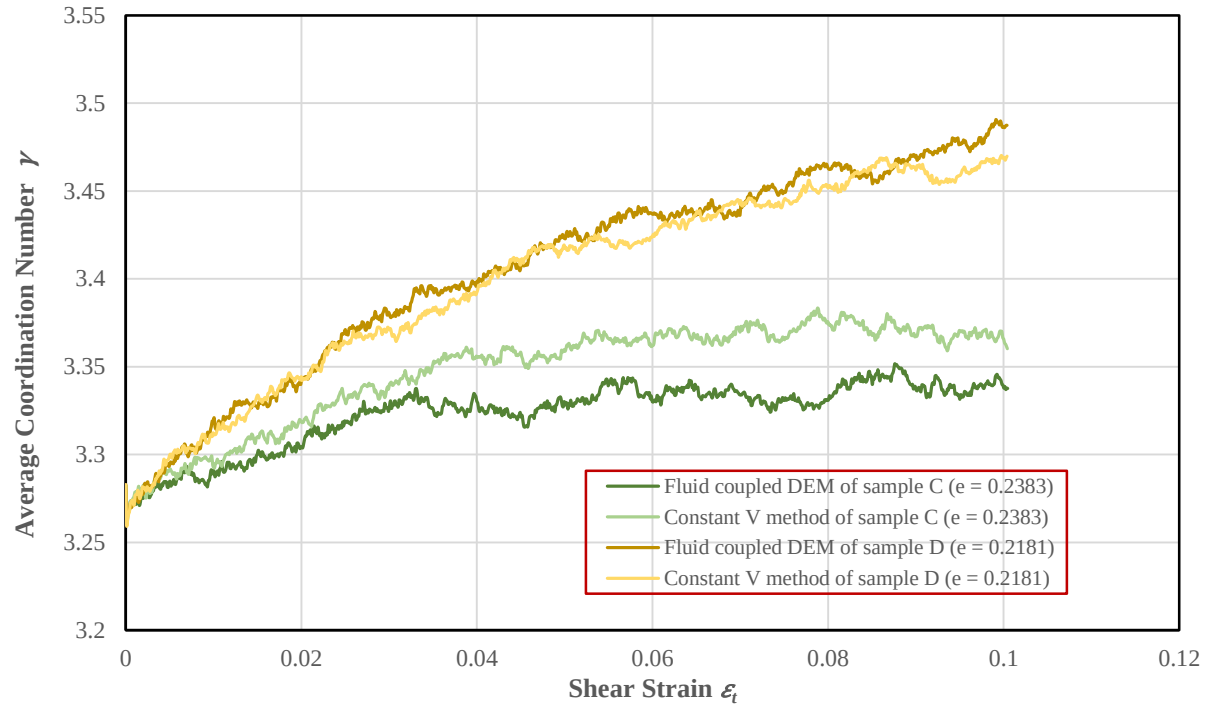

(b)

Figure 4.26 Comparison of the average coordination number γ between using fluid-coupled DEM and using constant volume method

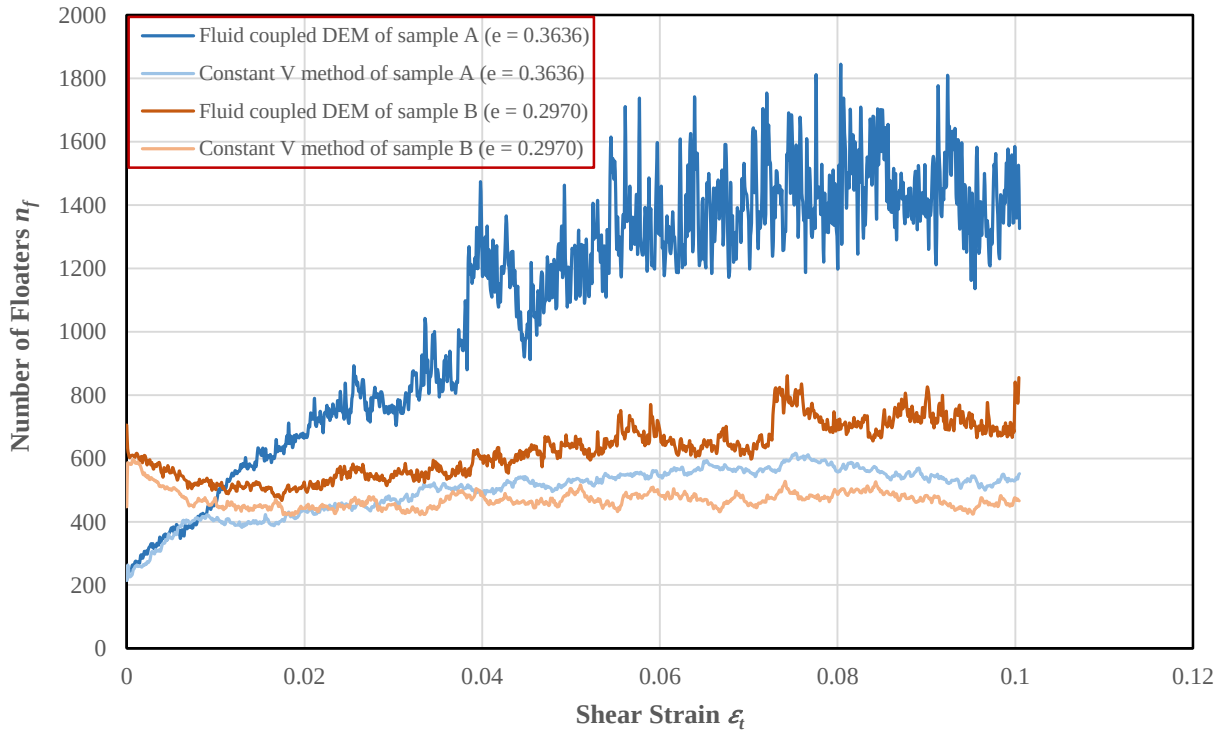

(a)

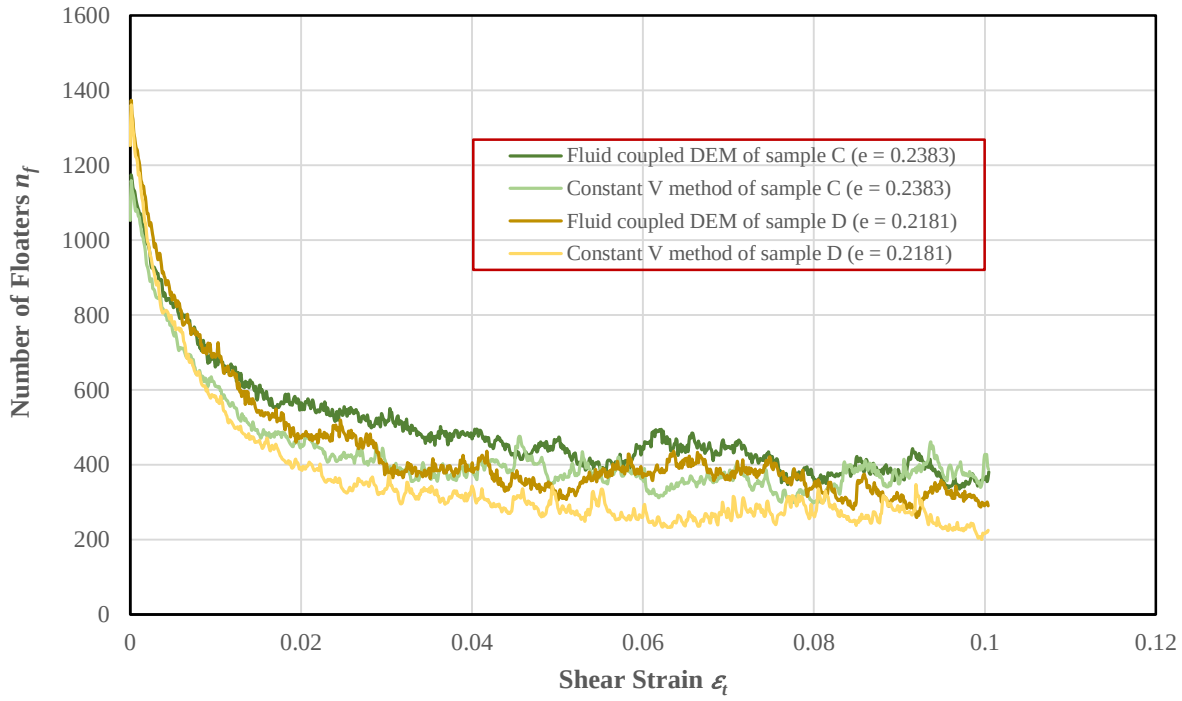

(b)

Figure 4.27 Comparison of the number of floaters n_f between using fluid-coupled DEM and using constant volume method

Contact normal anisotropy parameter a_n

The contact normal anisotropy parameter a_n responses extracted using the two methods for the four samples are shown in Fig. 4.28. It can be seen in Fig. 4.28a that at the initial stage of shearing, the plots given by the two methods for samples A and B are similar. However, after the initial stage, the gap between the results widened rapidly until the steady state was reached. For samples C and D, it can be seen in Fig. 4.28b that the difference between the plots obtained from the two methods continues for sample C although the amount is not large; while for sample D, the difference almost vanishes, and a_n values computed by using the two methods superimposed. The above differences in a_n values for the fours samples obtained by using the two methods can be attributed to the pore pressure effect. It was already shown in the previous section that when the sample is very loose, i.e. sample A, the pore pressure breaks the contacts in the horizontal direction with an increase in vertical load, which results in the formation of a high degree contact normal anisotropy. However, when using the constant volume method, the contacts in both directions only evolve following particles' movement in both directions. There is no extra force breaking the contacts from inside the system. Unlike in the loose sample, a negative pore pressure is generated in the dense sample, which does not break contacts, but on the contrary, it helps with creating new contacts in both directions. This is in accordance with the result of the constant volume test in which the vertical load leads to the

connection of the floaters with the surrounding particles in both directions although mainly in the vertical direction. Therefore, $a_n$values obtained by using the two methods are similar for a dense sample, but not for a loose sample.

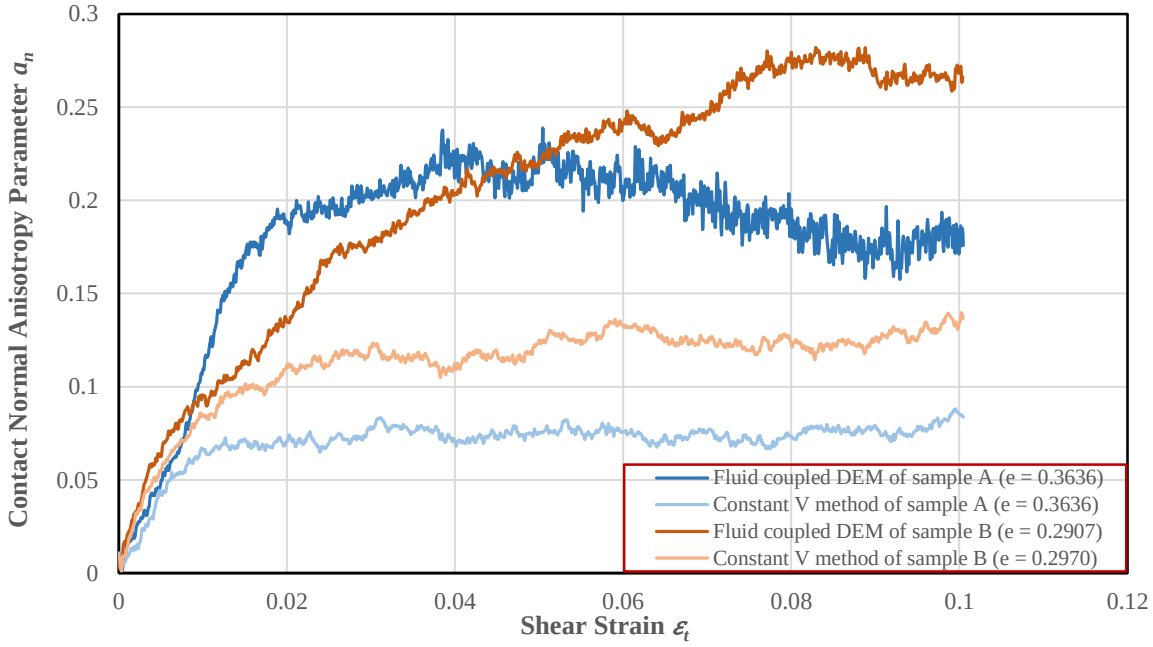

(a)

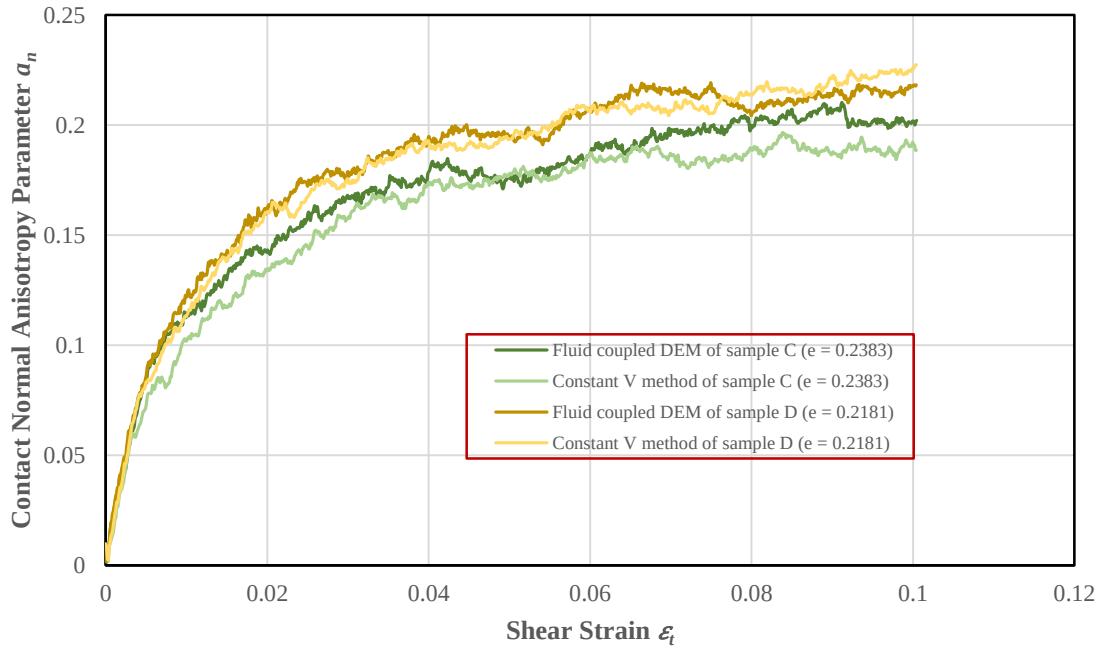

(b)

Figure 4.28 Comparison of the contact normal anisotropy parameter a_n between using the fluid-coupled DEM and using the constant volume method

Normal contact force anisotropy parameter a_f

A comparison of the normal contact force anisotropy a_f variations obtained by using the two methods for the four samples is seen in Fig. 4.29. Similar to the behavior of the contact normal anisotropy parameter a_n, the difference in a_f values after the initial shearing stage, is very large for samples A and B, much less for sample C, and almost disappears for sample D. The reason for these differences is similar to the differences of a_n among four samples. Since the positive pore pressure breaks the contacts in the horizontal direction when the fluid-coupled DEM is used for the loose sample, while this mechanism does not exist for the constant volume method. Thus, a large number of normal contact forces in the horizontal direction are broken accordingly results in a high a_f value when using the fluid-coupled DEM. However, in the dense sample, a negative pore pressure is generated, which helps with the creation of contact forces in both directions. Therefore, a_f values obtained by using the two methods are similar if the sample is very dense. From the above comparison of a_f for the four samples, it can be concluded that the pore pressure has a great impact on the a_f if the sample is loose, while its impact reduces with decreasing void ratio of the sample.

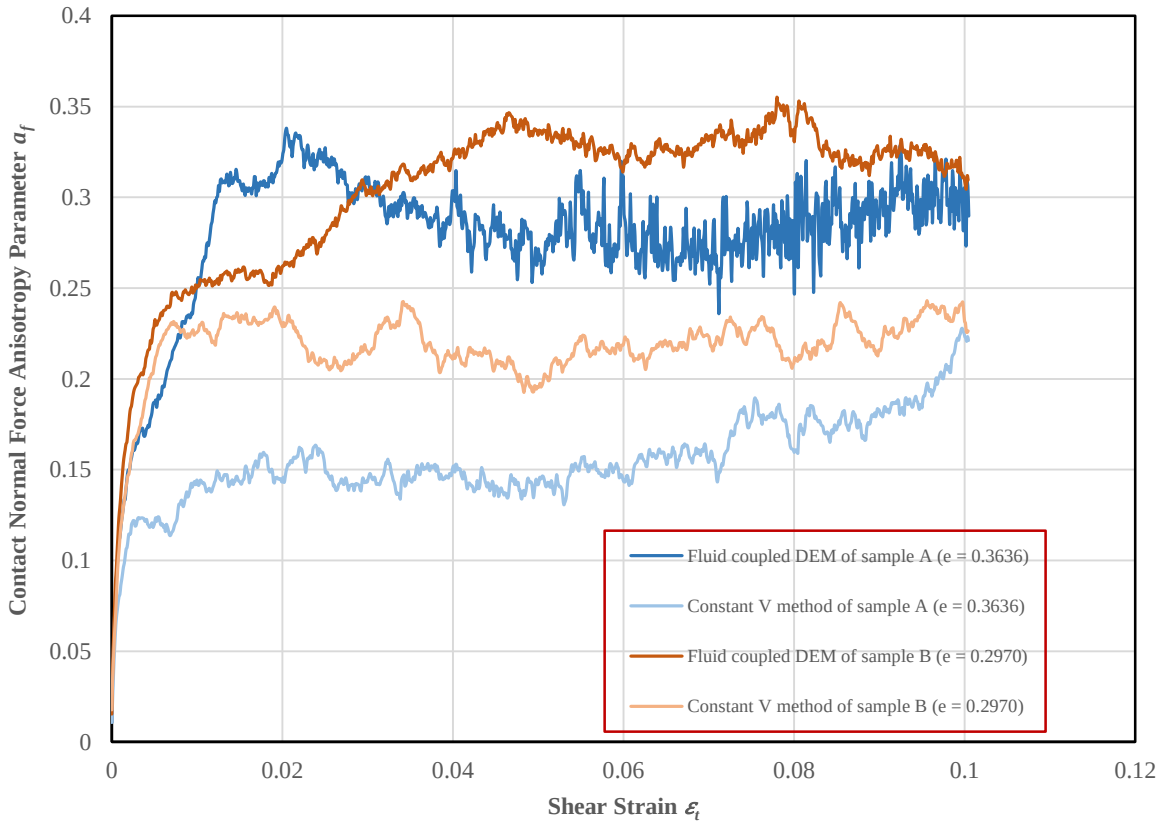

(a)

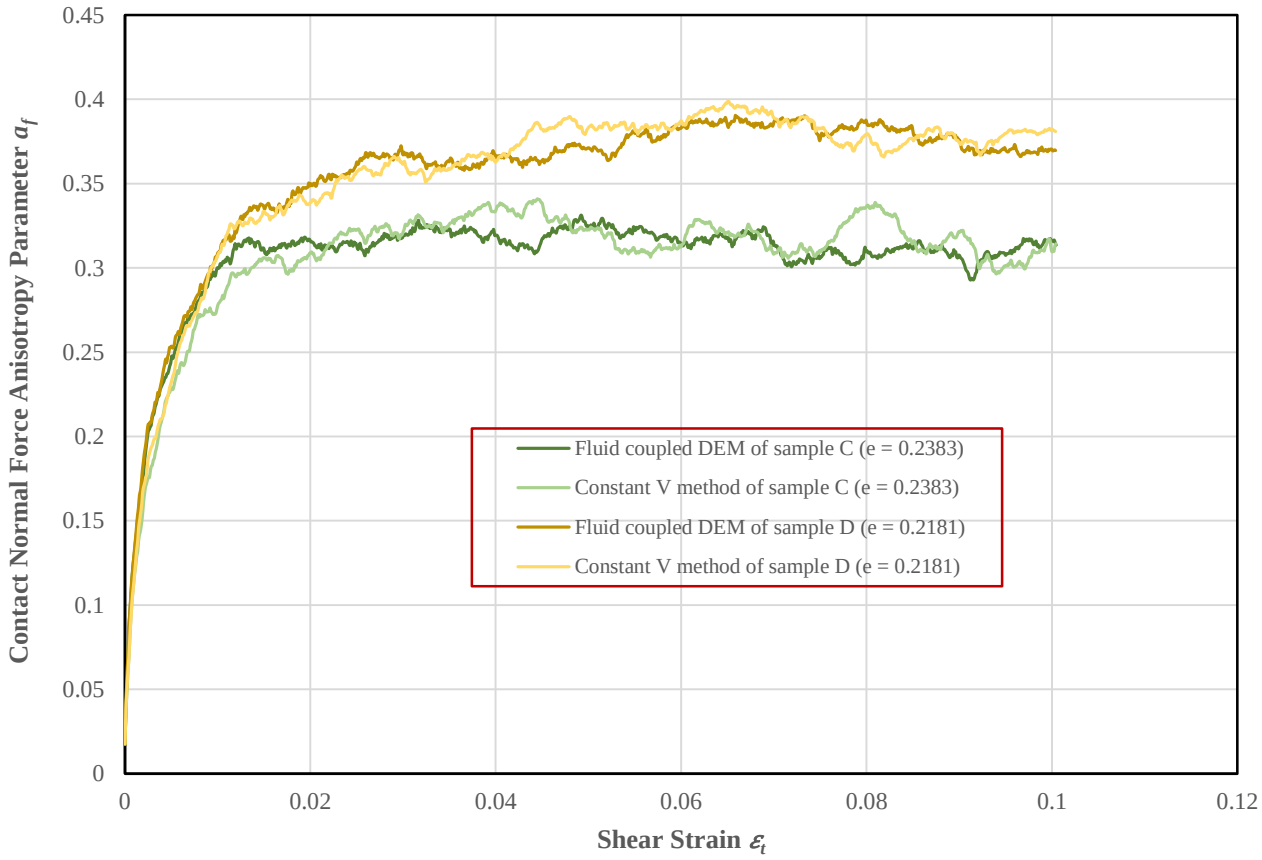

(b)

Figure 4.29 Comparison of the normal contact force anisotropy parameter a_f between using the fluid-coupled DEM and using the constant volume method

4.5.3 Comments

From the above analysis of the comparisons of the mechanical and micromechanical responses between the two methods, it can be seen that the discrepancy between the results given by the two methods is large for all the parameters presented above in the loose sample due to the effects of the positive pore pressure. This effect reduces with decreasing void ratio of a sample, and almost disappears for a dense sample up to intermediate strain level. Therefore, it can be concluded that the constant volume method may be applicable to the simulation of the undrained response of a very dense sample until certain strain level is reached, however, for a loose sample it fails to capture the pore pressure effect on the early breaking of contacts in the horizontal direction and later in both directions.

Chapter 5 Permeability Effect on the Static Liquefaction susceptibility

5.1 General background

This chapter presents a study of the effect of permeability on the static liquefaction susceptibility. In section 5.2, a test program aimed at simulating the permeability effect on the liquefiable granular assemblies under undrained shearing is designed. The corresponding results and analysis of the mechanical and micromechanical undrained behaviors of the liquefiable assemblies are presented in section 5.3. A comparison of the simulated results and related results from laboratory testing reported in the literature is shown in section 5.4.

5.2 Summary of the test program

To study the influence of permeability on the undrained response of the liquefiable granular assembly, a group of five simulation tests (I, II, III, IV, and V) are designed with exactly the same structure as Sample A from section 4.3.1 but different values of conduit diameters for the fluid flow through the granular system. The five different conduit diameters are selected based on the analysis performed in section 3.8.3. In test III, the conduit diameter is selected as 80 μm, which is exactly the same as those tests conducted in chapter 4. The conduit diameters of test II and I were selected to be double and quadruple of that in test III, they correspond to the permeability in the coarse sand range based on Fig. 3.16. The conduit diameters of tests IV and V are selected to be one fifth and two fifths of that in test III, they correspond to the permeability in the silty clay and clay range according to Fig. 3.16. Therefore, the five diameters are selected as 320 μm, 160 μm, 80 μm, 32 μm, and 16 μm, respectively. Besides, the same as the undrained simulations performed in chapter 4, the viscosity and the bulk modulus values for the fluid assigned in this chapter are also those of water at 20°, the values of which are $1 \times 10^{-3} Pa \cdot s$ and 2.0 GPa, respectively.

The five samples are sheared by undrained biaxial compression simulation under a confining stress of 100 kPa. All of them are sheared to 15% strain to attain a steady state. Some physical properties of each sample such as the initial average coordination number γ, the initial number of floaters n_f, and the conduit diameter d are shown as Table 5.1. The undrained biaxial compression simulation for each of the above samples is conducted using mode 3 introduced in section 3.4, which maintains the average stress σ_{11} constant, and meanwhile, increases the average stress σ_{22} by applying a constant strain rate $\dot{\epsilon}_{22}^{\beta}$ (at the boundary). The associated parameters for the simulations in this section also follow the values already presented in Table 4.4.

Table 5.1 Summary of initial physical properties of the tests

Test	Number of floaters (n_f)	Initial average coordination number (γ)	Void ratio (e)	Diameter of conduit (μm) (d)	Confining stress (kPa) (σ_1)
I	215	3.2045	0.3636	320	100
II	215	3.2045	0.3636	160	100
III	215	3.2045	0.3636	80	100
IV	215	3.2045	0.3636	32	100
V	215	3.2045	0.3636	16	100

5.3 Simulation results

5.3.1 Mechanical behaviors from simulations

Figs. 5.1 to 5.3 demonstrates the mechanical responses of the five undrained biaxial compression simulations with different conduit diameters. Figure 5.1 gives the stress-strain responses under shearing, Figure 5.2 shows the pore pressure variations throughout the tests, and Figure 5.3 presents the stress paths for the five undrained tests. It can be seen from the three figures that the diameter of the conduits affects the undrained response greatly, it controls almost the whole undrained behavior, especially the peak strength values. Tests II, III, and IV all show different levels of the peak strength followed by strain softening and liquefaction. Test I also displays strain softening and liquefaction after reaching the peak strength, but its strength regains a bit at the end of the test. Different from tests I to IV, test V exhibits initial strain hardening followed by strain softening and liquefaction. The specific characteristics of the five undrained behaviors seen in the three pictures are as follows:

Stress-strain response

The stress-strain curves from Fig. 5.1 show that all five tests exhibited strain softening but with different strength reductions. From I to V, the peak strength increases markedly. The residual strengths of tests II, III and IV all reach similar values, although the strain softening is initiated at different level of strain. This behavior indicates that within the conduit diameter range for tests II, III and IV (32-160 μm) the permeability does not alter the residual strength much. The stress-strain curve of test I is very close to that of test II, it reaches almost the same peak and minimum strengths as those of test II. However, test I softens a little earlier than test II, and in addition, test I displays strain hardening at about 10% strain after reaching the quasi-steady state. The similarity of the two overall responses of tests I and II is probably due to the

permeability of both of them being high enough (in the coarse sand range) for the individual pore pressure to dissipate among the voids. Therefore, there is very little change in the overall strength behavior. Nevertheless, the difference between the two stress-strain behaviors during the strain that the stress softening and at the large strain may be due to the fact that the permeability of test I is twice that of test II, so the pore pressure dissipation rate among the pores is higher for test I than for test II, which induces an earlier softening and a regaining of strength after reaching the minimum strength of test I. This effect can also be seen in tests III, IV, and V, which have even smaller diameters and dissipation rates. Compared to tests I and II, tests III, IV, and V show conspicuously higher peak strengths at much larger strains, but the residual strengths of III and IV merge with that of II, while the residual strength of test V is much higher than that of the other four tests. This indicates that the permeability although it does not affect the residual strength at ultimate state when it is within a certain range, it does affect the initial stages under shearing, including the peak strength and strain softening phase. In addition, Fig. 5.1 shows that compare to tests I and II, the strain softening stages of tests III, IV and V last much longer and the steady states are reached at much larger strain. This is because the permeabilities of III, IV, and V are much lower than those of tests I and II, thus, the dissipation among the pores is much slower in tests III, IV, and V than in tests I and II, and strain softening takes longer. It is worthwhile to note that unlike tests I, II, III and IV, test V exhibits strain hardening from a very small strain of about 0.2%, it hits the maximum strength value of 80 kPa at 1.6% strain. Afterwards, it starts to soften until it reaches the steady state at about 13.5% strain. The temporary strain hardening is due to the extremely low permeability (in the clay range) which impedes the dissipation and equalization of the pore pressures among the pores, therefore, the granular system of test V tends to dilate at an early stage of the test. This effect disappeared gradually with the later very slow dissipation of the pore pressures among the voids.

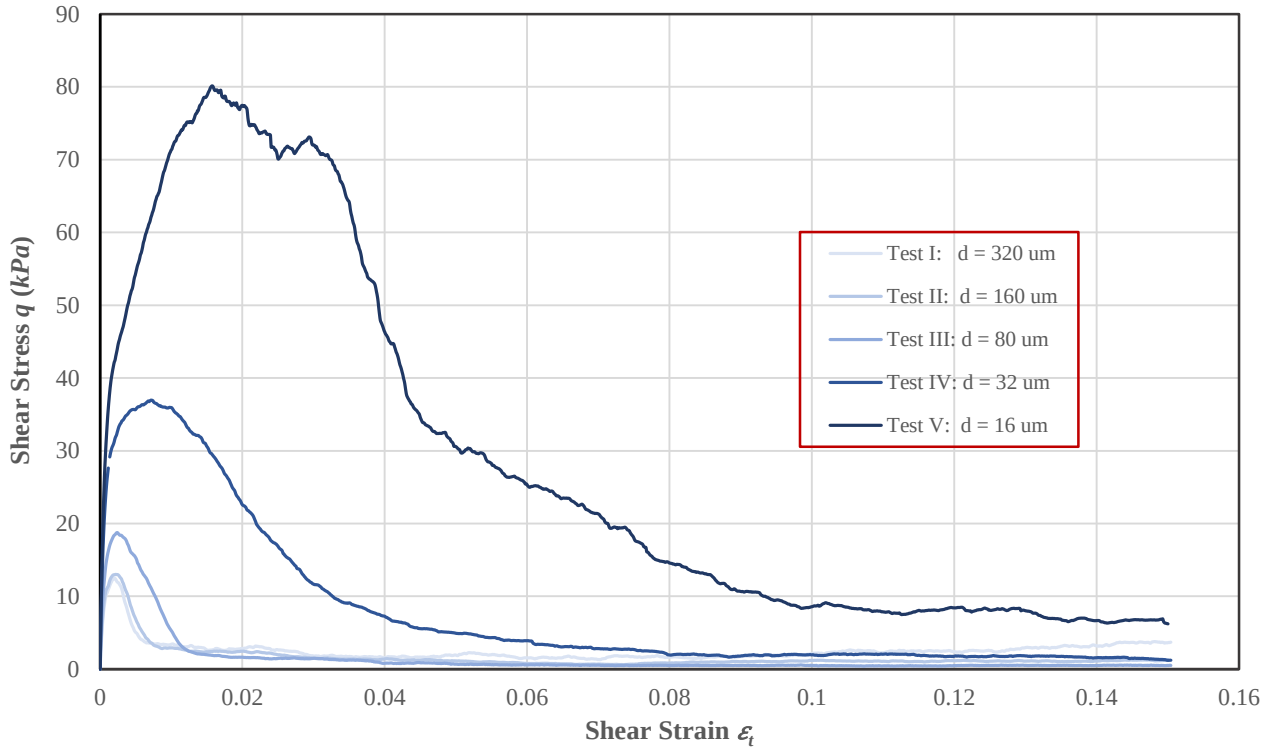

Figure 5.1 Stress-strain responses for assemblies with different conduit diameters

Pore pressure variations

The pore pressure variations of the five tests in Fig. 5.2 are consistent with their stress-strain responses shown in Fig. 5.1. The initial pore pressure build up rate before 0.2% strain for all five tests are similar, only test V is slightly higher than the other four tests due to its much lower permeability. This corresponds to the initial rapid shear stress increase stage in Fig. 5.1. After 0.2% strain, the pore pressure build up rate of tests I and II increases slightly, while it decreases significantly for tests IV and V, only test III maintains a constant rate of increase. The pore pressure of tests I, II, and III continues rapid increasing after 0.2% strain until reaching a value close to the confining stress of 100 kPa. Subsequently, there is a difference between the three tests in their individual maximum pore pressure values. In test I, the pore pressure reduces a bit until the end of test, which corresponds to the small strain hardening stage shown in Fig. 5.1. The pore pressure of test II almost maintain the maximum value, while the pore pressure of test III increases a bit until the end of the test. The pore pressure of test IV also increases to its peak value after 0.2% strain but at a reducing rate, and the peak occurs at the strain where its minimum shear strength is achieved in Fig. 5.1. The response of the pore pressure for test V is very different from that of the other four tests, it hits its initial peak value at a very low strain of about 0.4%. Subsequently, it gradually reduces to almost zero and then starts to increase again. Afterwards, the pore pressure of test V keeps on increasing until about 13.5% strain, it almost reaches its maximum value and then maintains this value indicating the sample enters into the

steady state. The very different pore pressure behavior of test V is a result of its very low permeability (in the clay range). When the permeability is very low, the generated individual pressure from each pore cannot dissipate into the neighbor pores rapidly, so the individual pore pressures generated initially are not uniform. This also explains why the overall initial pore pressure build up rate of test V is somewhat higher than that for the other four tests. Test V starts to show the tendency to dilate due to the very poor fluid connection between neighbor pores restricted the dissipation of pore pressure. Hence, the pore pressure reduces significantly accordingly. Upon achieving zero pore pressure, the tendency to dilate stopped, and the pore pressure gradually recovered with continue shearing. On the contrary, in tests I, II, and III, the generated individual pore pressures dissipate rapidly because of the relatively high permeability, therefore, they tend to keep on contracting with shearing, and there is softening after the peak strength. The permeability of test IV is also low (in the silty clay range), so the pore pressure build up rate reduces significantly after 0.2% strain due to the tendency to dilation. However, in this case, the permeability is not low enough to inhibit the connections among the pores, therefore, the tendency for contraction is still predominant in this test, and the pore pressure continue increases, but at a low rate.

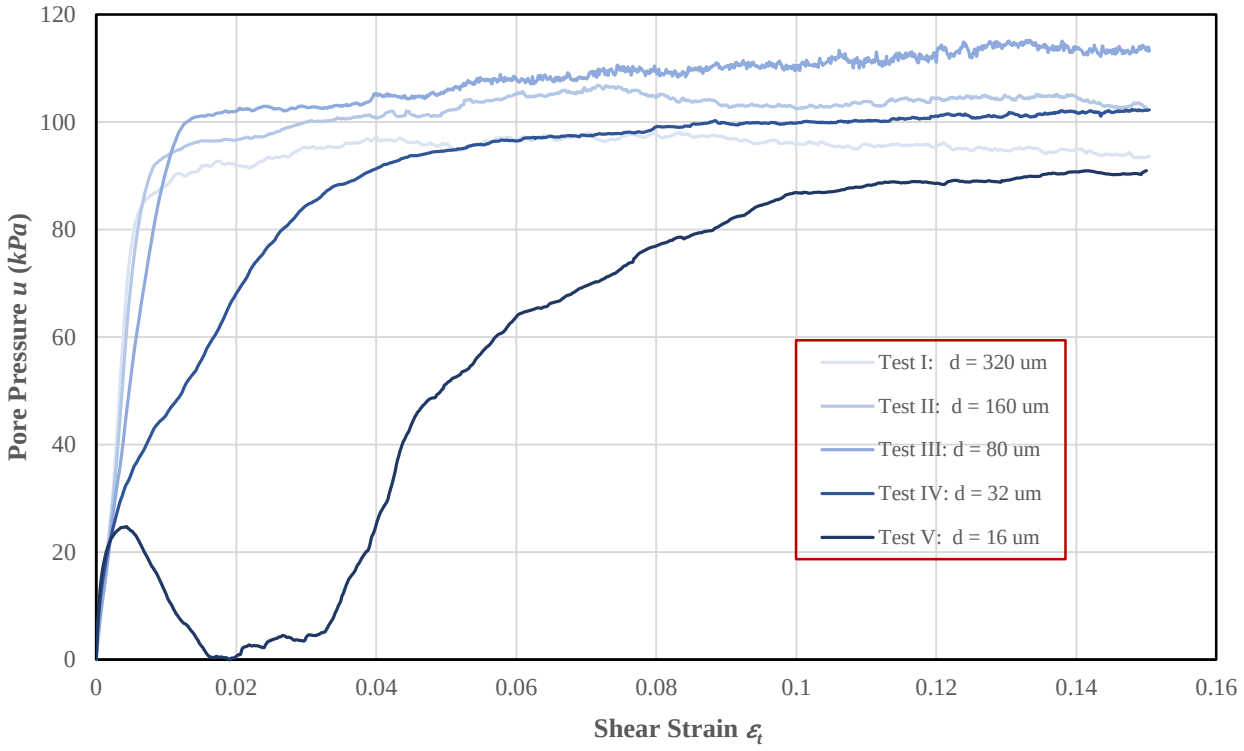

Figure 5.2 Pore pressure variations for assemblies with different conduit diameters

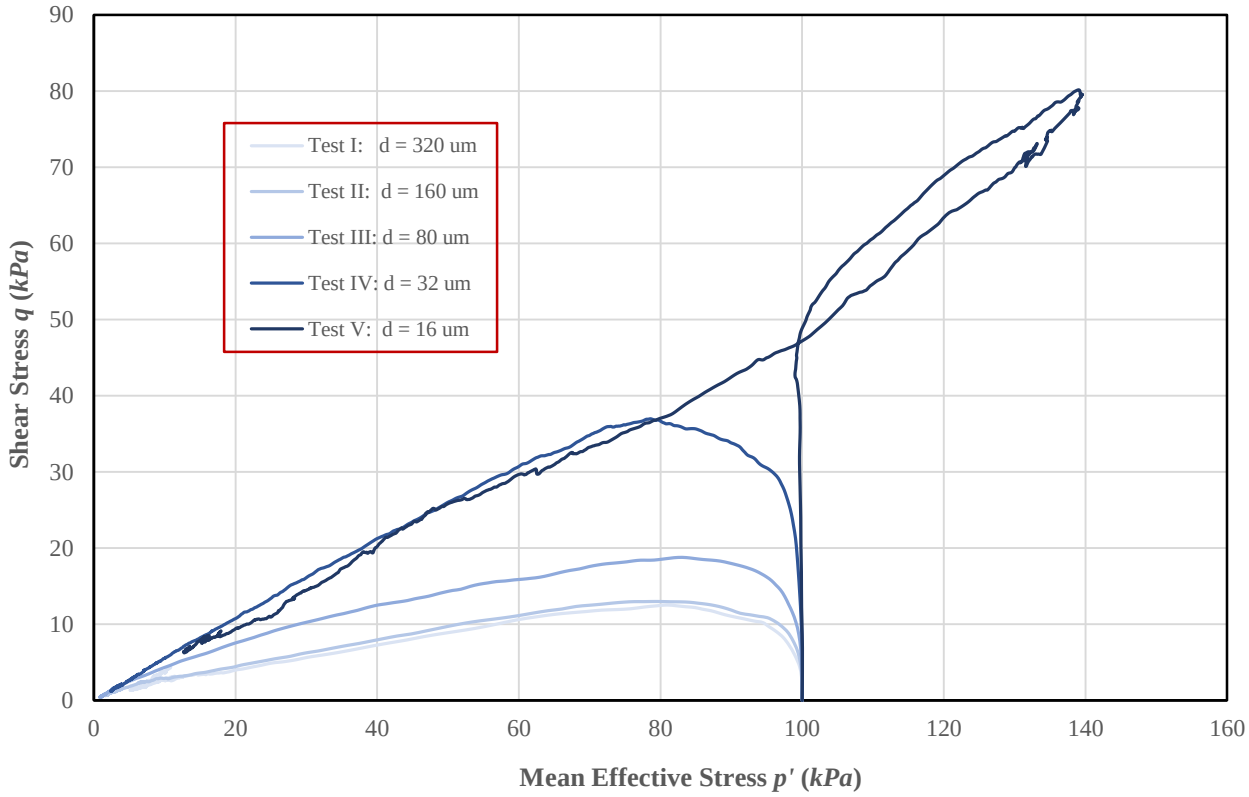

Figure 5.3 Stress paths for assemblies with different conduit diameters

Effective stress paths

The stress paths of all five tests shown in Fig. 5.3 are consistent with the associated stress-strain responses and the pore pressure variations shown in Fig. 5.1 and 5.2. The stress paths of tests I to IV all exhibit a strain softening type of behavior. They all start from the same point of (100, 0) due to the same confining stress of 100 kPa applied. Subsequently, with the decrease of the mean effective stress due to the generation of positive pore pressure, the corresponding shear stress of the four tests I, II, III, and IV all initially increase to the peak shear strength then start to soften with different changing rate until reaching the minimum strength, where all four tests liquefied. The stress paths of tests I and II are very close to each other, the only difference between them is that the stress path of test II being slightly higher that of test I throughout the whole simulations. The stress path of test III is also similar to those of tests I and II, but it displays a higher peak strength and a bit lower minimum strength at the steady state. In test IV, the overall stress path is similar to those of tests I, II, and III, but it exhibits a distinctly higher peak strength although its residual strength is quite close to those of the three former tests. Unlike tests I, II, III, and IV, the stress path of test V behaves quite differently. Although it also starts with the same point as those of the other four tests, however, it goes to a different direction after the initial increase of the shear stress indicating the tendency

to dilation and the occurrence of strain hardening. In this stage, with the increase of mean effective stress, the shear stress of test V also increases and follows an almost constant slope until reaching about 80 kPa. Afterwards, the stress path turns back and almost retrace the route and following a constant slope that is close to that of test IV. This corresponds to the reduction of the shear strength after the end of strain hardening and the recovery of the pore pressure after reaching zero value shown in Figs. 5.1 and 5.2. Then both the mean effective stress and the shear stress further decrease until achieving the steady state. Eventually, the stress path of test V terminates at a residual strength of 9 kPa with a mean effective stress equals to 12.5 kPa, both of them are higher than those in the other four tests, which is consistent with responses shown in Figs. 5.1 and 5.2.

5.3.2 Micromechanical Responses from the Simulation

Figs. 5.4 to 5.7 presents the micromechanical descriptors variations for the five tests. Fig 5.4 gives the change of the average coordination number γ during the tests, Fig. 5.5 shows the variation of the number of floaters n_f, Fig. 5.6 displays the development of the contact normal anisotropy parameter a_n, and Fig. 5.7 shows changes in the normal contact force anisotropy parameter a_f. In order to study how the permeability affects the undrained behavior of the five tests, these descriptors should be incorporated to our analysis. The specific characteristics of each test are illustrated as follows.

Micromechanical behavior of test I

It is shown in Fig. 5.4 that the average coordination number γ of test I did not change during initial shearing up to 0.25% strain, but both the contact normal anisotropy parameter a_n and the normal contact force anisotropy parameter a_f increased at a high rate, and the number of floaters n_f also increased rapidly. This indicates that the contacts were mainly created vertically and broken horizontally, but the totally number of contact creations and disintegrations were in balance. Subsequently, γ starts to decrease rapidly, while the increasing rate of a_n and a_f both reduce a bit compare to the first stage, and n_f temporarily stays constant. This means compared to the former stage, more contact breaks happened in both the vertical and horizontal directions in this stage along with the high pore pressure build up rate. This corresponds to the strain softening phase shown in Fig. 5.1, so the rapidly decreasing γ indicates that the strain softening is a result of the large number of contacts lost in both the vertical and horizontal directions. Beyond 0.5% strain, γ reduces gradually to the minimum value, n_f gradually increases to the maximum value, and the associated a_n and a_f both increase slowly to the initial peak values, which indicates that there is a small amount of contact creation in the vertical direction while many further contacts are lost in both directions along with the slow continuous pore pressure generation. All the four descriptors do not vary much with further shearing until about 8% strain where the quasi-steady state is reached. Afterwards, γ increases a bit and n_f

decreases a bit until the end of the test. The associated a_n and a_f also both increase in this stage indicating a bit more contacts are created in the vertical direction compare to the previous stage, which is in accordance with the small strain hardening shown in Fig. 5.1.

Micromechanical behavior of test II

The overall micromechanical response of test II is similar to that of test I, but the changes are greater than in test I over the whole strain range. As in test I, initial shearing did not alter γ until 0.25% strain was reached, but n_f, a_n, and a_f all increased rapidly, which means the contact loss mainly happened in the horizontal direction and the contact creation was mainly in the vertical direction. This is in accordance with the initial rapid shear stress increase and rapid pore pressure generation stage of Figs. 5.1 and 5.2. Subsequently, γ reduces rapidly, but the rate of increase of n_f and a_n remains the same as in the previous stage, while the rate of increase of a_f temporarily slows down followed by a rapid increase. These behaviors indicate contact losses in both directions as occurred in test I in this stage, however, changes in all descriptors are greater and last longer than in test I. This may be because the lower permeability of test II causes the individual pore pressures to take longer to dissipate. Thus, the locally high pore pressure breaks more contacts and results in a higher contact normal anisotropy and a greater number of floaters. Seen in the stress-strain response in Fig. 5.1 is a bit higher peak strength and a somewhat longer strain softening process in test II compare to those of test I. After the occurrence of strain softening shown in Fig. 5.1, γ continues to reduce gradually to a minimum value of about 2.94, and the associated n_f, a_f and a_n all slowly increase at a much lower rate than in the previous stage. At about 8% strain, the steady state is reached, and all four descriptors fluctuate about the steady state values until the end of the simulations. The value of γ in the steady state is much lower than that of test I, n_f and a_n are both much higher than those of test I, while a_f at the end of simulation from the two tests are quite close. Therefore, the liquefaction in test II is more complete than that in test I.

Micromechanical behavior of test III

The overall micromechanical response of test III is similar to that of tests I and II, but the changes are greater and it exhibits more distinct values at the steady state. With the initial shearing to the peak strength shown in Fig. 5.1, γ reduces a bit, while n_f, a_n and a_f all increase rapidly at similar rates to those of tests I and II in the same strain range. Hence, contacts are primarily created in the vertical direction and disintegrations in the horizontal direction, which is similar to the behavior in tests I and II, but more contact is lost in this stage than in the other two tests. Afterwards, concurrent with the decrease of the shear stress until 1.2% strain shown in Fig. 5.1, γ reduces greatly, while n_f, $a_n$and a_f all increase at the same rate as in the first phase, which indicates that contact disintegration is predominant in this stage and happens in both

directions although it is more prominent in the horizontal direction. From 1.2% to 5.2% strain, γ further reduces but with a somewhat lower rate than in the previous phase, n_f continues increasing at almost the same rate, while a_n and a_f both increase at a much lower rate initially which then reduces further. These responses indicate that the contact disintegration continues in both directions but is more severe in the vertical direction than in the previous stage. From 5.2% to 8% strain, γ and a_f both almost stopped reducing while n_f increases a bit and a_n reduces a bit indicating more contact lost occurs in the vertical direction. After 8% strain, all four descriptors stop changing and maintain at almost constant values until the end of simulation indicating the achievement of steady states. The value of γ at the steady state of test III is much lower than that of tests I and II, while values of n_f and a_f are both much greater than those of tests I and II, only a_n is close to that of test II. The same explanations proposed in the previous section apply here, these responses occur because the even lower permeability of test III causes the individual pore pressures take more time to dissipate among the pores. Furthermore, in the process of pore pressure dissipation, the local higher pore pressure breaks more contacts which results in a lower strength and a higher normal contact force anisotropy parameter a_f.

Micromechanical behavior of test IV

During the initial shearing, test IV behaves very differently from tests I, II, and III in terms of all four micromechanical descriptors presented in Figs. 5.4 to 5.7. γ decreases rapidly during the first 0.25% strain, while a_n and a_f both increase much faster than those in tests I, II, and III, although the initial rate of increase of floater numbers is almost the same as that in tests I, II, and III. This behavior suggests that the contact creation primarily occurs in the vertical direction and contact is lost primarily in the horizontal direction but the contact lost is much more drastic than in the former three tests at the comparative stage. This corresponds to a phase of initial rapid shear stress increase and pore pressure build up. The initial very rapid loss of contact and contact normal anisotropy construction is due to the very low permeability that inhibited a dissipation of the individual pore pressures, so that some relatively high pore pressures from local pores break the horizontal contacts when the vertical load is increased. From 0.25% to 1% strain, γ continue to reduce but with a much lower rate, while n_f, a_n, and a_f all further increase at a somewhat lower rate. Contact creation is still primarily in the vertical direction and loss of contact primarily in the horizontal direction but both are less drastic that the previous stage. During this phase the shear stress slowly increases to and temporarily maintains its peak value followed by the subsequent strain softening. After 1% strain, γ decreases rapidly again until about 8.5% strain, n_f initially further increases with constant rate then suddenly jumps at about 6% strain. a_n also slowly increases but with decreasing rate while a_f does not vary much initially but reduced a bit at about 6% strain. This indicates a loss of contact in the vertical

direction as well as in the horizontal direction, and results in the strain softening shown in the stress-strain curve in Fig. 5.1. At about 8.5% strain, all four descriptors stopped varying much and maintained constant values until the end of the test indicating the achievement of a steady state. All the four descriptor values except for a_n in the steady state of test IV are close to those of test III. a_n in test IV is a bit higher than that of test III.

Micromechanical behavior of test V

The micromechanical behavior of test V is different from that of the other four tests. γ drops very rapidly at the beginning of shearing associated with a very rapid increase of n_f, a_n, and a_f until about 0.2% strain. The response during this stage is similar to that of test IV. The contact lost is mainly in the horizontal direction and there is contact creation in the vertical direction. This results in a very fast initial shear stress increase and pore pressure build up, because the extremely low permeability induced locally high pore pressures in some pores that broke the contacts horizontally and created the contact normal anisotropy rapidly. This effect is more significant in test V than test IV because of the even lower permeability. From 0.2% to 0.6% strain, the rate decrease of γ and the rate of increase of n_f, a_n, and a_f all reduce greatly. This indicates that the loss of contact is still primarily the horizontal direction but it is not as drastic as in the previous stage. The corresponding pore pressure shown in Fig. 5.2 does not change much in this stage, but the shear stress shown in Fig. 5.1 increases rapidly exhibiting strain hardening. This is due to the fact that the granular system tends to dilate since the very low permeability inhibited it from dissipating pore pressure. From 0.6% to 4.0% strain, γ only slightly reduces, n_f initially continues at 400 and then slowly increases beyond 1.6% strain, a_n slowly increases until 1.6%, and maintains an almost constant value, and a_f decreases significantly. This behavior indicates that from 0.6% to 1.6% strain, the amount of contact creation in the vertical direction and contact disintegration in the horizontal direction are almost the same, but are much lower than in the previous stage, which is consistent with the reduction of pore pressure. The tendency of dilation still continues but is less intense with the slowly pore pressure dissipation. From 1.6% to 4.0%, γ and a_n both did not vary much, but n_f increased gradually and a_f decreased greatly. This is because there are more contact disintegrations in both directions as well as contact creation mainly in the vertical direction. After 4% strain, γ reduces gradually again, n_f and a_n continue to increase slowly, while a_f slowly decreases. This corresponds to the pore pressure reconstruction and strain softening stage seen in Figs. 5.1 and 5.2, during which the stress path reverses following the critical stress ratio line shown in Fig. 5.3. Loss of contact occurs in both directions in this stage. At about 13.5% strain, all four descriptors stopped varying and almost maintained constant values announcing the arrival of steady state. The steady state values of all descriptors except a_f for test V are close to those of tests III and IV.

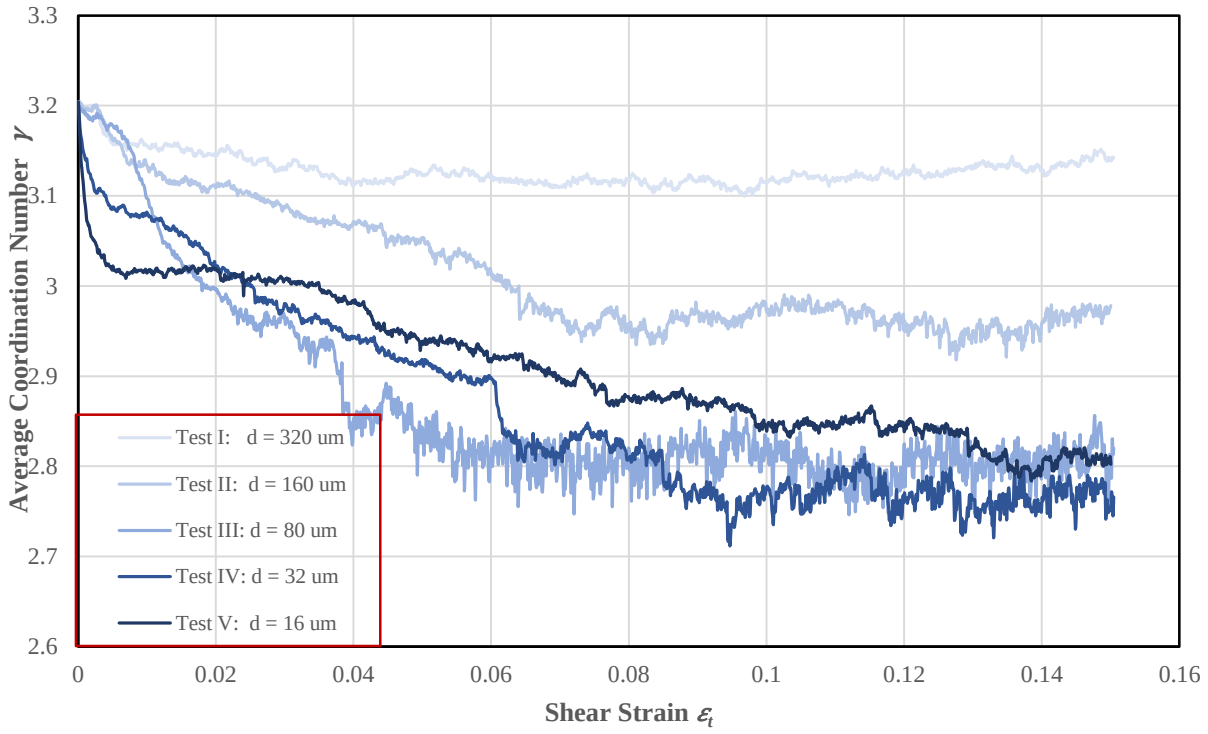

Figure 5.4 Variations of the average coordination number γ for assemblies with different conduit diameters

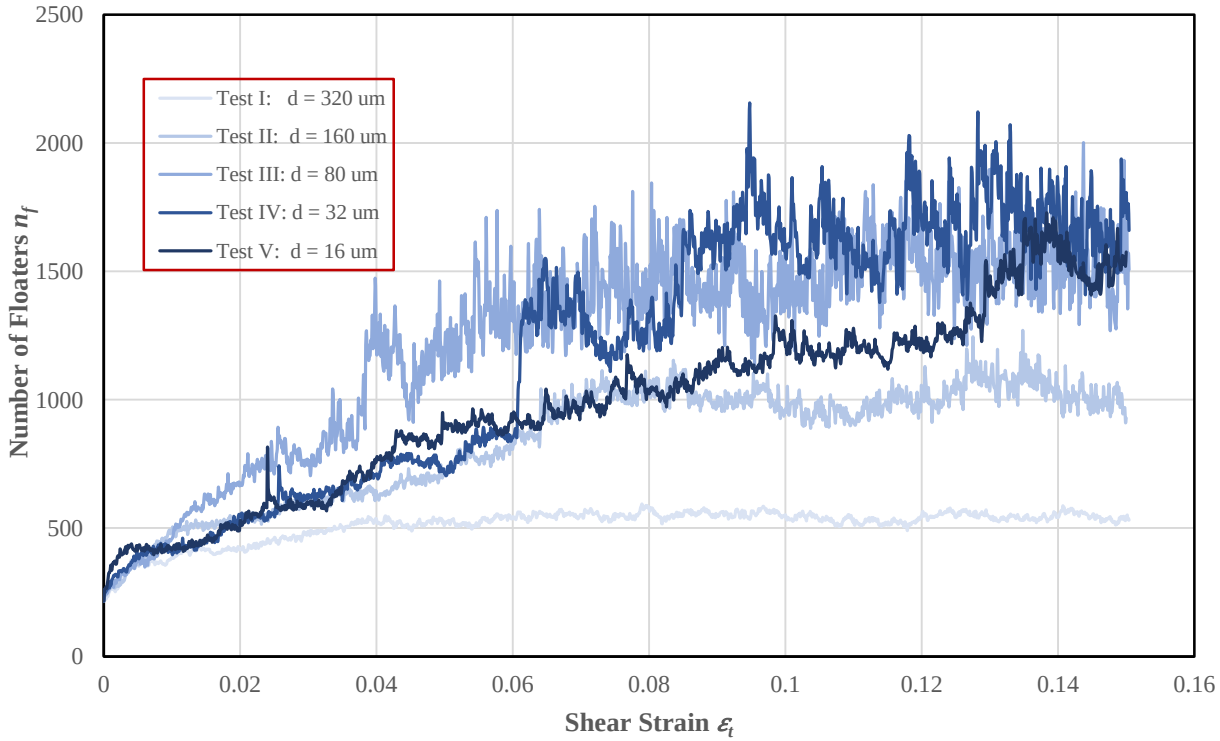

Figure 5.5 Number of floaters n_f variations for assemblies with different conduit diameters

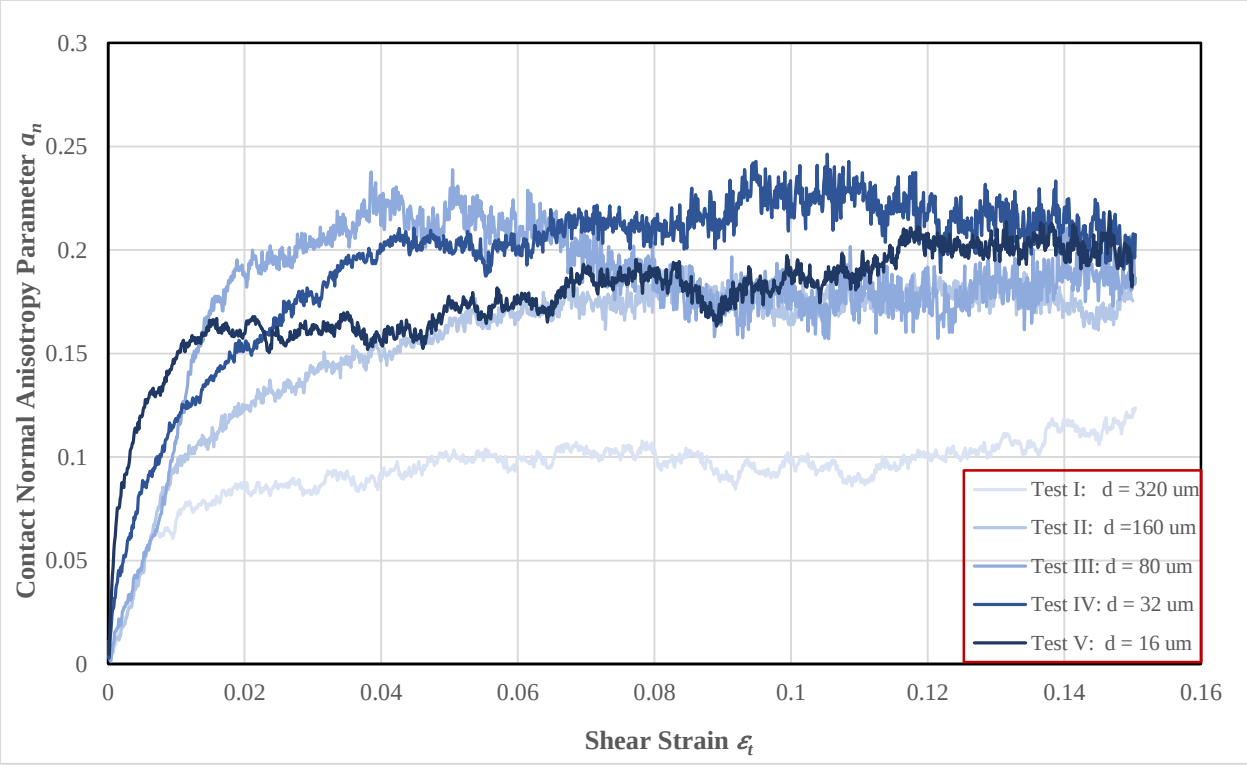

Figure 5.6 Contact normal anisotropy parameter a_n changes for assemblies with different conduit diameters

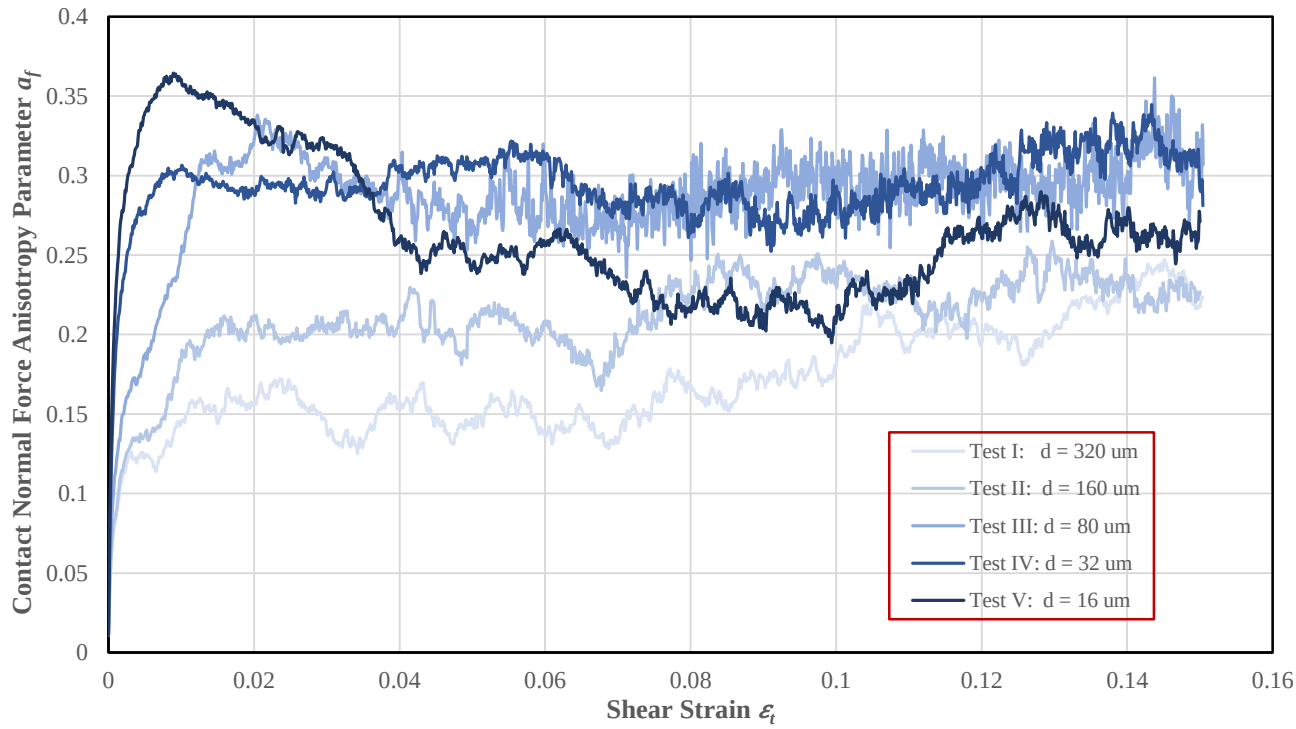

Figure 5.7 Normal contact force anisotropy parameter a_f variations for assemblies with different conduit diameters

Comments

Based on the above analysis of both mechanical and micromechanical responses of the five undrained simulations in which the conduit diameters were varied, some conclusions can be drawn as follows:

1). The contact variations for all five tests follow the pattern that they are initially broken mainly in the horizontal direction with the initiation of shearing to the peak strength, and subsequently, disintegration occurs in both directions with greatly increasing pore pressure. The occurrence of strain softening can be related to a large scale loss of contact in both directions.

2). The overall mechanical behaviors of tests I and II shown from Fig. 5.1 to Fig. 5.3 did not reveal much difference between the two tests, only small difference was exhibited in level of the peak and the residual strengths, and the maximum pore pressure values. However, the micromechanical responses of the two tests displayed in Fig. 5.4 to Fig. 5.7 presents very different behaviors for all four descriptors. Compared to test I, test II exhibited a more drastic strain softening, a much lower value of γ, and much higher values of n_f, a_n and a_f. Hence, the liquefaction in test II is more complete than that of test I although they displayed similar mechanical responses, which indicates that a micromechanical study of the undrained behavior is necessary to understand the corresponding mechanical behavior.

3). The overall undrained responses of all parameters shown in Figs. 5.1 to 5.7 for test I, II, and III are quite similar, but vary in the magnitude of the peak and residual strengths. The strain softening shown in test III is more severe and complete than that of tests I and II, and a greater number of contacts are lost and a higher anisotropy parameter can be seen. There is a large number of contact disintegrations in the vertical direction at the end of strain softening, which makes test III the most liquefied one of the five tests.

4). The undrained behaviors of tests IV and V are very different from those of tests I, II, and III due to their much lower permeabilities. Both of them present an initial rapid contact loss associated with a rapid a_n and a_f increase. Observations of local pore pressure in voids show that in samples of high permeability pore pressures do not vary significantly from one void to another, i.e. pore pressure equalization takes place. On the other hand, in samples of low permeability the variation of pore pressure from void to void is much greater, and, in fact pore pressure in some voids is negative, resulting in high local strength, as evidenced by areas of high force concentration seen in Figure 5.8(e). Areas of negative pore pressures effectively "strengthen" the sample and lead to higher macroscopic strength.

5). At large strains, the residual strength of V is somewhat higher than those in the other four tests, although its overall value of γ is lower than those of tests I and II. This is related to the non-uniform fluid paths created inside the assembly of tests V. These paths decrease the contact lost in both directions in the strain

softening stage. Because the permeability in the local flow path is much higher than the original permeability, fluid flows through this path first during shearing, which results in some locally incomplete liquefaction. However, the residual strengths for test V is not very high because the very low permeability makes the non-uniform fluid paths slow to evolve. It can be imagined that if the permeability is low enough, the residual strength will be much higher or even that strain hardening would be revealed.

6). The above non-uniform fluid paths are not obvious in tests I, II, and III because the higher permeability provides better connections between pores, hence, less contact lost exhibited initially when the pore pressure is dissipated by fluid flow. Therefore, the liquefaction usually does not happen in a coarse grained soil. Comparing the contact force variations of the five tests at large strains (see Fig. 5.9), it can be seen that liquefaction occurred uniformly at the center of samples I, II, and III, while incomplete liquefaction is exhibited in the center of tests IV and V. Some local regions that are not liquefied can be seen at the steady state in tests IV and V. This phenomenon helps explain why soils with very small grain sizes are less liquefiable sometimes.

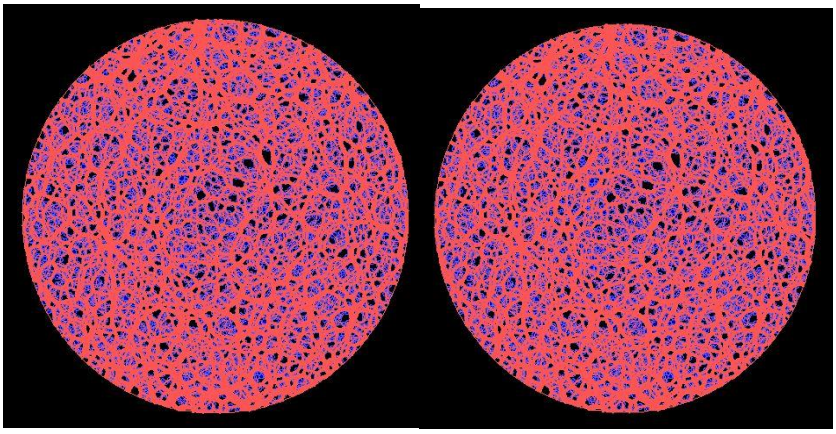

(a) Test I (b) Test II

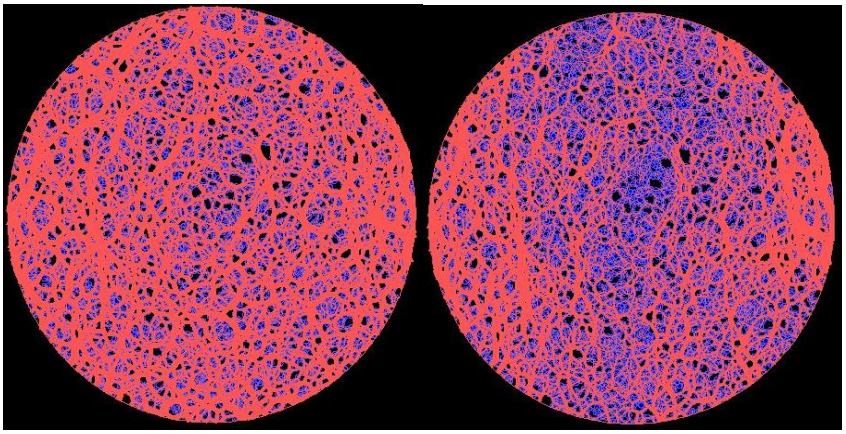

(c) Test III (d) Test IV

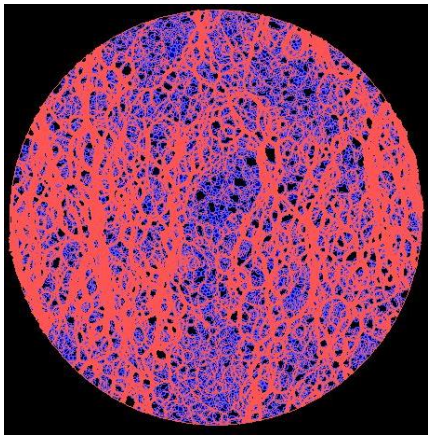

(e) Test V

Figure 5.8 Distribution of contact forces at early stage (non-uniform fluid paths are exhibited in tests IV and V)

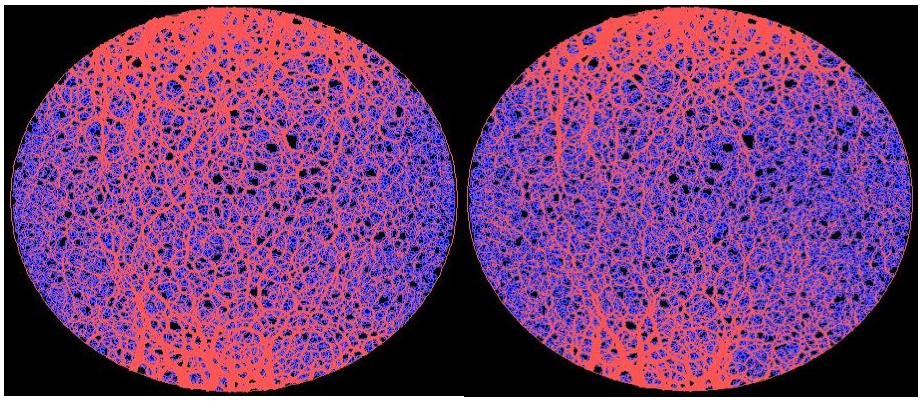

(a) Test I (b) Test II

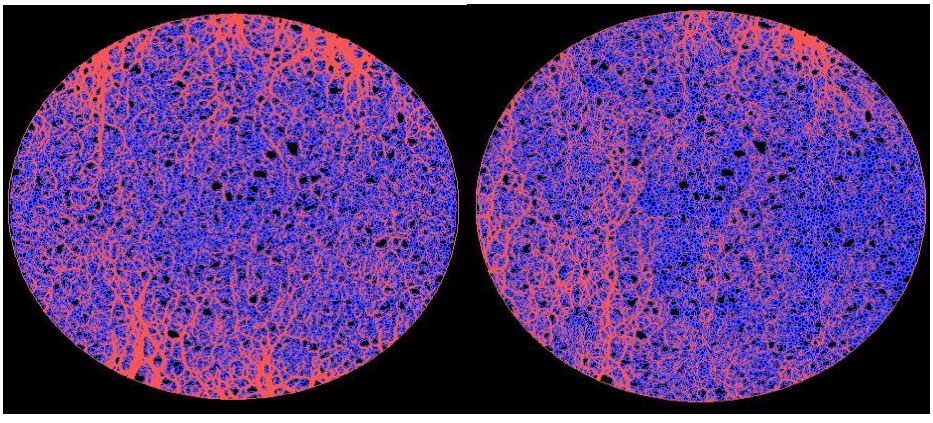

(c) Test III (d) Test IV

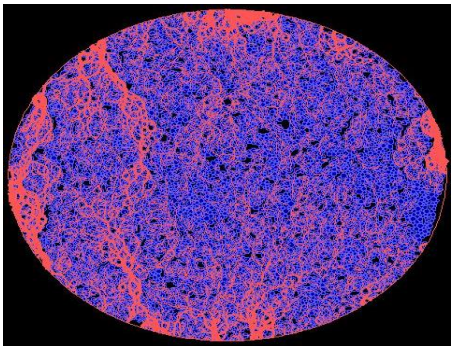

(e) Test V

Figure 5.9 Distribution of contact forces at large strains

5.4 Comparison of simulated results with experimental data taken from the literature

A comparison study of the simulated stress-strain responses for the assemblies with varied conduit diameters presented in Fig. 5.1 with those of two groups of laboratory monotonic triaxial compression tests reported by Pitman et al. (1994) was made. Fig. 5.10 represents two groups of deviator stress versus axial strain plots for varying constituents reported by Pitman et al. (1994). They were obtained by using a clean, uniform, sub-rounded quartz sand as the base sand, and adding different amounts and types of additional constituents. Fig. 5.10a was obtained by adding 0 to 40% of non-plastic crushed quartz fines below 74 μm varied in increments of 10%, and Fig. 5.10b was obtained by adding in increments of 10% from 0 to 40% of clean, sub-rounded, non-plastic quartz sand with a gradation between 0.25 and 0.075 mm. The D_{50} and D_{10} of the base sands are 0.39mm and 0.22mm, respectively, and the C_u is 1.7. All the ten stress-strain plots shown in Fig. 5.10 are obtained by performing a strain controlled monotonic triaxial compression test under a confining stress of 350 kPa. The moist tamping technique was adopted when preparing the loose samples with different percentages of additional materials.

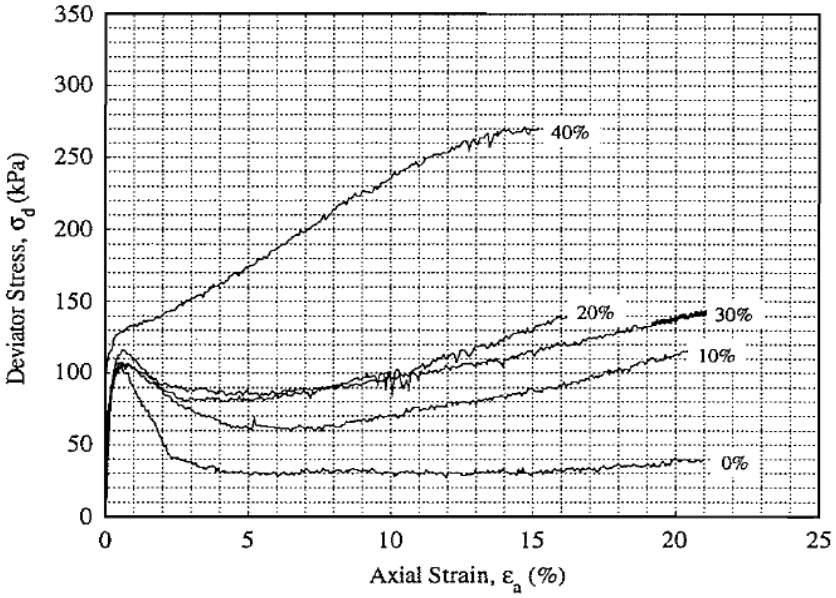

(a)

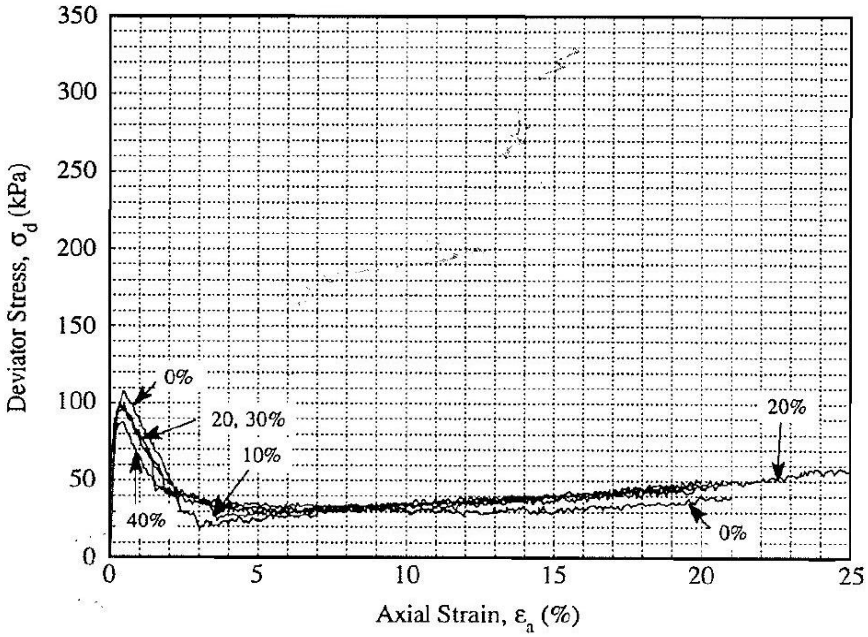

(b)

Figure 5.10 Plots of deviator stress vs. axial strain for varying different percentages of additional constituents. (a) various percentages of crushed silica fines (b) various percentages of silica sand (Pitman et al., 1994)

It can be seen from the stress-strain responses exhibited in Fig. 5.10a that with the increasing percentage of the non-plastic fines from 0 to 40%, the behavior of the stress-strain curves changes from strain softening (0% fines) to limited liquefaction (10-30% fines), then to strain hardening (40% fines). However, the stress-strain plots shown in Fig. 5.10b are all very close to each other, although the samples of them varied in the percentages of fine sand between 0 to 40%. Two associated groups of SEM photographs at varying the

scales for the 20% and 40% crushed silica fines samples used in Fig. 5.10a are shown in Fig. 5.11. It can be seen from Fig. 5.11 that the Ottawa sands are surrounded by the crushed silica fines, which in terms of fluid connectivity of the system resembles the loose assembly with low permeability of the previous section.

Compared to Fig. 5.1, it can be seen that the early stages of the stress-strain response exhibited in Fig. 5.10a agrees with that Fig. 5.1. Both show that the peak strength increases with increasing percentages of the fine component (and lower permeability). This phenomenon is not shown in the plots of Fig. 5.10b since the samples were prepared by varying the percentages of silica sand with a gradation between 0.25 and 0.075mm. The permeability for sands within this gradation does not vary much, so the stress-strain behavior for all five groups of Fig. 5.10b are close to each other. Similar behavior is seen in the stress-strain curves for tests I and II shown in Fig. 5.1. Since the permeability of the two tests are close to each other, it would be expected that their mechanical behavior would be similar throughout the whole strain range.

At intermediate and large strains, the stress-strain behavior of the Ottawa sand with different percentages of non-plastic fines shown in Fig. 5.10a is different than the simulated undrained stress-strain response shown in Fig. 5.1. This may be because the simulations directly control the permeability, which restrains the rate of individual pore pressure dissipation based on different assigned values of the conduit diameters. However, the process of pore pressure dissipation takes place slowly as the shear reaches intermediate and large strains. Thus, the five tests obtained from simulations display similar responses at intermediate and large strains, although test V exhibits strain hardening at an early stage. Unlike the simulation results, the various permeabilities for the laboratory test results presented in Fig. 5.10a were indirectly achieved by controlling the percentage of fines, in which case the constitution of the sample itself was changed, thus, all five samples display different behaviors at intermediate and large strains. Therefore, based on a comparison of the results from the undrained simulations and the two groups of laboratory tests, it can be concluded that permeability affects the stress-strain behavior of undrained sand, especially during the initial shearing stage, and the value of the peak and residual strengths.

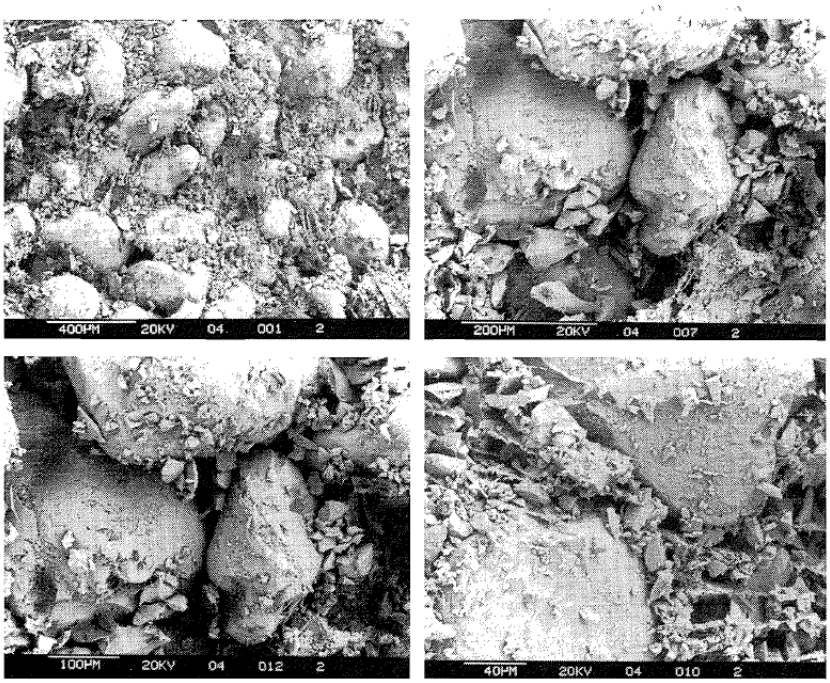

(a)

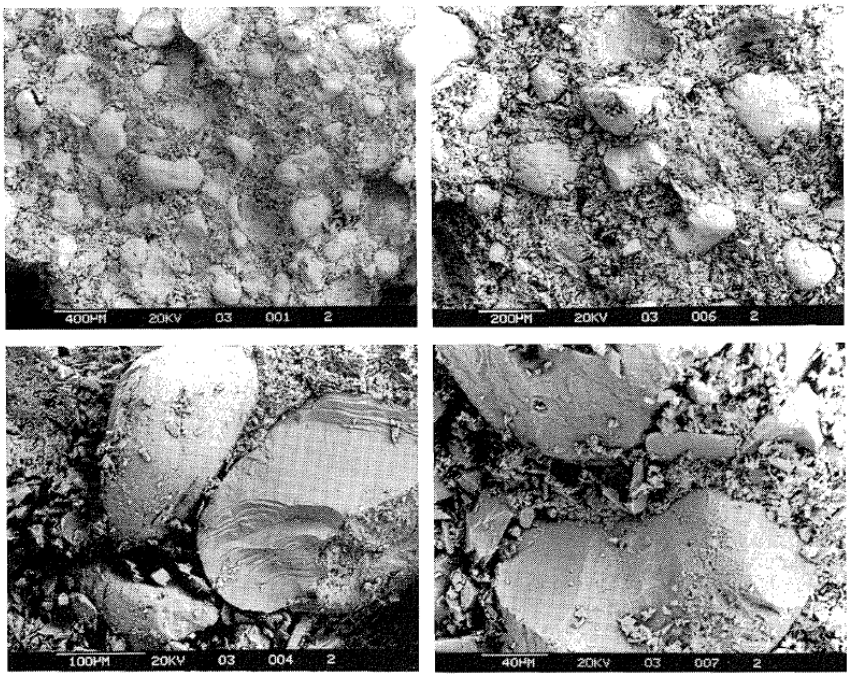

(b)

Figure 5.11 SEM photographs of the crushed silica fines sample (a) 20% fines (b) 40% fines (Pitman et al., 1994)

Chapter 6 Consistency of the Critical State Line and the Steady State Line

6.1 General background

This chapter presents a study of the consistency between the critical state line from drained simulations and the steady state line from undrained simulations. The main objective of this study is to explore the physical legitimacy of treating liquefaction as a critical state phenomenon. In section 6.2, a series of drained biaxial compression simulations on the granular disk assemblies using the DEM are conducted to a large strain. The results are presented in terms of the impacts of the initial void ratio and confining stress on the drained behavior of granular media. The critical state point selected from each test is applied for the construction of the critical state line. Section 6.3 introduces some undrained simulations in addition to those already presented in chapter 4. They are used to construct the steady state line for a wide range of void ratios. In section 6.4 the consistency between the critical state line and the steady state line is examined in terms of both mechanical and micromechanical descriptors based on the simulated results from sections 6.2, 6.3 and 4.3. A comparison of the consistency obtained in this study with that from the laboratory tests reported in the literature is then presented at the end of the chapter.

6.2 Drained simulations to the critical states

In order to construct a critical state line of the granular media adopted in this research, a series of biaxial compression simulations are conducted to simulate drained behavior up to the point where a critical state is reached. Since the initial void ratio and the confining stress are the two main factors affecting a granular media's drained behavior, the biaxial compression simulations and their corresponding results obtained in this chapter will be described in terms of these two aspects in the following.

6.2.1 Effect of initial void ratio

6.2.1.1 Summary of the test program

To demonstrate the impact of initial void ratio on the drained behavior of the granular media used in this research, a group of four biaxial compression simulation tests (DA, DB, DC, and DD) were conducted using granular assembly samples that are exactly the same as those already presented in Table 4.3 of section 4.3.1. All the four assemblies are sheared to very large strain (about 40% strain) to guarantee the achievement of the critical state. The associated physical properties of the disc particles used in the simulations such as Young's Modulus, Poisson's Ratio, inter-particle friction coefficient, and density follow those of Table 4.1 in section 4.2.1. The biaxial compression simulations for the four samples all use mode 3 that was introduced in section 3.4, which maintains the average stress σ_{11} constant, and meanwhile, increases the average stress σ_{22} by applying a constant strain rate $\dot{\epsilon}_{22}^{\beta}$ (at the boundary). The parameters for the biaxial

compression simulations such damping effect, time step and vertical strain rate follow the values shown in Table 4.4.

6.2.1.2 Simulation results

Mechanical behaviors from simulations

Figs. 6.1 to 6.4 shows the mechanical behaviors for the four drained biaxial compression tests with different initial void ratios DA, DB, DC, and DD, respectively. Figure 6.1 gives the stress-strain responses of the four samples under shearing, Figure 6.2 shows the volumetric strain variations throughout the four tests, Figure 6.3 presents the stress paths for the four drained tests, Figure 6.4 exhibits the void ratio changes of the four assemblies throughout the test. From these figures, it can be seen that the initial void ratio affects the drained mechanical behavior of the granular assemblies significantly. Overall, sample A fails at a very early stage of about 0.5% strain due to its extremely high void ratio. Sample B exhibits a typical loose sample type of response under shearing. Sample C displays some dilation under shearing, and sample D shows a classical dense sample type of response. A detailed interpretation of the mechanical drained behaviors of the four samples is reported as follows:

Test DA

Sample A fails at a very early stage of straining due to the extremely high initial void ratio. We see in Fig. 6.1 that the shear stress of sample A increases rapidly during the initial shearing and reaches its peak strength of 16.7 kPa at a strain of only 0.25%. Subsequently, the shear stress decreases and failure suddenly occurs at about 0.5% strain. The corresponding volumetric strain variations shown in Fig. 6.2 show a continuous contraction of sample A from beginning of the simulation until failure. It initially contracts slowly then suddenly contracts rapidly and fails. The void ratio of sample A shown in Fig. 6.4 decreases from the start of the test until sudden failed failure occurs.

Test DB

Sample B displays a typical loose sample type of behavior throughout the simulation. It exhibits very high rate of increase of the shear stress upon initial shearing and reaches an initial peak strength of 44 kPa at 1.5% strain. During this process, the corresponding volumetric strain and void ratio of sample B both change at an almost constant rate indicating that contraction occurs during the shearing. Subsequently, from 1.5% to 3% strain, the shear stress maintains the peak value, and then reduces to 29 kPa at 4% strain. From 3% to 4% strain, the rate of change of volumetric strain and void ratio both suddenly increase corresponding to the sudden shear stress drop due to the macropores formed in the assembly when preparing the sample. They result in a temporary loss of strength of the sample during shearing, which explains the fact that sample A failed shortly after reaching its peak strength. After the temporary drop of the shear stress,

continued shearing of sample B leads to a stress increase and to a much higher value at a nearly constant rate until about 28% strain where the rate of increase starts to reduce gradually to zero. The corresponding volumetric strain and the void ratio continue to show a contraction at a much lower rate than in previous stage. The sample reaches the critical state at about 40% strain, where the volumetric strain and the void ratio both stop changing and maintain almost constant values.

Test DC

Unlike sample B, sample C did not contract under shearing but displayed a small dilation. During initial shearing, the shear stress increases rapidly and reaches a much higher stress than sample B did in the same strain range. The volumetric strain changes in this stage indicate a small contraction. Subsequently, the shear stress increases very slowly and reaches 80 kPa at about 5% strain. It then fluctuated about 80 kPa with very little increase with further shearing until the end of the simulation when the critical state is achieved. During this process, the volumetric strain increased after the initial small contraction. It reached 0.2% volumetric strain at 5% shear strain, then it started to fluctuate between 0.2% and 0.3% of ε_v until the end of the test, indicating the occurrence of a small dilation of sample C with shearing until the critical state was reached. The void ratio of sample C barely changed throughout the test, it only increased from 0.238 to 0.242 at very low rate of increase distributed uniformly throughout the simulation.

Test DD

Sample D shows a typical medium dense type of behavior and exhibits a higher peak strength than the other samples throughout the simulation until the critical state is reached. It is shown in Fig. 6.1 that the shear stress of sample D increases more rapidly upon initial shearing, than for the other tests. The corresponding volumetric strain in this stage shows a small contraction. The shear stress reaches a value of 80 kPa at 2% strain. Afterwards, the rate of increase reduces, and the shear stress increases slowly to its peak value of about 100 kPa at 12% strain and then maintains that value with some fluctuations until 35% strain. The volumetric strain in this stage keeps on increasing but at a decreasing rate after the initial contraction. From 35% strain to the end of the test, the shear stress reduces a bit while the associated volumetric strain almost remains constant, indicating the achievement of the critical state. The void ratio of the sample slowly and uniformly increases from the beginning of simulation until about 35% strain when it reaches a maximum value of 0.243. It then almost maintains value of 0.243 until the end of test indicating the achievement of the critical state.

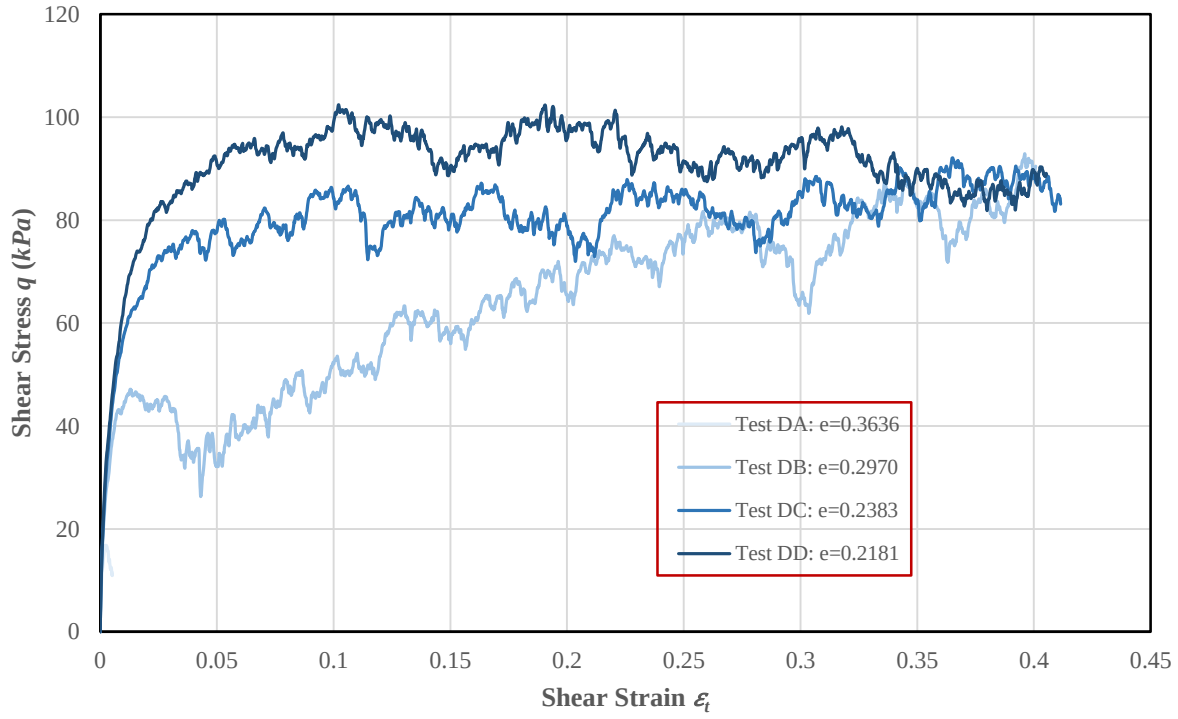

Figure 6.1 Drained stress-strain responses for assemblies with different initial void ratios

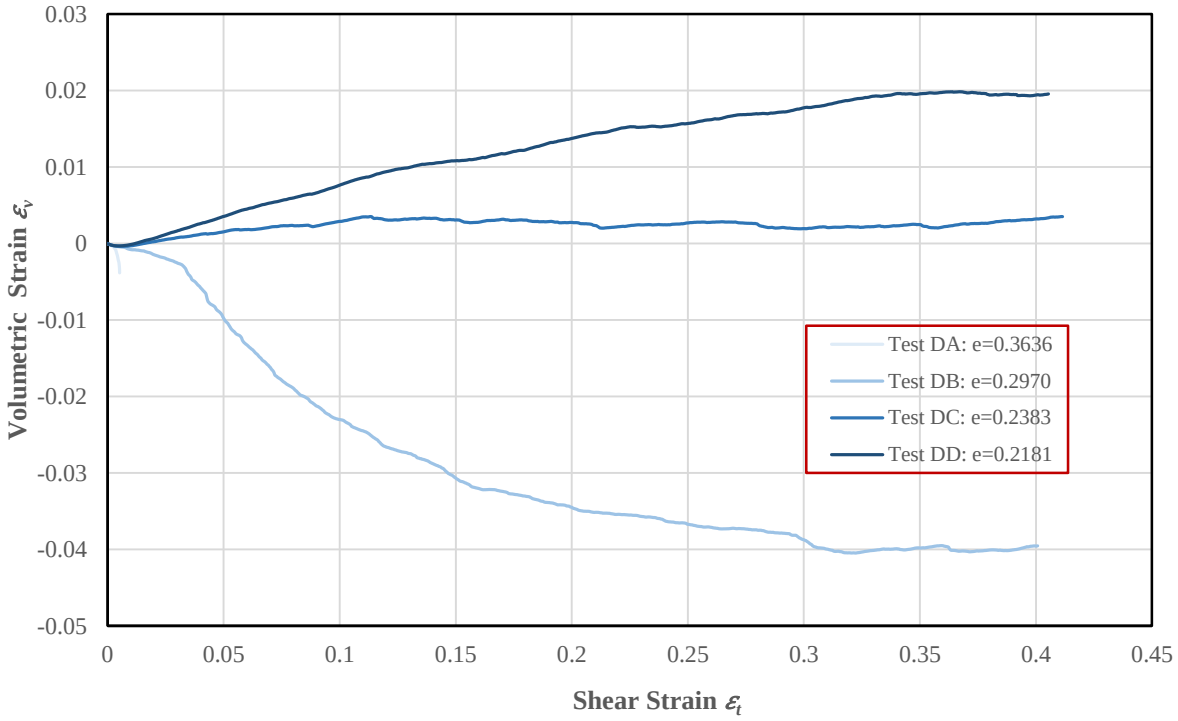

Figure 6.2 Drained volumetric strain variations for assemblies with different initial void ratios

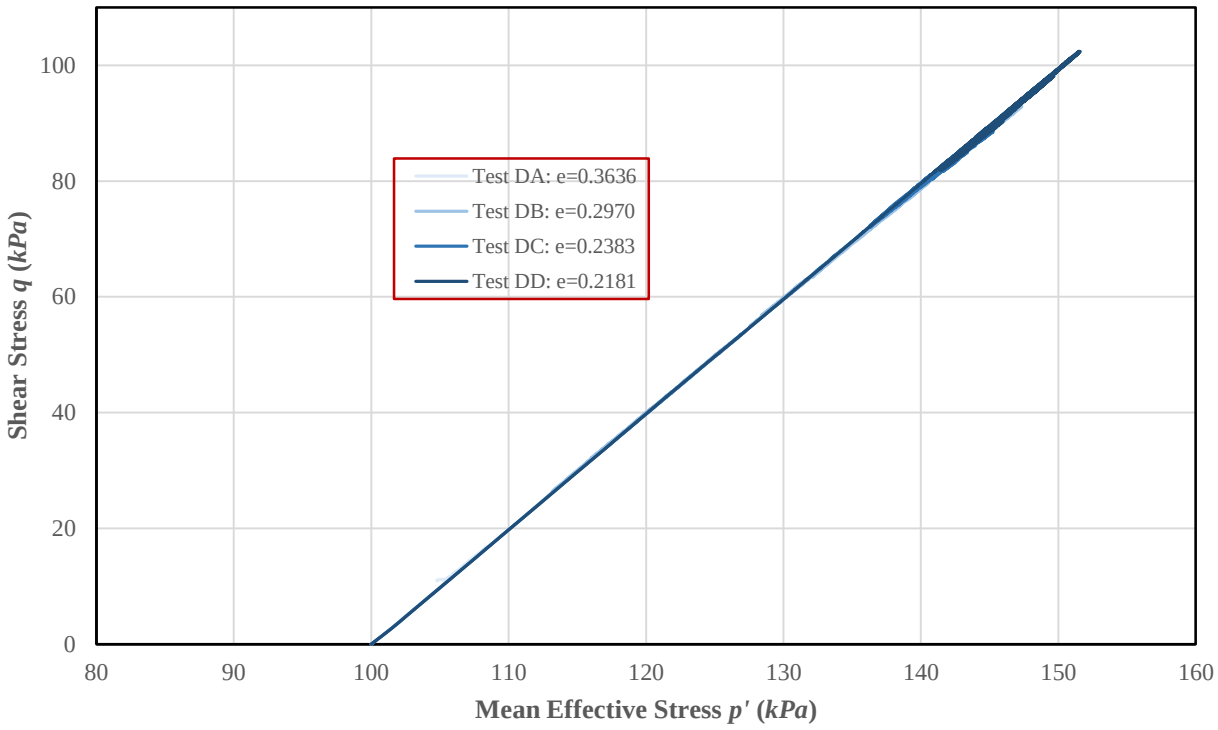

Figure 6.3 Drained stress paths for assemblies with different initial void ratios

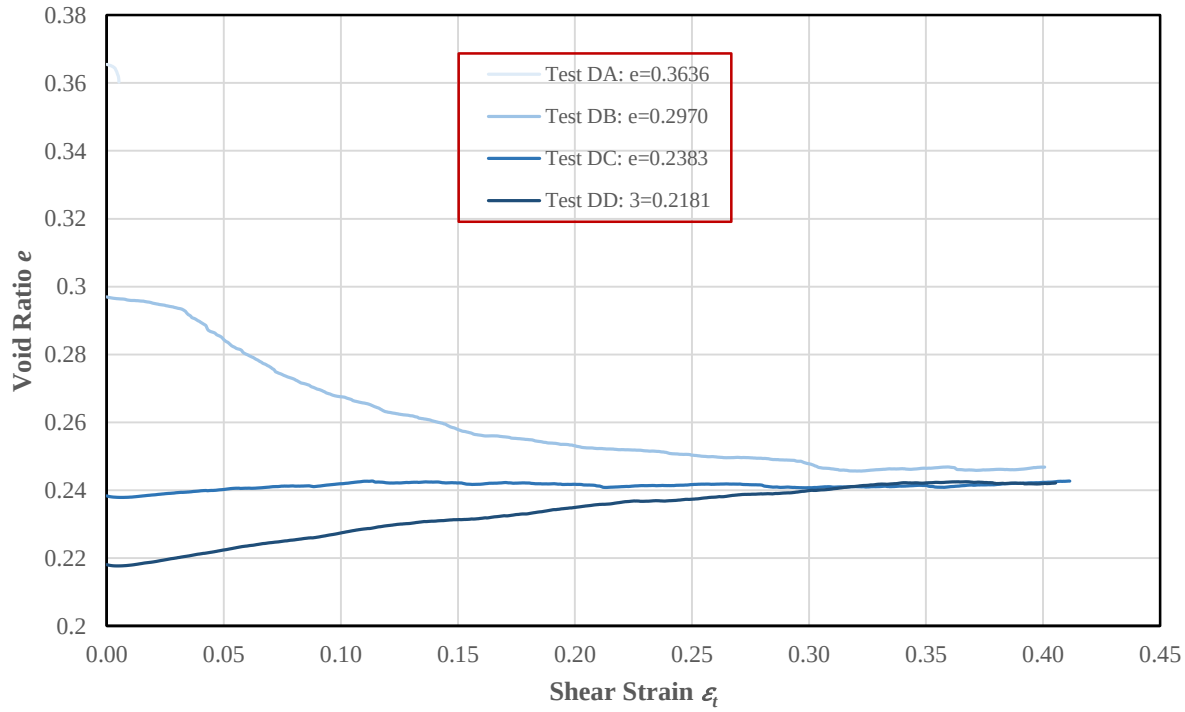

Figure 6.4 Drained void ratio variations for assemblies with different initial void ratios

Comments

Comparing the drained behavior of the four samples shown in Figs. 6.1 to 6.4, it can be seen that the stress-strain responses, the volumetric strain variations, and the void ratio changes for the four samples differ markedly. However, the stress paths for all the tests shown in Fig. 6.3 merge because the same confining stress is applied to all the assemblies. The slope of all of the stress paths shown in the figure are equal to 2 as expected. The highest point of the stress path of test DD shown in Fig. 6.3 is a bit higher than the other three tests due to its higher peak shear strength, which is evident in Fig. 6.1. The initial rate of shear stress increase increases for the sequence A to D. Sample A fails very early, sample B contracts and develops typical loose type of behavior, sample C dilates a bit, while sample D displays more dilation and typical medium dense type of behavior. At very large strains, all samples other than sample A, which was failed at a very early stage, merge to similar shear stress and void ratio values indicating the achievement of the critical state. The critical void ratio of samples B, C, and D is all about 0.245.

Micromechanical behaviors from simulations

Figs. 6.5 to 6.8 present variations of the micromechanical descriptors of the four samples during drained shearing. Fig. 6.5 shows the changes of the average coordination number γ, Fig. 6.6 displays the changes in the number of floaters n_f, Fig. 6.7 presents the contact normal anisotropy parameter a_n variations, and Fig. 6.8 presents the normal contact force anisotropy parameter a_f changes. Based on the variations of these descriptors throughout the drained simulations for the four samples, the micromechanical behaviors of them under shearing are interpreted as follows:

Test DA

Sample A failed at very early stage. It can be seen from Figs. 6.5 to 6.8 that at initial shearing, both the average coordination number γ and the number of floaters n_f increase, and meanwhile, both the contact normal anisotropy parameter a_n and the normal contact force anisotropy parameter a_f increase steadily. These responses indicate in this stage although overall the contact creation is predominant and occurs mainly in the vertical direction, many contacts are lost in both directions as shown by the growth in the number of floaters. Continued shearing induced a failure of the sample at about 0.5% strain, where γ, a_n, and a_f all suddenly dropped indicating a significant loss of contact in both directions and resulting in a failure of the sample. The failure at a very early stage is due to the macropores formed during the creation of the very loose sample. During shearing, the movement of particles destroys the macropores which made the system become less stable and led to failure. This is consistent with the rapid reduction of the volumetric strain shown in Fig. 6.2.

Test DB

At the beginning of the shearing of sample B, γ, a_n, and a_f all increase rapidly while n_f dropped abruptly, which indicates that vertical contact creation is predominantly and aided by connections made with the floaters in the macropores. Subsequently, continued shearing leads to all four micromechanical descriptors remaining temporarily constant, which corresponds to the temporarily constant shear stress stage seen in Fig. 6.1. These responses indicate that the initial fast contact creation in the vertical direction obtained by making connections with the floaters is terminated, and in addition, that the contact creation and contact disintegration in this stage are in balance. From 3% to 4% strain, γ, a_n, and a_f all drop a bit suddenly, while n_f increases a bit, which is in accordance with the sudden drops of shear stress in this stage shown in Fig. 6.1. Contact disintegration is predominant in this stage and mainly in the vertical direction. As already explained in the above, it is the macropores generated when preparing the samples that results in the suddenly contact loss in the vertical direction upon the application of load. After this temporary drop, from 4% strain to the end of the test, a_n and a_f both grow steadily and gradually approach to their maximum values at a very large strain, then stay at this maximum value until the end of the test. γ does not vary much, it only increases a bit and reaches the maximum value and then maintains at this value until the end of test. n_f did not change until about 15% strain, then it decreased a bit and then fluctuated about a constant value until the end of test. These responses indicate that the contact creation in the vertical direction and the contact disintegration in the horizontal direction continued to develop in this stage leading to the critical state where contact creation and disintegration in the assembly is in balance.

Test DC

Upon initial shearing to about 2% strain, γ, a_n, and a_f of sample C all increase very rapidly while n_f decreases significantly indicating contact creation is primarily in the vertical direction due to connections made with the floating particles under loading. Higher values of γ, a_n, and a_f and a lower value of n_f of sample C compared to those of sample B which can be seen in this stage is due to a larger number of initial floating particles created in sample C during its preparation. From 2% to 12% strain, a_n and a_f both slowly increase to their peak values, γ slowly reduces a bit, while n_f does not change much, which indicates that in this stage contact creation is still primarily in the vertical direction and contact disintegration is in the horizontal direction. The small reduction of γ occurs because a small number of contact disintegration happened in both directions due to the dilation of the sample in this stage, which can also be seen in Fig. 6.2. From 12% strain to the end of the test, all the four descriptors maintain almost constant values, which means that contact creation and disintegration in both directions are in balance, and the system comes to the critical state.

Test DD

The micromechanical behavior of sample D in terms of the responses of descriptors shown in Figs. 6.5 to 6.8 is similar to that of sample C. From the beginning to about 2% strain, the four descriptors respond similarly to those of sample C but more strongly. γ, a_n, and a_f all increase rapidly while n_f decreases abruptly. Contacts are made rapidly in the vertical direction through connections with the floaters that were created in the macropores during specimen fabrication, and contacts are mainly lost in the horizontal direction. From 2% to 10% strain, a_n and a_f both increase slowly, while γ and n_f remain nearly constant. This means that in this stage, although contact creation is still primarily in the vertical direction while contact disintegration is mainly in the horizontal direction, however, the responses are less intense compared to the previous stage due to initiation of dilation in sample D (see Fig. 6.2). Subsequently, from 10% to about 35% strain, γ and a_f both decrease a bit, a_n first increases and then decreases a bit, while n_f remains nearly constant. These responses indicate that a number of vertical contact disintegration occurs in this stage along with the horizontal contact lost accompanied by dilation, which agrees with the mild strain softening seen in Fig. 6.1. From 35% strain to the end of the test, all the four descriptors remain constant indicating that contact creation and disintegration in both directions are in balance and the assembly enters into the critical state.

Comments

Comparing the variations of the micromechanical descriptors of the four samples shown in Figs. 6.5 to 6.8, it can be seen that samples C and D exhibit similar responses, which are distinctly different from that of samples A and B. The difference in the micromechanical behaviors between samples C and D occurs because a number of contact lost occurs in the vertical direction of sample D at an intermediate strain range due to the severe dilation of the assembly under shearing.

Due to the connections made with the floating particles in the macropores during initial shearing of all the samples except sample A, γ, a_n, and a_f all increase rapidly while there is a significant decrease in the number of floaters n_f. The different initial peak values of a_n is due to the different initial number of floaters n_f in the samples. All descriptors change more slowly after the initial stage of shearing and then slowly evolve until a critical state is reached. Since the void ratio of sample D is low, it dilates and results in some loss of contacts in both directions before reaching the critical state. At the critical state, the descriptors shown in Figs. 6.5 to 6.8 for all tests merge together and contact creation and disintegration enter into a balance in both directions. For all four samples, the average coordination number γ at the critical state is about 3.3 and the number of floaters n_f at the critical state is about 400.

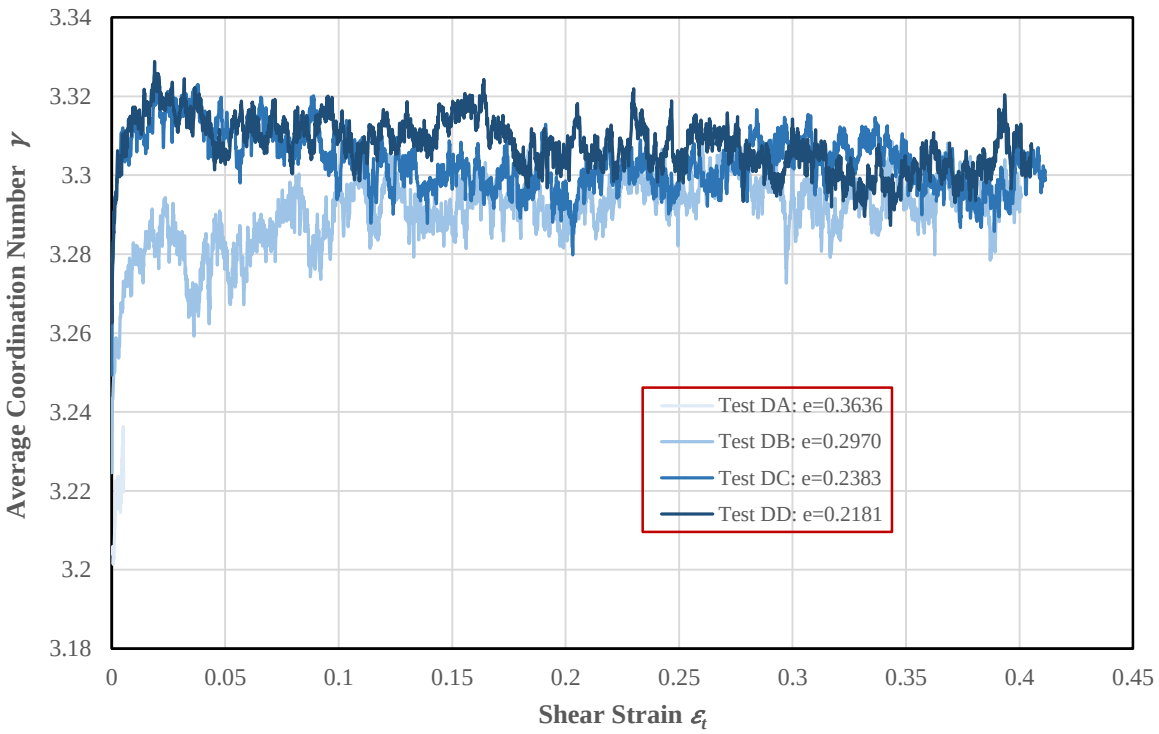

Figure 6.5 Average coordination number γ variations for assemblies with different initial void ratios

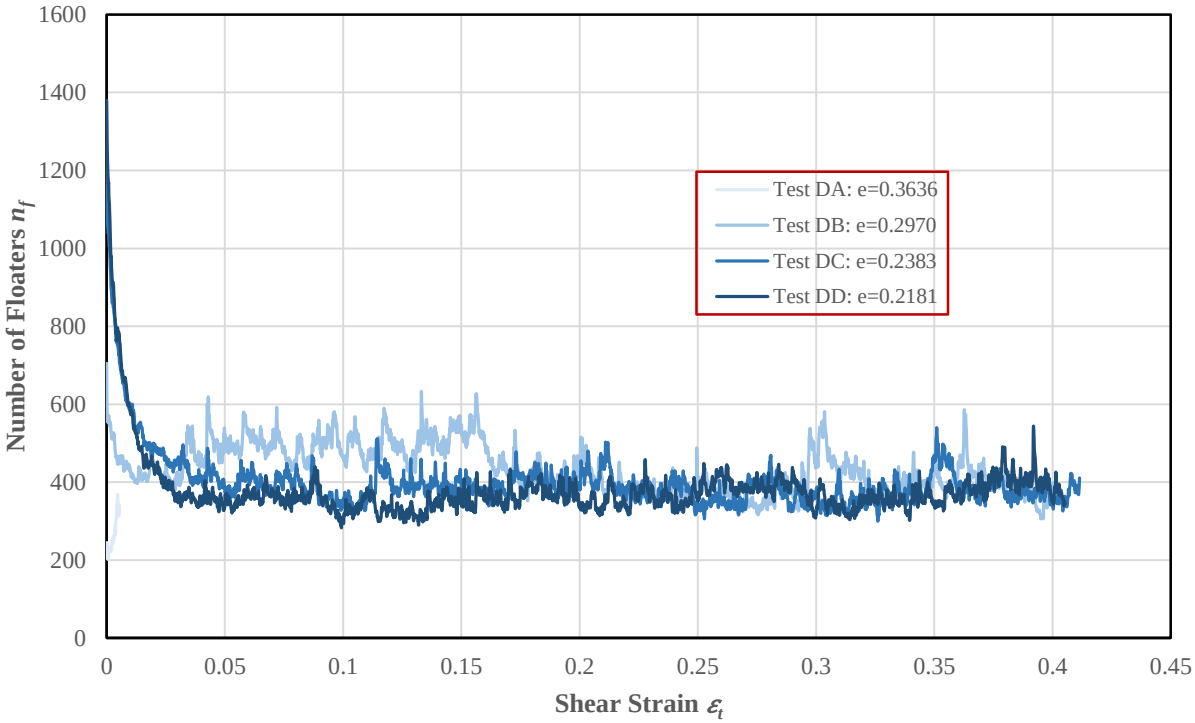

Figure 6.6 Number of floaters n_f variations for assemblies with different initial void ratios

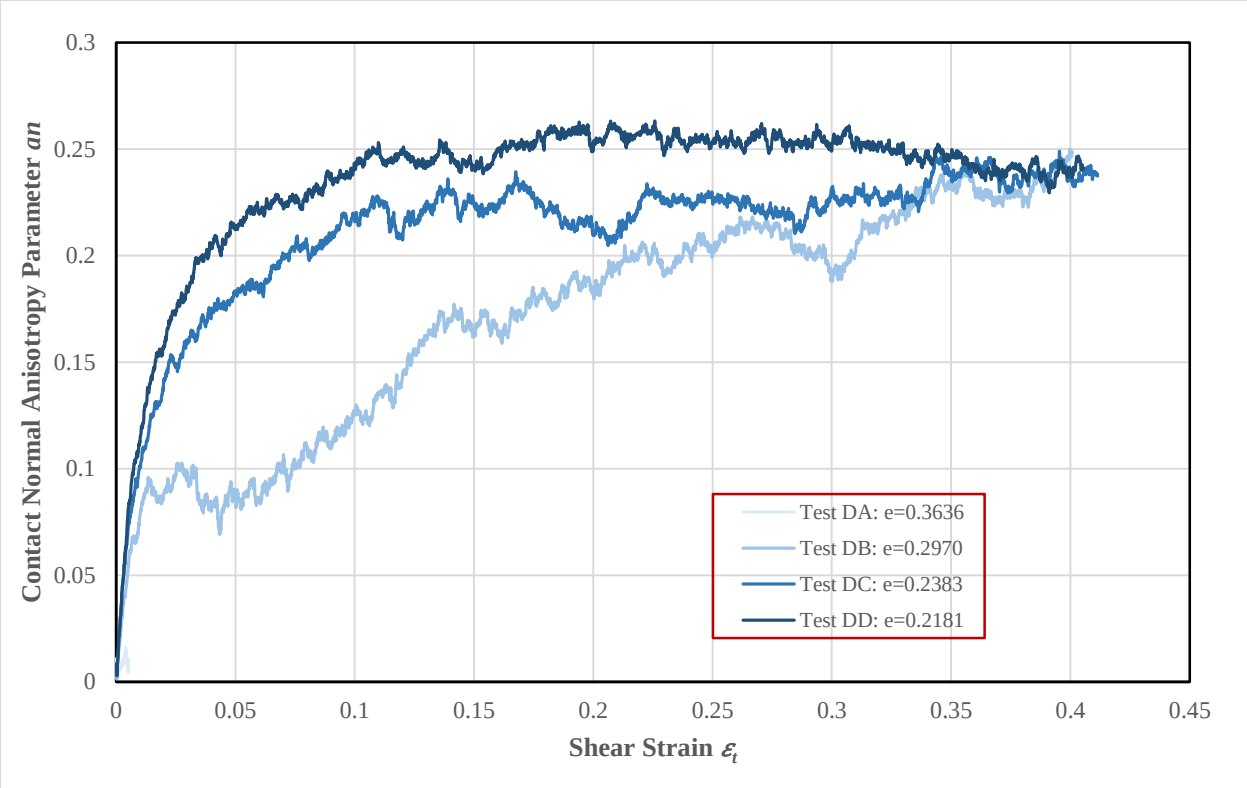

Figure 6.7 Contact normal anisotropy parameters a_n variations for assemblies with different initial void ratios

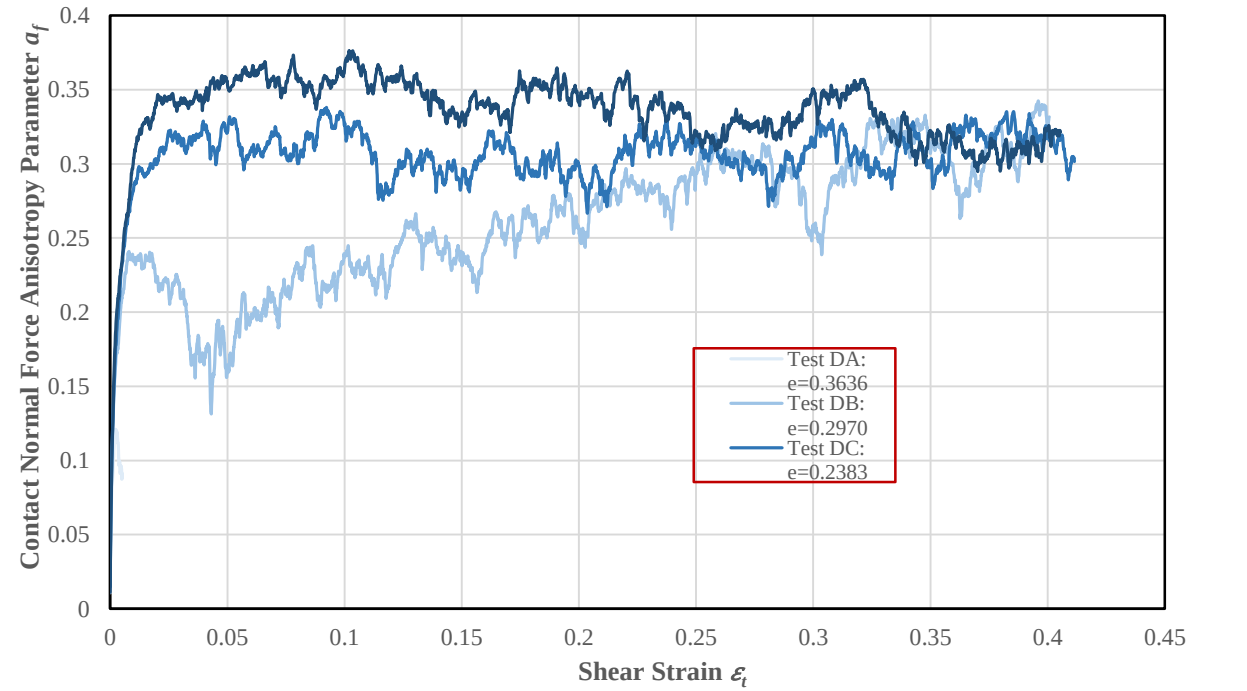

Figure 6.8 Normal contact force anisotropy parameter a_f changes for assemblies with different initial void ratios

6.2.2 Effect of confining stress

6.2.2.1 Summary of the Test Program

To construct a critical state line for the adopted granular assemblies, and meanwhile, study the effect of confining stress on the drained behavior of granular media, a group of thirteen simulation tests (D1, D2, D3, D4, D5, D6, D7, D8, D9, D10, D11, D12, and D13) were designed with close initial void ratios but different confining stresses that varied from 50 kPa to 1600 kPa. The significantly different confining stresses allows the construction of the critical state line for a wide range of mean effective stress. It can be seen from Fig. 6.4 that under the same confining stress, even if the void ratios of the samples are very different at the beginning of the tests, they become very similar at the ultimate state. Therefore, a series of biaxial compression tests with different confining stresses are necessary to obtain the critical void ratios on the critical state line. In addition, to avoid the impact of the initial fabric of the granular assemblies on the critical state and maximize the differences between the initial conditions of drained and undrained simulations, a different sample preparation method is employed for the same disc particles in this section. The method resembles the air pluviation method in laboratory testing, the process of which is summarized as follows:

1. Create an initial assembly and set a very high value of coefficient of contact friction (i.e. 10) for the particles in the assembly. Subsequently, increase the boundary stress to the target level uniformly by using mode 2 introduced in section 3.4. Loading and unloading are applied alternately and are continued until an assembly with uniformly distributed stresses is achieved.

2. Decrease the contact friction coefficient between the particles slowly from 10 to 0.5 under the target confining stress using mode 1.

3. Continue to adjust the boundary stress to the target value using mode 1 with a coefficient of contact friction of 0.5, until the whole system achieves an equilibrium condition so that a loose sample is created.

Similar to the drained biaxial compression simulations with different initial void ratios conducted in the previous section, the simulations in this section for the above samples were also conducted using mode 3, which maintains the average stress σ_{11} constant, and meanwhile, increases the average stress σ_{22} by applying a constant strain rate $\dot{\epsilon}_{22}^{\beta}$ (at the boundary). The associated physical properties of the disc particles applied in the simulation such as Young's Modulus, Poisson's Ratio, and inter-particle friction coefficient also follow those of Table 4.1 in section 4.2.1. The parameters for the biaxial compression simulations such as damping effect, time step and vertical strain rate follow the values shown in Table 4.4. And some initial physical properties for each sample used in this section are shown as Table 6.1.

Table 6.1 Summary of initial physical properties of the tests

Test	Sample	Number of floaters n_f	Average coordination number γ	Void ratio (e)	Confining stress (kPa) (σ_1)
D1	**D1**	765	3.2441	0.2547	50
D2	**D2**	817	3.3269	0.2545	100
D3	**D3**	496	3.3083	0.2518	200
D4	**D4**	476	3.3622	0.2504	300
D5	**D5**	414	3.3873	0.2492	400
D6	**D6**	484	3.3930	0.2478	500
D7	**D7**	317	3.4291	0.2465	600
D8	**D8**	298	3.4459	0.2453	700
D9	**D9**	272	3.4676	0.2441	800
D10	**D10**	243	3.5017	0.2417	1000
D11	**D11**	195	3.5244	0.2394	1200
D12	**D12**	174	3.5509	0.2372	1400
D13	**D13**	183	3.5749	0.2349	1600

6.2.2.2 Simulation results

For the purpose of explaining the effect of confining stress on the drained behavior of granular media and avoiding repetition, in this section, the interpretation will only be based on samples D1 to D5 in terms of both mechanical and micromechanical descriptors. The impact of confining stress on the drained behavior of the rest of the samples in this section are similar to those shown by D1 to D5. The specific results of the rest tests are presented in Appendix A.

Mechanical behaviors from simulations

Figs. 6.9 to 6.12 show the results of biaxial compression simulations (drained) using samples D1 to D5. Figure 6.9 shows the stress-strain responses, Figure 6.10 shows volumetric strain variations, Figure 6.11 presents the stress paths changes, and Figure 6.12 exhibits the void ratio variations. From these figures, it can be seen that confining stress affects the mechanical behavior of the granular assemblies significantly. Since all the five samples display a typical loose type of behavior similar to that of test DB shown in the

previous section, hence, in this section the interpretation of mechanical behaviors for samples D1 to D5 will mainly focus on a comparison of the impacts of the confining stress in the five simulations. A detailed interpretation is given in the following:

Stress-strain response

The overall stress-strain responses of all five samples shown in Fig. 6.9 are quite similar, all of them display the typical behavior of a loose sample. They all show a rapid initial shear stress increase followed by a slow reduction of the rate of stress increase until a maximum is reached and maintained to a large strain. The differences between the five samples are in their initial rates of increase of shear stress and the maximum shear stress values at the critical state. For tests D1 to D5, the initial rate of shear stress increase and the maximum shear stress at the critical state both increase with increasing confining stress.

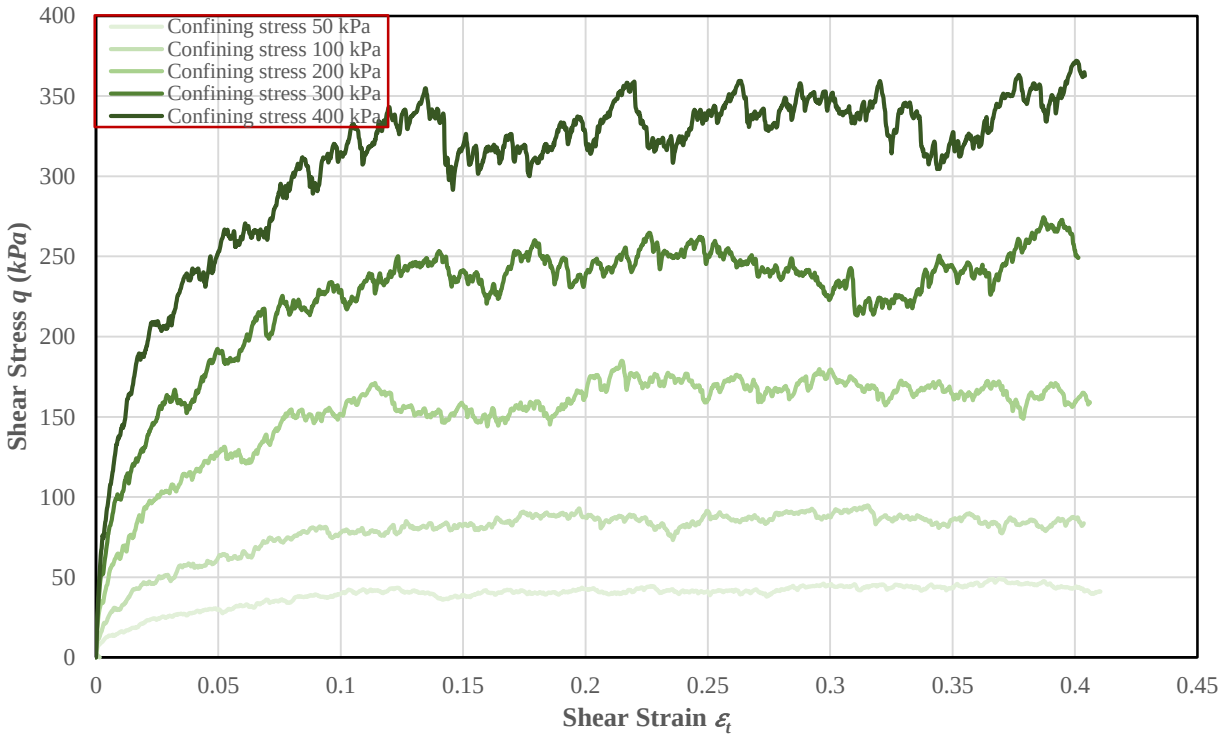

Figure 6.9 Drained stress-strain responses for assemblies with different confining stresses

Volumetric strain variations

Fig. 6.10 shows the volumetric strain variations for the five samples with respect to the development of shear strain. It can be seen from the figure that all five samples exhibit a contraction from the beginning of shearing until the critical state due to the high initial void ratios. The overall volumetric strain responses for all five samples are similar. Initially the volumetric strain decreases rapidly then levels off at an

intermediate strain. Further shearing results in a bit volumetric strain increase until at about 30% it becomes stable as the critical state is reached.

The effect of the confining stress on the volumetric strain variations is exhibited in an increase in the initial rate of increase and in the maximum value of the volumetric strain. The increase in the confining stress from D1 to D5 result in lower initial rate of increase of the volumetric strain. However, this pattern is not strictly exhibited in Fig. 6.10 because the initial void ratios of the five samples are not exactly the same but decrease a bit with higher confining stress from D1 to D5. Therefore, some irregularities are exhibited.

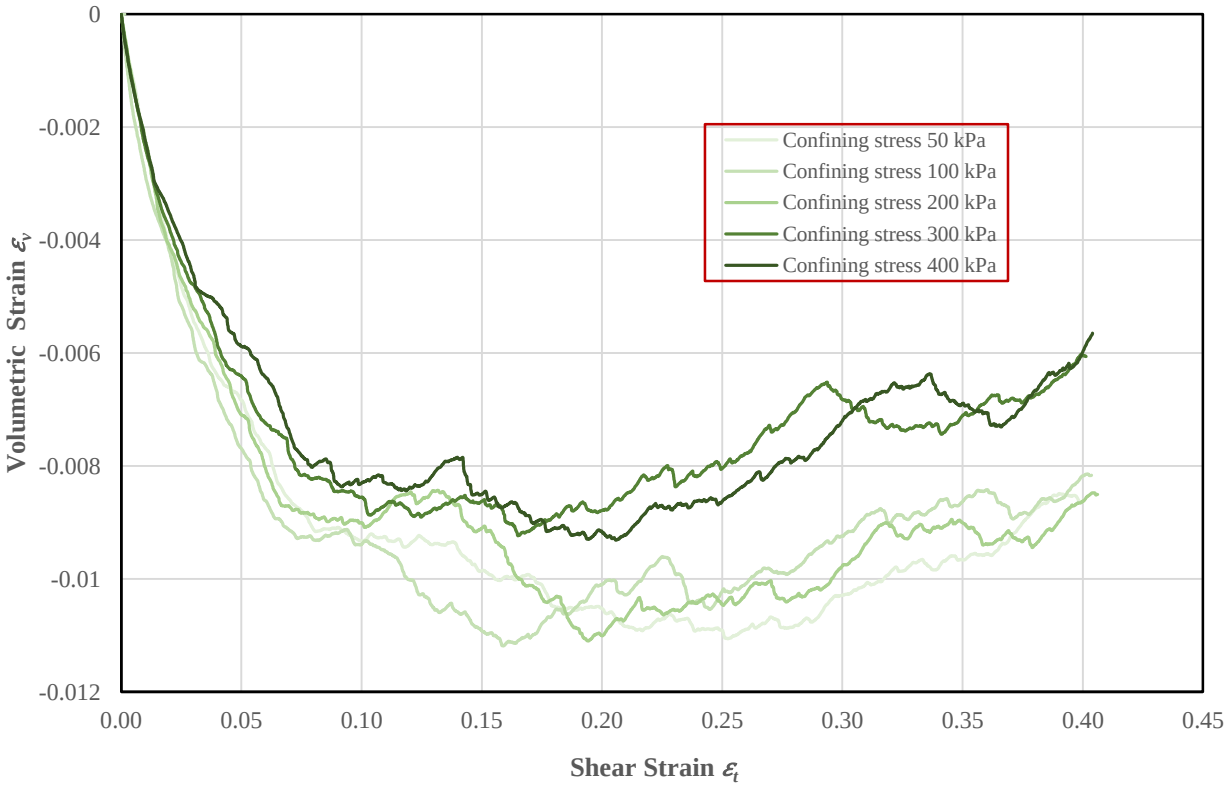

Figure 6.10 Drained volumetric strain changes for assemblies with different confining stresses

Stress path behaviors

The stress path variations for all the five samples shown in Fig. 6.11 are very similar. Although starting from different values due to different confining stresses were applied, they all increase linearly with the same slope of 2 as expected. The shear stress of all five samples increases with increasing mean effective stress. The impact of different confining stress is with the increase of mean effective stress from sample D1 to D5, the maximum shear stress on the corresponding stress path grows proportionately, which is also evident in Fig. 6.9.

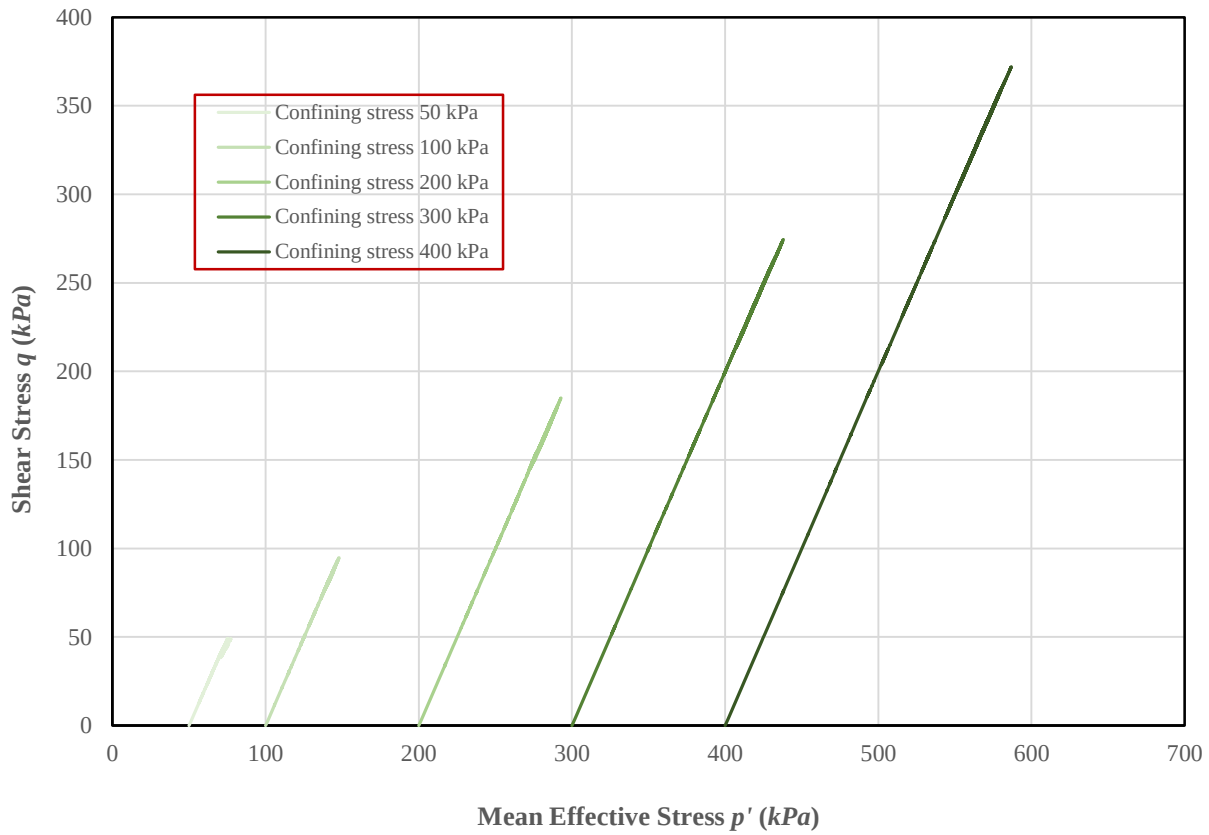

Figure 6.11 Drained stress paths changes for assemblies with different confining stresses

Void ratio variations

The void ratio variations of the five samples under shearing are very similar too. They all display contraction due to their initial high void ratios. The initial rate decrease of void ratio for all five samples shown in Fig. 6.12 are similar although they start from different initial void ratios. After the initial shearing, the rate of decrease of void ratio for all samples slowly reduces to zero at an intermediate strain range and then increase a bit before the curve becomes flat at the critical state. From Fig. 6.12, the effect of the confining stress on the void ratio variations are not obvious, this is because the initial void ratios are not exactly the same among the five samples although they are close to each other. Since the different confining stresses from samples D1 to D5 are achieved by increasing the confining stress from that of the same original sample, with the growth of the applied target confining stresses, the void ratios decrease accordingly. Therefore, the state parameters of these samples are close to each other leading to very similar void ratio responses.

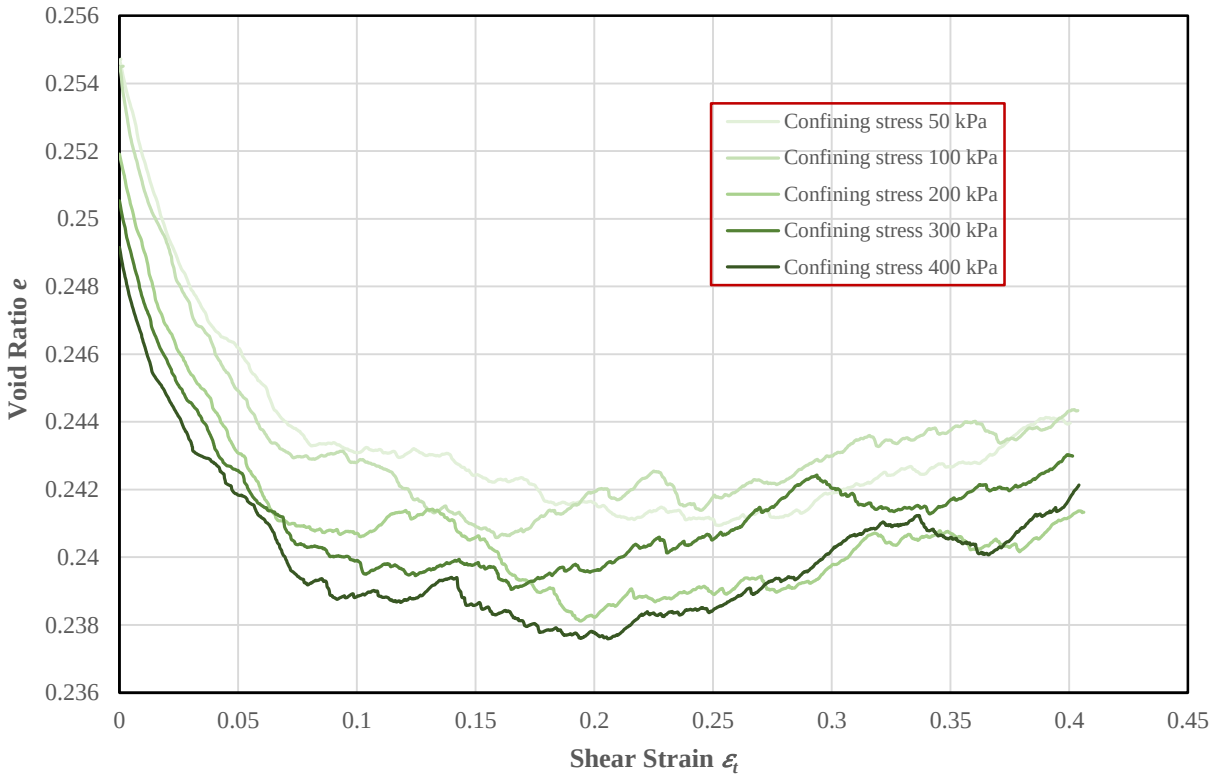

Figure 6.12 Drained void ratio variations of assemblies with different confining stresses

Comments

Comparing the drained behavior of the five samples shown in Figs. 6.9 to 6.12, it can be seen that the overall responses of the stress-strain relationship, the volumetric strain variations, the stress paths, and the void ratio changes for the five samples are all similar, although some specific differences can also be seen. The effect of confining stress on the drained behavior of granular media mainly manifests itself in changes in the initial rate of increase of shear stress and volumetric strain, and the peak and ultimate values of the shear stress, volumetric strain, and void ratio. From D1 to D5, the initial rate of shear stress increase and the peak strength value both increase while the initial rate of volumetric strain increases and the maximum and ultimate values of volumetric strain all decrease. With respect to the void ratio changes, the maximum and ultimate values of void ratio both decrease for the sequence D1 to D5. However, the volumetric strain and void ratio variations are not strictly exhibited in Fig. 6.10 and Fig. 6.12 because the initial void ratios of the five samples are not exactly the same but decrease a bit with higher confining stress from D1 to D5. Therefore, some irregularities are exhibited. With respect to the stress paths, confining stress affects the highest point on the stress paths of the five samples although the slope of them are the same.

Micromechanical behaviors from simulation

Figs. 6.13 to 6.16 present the variation of the micromechanical descriptors of the five samples D1 to D5 during drained shearing. Fig. 6.13 shows the changes of average coordination number γ, Fig. 6.14 displays the number of floaters n_f variations, Fig. 6.15 presents the contact normal anisotropy parameter a_n variations and Fig. 6.16 presents the normal contact force anisotropy parameter a_f changes. Based on the responses of these descriptors throughout the simulations, the impact of the confining stress on the micromechanical behaviors of the five samples are described as follows:

Average coordination number γ

The overall average coordination number γ responses of the five samples shown in Fig. 6.13 are similar although different at an early stage. From 0 to 10% strain, the average coordination number γ in these five tests all increases but with reduced increasing rate from samples D1 to D5. Subsequently, the increasing rate of all five samples slows down and upon reaching the critical state at a large strain fluctuates around the critical state value until the end of shearing. Hence, the effect of the confining stress on the average coordination number γ mainly lies in the initial increasing rate of γ, with the increase of confining stress from samples D1 to D5, the growth of γ in the early state decreases .

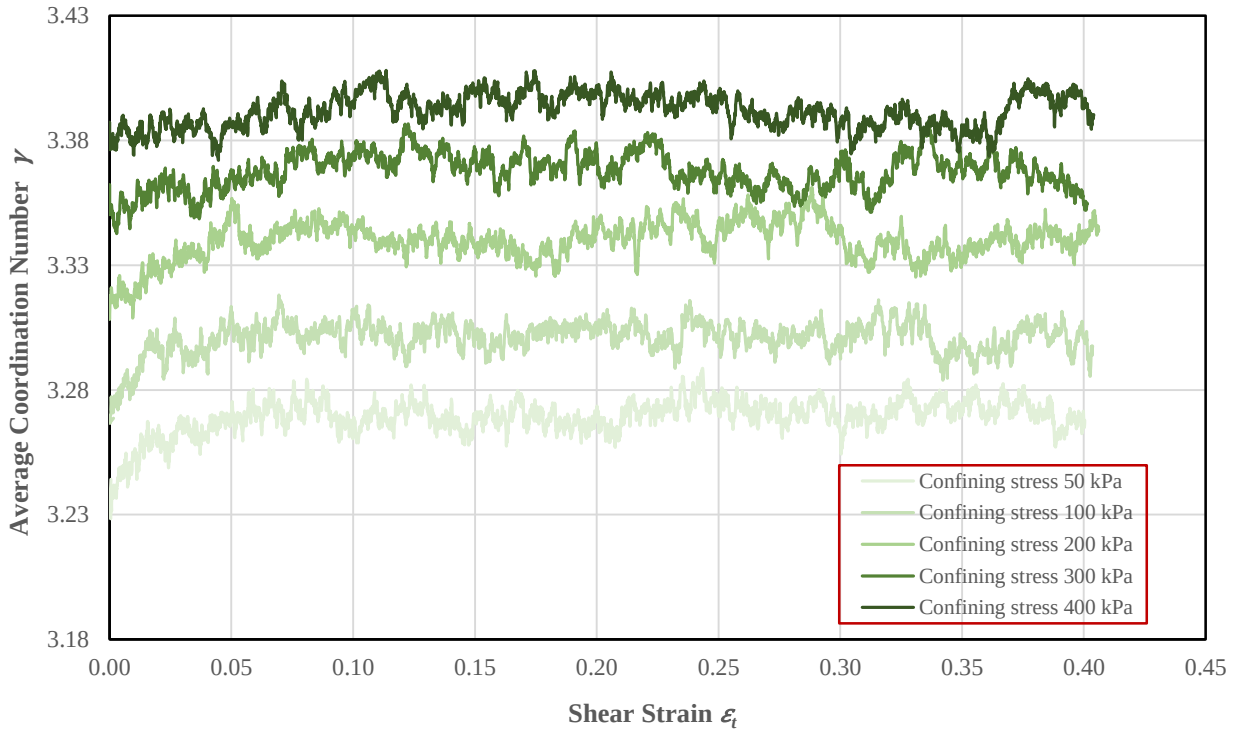

Figure 6.13 Average coordination number γ changes of assemblies with different confining stresses

Number of floaters n_f

Fig. 6.14 shows the variations of n_f for the five samples during shearing. It can be seen from the figure that the n_f values for all five tests are quite close to each other although their initial values are very different. At the beginning of simulations, n_f values from all the tests increase instantly and greatly. Afterwards, it starts to decrease for all samples. The reduction rates for all the samples are initially high and then gradually reduce and then maintain constant values when the samples enter into the critical state. In sequence from samples D1 to D5 (as the confining stress increases), the initial reduction rate decreases, and the overall value of n_f also decreases, although the difference of n_f among the five samples was small.

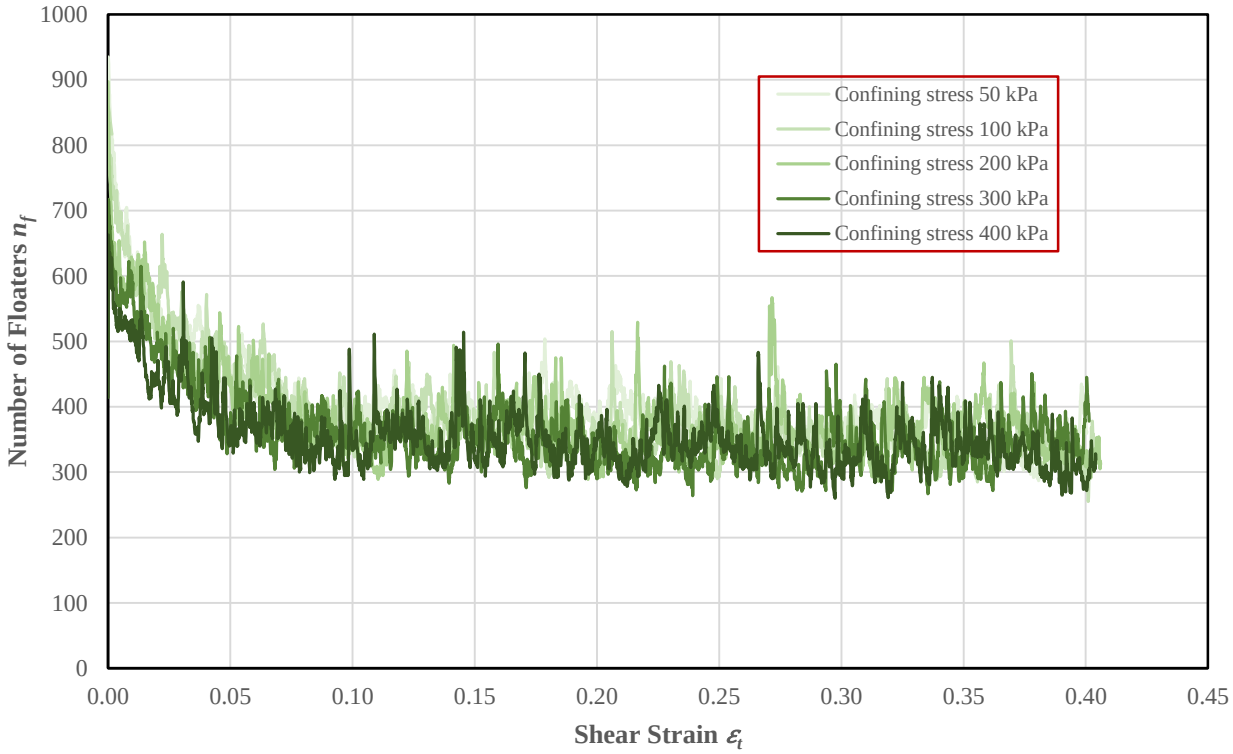

Figure 6.14 Number of floaters n_f variations for assemblies with different confining stresses

Contact normal anisotropy a_n

The contact normal anisotropy parameter a_n curves for all five tests shown in Fig. 6.15 are very close to each other, although it is somewhat higher for the samples with lower confining stresses. The initial rapid creation of the contact normal anisotropy is conspicuous for all the five samples, which is associated with the abrupt drop of n_f shown in Fig. 6.14 indicating that a large amount of contact creation occurred in the vertical direction for all the tests. Although the initial increase rate of γ and the initial reduction rate of n_f

for all five samples are different, however, the different confining stresses counterbalanced this effect and thereby resulted in very similar a_n responses for all the five samples. Specifically, γ increases in tests D1 to D3 as a large number of vertical contacts are constructed by making connections with the floaters, leading to a rapid increase of a_n. In tests D4 and D5, although less vertical contacts are constructed through the connections with floaters compared to those in tests D1 to D3, however, due to the higher confining stresses applied in these tests, there are more contacts lost in the horizontal direction which is consistent with the much smaller increase of γ for samples D4 and D5 shown in Fig. 6.13. The result is that overall a_n responses very close to each other for all five samples.

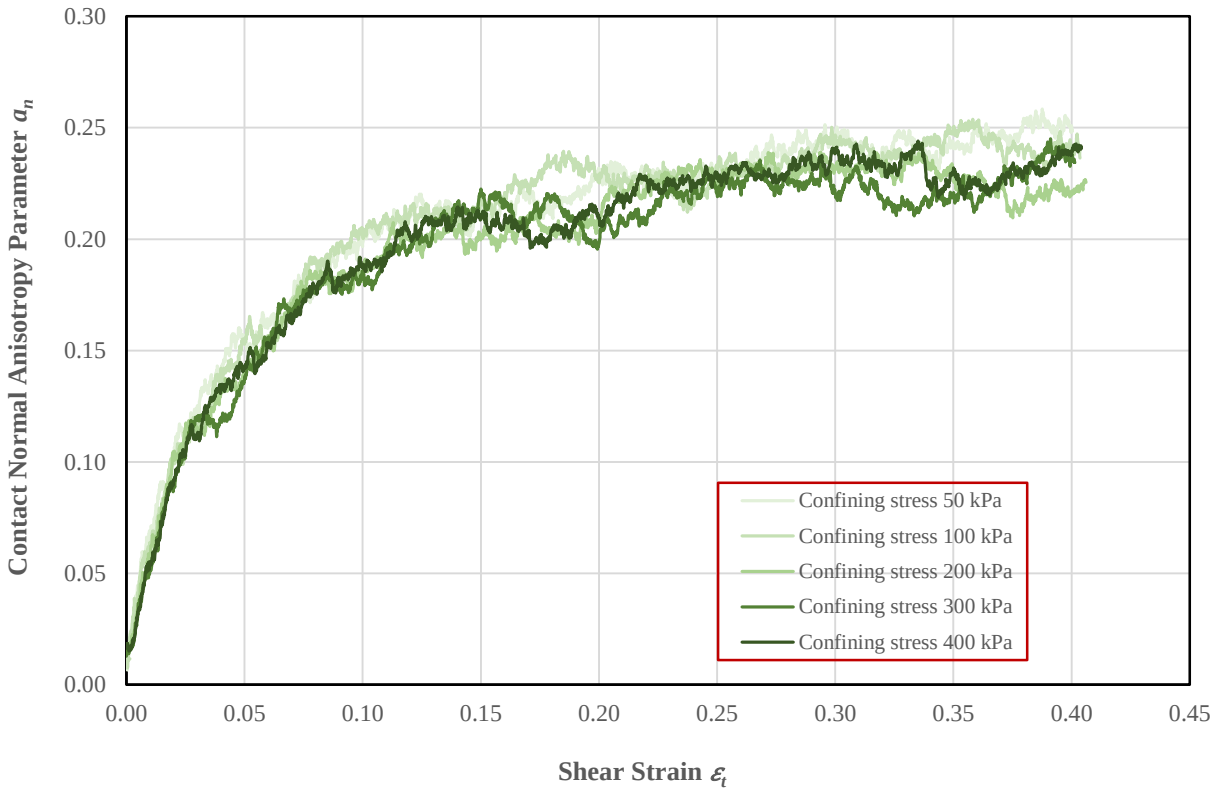

Figure 6.15 Contact normal anisotropy parameter a_n variations for assemblies with different confining stresses

Normal contact force anisotropy parameter a_f

Similar to the response of a_n for the five samples shown in the above, the curves for the normal contact force anisotropy parameter a_f from all five tests are also very similar due to the similar counterbalancing effect of γ, n_f, and the confining stress. For the same reason, γ increases in tests D1 to D3 due to the large number of normal contact forces that are created vertically through connections made with the floaters, therefore resulting in a rapid increase of a_f. In tests D4 and D5, although there is less normal contact force creation in the vertical direction from the floater effect than in tests D1 to D3, however, due to the higher

confining stresses that are applied in tests D4 and D5, more normal contact force is lost in the horizontal direction. Therefore, the overall values of a_f are about the same for the five samples.

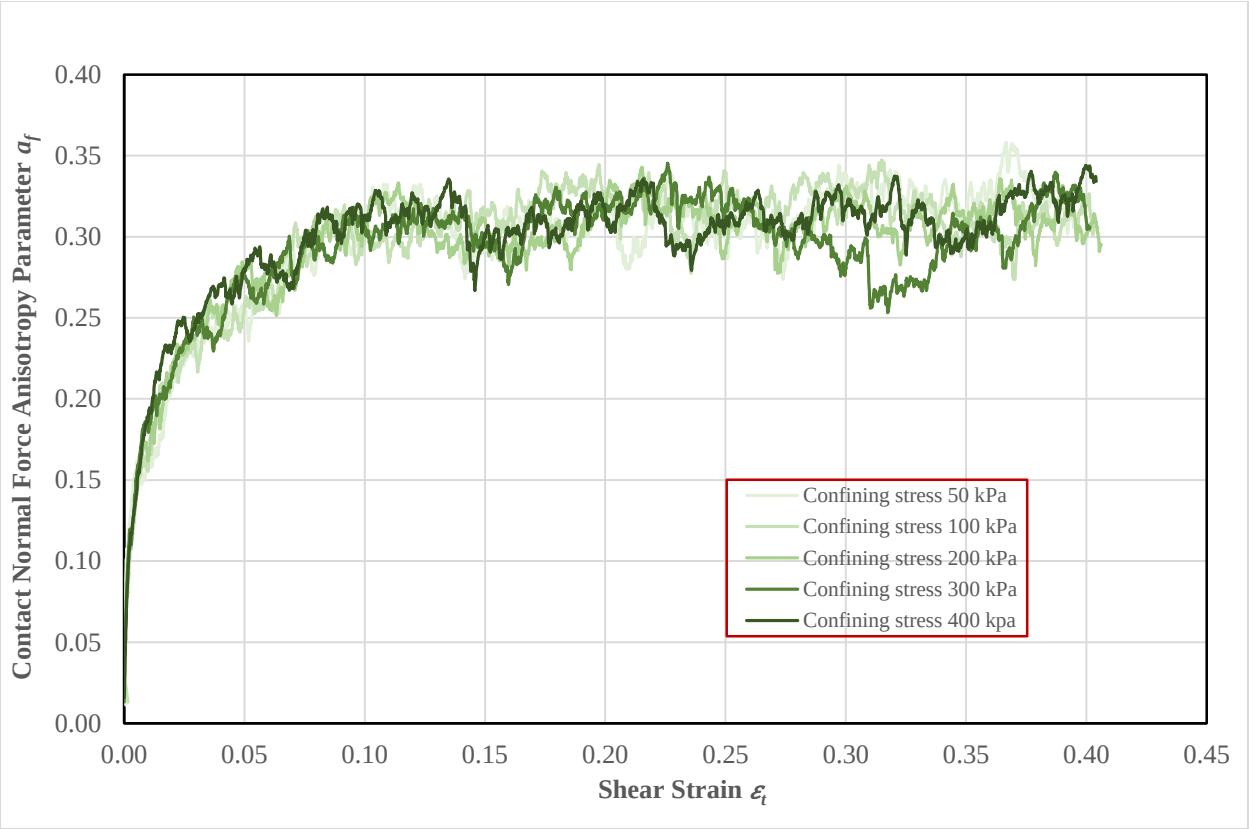

Figure 6.16 Normal contact force anisotropy parameter a_f for assemblies with different confining stresses

Comments

Comparing the variations of the micromechanical descriptors of the five samples shown in Figs. 6.13 to 6.16, it can be seen that all five samples exhibit similar overall responses with some differences due to the different confining stresses applied. In general, the impact of the confining stress on the average coordination number γ mainly lies in the initial increasing rate, while the impact of the confining stress on the number of floaters n_f is primarily the initial reduction rate and the overall value. Specifically, with the increase of confining stresses from sample D1 to D5, the growth of γ in the early state decreases, and the initial reduction rate and the overall value of n_f also both decrease, although the difference of n_f among the five samples was small. Different from the variations of γ and n_f, plots of a_n and a_f for all five samples almost merge through out the tests due to the counterbalancing effects of γ, n_f, and the confining stress. Therefore, the confining stress effect on a_n and a_f in these series of tests are not obvious since the initial void ratio and the number of floaters for the five samples are not exactly the same.

6.3 Undrained simulations to the steady states

6.3.1 Summary of the test program

To construct a steady state line for the granular assemblies adopted in this research, a series of undrained simulations sheared to the steady state are needed. Since the void ratio of the granular assembly does not change during the undrained simulation, a small number of simulations with different initial void ratios can be performed to construct a steady state line. Following this idea, in addition to the undrained simulations already presented in Chapter 4, a group of seven simulation tests (U1, U2, U3, U4, U5, U6, and U7) are designed to supplement the void ratio range for the formation of the steady state line. All the seven samples were prepared based on the loose sample A in section 4.3.1, but the void ratios were decreased through increasing the confining stress to different levels using mode 1. After bringing the samples to their target level of void ratios, their associated confining stresses are recorded. Subsequently, the assemblies are brought into an equilibrium state for the following undrained simulations. The initial physical properties for the seven samples are shown as Table 6.2.

Table 6.2 Summary of initial physical properties of the tests

Test	**Sample**	**No. of floaters** (n_f)	**Initial average coordination number (γ)**	**Void ratio (*e*)**	**Confining stress (*kPa*)** (σ_1)
U1	**U1**	783	3.3296	0.2825	350
U2	**U2**	673	3.4023	0.2789	650
U3	**U3**	564	3.4740	0.2746	1000
U4	**U4**	284	3.5740	0.2613	1700
U5	**U5**	171	3.6535	0.2523	2500
U6	**U6**	132	3.7087	0.2454	3100
U7	**U7**	133	3.8301	0.2348	4900

Similar to the undrained biaxial compression simulations conducted in chapter 4, the simulations in this section for the above samples were also conducted using mode 3, which maintains the average stress σ_{11} constant, and meanwhile, increases the average stress σ_{22} by applying a constant strain rate $\dot{\epsilon}_{22}^{\beta}$ (at the boundary). The associated physical properties of the disc particles and the fluid applied in the simulations also follow those of Tables 4.1 and 4.2 in section 4.2.1. And the parameters for the biaxial compression

simulations such as damping effect, time step and vertical strain rate follow the values already shown in Table 4.4.

6.3.2 Simulations results

Since different initial void ratios of samples U1 to U7 were prepared through increasing the confining stress from the very loose sample A in section 4.3.1, they are in essence the same as preparing the samples with different confining stresses. Hence, it can be expected that the effect of confining stresses on the associated undrained responses will be similar to those already reported in section 4.3.2. Therefore, to avoid repetition, the undrained behaviors of samples U1 to U7 will not be interpreted in this section. The specific undrained simulation results for these seven samples are presented in Appendix B.

6.4 Consistency of the critical state line and the steady state line

6.4.1 Comparison of the critical state line and the steady state line in terms of void ratio versus mean effective stress

Based on the drained and undrained simulations performed in the above sections, a critical state line from drained simulations and a steady state line from undrained simulations were constructed. Fig. 6.17 presents a comparison of the critical state line and the steady state line in terms of the relationship between void ratio e and the logarithm of the mean effective stress p'. All the critical state points and the steady state points shown in the figure are selected at large strain from each test where the whole assembly comes into a stable state and almost all descriptors stop changing. Since grain crushing may occur at high confining stress, only mean effective stresses that are less than 3000 kPa are considered. Besides, due to the difficulty of conducting drained test under very low confining pressures, only mean effective stresses that were greater than 75 kPa were included in the drained simulations.

It can be seen from Fig. 6.17 that at the same mean effective stress level, the void ratios at the steady state from undrained simulations are in general somewhat higher than those of the critical states from the drained simulations. Both the critical state line obtained by connecting each critical state point and the steady state line obtained by connecting each steady state point have shallow slopes. A representation of the comparison of the critical state line and the steady state line from the drain and undrained monotonic triaxial compression tests on an Erksak sand that was reported by Been, Jefferies and Hachey in 1991 is shown in Fig. 6.18 (Been et al., 1991). It can be seen from the figure that the critical state and the steady state data from the drained and undrained tests at comparable mean effective stress levels are quite close to each other, although some of the critical state points shown in the figure are below the steady state points at the same mean effective stress. However, it was stated by Been et al. that some of the dense samples were still dilating at the end of the tests and that shear localization also occurred. Therefore, from both the simulation and the

laboratory results, it is reasonable to assume that the critical state line and steady state line are almost the same in terms of void ratio versus mean effective stress relationship, although they are not exactly the same. The steady state line has a somewhat higher slope than the critical state line in terms of void ratio versus mean effective stress in general.

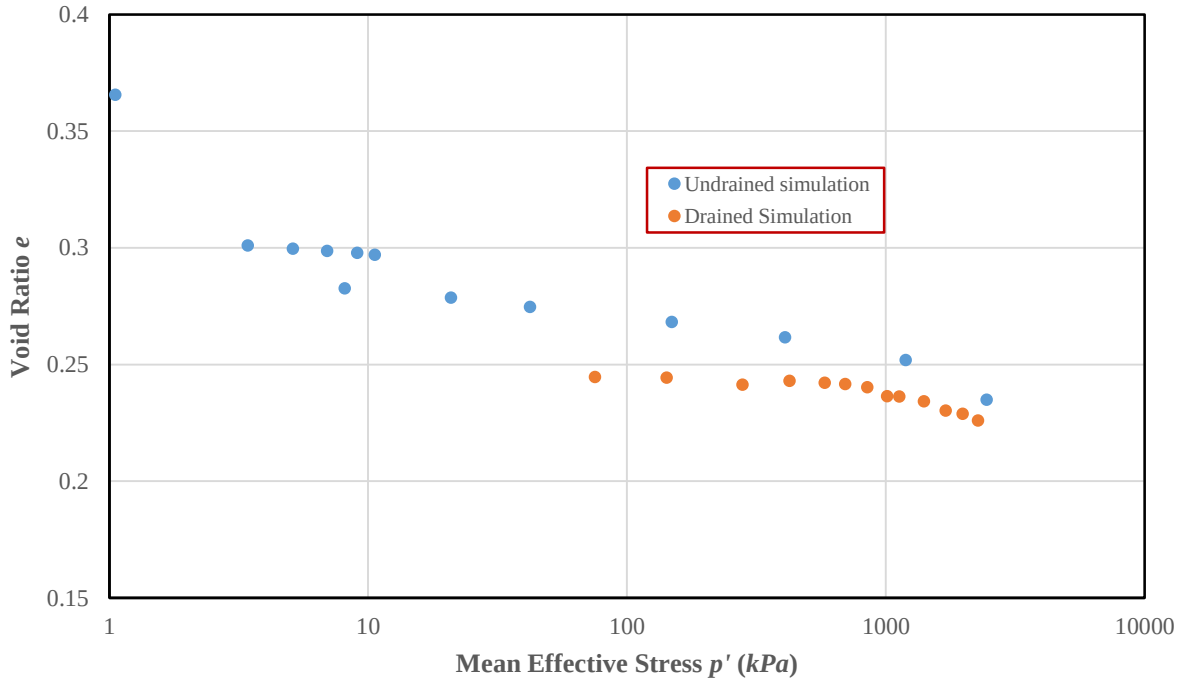

Figure 6.17 Comparison of the critical state from drained simulations and the steady state from undrained simulations in terms of the void ratio

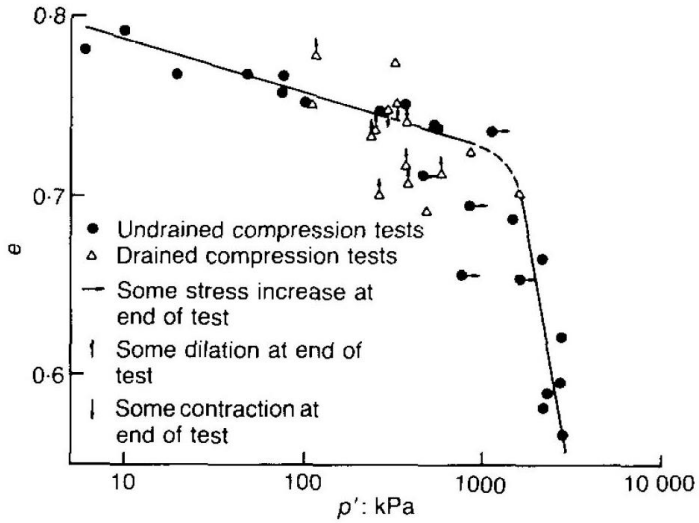

Figure 6.18 Comparison of the critical state from drained tests and the steady state from undrained tests (Been et al., 1991)

6.4.2 Consistency of the critical state line and the steady state line in terms of the average coordination number versus mean effective stress

Due to the fact that the void ratio and the average coordination number are correlated (Athanasiou-Grivas and Harr, 1980; Smith et al., 1929), and both of them vary with the density of a sample, a comparison was made between the critical state line and the steady state line in terms of the average coordination number γ versus the mean effective stress as shown in Fig. 6.19. Data for the critical state and the steady state are selected at the same points as the data of Fig. 6.17 but here they are represented by the average coordination number γ instead of the void ratio. Again the mean effective stress range of 75 kPa to 3000 kPa is selected for conducting the comparisons to avoid the grain crushing effect that may occur at high confining stresses during consolidation and shearing, and the difficulty of conducting drained testing under low confining stresses.

It can be seen from Fig. 6.19 that in the comparison range used, the critical state points and the steady state points in terms of the average coordination number γ versus mean effective stress almost merge into one unified linear curve. The differences between the critical state line and steady state line shown in Fig. 6.19, are much smaller than when the data were plotted in terms of void ratio versus the mean effective stress.

The reason that the average coordination number γ indicates a greater consistency of the critical state line and the steady state line than that obtained by using the void ratio may be understood from the definitions of the two variables. Although both of them can indicate the denseness of a given sample of granular material, the void ratio describes the overall volume of voids to that of the total volume of the particles, whereas the average coordination number γ describes the compactness of the particles. So the former can describe how much space that the voids occupy in a sample, which depends on both the voids and the particles, while the latter describes the intensity and denseness of particle packing which only depends on the particles themselves. Since the critical state and the steady state are the states that a granular media exhibits at an ultimate condition, they are properties that should only be related to the granular material type itself. Therefore, if the critical state line and the steady state line are the same for a given granular media, the average coordination number γ should give better consistency since it comes purely from the consideration of the particles. Besides, in an undrained testing, the void ratio does not change throughout the test due to the constraint of the fluid from flowing outside the sample, which is a prescribed boundary condition that cannot vary depending on the extent of shearing. In contrast, the average coordination number in an undrained test can change with shearing and represent the stableness of the system, therefore, it can indicate the shearing condition at the steady state more precisely.

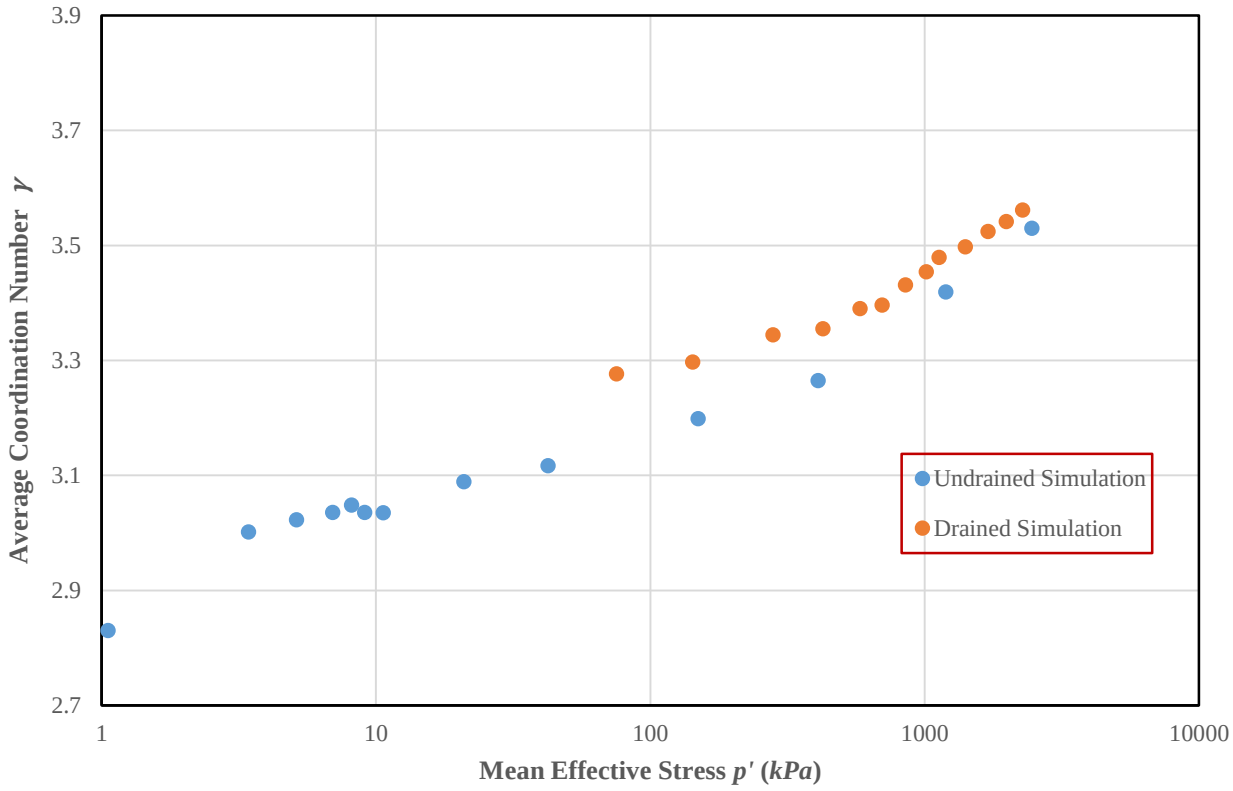

Figure 6.19 Comparison of the critical state from drained simulations and the steady state from undrained simulations in terms of the average coordination numbers γ

Chapter 7 Conclusions and Recommendations

7.1 General

In this study, a further developed version of the fluid-coupled DEM model that was first proposed by Olivera in 2004 was developed to simulate the undrained behavior of a two-dimensional granular media and interpret its behavior using micromechanical descriptors. The key modification relates to the development of a robust pore identification mechanism that can handle rapid changes in pore structure due to creation and disintegration of inter-granular contacts. The algorithm keeps track of "pore groups" where some voids may coalesce due to contact disintegration while other voids are subdivided into parts due to contact creation. More common is an extremely complex modification of pore space when both coalescence and subdivision of voids takes place affecting a group of voids simultaneously.

Using this "pore groups" idea incorporated by a fluid-coupled DEM scheme, an undrained biaxial compression simulation of a large circular assembly made up of l0000 disc particles was performed under different initial conditions. The simulation yielded reasonable results and showed undrained behavior similar to that of laboratory tests. A qualitative comparison of the simulated results with physical data from laboratory tests showed a high level of similarity. Based on the variations of the micromechanical descriptors extracted from the simulation, a micromechanical study of the undrained behaviors of granular media under different initial conditions was conducted. An analysis of the granular media undrained behaviors from the micromechanical framework was performed.

Using the successful simulation of the undrained behavior of a granular media obtained from the proposed further developed fluid-coupled DEM scheme, a study of the mechanism of liquefaction formation from both classical soil mechanics and micromechanics perspectives was conducted using a very loose assembly of a granular media. To depict and visualize the liquefaction formation mechanism, disc particles were combined with a particular assembly creation method that resembles the moist tamping method of sample preparation in traditional laboratory testing to model the occurrence of liquefaction. It is believed that, the methodology proposed in this research will also apply to elliptical particles with different values of eccentricity. Through the simulations conducted on a very loose sample, factors that affect the occurrence of liquefaction were analyzed and studied. Particularly, the influence of permeability on the liquefaction susceptibility was studied by using five different values of conduit pipe diameter. The results demonstrated that the permeability affects the peak and residual strengths to a very large extent.

With respect to the ultimate state, a comparison of the critical state line from drained simulation tests and the steady state line from undrained simulation tests was performed by using both the void ratio versus the mean effective stress relationship and by using the newly proposed average coordination number versus the mean effective stress relationship. The results indicate that compare to the void ratio, the average

coordination number can describe the granular media's property at the ultimate state more effectively due to its representation of the overall denseness.

The following sections highlight specific conclusions and recommendations derived from this thesis, and some suggested future work. Section 7.2 gives the conclusions drawn from this thesis, section 7.3 includes recommendations and some proposed future work.

7.2 Conclusions

7.2.1 Pore pressure evolution scheme

In the methodology of this thesis, the main idea is to compute the contact interactions between each pair of neighboring particles, and couple the fluid flow effects with nearby particles in the deformation of an assembly. This follows closely from the approach proposed by Olivera in 2004. The computations of the individual pore pressures are accomplished through detecting each pore's volumetric strain from each step. This combined with the bulk modulus of the water yields updated individual pore pressures. However, to successfully simulate the undrained behavior, especially the liquefaction behavior of a granular media, an effective scheme to describe pores evolution is essential. This is because the individual pores are changing all the time and are frequently separated into or combined with other pores rapidly due to the movement of particles. More common is an extremely complex modification of pore space when both coalescence and subdivision of voids takes place affecting a group of voids simultaneously. The proposed method keeps track of "pore groups", which groups related neighbour pores before and after contact creation or disintegration in each successive step successfully solved this problem. This resulted in a robust pore identification mechanism and an accurate computation of the pore pressure forces on the ambient particles.

The idea of "pore groups" is also very effective in correctly computing the pore pressures when the phenomenon of local liquefaction occurs. Since the local liquefaction usually results in a few particles floating inside the pores, when computing pore pressure effect of these pores, the volume of these particles are deducted from their outside pores directly so that a comparison of these newly formed pores' volume and the pore group's volume in the previous step can be achieved. Consequently, a correctly converted pore pressure force from the pores onto the involved ambient particles results.

7.2.2 Comparison study on the fluid-coupled DEM model with behavior of a poroelastic configuration

In order to evaluate the effectiveness of the proposed further developed fluid flow scheme, a comparison study was conducted on a rectangular assembly of 10000 disc particles. Two simulation tests, a pore pressure equalization test and a pore pressure dissipation test were performed on the assembly. The particles

movements are restricted in these two tests to examine the pore pressure dissipation among the pore system. From this comparison study, two main results related to the pore pressure dissipation were obtained:

- In the pore pressure equalization testing, the initial assigned pore pressures of the six selected pores were very different at the beginning of the test, but all tended to merge together after 1 second. The pore pressure changes for all the six pores were rapid at the beginning of the tests, and then gradually slowed down to almost zero by the end of the tests. The ultimate pore pressure for all pores was about 25 kPa. So the proposed fluid flow scheme can be taken as effective.
- For the pore pressure dissipation test, a comparison of the simulated pore pressure variations with those obtained from an analytical solution of Terzaghi's classical one-dimensional consolidation theory at selected cycles was studied. From the comparison, the simulated pore pressures at different heights of the assembly perfectly matched those derived from the analytical solution at the same height. Therefore, the proposed fluid flow scheme can be taken as effective.

7.2.3 Undrained simulation results

In chapter 4, a series of undrained biaxial compression simulations under different initial conditions were conducted and compared with those derived by using the constant volume method. The assemblies with different initial void ratios that were used to conduct the simulations were generated through a special process, which combines the alternation between cyclic and compacted mode of the assembly, and a floater removing scheme after the completion of all alternation actions. The reason for adopting this technique to generate the samples is that assemblies created by this method results in a structure of aggregates and macropores, which resembles the samples prepared by using the moist tamping technique. A qualitative comparison of the simulated results with physical data from the literature showed a very high level of similarity. The conclusions from these simulations are listed as follows:

- Under the same confining stress, the initial void ratio controls the undrained behavior of the granular assembly. The lower the initial void ratio, the less likely is the occurrence of liquefaction, and the more likely is strain hardening. In terms of the micromechanical behavior, the initial number of floaters affects the undrained behavior of the granular system greatly. The higher the number of floaters in the pores, the more stable will be the assembly. For the samples that exhibited liquefaction, contacts were mainly disintegrated in the horizontal direction in the initial shearing stage, which then turned into disintegrate in both directions corresponding to the strain softening stage. In these samples, a reduction of the average coordination number and an increase of the number of floaters were characteristically displayed accompanied by the generation of the pore pressure until the steady state was reached, and both reached their ultimate values.

- When the initial void ratios of the assemblies are the same (i.e. the same loose sample which can trigger liquefaction) but the confining stresses are increased, their undrained behaviors are characterised by corresponding increases in the values of the peak strength combined with higher pore pressure generation rates, although their residual shear strengths were very close to each other. The simulated micromechanical behaviors show that the initial number of floaters in the assembly affects the durations of the peak shear strength. The higher the number of floaters, the longer is the duration of the peak shear strength. A higher confining stress also induces a higher rate decrease of the initial average coordination number and a lower rate of the construction of initial anisotropy. During initial shearing, contacts are lost in both directions due to a rapid pore pressure generation, rather than the predominant loss of connections in the horizontal direction when the confining stress is low. Therefore, under the same initial void ratios, the confining stresses determine the undrained behavior of the granular assembly.
- A comparison of the results of undrained simulations on the samples with different initial void ratios by using the fluid-coupled DEM and using the constant volume method demonstrates that the two methods yield similar undrained responses for dense and very dense samples until an intermediate strain range, however, they resulted in very different behaviors when the simulated material was loose. The constant volume method yielded a much lower peak strength than that obtained by using the fluid-coupled DEM scheme. With regards to the micromechanical response, applying the fluid-coupled DEM to the very loose sample yields a faster reduction of the average coordination number and a more rapid growth of the number of floaters accompanied with a higher rate of construction of the contact normal anisotropy and normal contact force anisotropy. All of these behaviors were absent in the simulations that used the constant volume method because it failed to capture the pore pressure contribution to breaking the contacts in the horizontal direction in the early part of a test and to breaking contacts in both directions at a later stage in the test. Therefore, the constant volume method may be capable of simulating the undrained response of a very dense sample up to an intermediate strain range, but it should not be used for the loose samples.

7.2.4 Effects of permeability

A study of the effect of permeability on liquefaction susceptibility was performed in this research. Five undrained simulation tests were conducted using exactly the same liquefiable samples under the same confining stress but different conduit diameters representing different values of permeabilities. The results indicate that the permeability affects the undrained behaviors of the liquefiable granular assembly significantly, especially the peak and residual strength values and the pore pressure generation rate. Some of the simulation results are given in the following:

- The mechanical undrained behaviors affected by the decreasing values of permeability are mainly manifested as: a higher peak strength value accompanied by a faster pore pressure generation rate upon initial shearing, a slower strain softening process accompanied by a reduced rate of increase in pore pressure in the medium strain range, and a higher residual strength accompanied by a lower maximum pore pressure if the applied permeability is low enough. These behaviors are due to the much lower pore pressure dissipation rate from the reduced permeability. If the permeability is low enough, strain hardening can be seen in the early stages of shearing accompanied by the tendency to dilation of the assembly which results from the restriction of the pore pressure dissipation among the pores due to the very low permeability. Strain hardening is transformed into strain softening with continuing shearing due to the very slow pore pressure dissipation process but the resulting residual strength is still higher than samples with higher permeabilities.
- Micromechanically, all the five tests exhibit a similar liquefaction pattern in terms of the overall contact variations. They all display the occurrence of vertical contact creation and horizontal contact disintegration in the initial shearing stage, which subsequently turns into contact disintegrations in both directions in the following strain softening stage. At the steady state, the contact creation and disintegration come into a balance indicating the steady state is achieved. The differences in the undrained micromechanical responses among the five tests with decreasing permeabilities are mainly the rate of horizontal contact loss during initial shearing and the rate and duration of contact loss in the intermediate strain range corresponding to strain softening. The initial contacts lost in the horizontal direction increase with a lower permeability due to a faster pore pressure generation and a reduced the pore pressure dissipation among the pores. While in the intermediate strain range, a lower coordination number, a higher number of floaters, and a higher contact normal anisotropy parameter are induced when the permeability is lower because the pore pressure dissipation takes longer time and the pore pressure has time to break more contacts in both directions.
- In samples of high permeability, pore pressures do not vary significantly from one void to another. On the other hand, in samples of low permeability, the variation of pore pressure from void to void is much greater. Pore pressure in some voids is negative, resulting in high local strength. Areas of negative pore pressures effectively “strengthen” the sample and lead to higher macroscopic strength.
- A very low permeability can induce the formation of non-uniform fluid flow paths and incomplete liquefaction upon shearing, which leads to a locally higher permeability and allows a higher amount of fluid to pass between pores. Thus, the non-uniform fluid paths help reduce the number of contacts

lost in both directions in the strain softening stage, and thereby lead to a higher residual strength at the steady state.

- A higher permeability provides better connections of fluids between the pores, so that there is less initial loss of contact and less occurrences of liquefaction in the coarse grained soil. When the permeability is very low, the non-uniform fluid paths and incomplete liquefaction are triggered, which explains why soils with small grains are less liquefiable than those of medium grain sizes.
- When the permeability is relatively high (in coarse sand range), the mechanical undrained behaviors of two granular assemblies with two different high permeabilities may be close to each other, however, their micromechanical behaviors can be very different.

7.2.5 Comparison of the critical state line and the steady state line

A comparison between the critical state line and the steady state line is carried out in this research. The critical state line and the steady state line that are frequently used in classical soil mechanics are employed to perform the comparison in the macroscopic scale. Both of them are expressed in terms of the relationship between the void ratio and the mean effective stress. Since the average coordination number is a parameter from micromechanics which not only indicates the denseness of the samples but also reflects particles' structure and compactness, it is employed accompanied with the mean effective stress in this research to represent the critical state line and the steady state line and perform the comparison of the two lines in the microscopic scale. Based on the comparison of the critical state line and the steady state line using the relationships between the void ratio and the mean effective stress and also between the average coordination number and the mean effective stress, the following two main conclusions can be drawn:

- The critical state and the steady state, both of which are the ultimate states of a granular media under shearing are almost consistent when described by the critical state line and the steady state line. Both void ratio and the average coordination number from the two states converge together with somewhat variations when plotted with respect to the mean effective stress.
- Compared to the plots obtained by using the void ratio versus the mean effective stress, the plots of the average coordination number versus the mean effective stress show a greater consistency of the critical state line and the steady state line. This can be explained by the different definitions of the two variables. The former describes the overall volume ratio of total voids to total particles which depends on both the particles and the voids, whereas the latter describes the compactness of the particles which only depends on the particles themselves. Therefore, the average coordination number gives a better consistency since it comes purely from a consideration of the particles. In addition, unlike the average coordination number, the void ratio does not change throughout an undrained test due to the constraint of the fluid from flowing outside of the sample, so it is a

prescribed boundary condition that cannot vary according to the specific shearing condition. However, the average coordination number can change anytime with shearing and represents the stability of the system, therefore, it can indicate the shearing condition at the steady state more precisely.

- There appears to be no distinction in values of induced asymptotic anisotropy in drained and undrained conditions, however, this topic requires further studies.

7.3 Recommendations and future work

Based on the study of the proposed further developed fluid-coupled DEM and the micromechanical study of the undrained behavior of the granular media, some recommendations for future study are put forward in the following.

- *Model improvement and computational efficiency*

  The further developed fluid-coupled DEM model that currently used detects the contacts between neighbouring particles and computes the pore pressure for each pore, and then calculates the weighted average pore pressure as a representation of macroscopic pore pressure using each pore's volume as a weight. Although the fluid flow scheme has been shown as very effective and the results from the undrained simulations are close to the physical data from the laboratory test, the computational requirement of this method on a large assembly is strenuous. Thus, in addition to a parallel algorithm that may be applied to help save computational time, other methods such as the one proposed by (Nakase et al., 1999), which considers square cells to compute the volume change, might be modified for use with the proposed further developed fluid-coupled DEM to save computing time.

- *Three dimensional model*

  The proposed further developed fluid-coupled DEM model in this research has been shown as very effective in simulating the undrained behavior of a two-dimensional granular assembly. The fluid flow scheme should be equally effective in a three dimensional condition, just the flow network system is more complex. Therefore, the proposed model should be able to be extended to a three-dimensional case to depict the micromechanical undrained behavior of the granular media in a more practical perspective.

- *Induced asymptotic in drained and undrained conditions*

  The values of induced asymptotic in drained and undrained simulations obtained in this research do not show much difference. However, to verify that there is no distinction between them requires additional tests using different samples under different initial conditions. Particularly, samples prepared using different methods are necessary. This study will be conducted in the future work.

- *The phenomenon of quasi-steady state*

  The granular assembly samples adopted in chapter 4 to study the effect of initial void ratios onto the undrained behaviors are obtained by a particular floater removing scheme. The different initial void ratios of the samples are achieved by removing a certain amount of floaters each time to guarantee the stability and the isotropy of the assembly. The two samples that exhibited the phenomenon of strain softening were obtained by removing two and all the floaters from each pore respectively, while the two samples displayed the phenomenon of strain hardening were obtained by removing one and no floaters from each pore. Although the phenomenon of the quasi-steady state is captured in the simulations of a loose assembly with a very high permeability in chapter 5, it is known from classical soil mechanics, that under the same confining stress, the quasi-steady state is usually displayed in a soil sample whose relative density is between the relative densities that can trigger strain softening and strain hardening. Hence, it can be expected that a quasi-steady state can be caught by using the adopted granular assembly but removing a certain amount of floaters. Theoretically, the number of removed floaters should be between the removed floaters that induced the strain softening and the number that induced strain hardening. With addition of an undrained simulation for samples that display a quasi-steady state under shearing, a full picture of liquefaction potential classification in terms of the average coordination and the mean effective stress may be achieved. This study will be conducted in the future work.

- *Under cyclic loading*

  As illustrated in chapter 2, to understand seismically induced liquefaction, two aspects are important: the onset condition and the post-seismic stability (Ishihara, 1993). The latter is controlled by the steady state strength, which has been shown to have a unique value no matter if it is from static or cyclic load (Baki et al., 2012; Castro, 1969; Dobry et al., 1985; Vaid and Chern, 1985; Yang et al., 2009). The current study has shown the mechanism of the static liquefaction through the use of micromechanics descriptors. The former is governed by cyclic strength, which should be studied under cyclic loading conditions. Due to the success of applying the proposed further developed fluid-coupled DEM to the analysis of the static liquefaction, a similar fluid-coupled DEM scheme may be applied to cyclic load conditions by alternating the boundary control between the biaxial compression and tension. Therefore, it should be feasible to examine the micromechanics characteristics of sand's cyclic strength and describe the onset condition of the liquefaction using a fluid-coupled DEM but under cyclic load.

References

Alarcon, A., & Leonards, G. (1988). Discussion of "Liquefaction evaluation procedure" by steve J. poulos, gonzalo castro, and john W. france (june, 1985, vol. 111, no. 6). *Journal of Geotechnical Engineering, 114*(2), 232-236.

Alarcon-Guzman, A., Leonards, G., & Chameau, J. (1988). Undrained monotonic and cyclic strength of sands. *Journal of Geotechnical Engineering, 114*(10), 1089-1109.

Ashmawy, A. K., Hoang, V. V., & Sukumaran, B. (2003). Evaluating the influence of particle shape on liquefaction behavior using discrete element modeling. Paper presented at the Thirteenth International Offshore and Polar Engineering Conference,

Athanasiou-Grivas, D., & Harr, M. E. (1980). Particle contacts in discrete materials. *Journal of Geotechnical and Geoenvironmental Engineering, 106*(ASCE 15433)

Baki, M. A., Rahman, M., Lo, S., & Gnanendran, C. (2012). Linkage between static and cyclic liquefaction of loose sand with a range of fines contents. *Canadian Geotechnical Journal, 49*(8), 891-906.

Bathurst, R. J., & Rothenburg, L. (1988). Note on a random isotropic granular material with negative poisson's ratio. *International Journal of Engineering Science, 26*(4), 373-383.

Bathurst, R. J., & Rothenburg, L. (1990). Observations on stress-force-fabric relationships in idealized granular materials. *Mechanics of Materials, 9*(1), 65-80.

Bathurst, R. J. (1985). A study of stress and anisotropy in idealized granular assemblies. (Ph.D. thesis, University of Waterloo)

Bathurst, R., & Rothenburg, L. (1988). Micromechanical aspects of isotropic granular assemblies with linear contact interactions. *Journal of Applied Mechanics, 55*(1), 17-23.

Been, K., Jefferies, M., & Hachey, J. (1991). The critical state of sands. *Geotechnique, 41*(3), 365-381.

Been, K., & Jefferies, M. G. (1985). A state parameter for sands. *Geotechnique, 35*(2), 99-112.

Benahmed, N., Canou, J., & Dupla, J. (2015). Liquefaction properties and initial structure of a loose sand. Paper presented at the *6th International Conference on Earthquake Geotechnical Engineering*, 1-4.

Biarez, J., Wiendieck, K., (1963). La comparaison qualitative entre l'anisotropie mécanique et l'anisotropie de structure des milieux pulvérulents. *Comptes Rendus de l'Académie des Sciences* 256, 1217-1220.

Bolton, M. (1986). The strength and dilatancy of sands. *Geotechnique, 36*(1), 65-78.

Bonilla, R. R. O. (2004). *Numerical Simulations of Undrained Granular Media* (Ph.D. thesis, University of Waterloo)

Casagrande, A., & Watson, J. (1938). Compaction tests and critical density investigations of cohesionless materials for franklin falls dam, merrimack valley flood control. corps of engineers. *US Army Engineering Office,*

Casagrande, A. (1940). Characteristics of cohesionless soils affecting the stability of slopes and earth fills. *Contributions to Soils Mechanics, 1925-1940,*

Casagrande, A. (1976). Liquefaction and cyclic deformation of sands-a critical review. *Harvard Soil Mechanics Series, Harvard University, Cambridge, Massachusetts.,* (88)

Castro, G. (1969). *Liquefaction of* sands. Ph.D. thesis, Harvard Soil Mechanics Series, No. 81, Harvard University, Cambridge, MA.

Castro, G. (1975). Liquefaction and cyclic mobility of saturated sands. *Journal of the Geotechnical Engineering Division, 101*(6), 551-569.

Castro, G., Enos, J., France, J. W., & Poulos, S. (1982). Liquefaction induced by cyclic loading. *NASA STI/Recon Technical Report N, 83,* 13308.

Castro, G., & Poulos, S. J. (1977). Factors affecting liquefaction and cyclic mobility. *Journal of the Geotechnical Engineering Division, 103*(6), 501-506.

Cundall, P. (1971). A computer model for simulating progressive, large-scale movements in blocky rock systems, symposium soc. *Internat.Mechanique Des Roches, Nancy, Paper II-8,*

Cundall, P. A., & Strack, O. D. (1979). A discrete numerical model for granular assemblies. *Geotechnique, 29*(1), 47-65.

Dantu, P. (1957). A contribution to the mechanical and geometrical study of non-cohesive masses. Paper presented at the *Pros. 4th Int. Conf. Soil Mech. and found. Eng.* 144-148.

Dantu, P. (1968). Etude statistique des forces intergranulaires dans un milieu pulverulent. *Géotechnique, 18*(1), 50-55.

Das, B. M., & Sivakugan, N. (2016). Fundamentals of geotechnical engineering Cengage Learning.

De Josselin de Jong, G., Verruijt, A., 1969. Etude photo-elastique d'un empilement de disques, Cahiers du group Francais de Rheologie, Janvier 1969, No. 2, 73-86

Dewoolkar, M. M., Ko, H., Stadler, A. T., & Astaneh, S. (1999). A substitute pore fluid for seismic centrifuge modeling. *Geotechnical Testing Journal, 22*(3), 196-210.

Dobry, R., Vasquez-Herrera, A., Mohamad, R., & Vucetic, M. (1985). (1985). Liquefaction flow failure of silty sand by torsional cyclic tests. Paper presented at the *Advances in the Art of Testing Soils Under Cyclic Conditions*, 29-50.

Drescher, A., & De Jong, G De Josselin. (1972). Photoelastic verification of a mechanical model for the flow of a granular material. *Journal of the Mechanics and Physics of Solids, 20*(5), 337-340.

El Shamy, U., & Zeghal, M. (2005). Coupled continuum-discrete model for saturated granular soils. *Journal of Engineering Mechanics, 131*(4), 413-426.

Evans, M. D., & Zhou, S. (1995a). Liquefaction behavior of sand-gravel composites. *Journal of Geotechnical Engineering, 121*(3), 287-298.

Field, W. (1963). Towards the statistical definition of a granular mass. Paper presented at the *Proceedings of 4th Austria-New Zealand Conf. on Soil Mechanics and found. Eng*, 143-148.

Franklin, J. A., & Dusseault, M. B. (1991). Rock engineering applications, 1991.

Hakuno, M. (1995). Simulation of the dynamic liquefaction of sand. *Earthq.Geotechnical Engineering,* , 857-862.

Hakuno, M., & Tarumi, Y. (1988). Sand liquefaction analysis by granular assembly simulation. Paper presented at the *Proceedings of Ninth World Conference on Earthquake Engineering, 8* 231-236.

Hazen, A. (1920). Hydraulic-fill dams. *Transactions of the American Society of Civil Engineers, 83*(1), 1713-1745.

Hill, R. (1963). Elastic properties of reinforced solids: Some theoretical principles. *Journal of the Mechanics and Physics of Solids, 11*(5), 357-372.

Horne, M. (1965). The behavior of an assembly of rotund, rigid, cohesionless particles. I. *Proceedings of the Royal Society of London.Series A.Mathematical and Physical Sciences, 286*(1404), 62-78.

Ishihara, K. (1993). Liquefaction and flow failure during earthquakes. *Geotechnique, 43*(3), 351-451.

Ishihara, K., Tatsuoka, F., and Yasuda, S. (1975). Undrained deformation and liquefaction of sand under cyclic stresses. *Soils and Foundations, 15*(1), 29-44.

Iwashita, K., & Oda, M. (1999). *Mechanics of granular materials: An introduction* CRC press.

Jafarian, Y., Ghorbani, A., Salamatpoor, S., & Salamatpoor, S. (2013). Monotonic triaxial experiments to evaluate steady-state and liquefaction susceptibility of babolsar sand. *Journal of Zhejiang University SCIENCE A, 14*(10), 739-750.

Jefferies, M., & Been, K. (2006). Soil liquefaction: A critical state approach CRC Press. http://www.golder.com/liq

Keramatikerman, M., & Chegenizadeh, A. (2017). Effect of particle shape on monotonic liquefaction: Natural and crushed sand. Experimental Mechanics, 57(8), 1341-1348.

Konishi, J. (1978). (1978Microscopic model studies on the mechanical behavior of granular materials. Paper presented at the *Proc. US-Japan Seminar on Continuum-Mechanical and Statistical Approaches in the Mechanics of Granular Materials*, 27.

Konrad, J. (1990a). Minimum undrained strength of two sands. *Journal of Geotechnical Engineering, 116*(6), 932-947.

Konrad, J. (1990b). Minimum undrained strength versus steady-state strength of sands. *Journal of Geotechnical Engineering, 116*(6), 948-963.

Kramer, S. L., & Seed, H. B. (1988). Initiation of soil liquefaction under static loading conditions. *Journal of Geotechnical Engineering, 114*(4), 412-430.

Lade, P. V., & Pradel, D. (1990). Instability and plastic flow of soils. I: Experimental observations. *Journal of Engineering Mechanics, 116*(11), 2532-2550.

Lade, P. V., & Yamamuro, J. A. (1997). Effects of nonplastic fines on static liquefaction of sands. *Canadian Geotechnical Journal, 34*(6), 918-928.

Landau, L. D., & Lifshitz, E. (1980). Statistical physics. part 1: Course of theoretical physics.

Law, K., & Ling, Y. (1992a). Liquefaction of granular soils with non-cohesive and cohesive fines. Paper presented at the *Proceedings of the Tenth World Conference on Earthquake Engineering,* 1491-1496.

Mehrabadi, M. M., Nemat-Nasser, S., & Oda, M. (1982). On statistical description of stress and fabric in granular materials. *International Journal for Numerical and Analytical Methods in Geomechanics, 6*(1), 95-108.

Mohamad, R., & Dobry, R. (1986). Undrained monotonic and cyclic triaxial strength of sand. *Journal of Geotechnical Engineering, 112*(10), 941-958.

Mulilis, J. P., Arulanandan, K., Mitchell, J. K., Chan, C. K., & Seed, H. B. (1977). Effects of sample preparation on sand liquefaction. *Journal of the Geotechnical Engineering Division, 103*(2), 91-108.

Nakase, H., Takeda, T., & Oda, M. (1999). A simulation study on liquefaction using DEM. *Earthquake Geotechnical Engineering.Balkema, Rotterdam,* , 637-642.

Oda, M. (1972a). The mechanism of fabric changes during compressional deformation of sand. *Soils and Foundations, 12*(2), 1-18.

Oda, M., & Konishi, J. (1974a). Microscopic deformation mechanism of granular material in simple shear. *Soils and Foundations, 14*(4), 25-38.

Oda, M., & Konishi, J. (1974b). Rotation of principal stresses in granular material during simple shear. *Soils and Foundations, 14*(4), 39-53.

Oda, M. (1972b). Deformation mechanism of sand in triaxial compression tests. *Soils and Foundations, 12*(4), 45-63.

Oda, M. (1972c). Initial fabrics and their relations to mechanical properties of granular material. *Soils and Foundations, 12*(1), 17-36.

Okada, Y., & Ochiai, H. (2007). Coupling pore-water pressure with distinct element method and steady state strengths in numerical triaxial compression tests under undrained conditions. *Landslides, 4*(4), 357-369.

Pitman, T., Robertson, P., & Sego, D. (1994). Influence of fines on the collapse of loose sands. *Canadian Geotechnical Journal, 31*(5), 728-739.

Poulos, S. J. (1981). The steady state of deformation. *Journal of Geotechnical and Geoenvironmental Engineering, 107*(ASCE 16241 Proceeding)

Poulos, S. J., Castro, G., & France, J. W. (1985). Liquefaction evaluation procedure. *Journal of Geotechnical Engineering, 111*(6), 772-792.

Poulos, S. J., Castro, G., & France, J. W. (1988). Closure to "Liquefaction evaluation procedure" by steve J. poulos, gonzalo castro, and john W. france (june, 1985, vol. 111, no. 6). *Journal of Geotechnical Engineering, 114*(2), 251-259.

Roscoe, K. H., Schofield, A., & Wroth, C. (1958). On the yielding of soils. *Geotechnique, 8*(1), 22-53.

Roscoe, K., & Poorooshasb, H. (1963). A theoretical and experimental study of strains in triaxial compression tests on normally consolidated clays. *Geotechnique, 13*(1), 12-38.

Rothenburg, L., & Selvadurai, A. (1981). A micromechanical definition of the Cauchy stress tensor for particulate media. In A. P. S. Selvadurai (Ed.), Mechanics of Structured Media, pp. 469–486. Elsevier, Amsterdam.

Rothenburg, L. (1980). Micromechanics of idealized granular systems. (Ph.D. thesis, Carlton University)

Rothenburg, L., & Bathurst, R. J. (1991). Numerical simulation of idealized granular assemblies with plane elliptical particles. *Computers and Geotechnics, 11*(4), 315-329.

Rothenburg, L., & Bathurst, R. (1989). Analytical study of induced anisotropy in idealized granular materials. *Geotechnique, 39*(4), 601-614.

Rowe, P. W. (1962). The stress-dilatancy relation for static equilibrium of an assembly of particles in contact. *Proceedings of the Royal Society of London.Series A.Mathematical and Physical Sciences, 269*(1339), 500-527.

Satake, M. (1978a). Constitution of mechanics of granular materials through the graph theory. *Continuum Mechanical and Statistical Approaches in the Mechanics of Granular Materials*, 47-62.

Satake, M. (1978b). Constitution of mechanics of granular materials through the graph theory. Paper presented at the *Proc. US-Japan Seminar on Continuum Mech. Stat. Appr. Mech. Granul. Mater., Sendai*, 203-215.

Schneebeli, M. (1956). Mechanique des soils-une analogie mechanique pour les terres sans cohesion. *Comptes Rendes Hebdomaires Des Seances De L'Academie Des Sciences, 243*, 125-126.

Schofield, A., & Wroth, P. (1968). Critical state soil mechanics.

Seed, H. B., Lee, K. L., Idriss, I. M., & Makdisi, F. I. (1975). The slides in the san fernando dams during the earthquake of february 9, 1971. *Journal of Geotechnical and Geoenvironmental Engineering, 101*(ASCE# 11449 Proceeding)

Shafipour, R., & Soroush, A. (2008). Fluid coupled-DEM modelling of undrained behavior of granular media. *Computers and Geotechnics, 35*(5), 673-685.

Sladen, J., D'hollander, R., & Krahn, J. (1985). The liquefaction of sands, a collapse surface approach. *Canadian Geotechnical Journal, 22*(4), 564-578.

Smith, W., Foote, P. D., & Busang, P. (1929). Packing of homogeneous spheres. *Physical Review, 34*(9), 1271.

Strack, O., & Cundall, P. A. (1978). *The distinct element method as a tool for research in granular media* Department of Civil and Mineral Engineering, University of Minnesota.

Tatsuoka, F., Ochi, K., Fujii, S., & Okamoto, M. (1986a). Cyclic undrained triaxial and torsional shear strength of sands for different sample preparation methods. *Soils and Foundations, 26*(3), 23-41.

Terzaghi, K. (1951). *Theoretical soil mechanics* Chapman And Hall, Limited.; London.

Thallak, S. (1991). *Numerical simulation of hydraulic fracturing in granular media*. (Ph.D. thesis, University of Waterloo)

Vaid, Y., & Chern, J. (1985). Cyclic and monotonic undrained response of saturated sands. Paper presented at the *Advances in the Art of Testing Soils Under Cyclic Conditions,* 120-147.

Vaid, Y., Chung, E., & Kuerbis, R. (1990). Stress path and steady state. *Canadian Geotechnical Journal, 27*(1), 1-7.

Verdugo, R., & Ishihara, K. (1996). The steady state of sandy soils. *Soils and Foundations, 36*(2), 81-91.

Weber, J. (1966). Recherches concernant les contraintes intergranulaires dans les milieux pulvérulents. *Bulletin De Liaison Des Ponts Et Chaussées, 20*, 1-20.

Yamamuro, J. A., & Lade, P. V. (1997). Static liquefaction of very loose sands. *Canadian Geotechnical Journal, 34*(6), 905-917.

Yang, J., Sze, H., & Heung, M. (2009). Effect of initial static shear on cyclic behavior of sand. Paper presented at the *Proceedings of the 17th International Conference on Soil Mechanics and Geotechnical Engineering,*

Yang, J. & Wei, L. M. (2012). Collapse of loose sand with the addition of fines: the role of particle shape. Geotechnique 62(12), 1111–1125

Yang, Z., & Elgamal, A. (2002). Influence of permeability on liquefaction-induced shear deformation. *urnal of Engineering Mechanics, 128*(7), 720-729.

Zeghal, M., & El Shamy, U. (2004). A continuum-discrete hydromechanical analysis of granular deposit liquefaction. *International Journal for Numerical and Analytical Methods in Geomechanics, 28*(14), 1361-1383.

Appendix A Drained Simulation Results

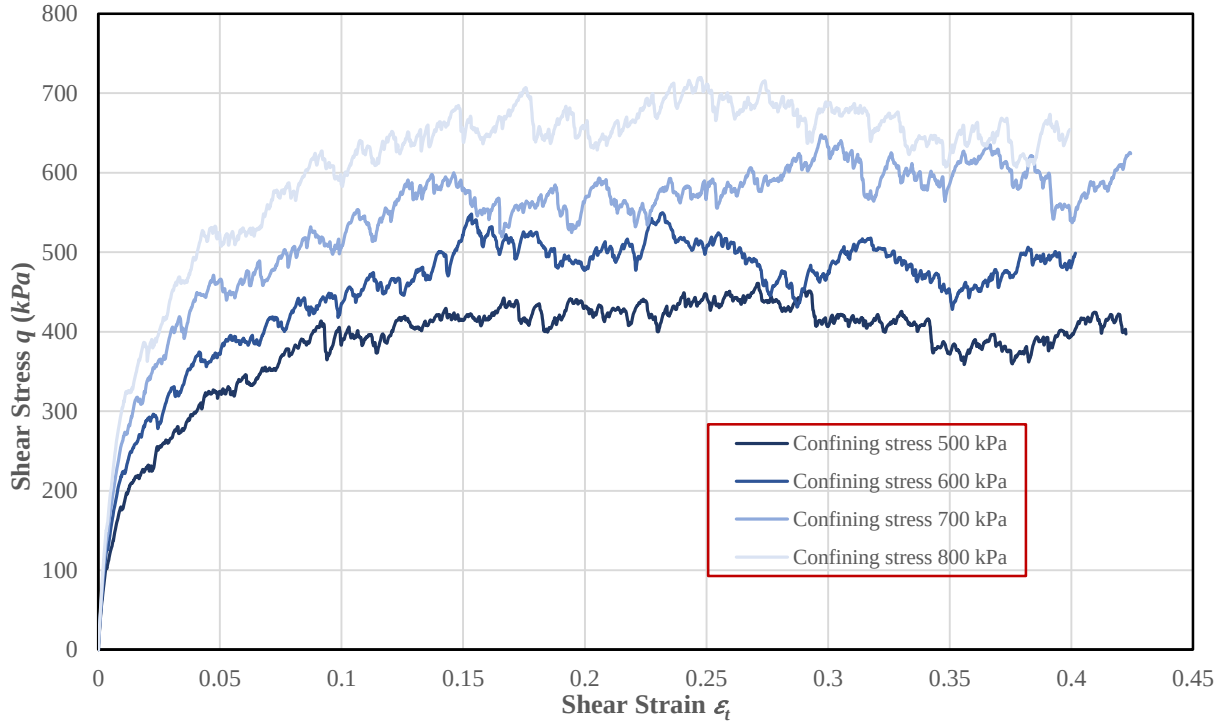

Figure A.1 Stress-strain responses for Tests D6 to D9

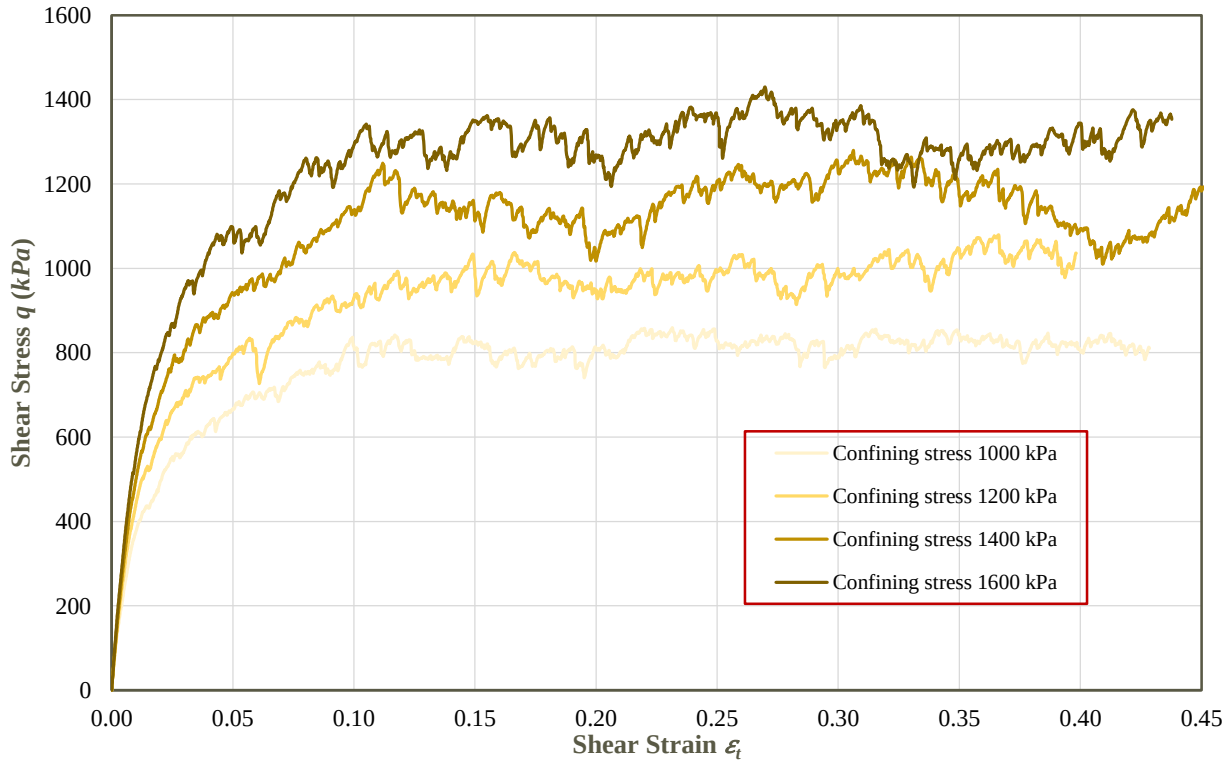

Figure A.2 Stress-strain responses for Tests D10 to D13

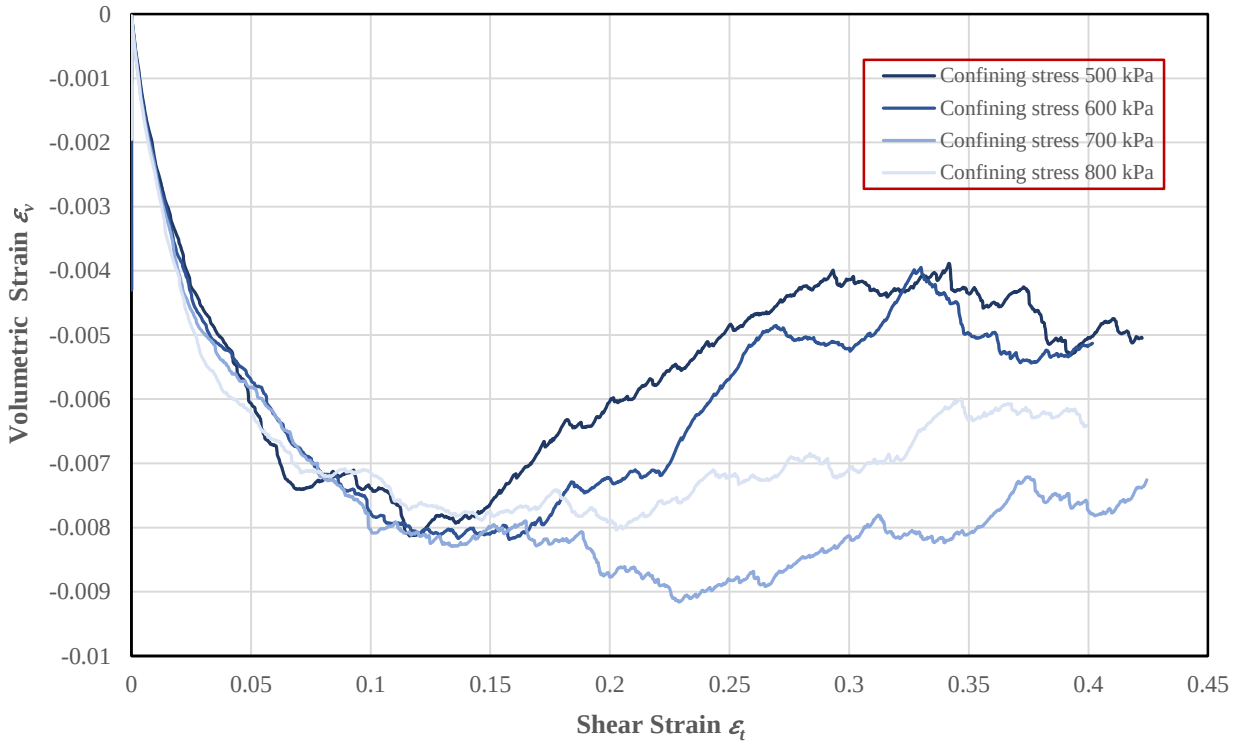

Figure A.3 Volumetric strain changes for Tests D6 to D9

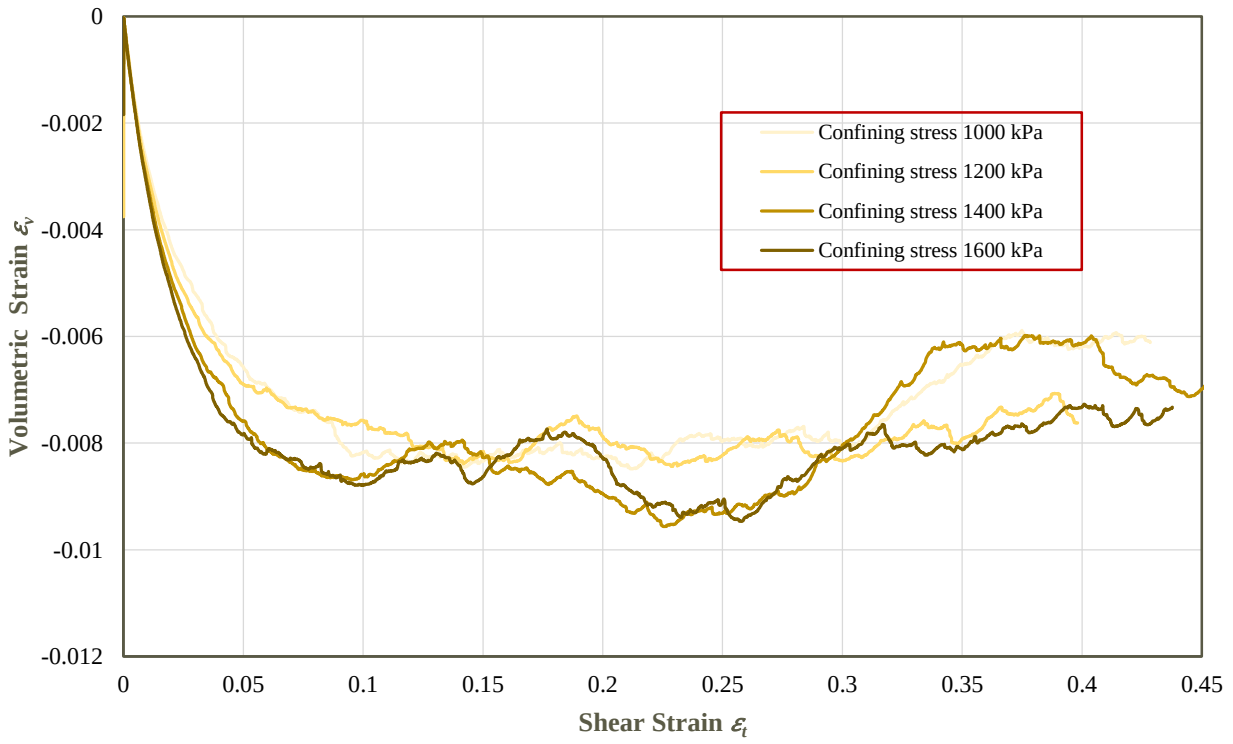

Figure A.4 Volumetric strain changes for Tests D10 to D13

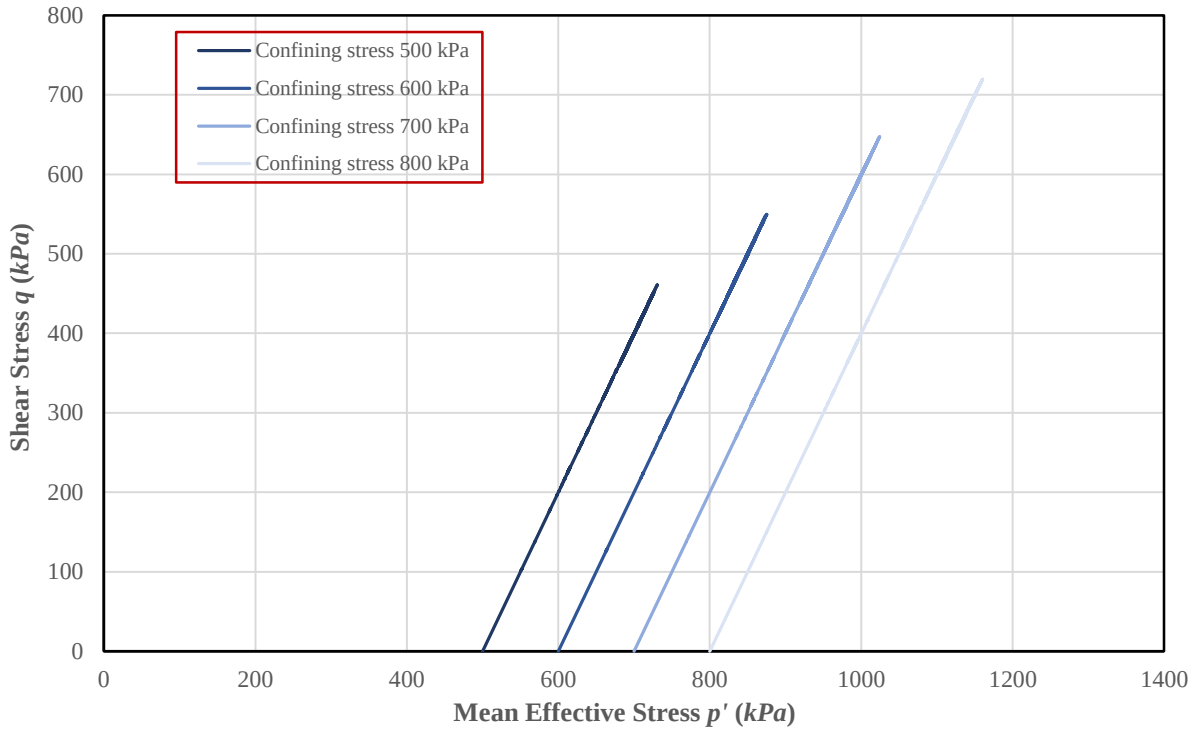

Figure A.5 Stress paths for Tests D6 to D9

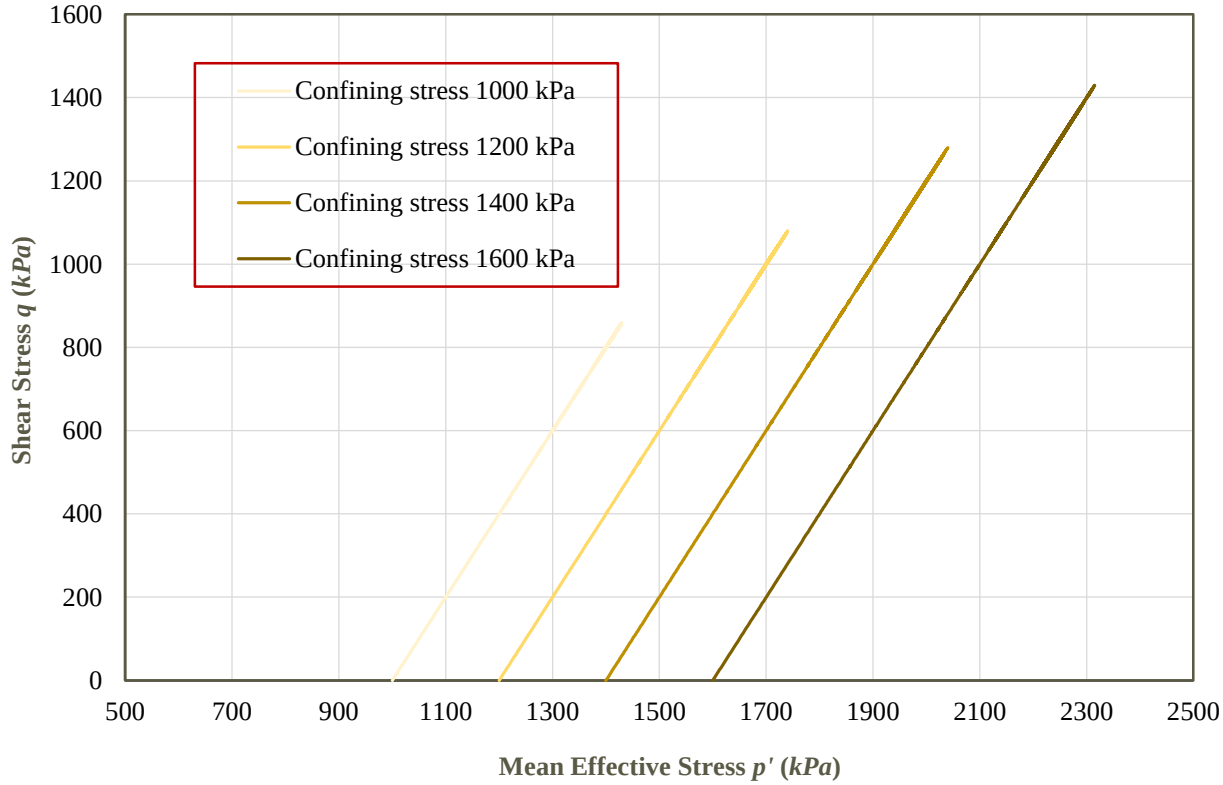

Figure A.6 Stress paths for Tests D10 to D13

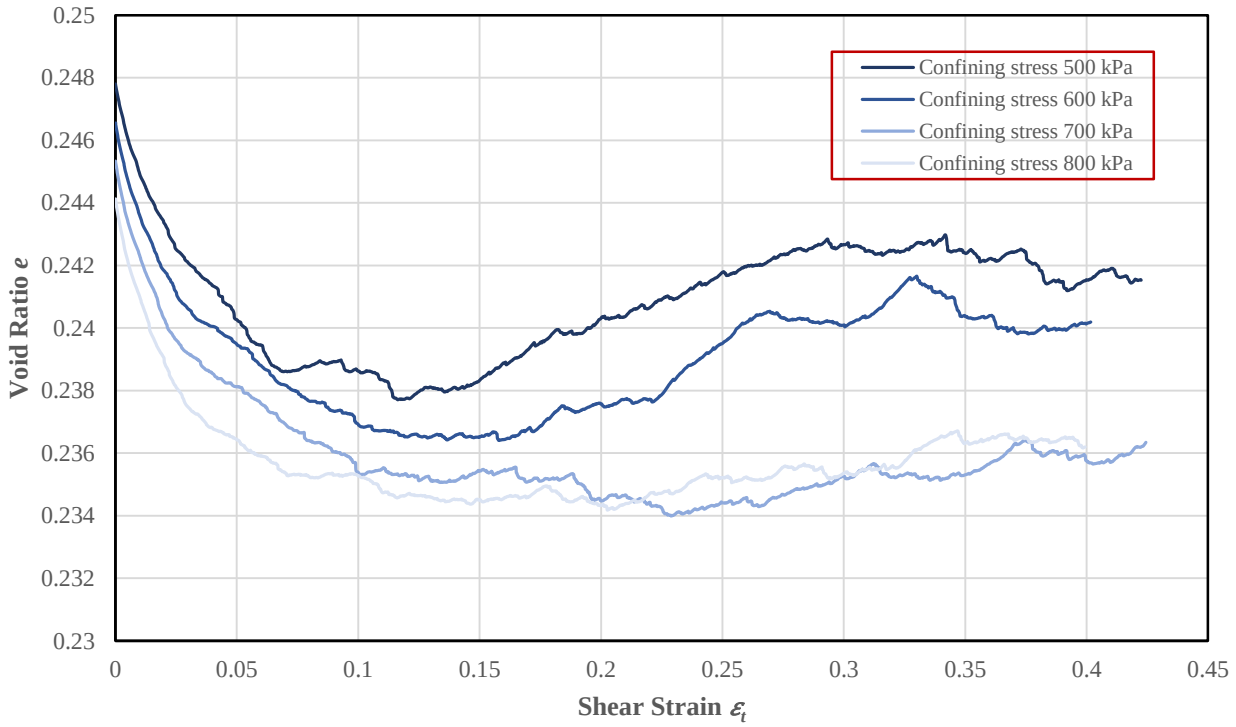

Figure A.7 Void ratio variations for Tests D6 to D9

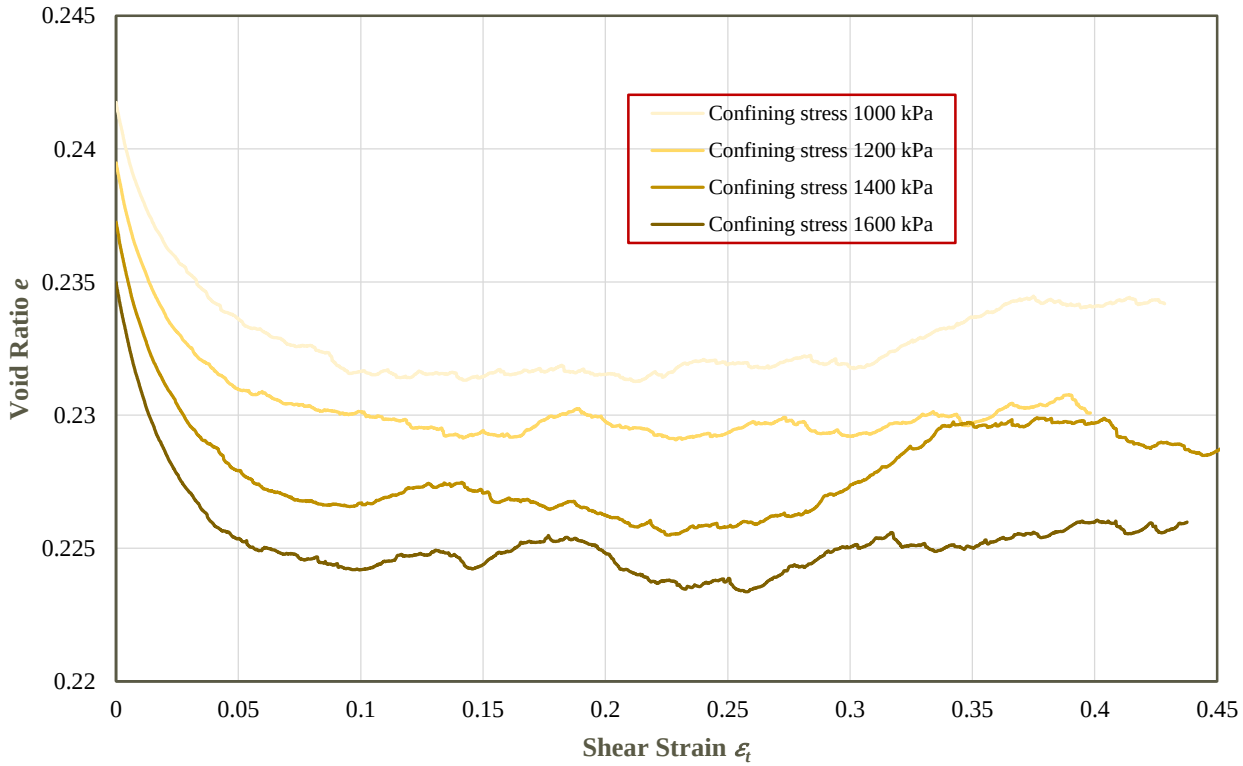

Figure A.8 Void ratio variations for Tests D10 to D13

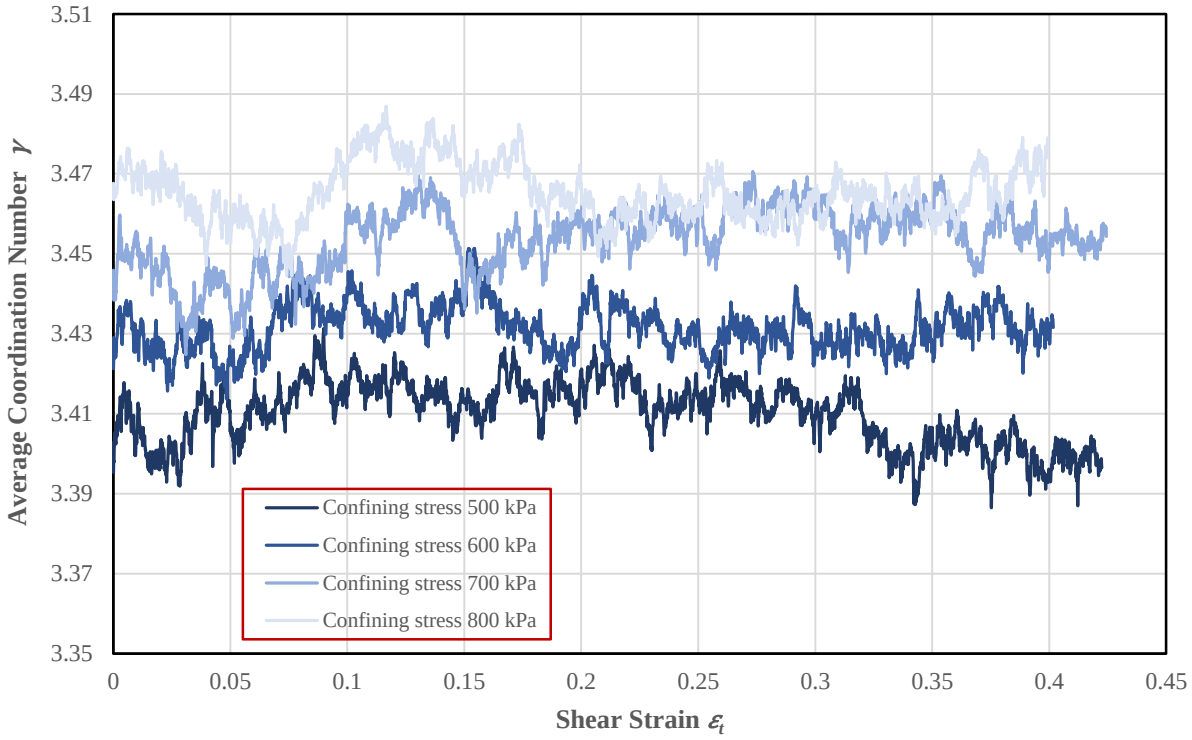

Figure A.9 Average coordination number γ changes for Tests D6 to D9

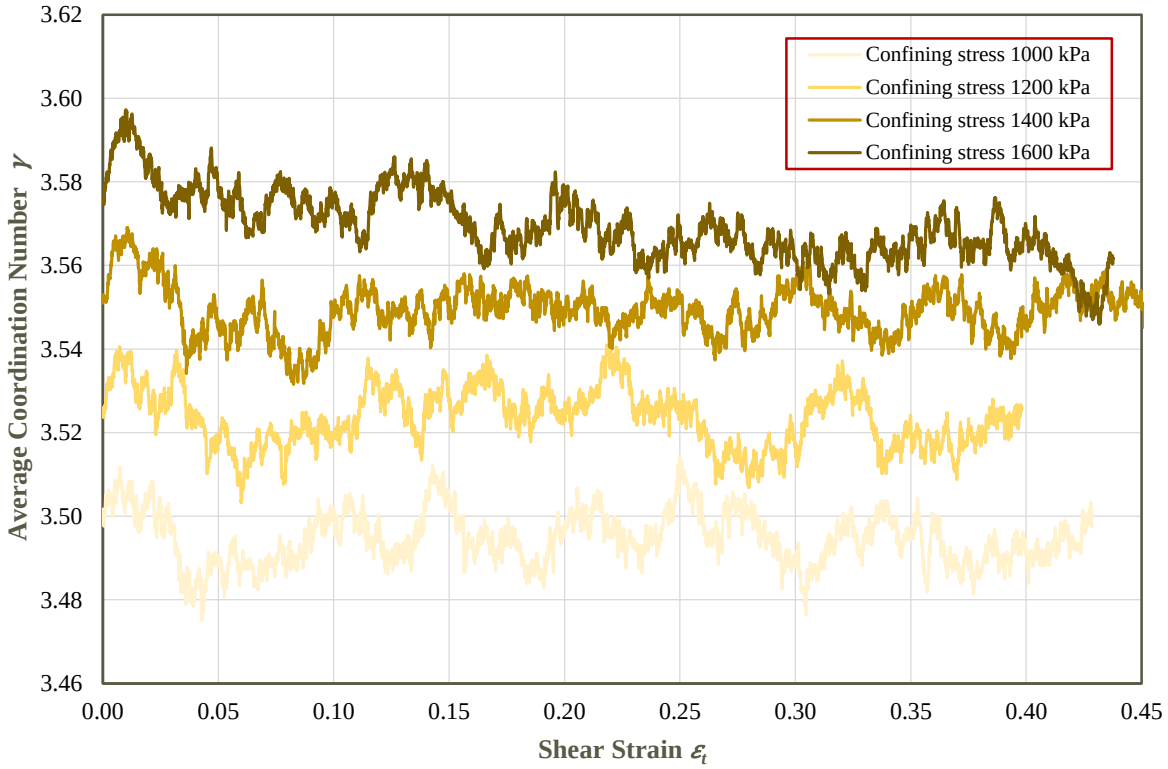

Figure A.10 Average coordination number γ changes for Tests D10 to D13

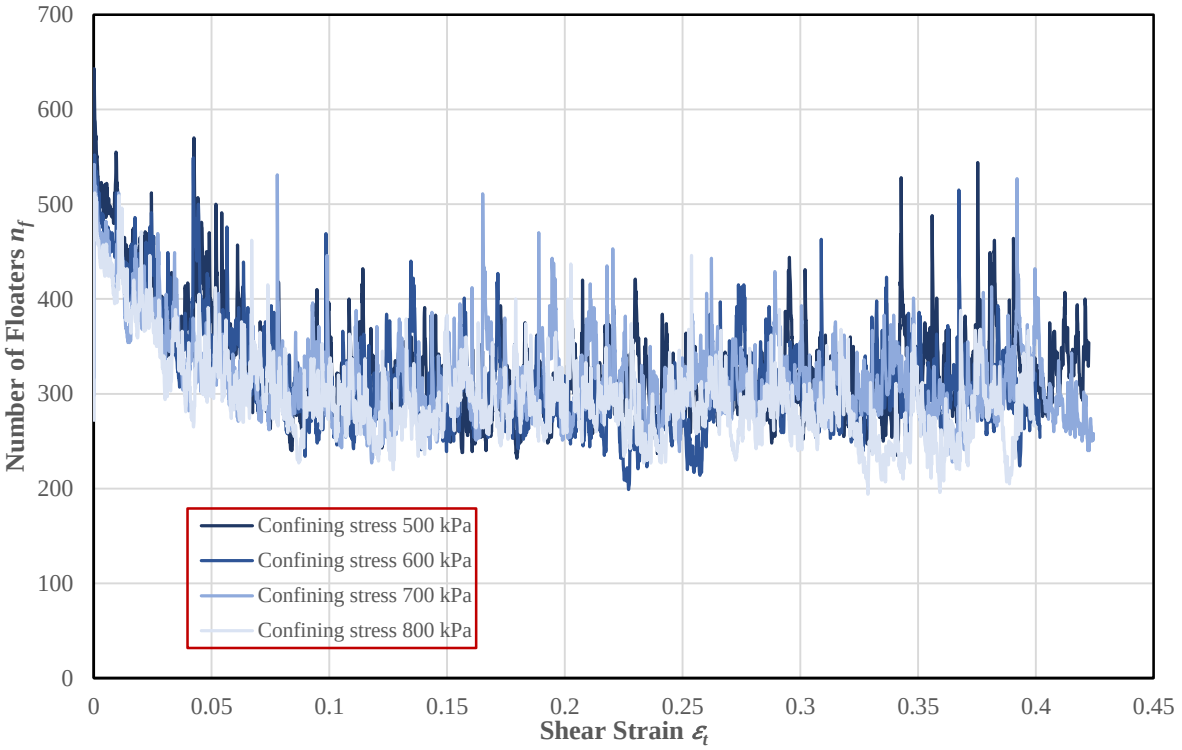

Figure A.11 Number of floaters nf variations for Tests D6 to D9

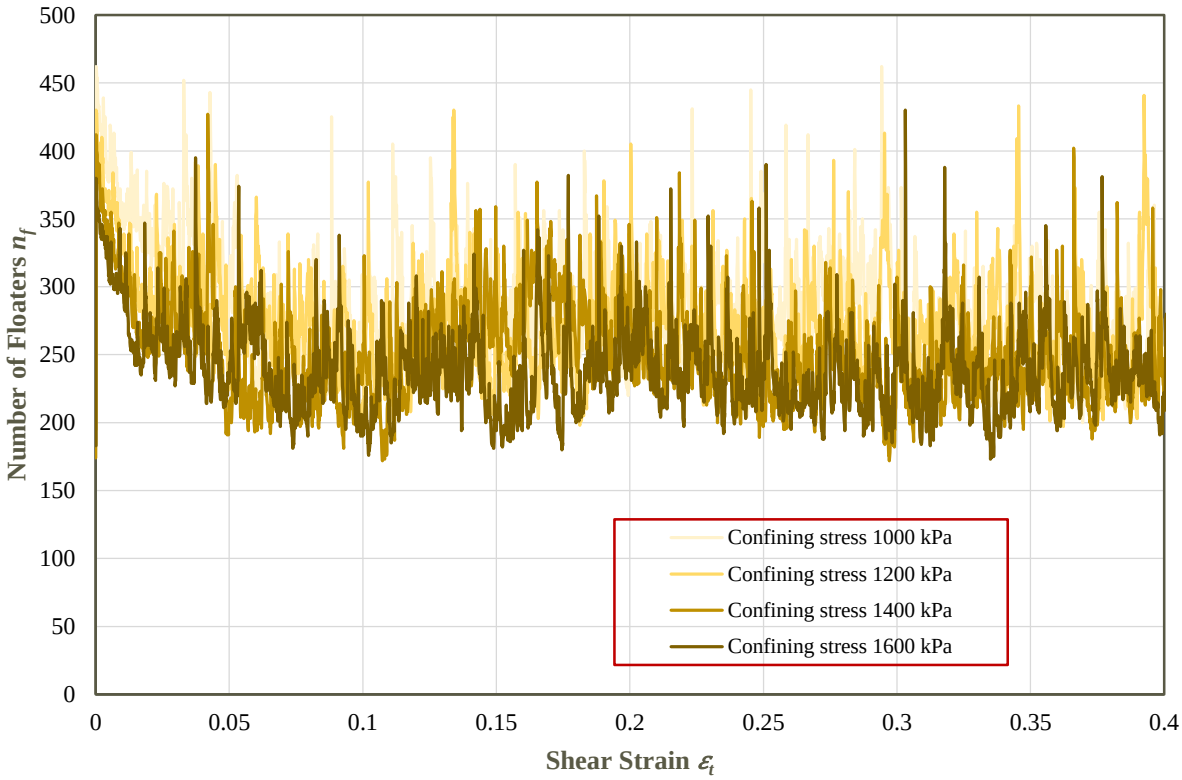

Figure A.12 Number of floaters nf variations for Tests D10 to D13

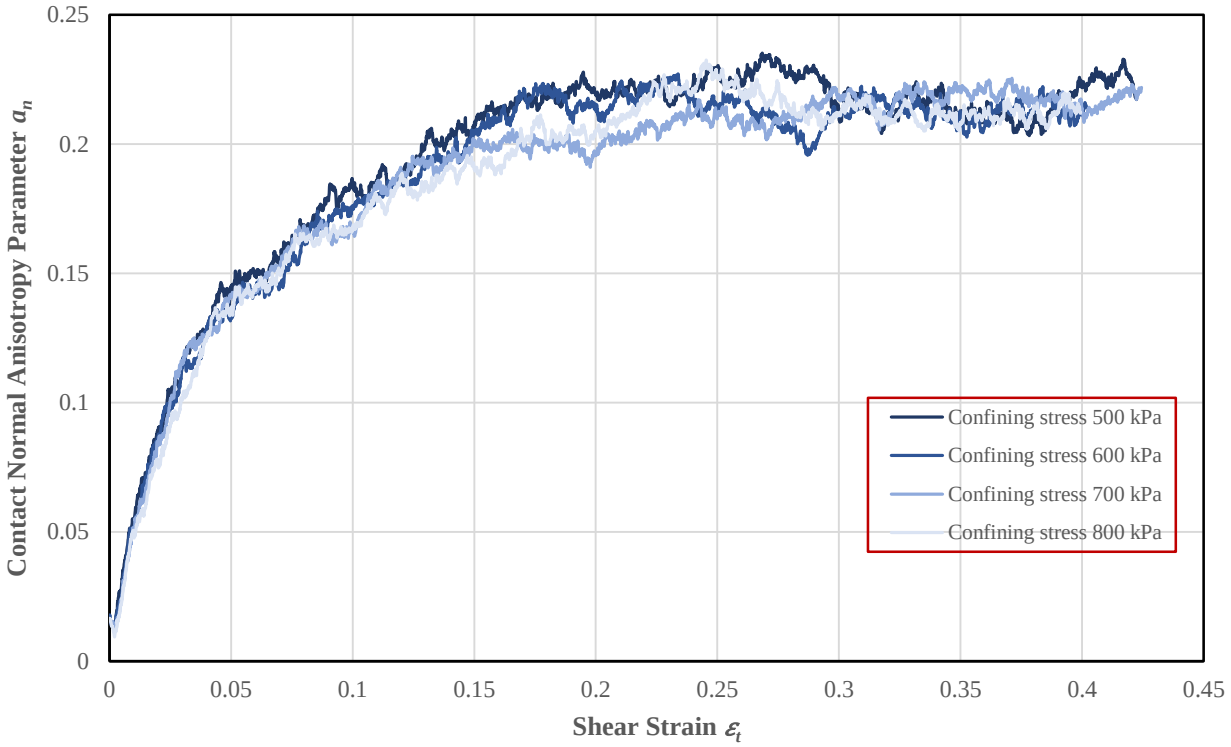

Figure A.13 Contact normal anisotropy parameter an variations for Tests D6 to D9

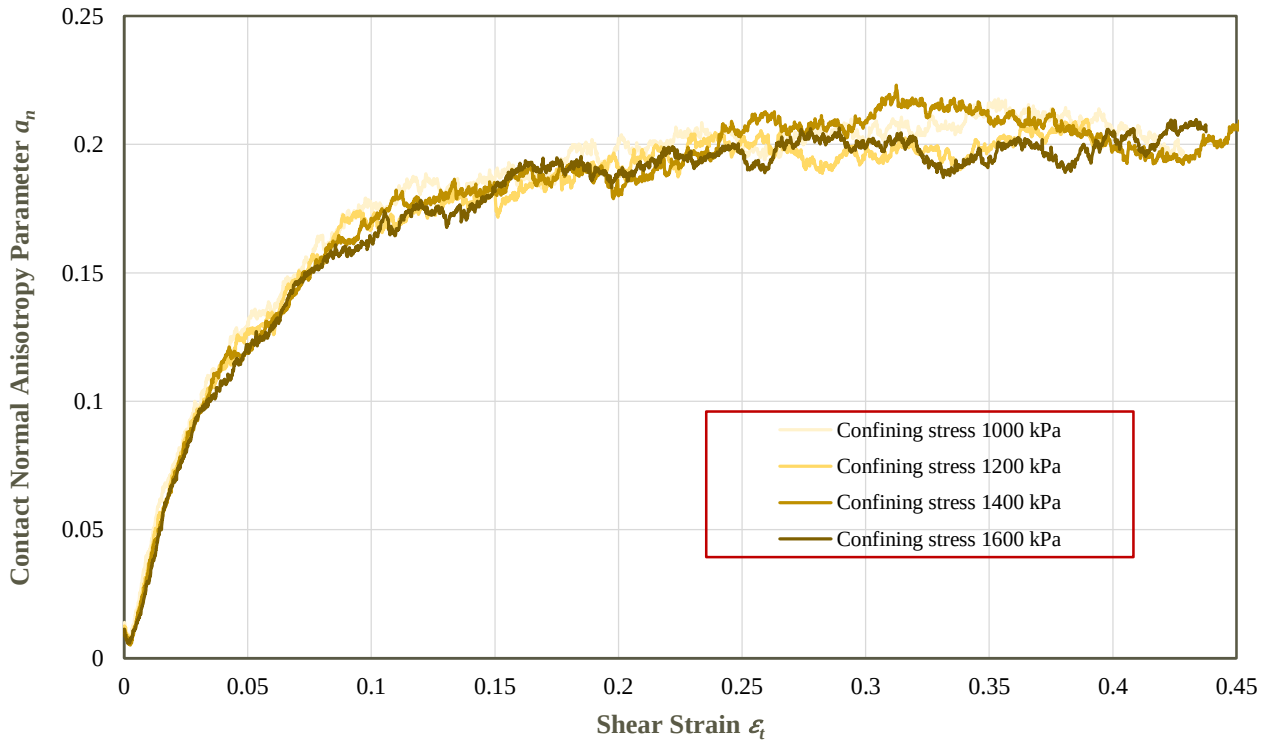

Figure A.14 Contact normal anisotropy parameter an variations for Tests D10 to D13

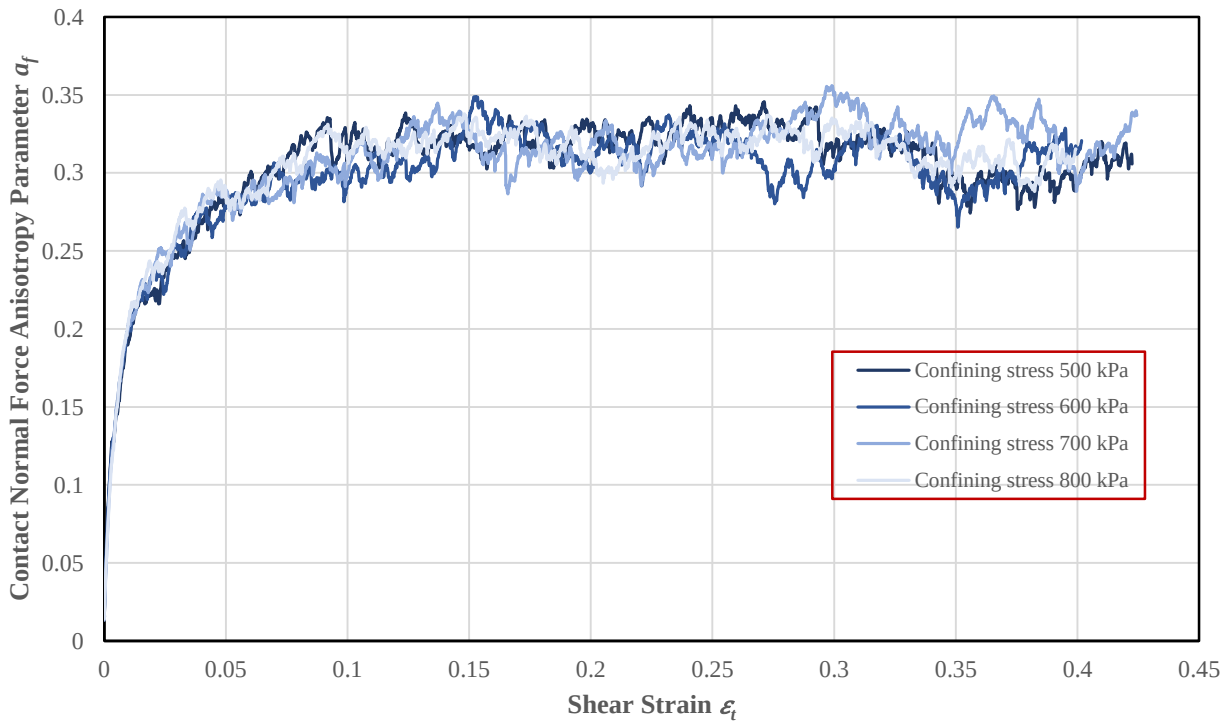

Figure A.15 Normal contact force anisotropy parameter af variations for Tests D6 to D9

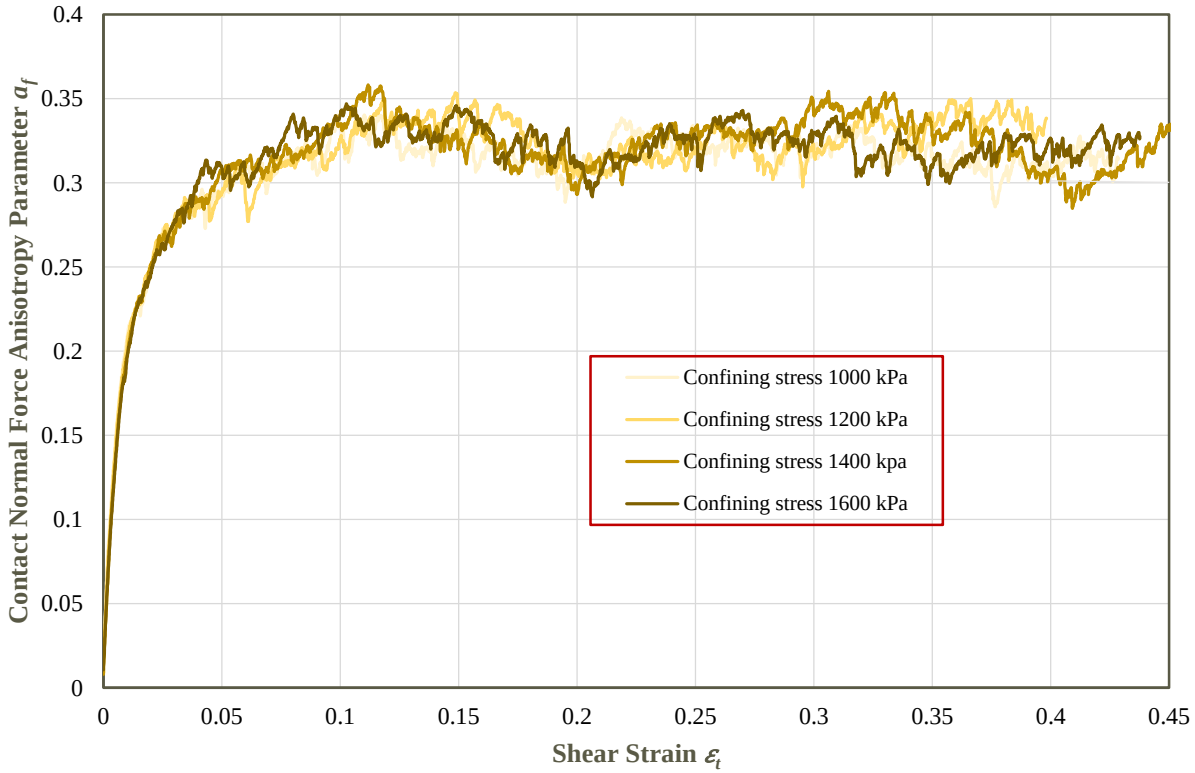

Figure A.16 Normal contact force anisotropy parameter af variations for Tests D10 to D13

Appendix B Undrained Simulation Results

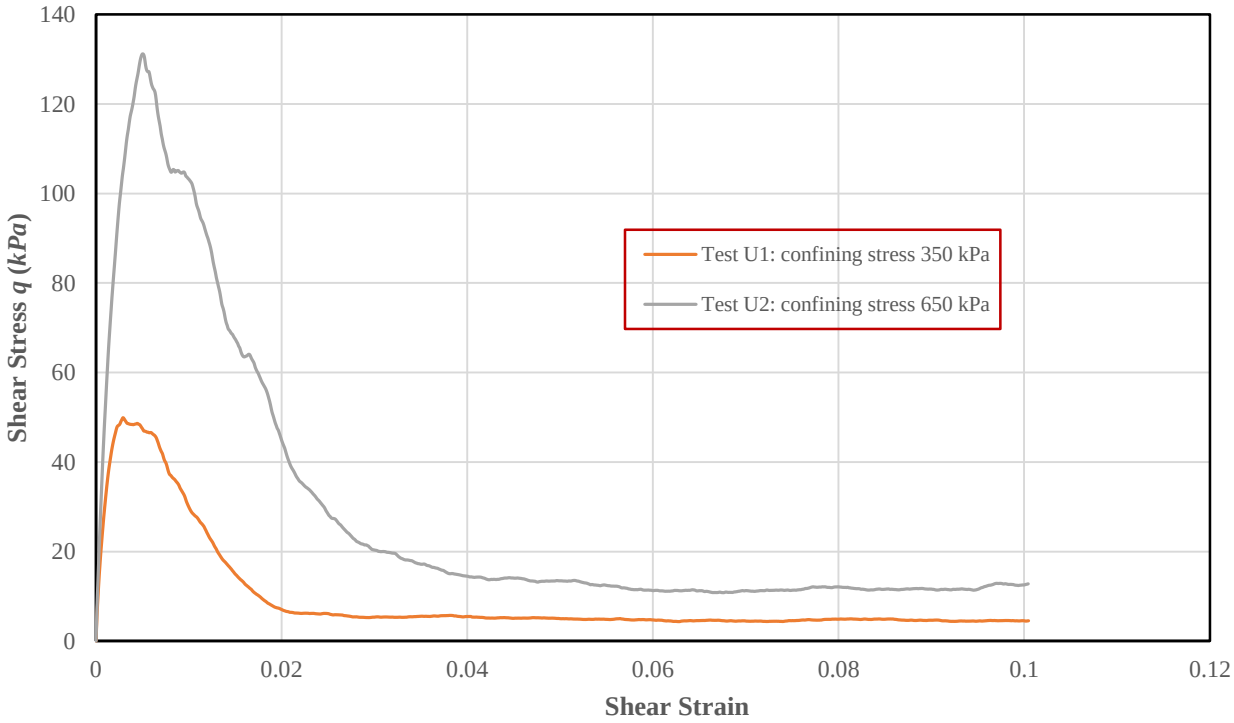

Figure B.17 Stress-strain responses for Tests U1 and U2

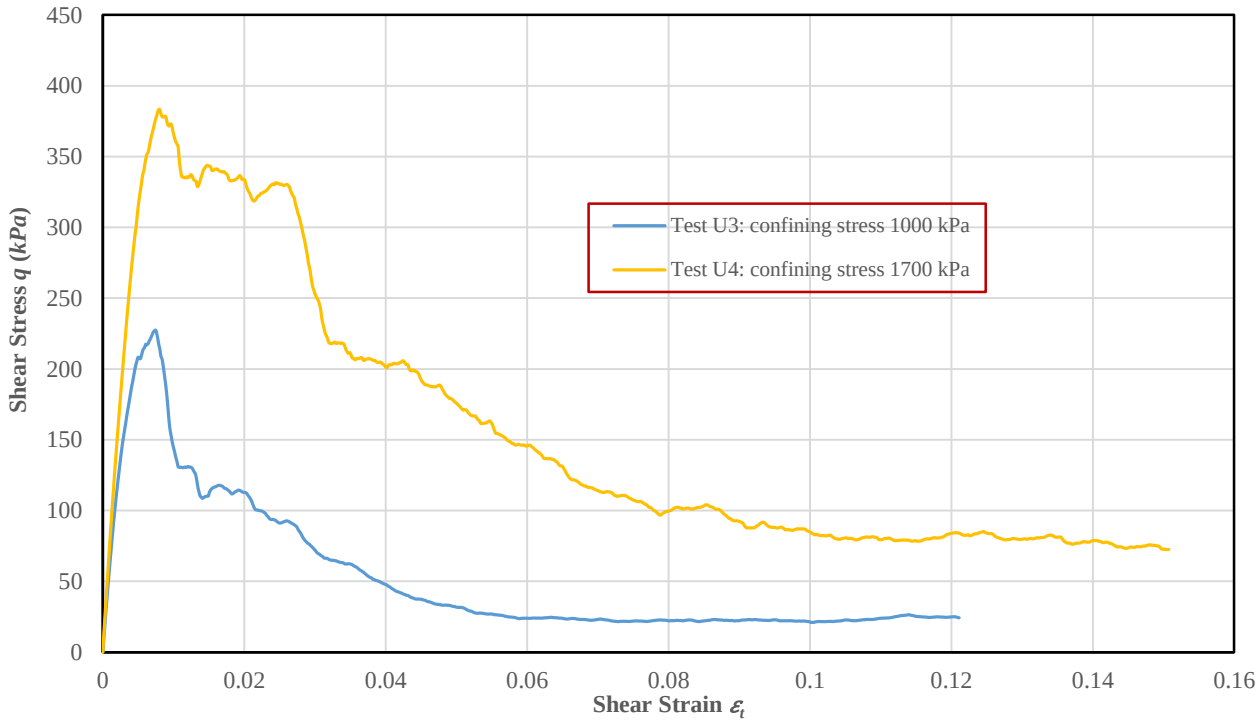

Figure B.2 Stress-strain responses for Tests U3 and U4

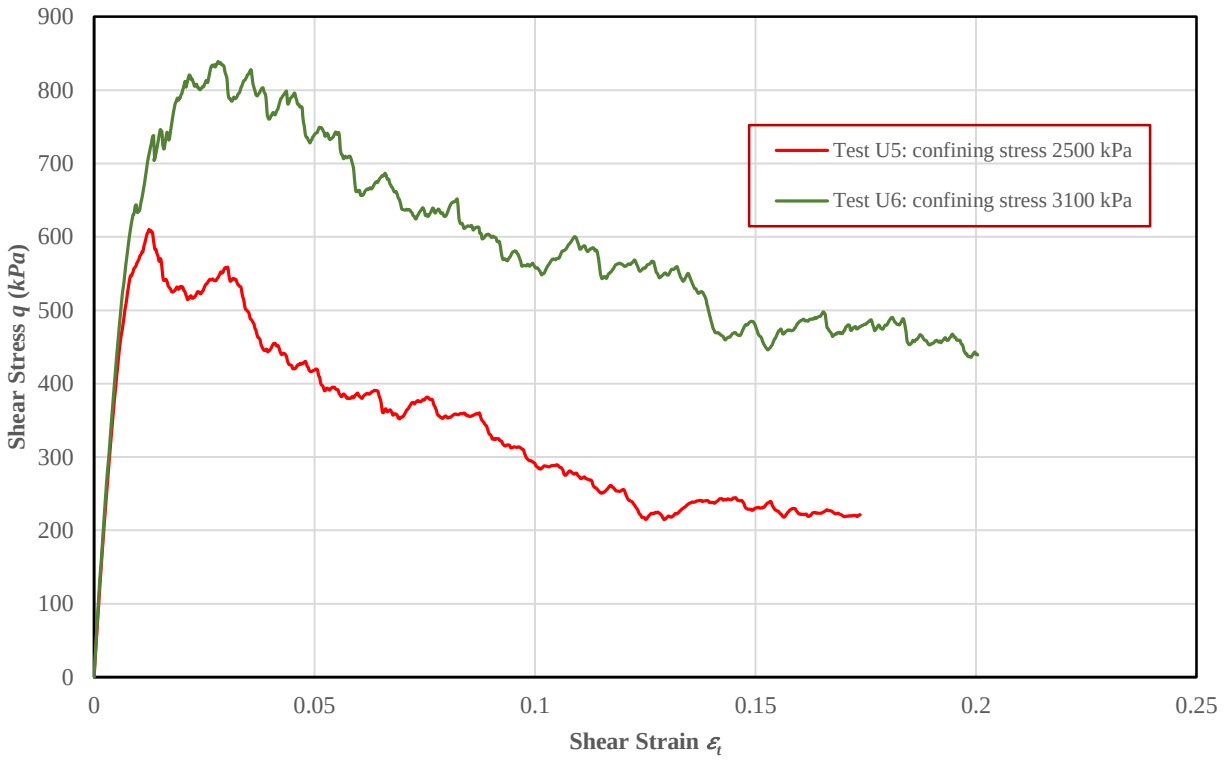

Figure B.3 Stress-strain responses for Tests U5 and U6

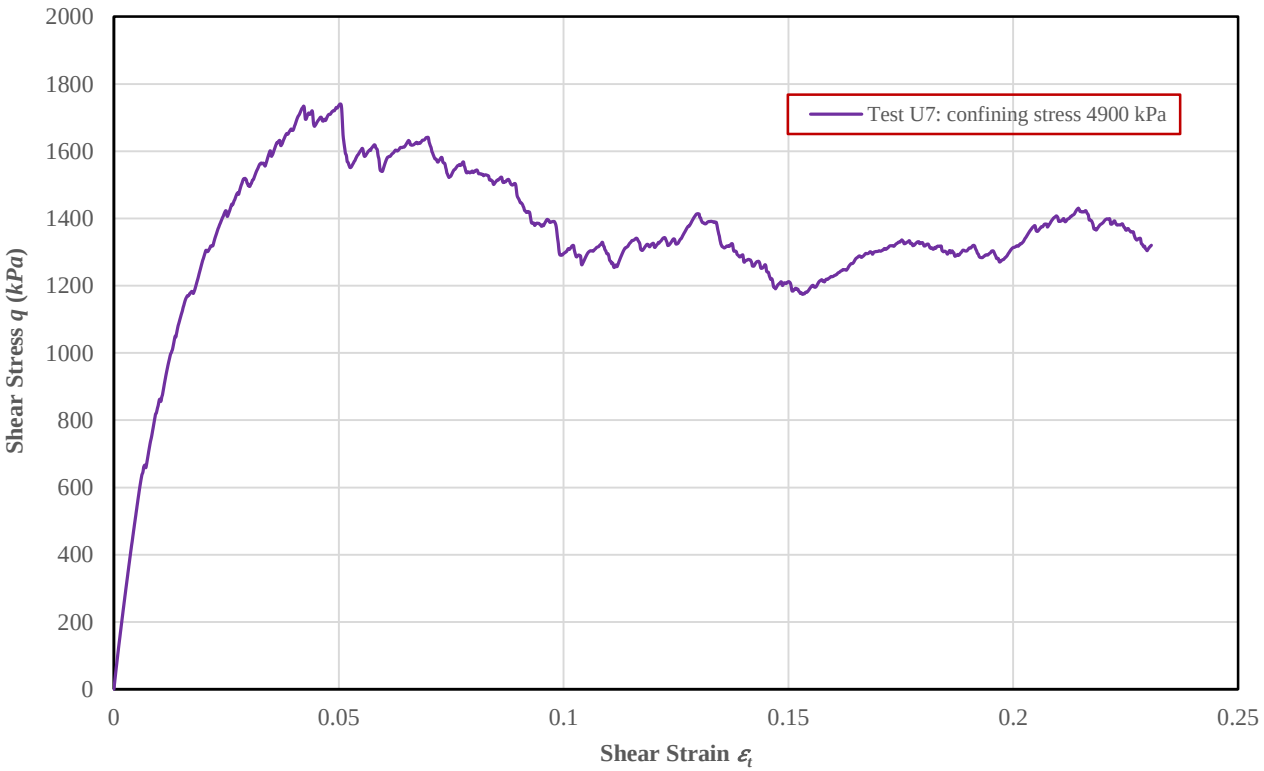

Figure B.4 Stress-strain responses for Test U7

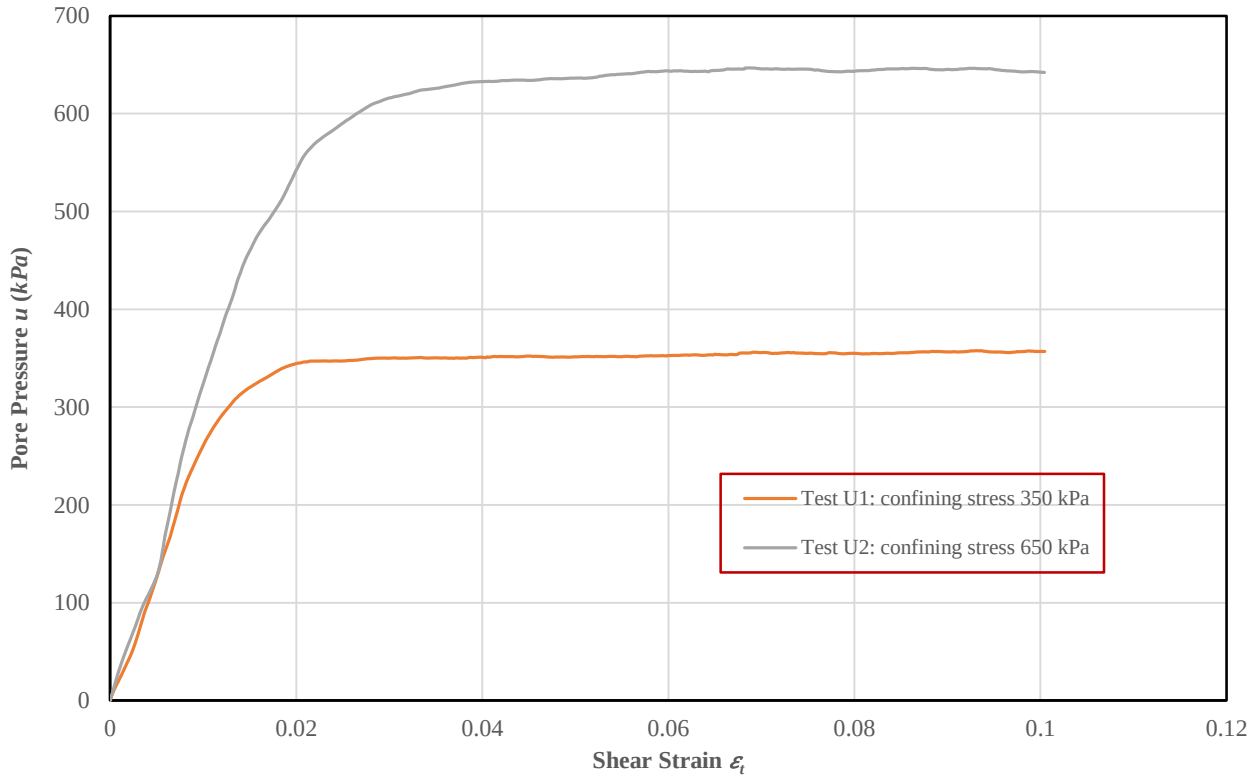

Figure B.5 Pore pressure variations for Tests U1 and U2

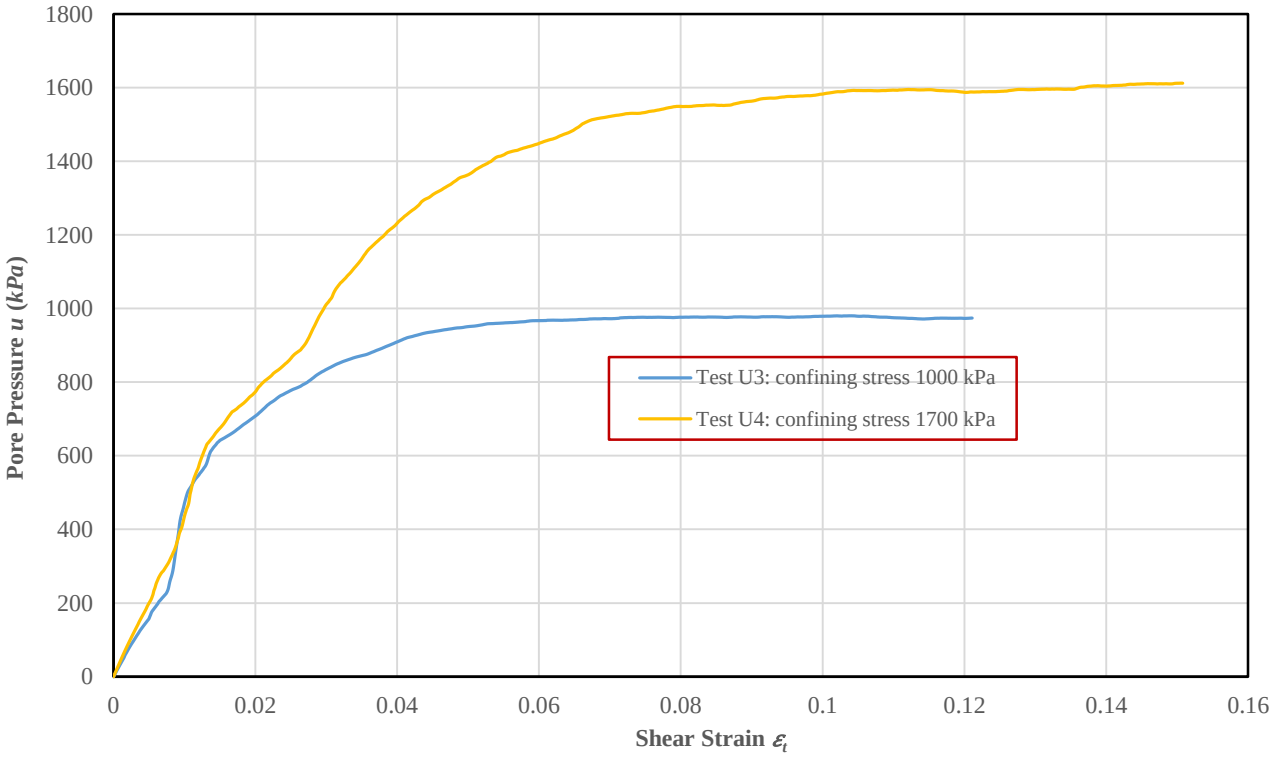

Figure B.6 Pore pressure variations for Tests U3 and U4

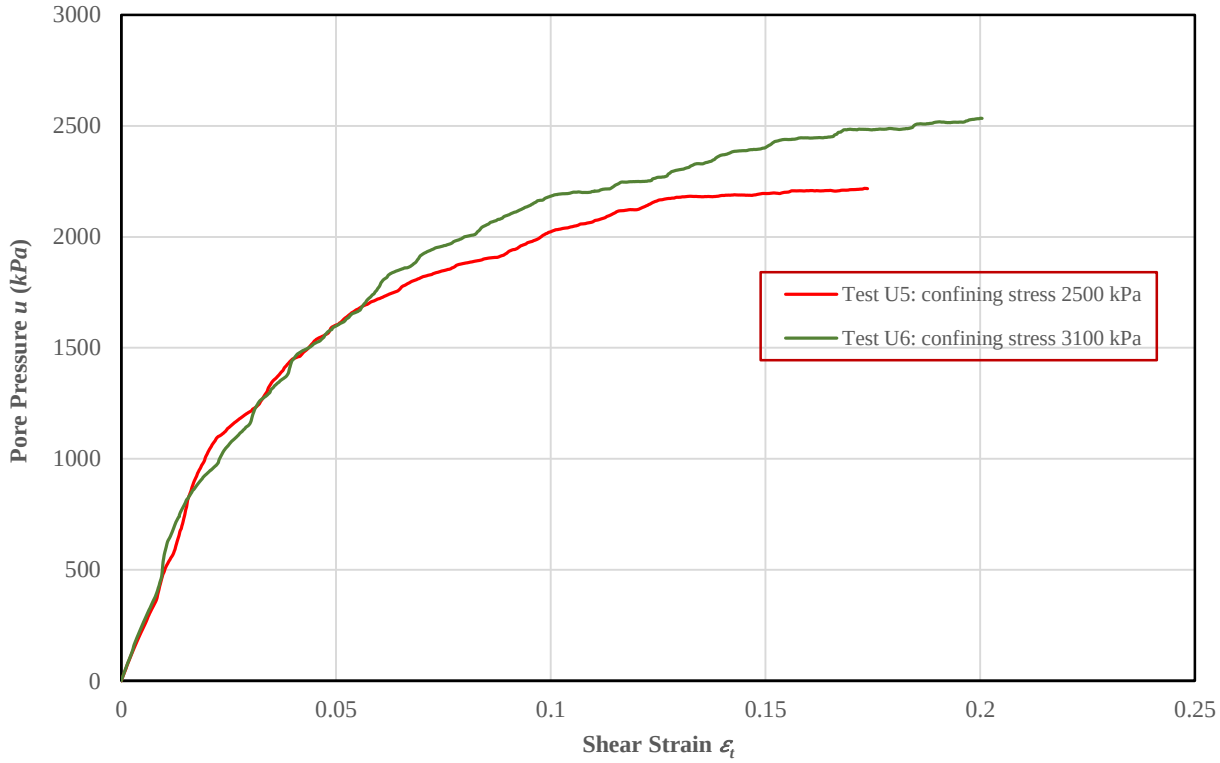

Figure B.7 Pore pressure variations for Tests U5 and U6

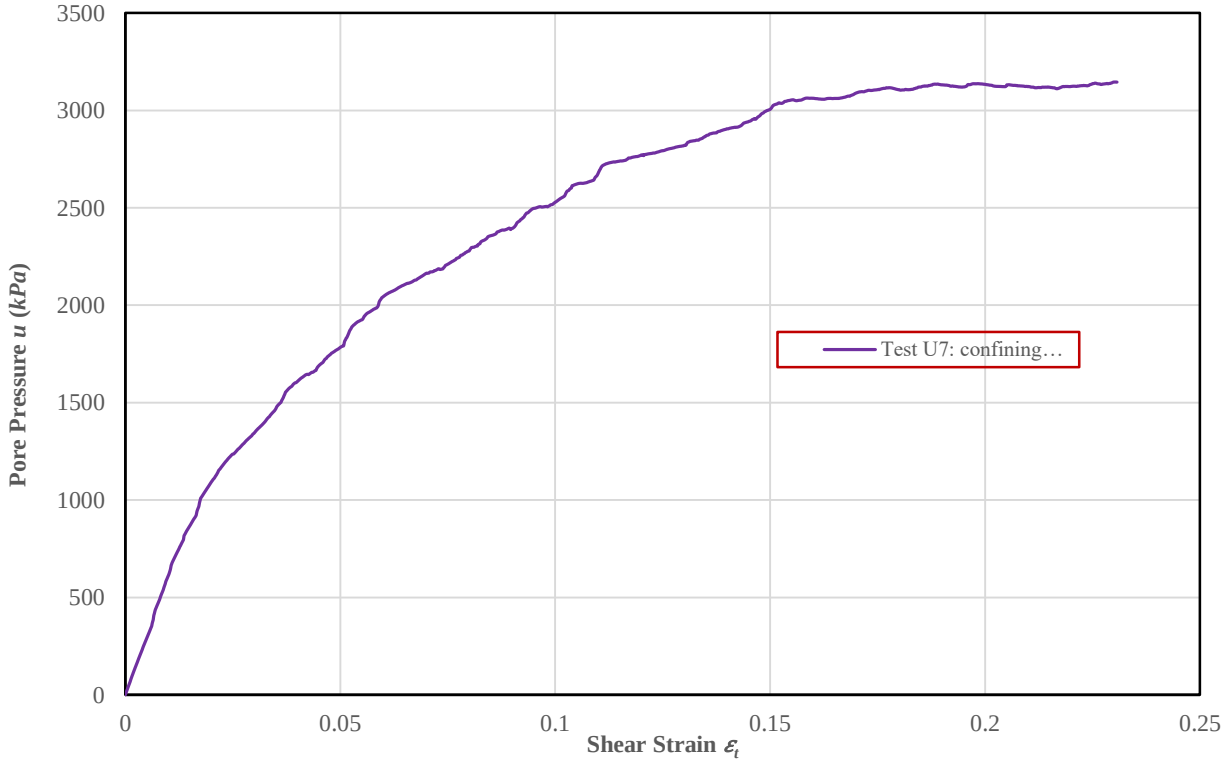

Figure B.8 Pore pressure variations for Test U7

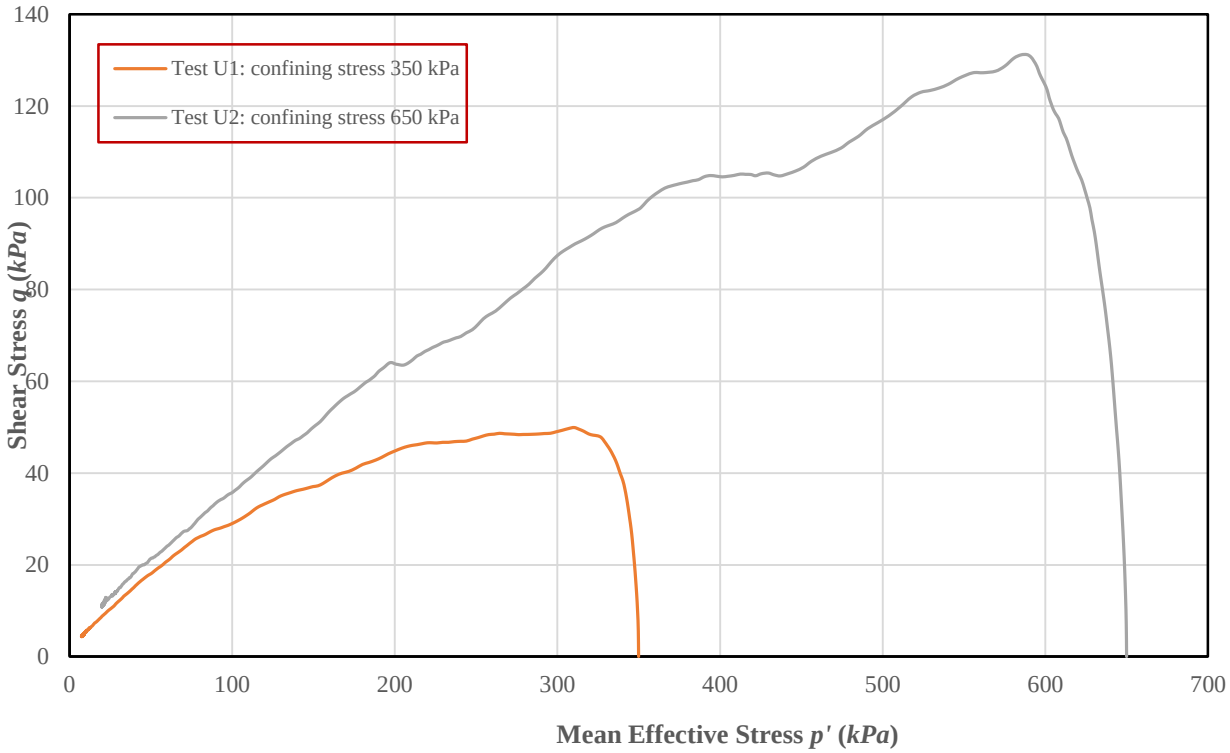

Figure B.9 Stress paths for Tests U1 and U2

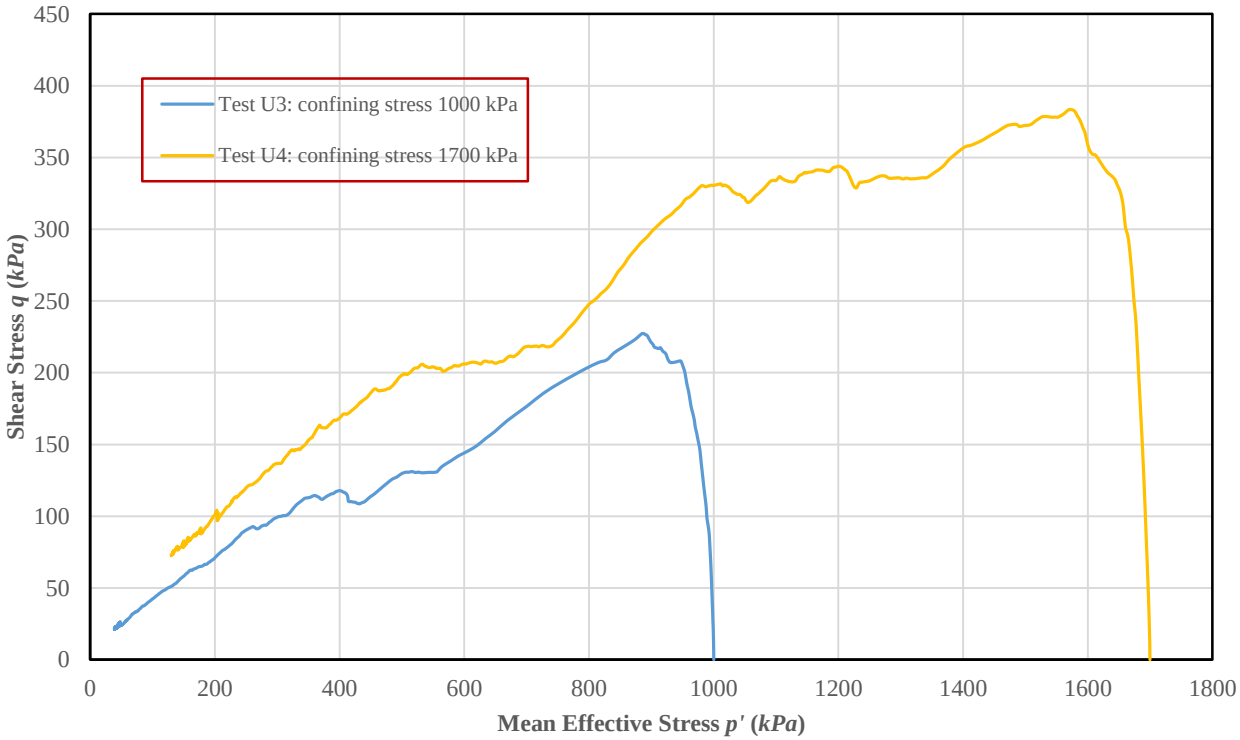

Figure B.10 Stress paths for Tests U3 and U4

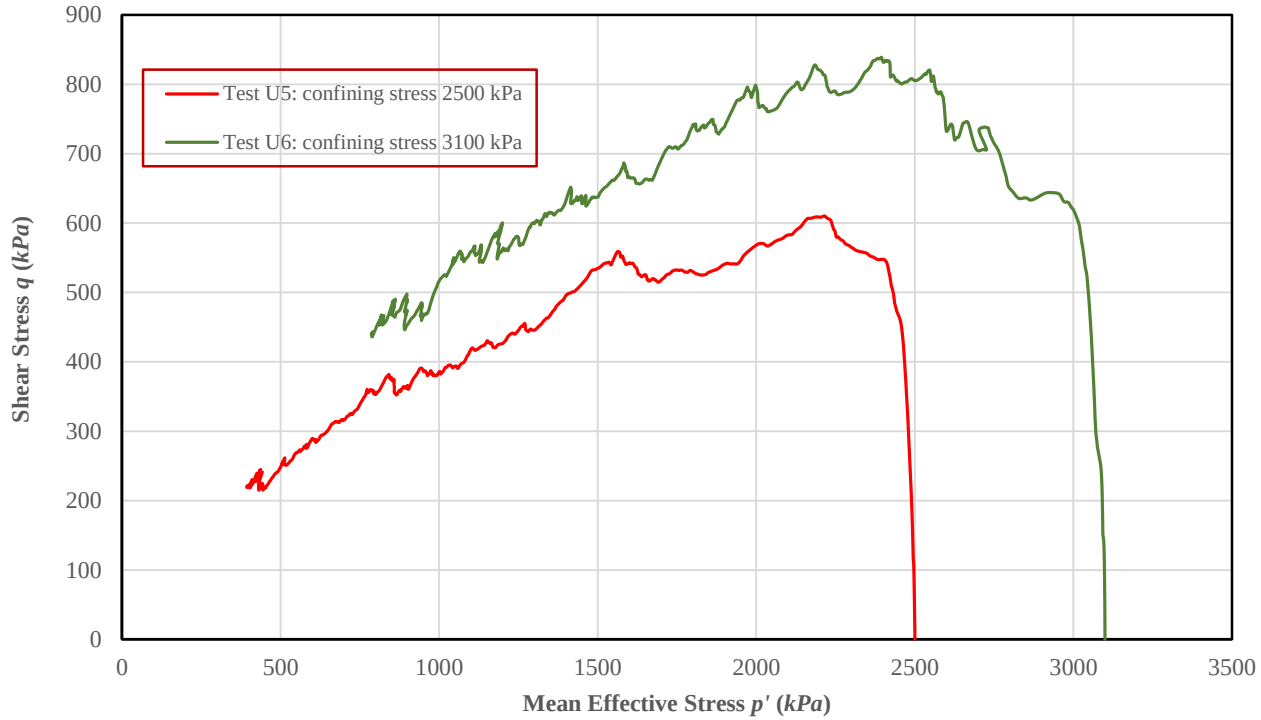

Figure B.11 Stress paths for Tests U5 and U6

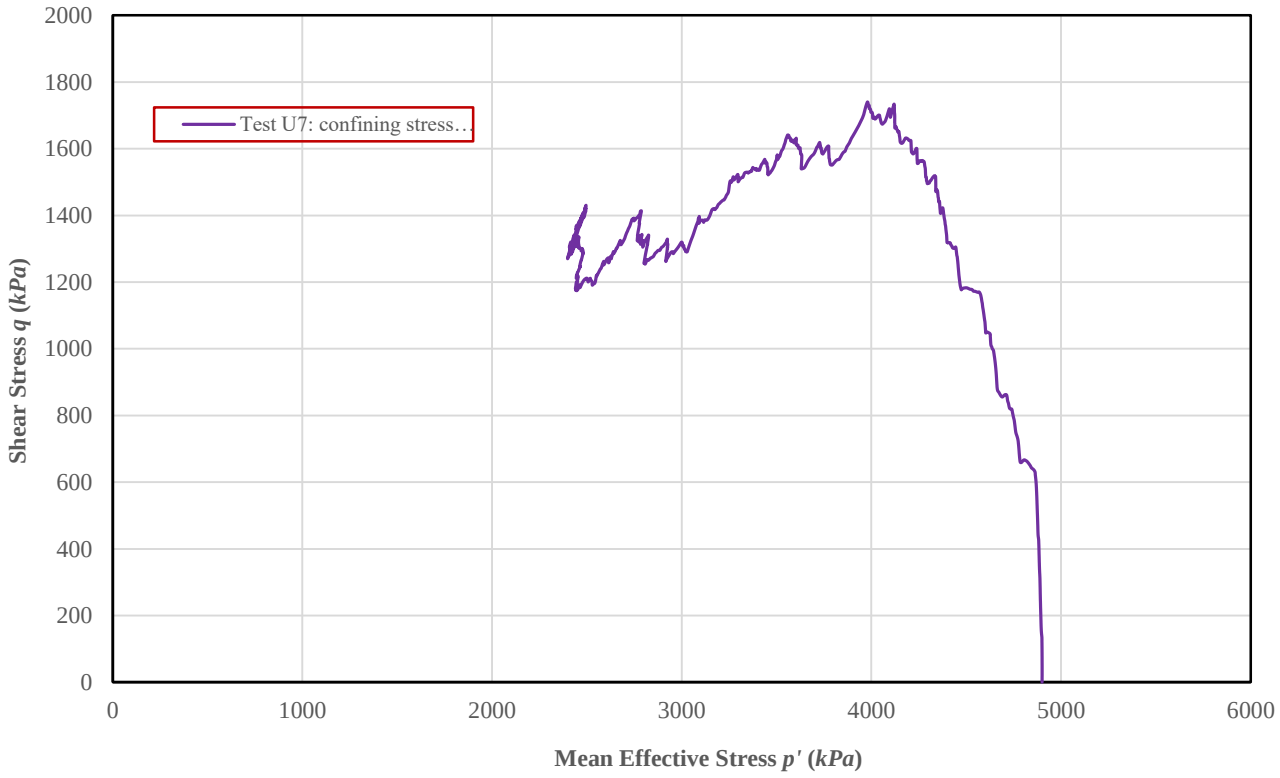

Figure B.12 Stress path for Test U7

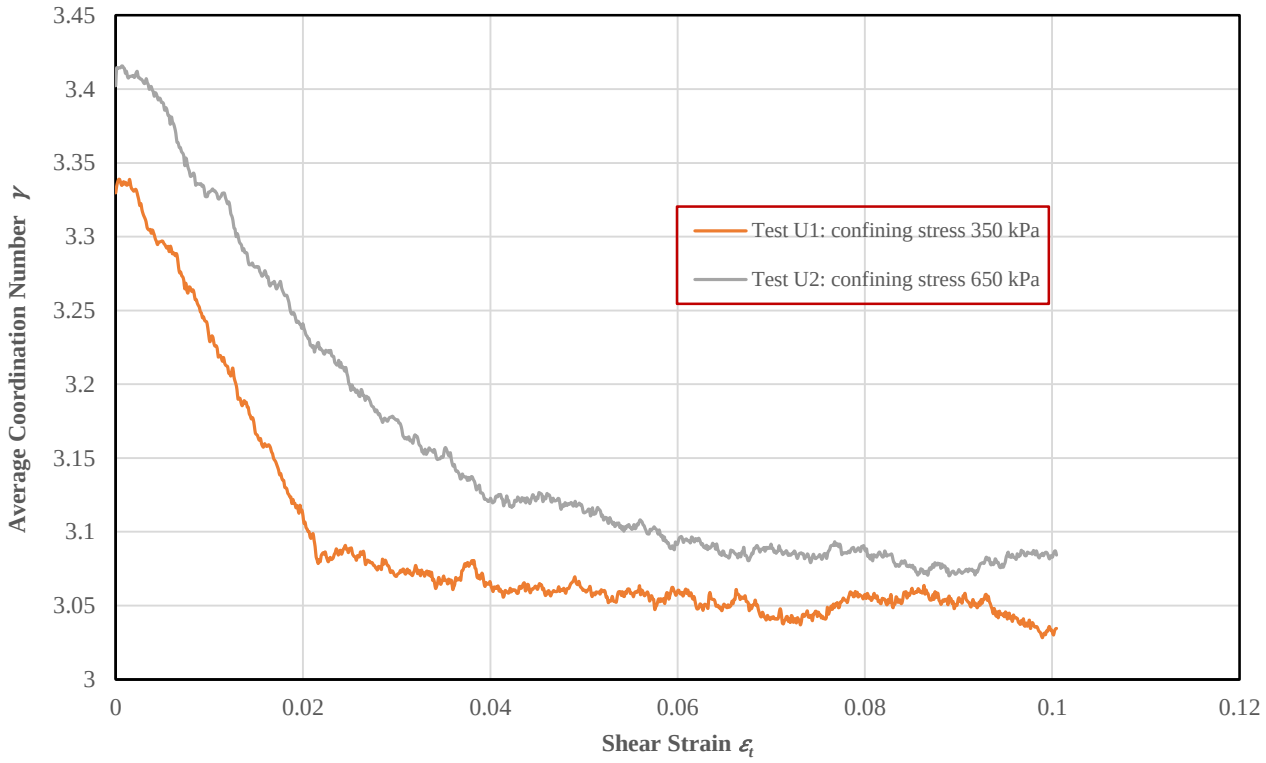

Figure B.13 Average coordination number γ variations for Tests U1 and U2

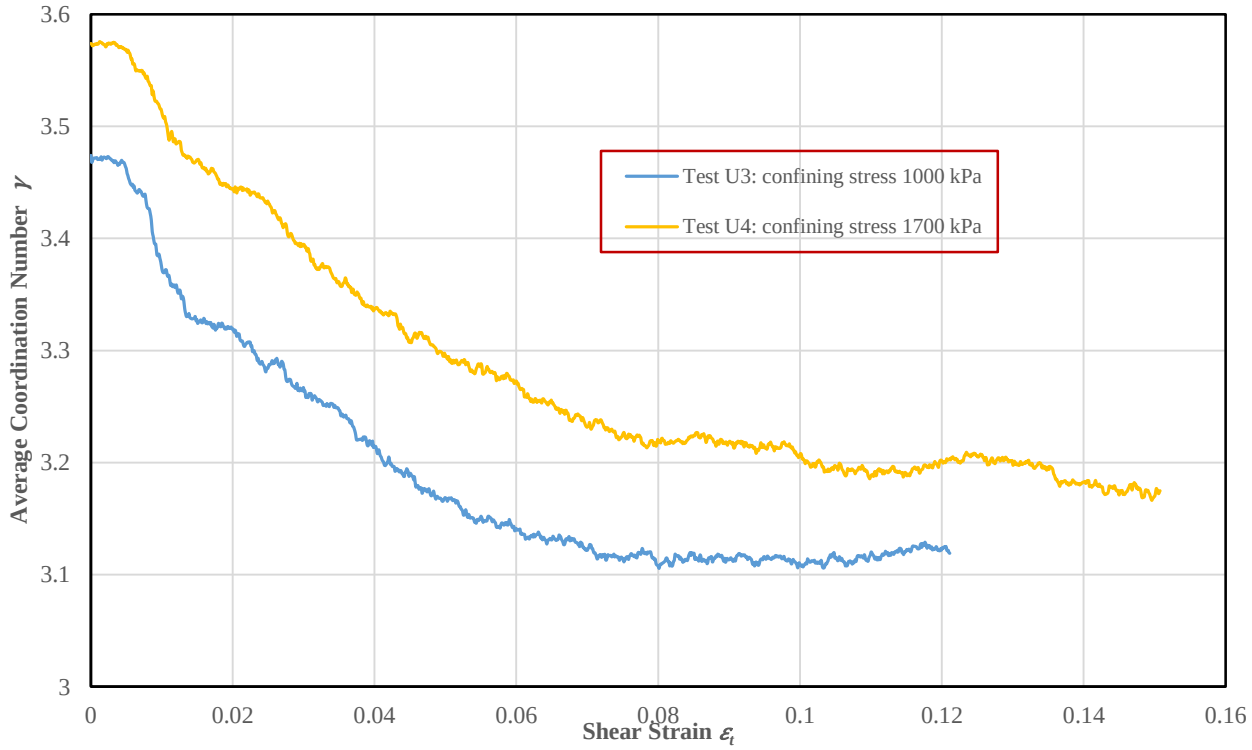

Figure B.14 Average coordination number γ variations for Tests U3 and U4

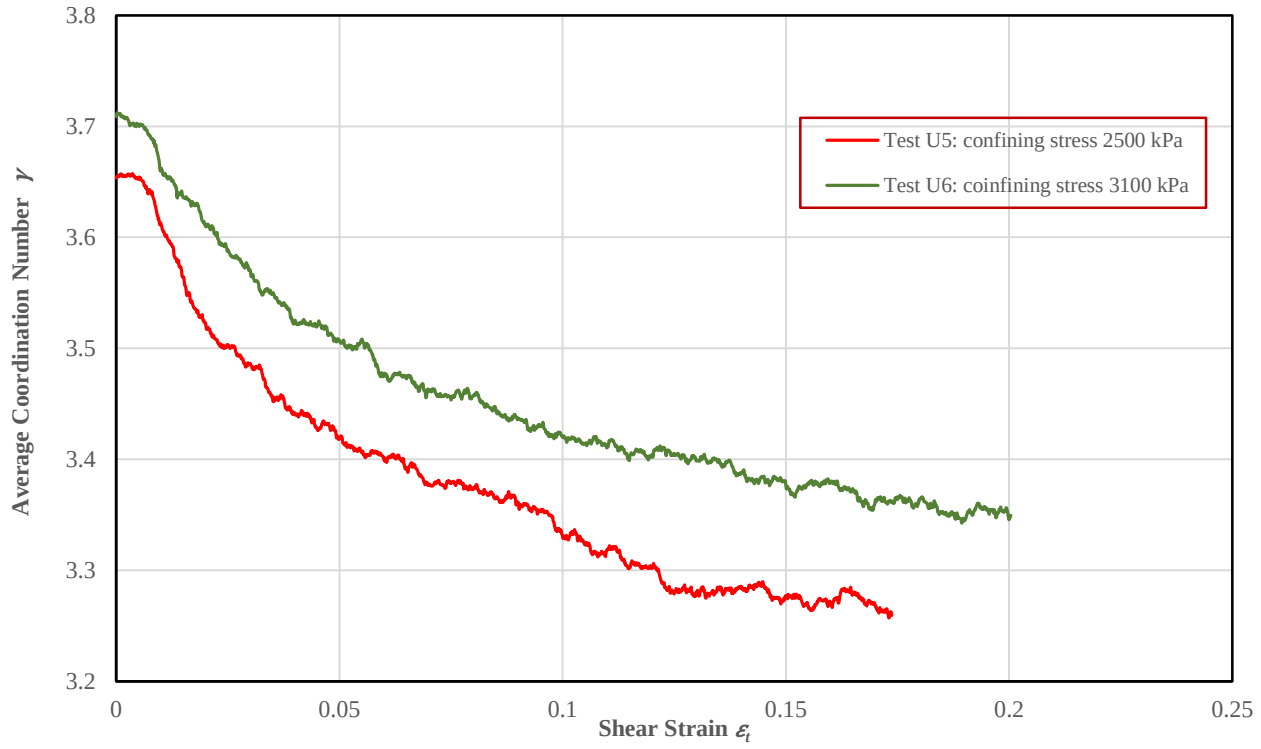

Figure B.15 Average coordination number γ variations for Tests U5 and U6

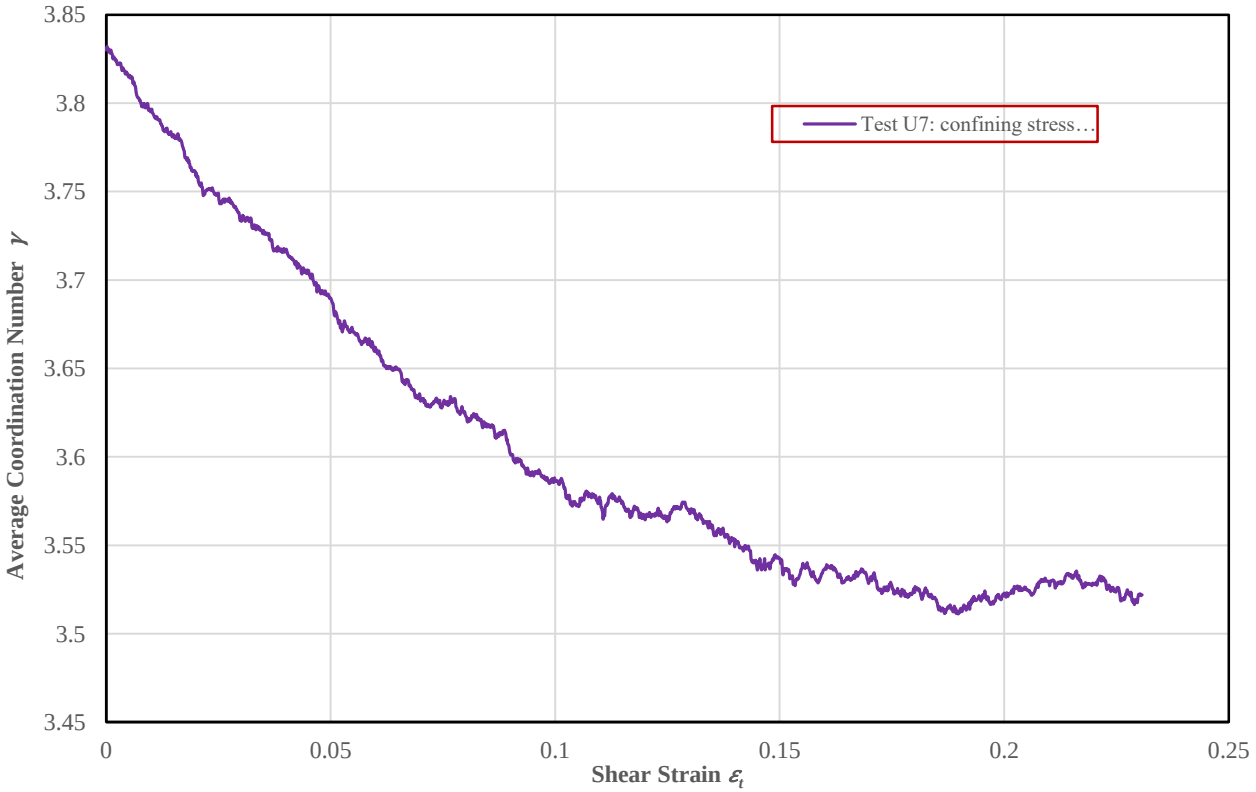

Figure B.16 Average coordination number γ variations for Test U7

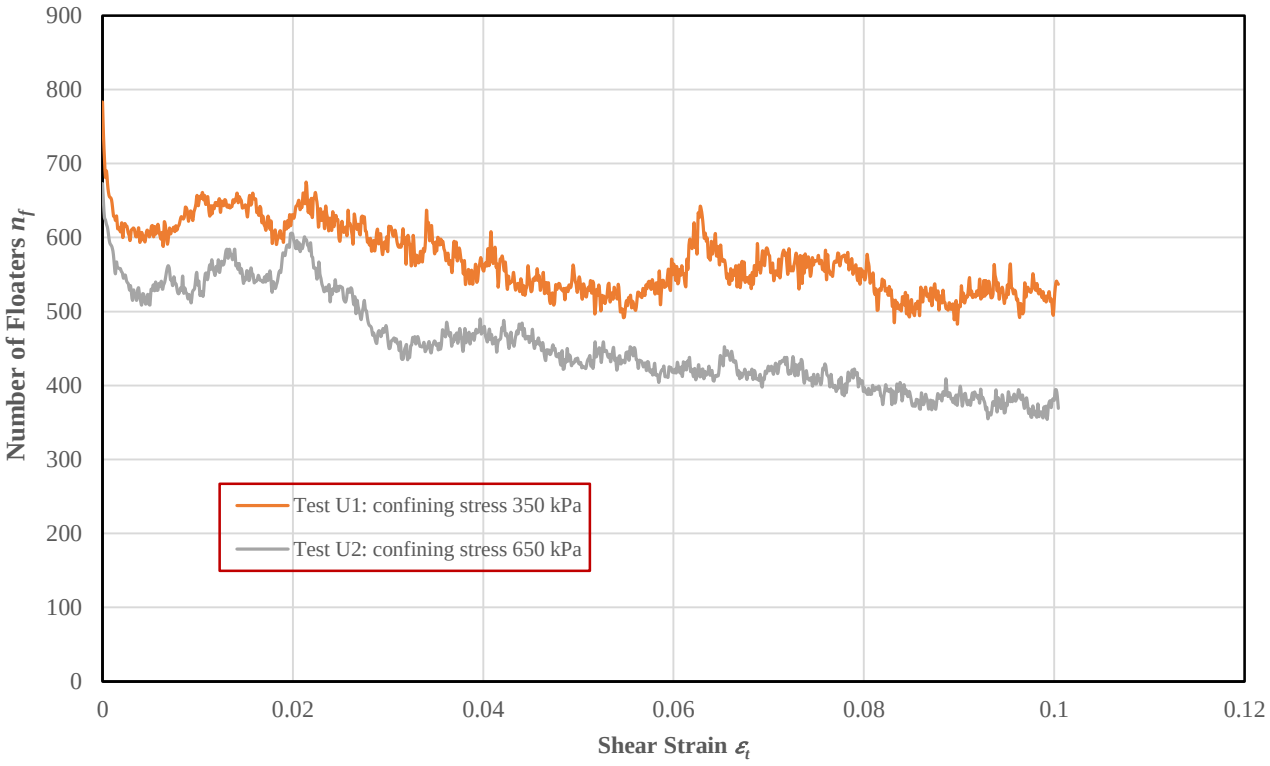

Figure B.17 Number of floaters nf variations for Tests U1 and U2

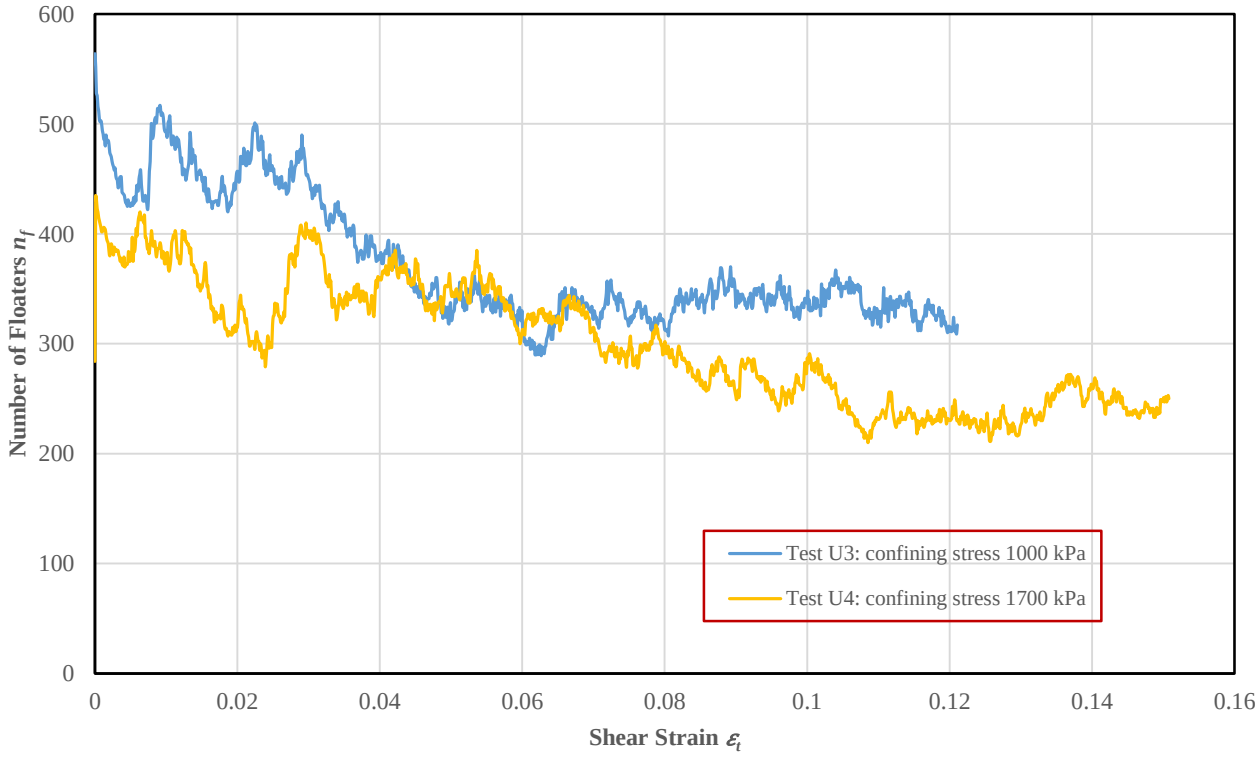

Figure B.18 Number of floaters nf variations for Tests U3 and U4

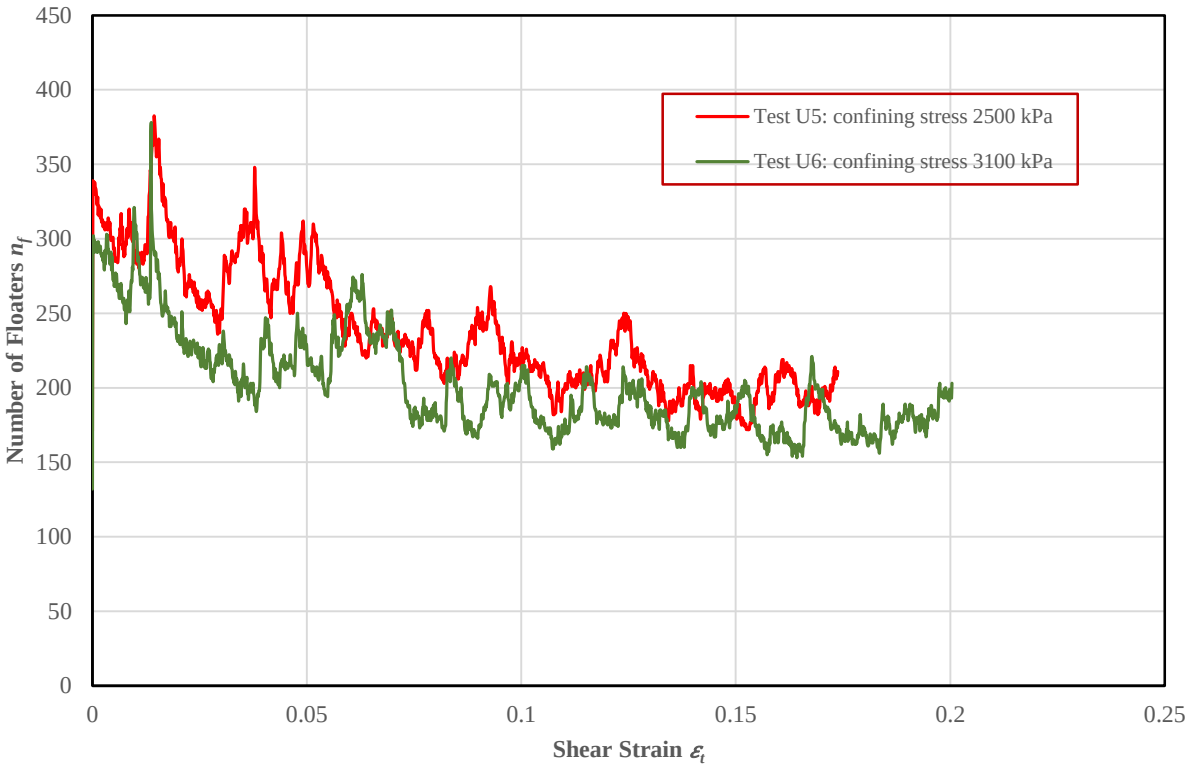

Figure B.19 Number of floaters nf variations for Tests U5 and U6

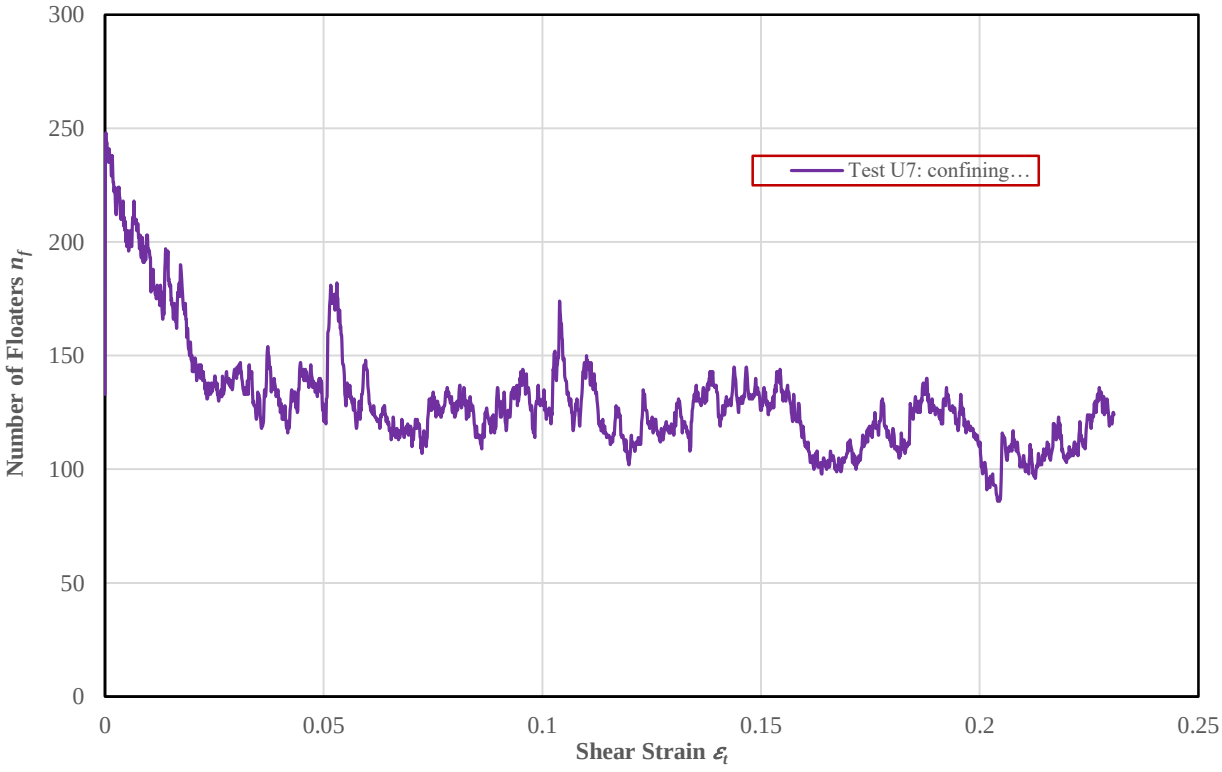

Figure B.20 Number of floaters nf variations for Test U7

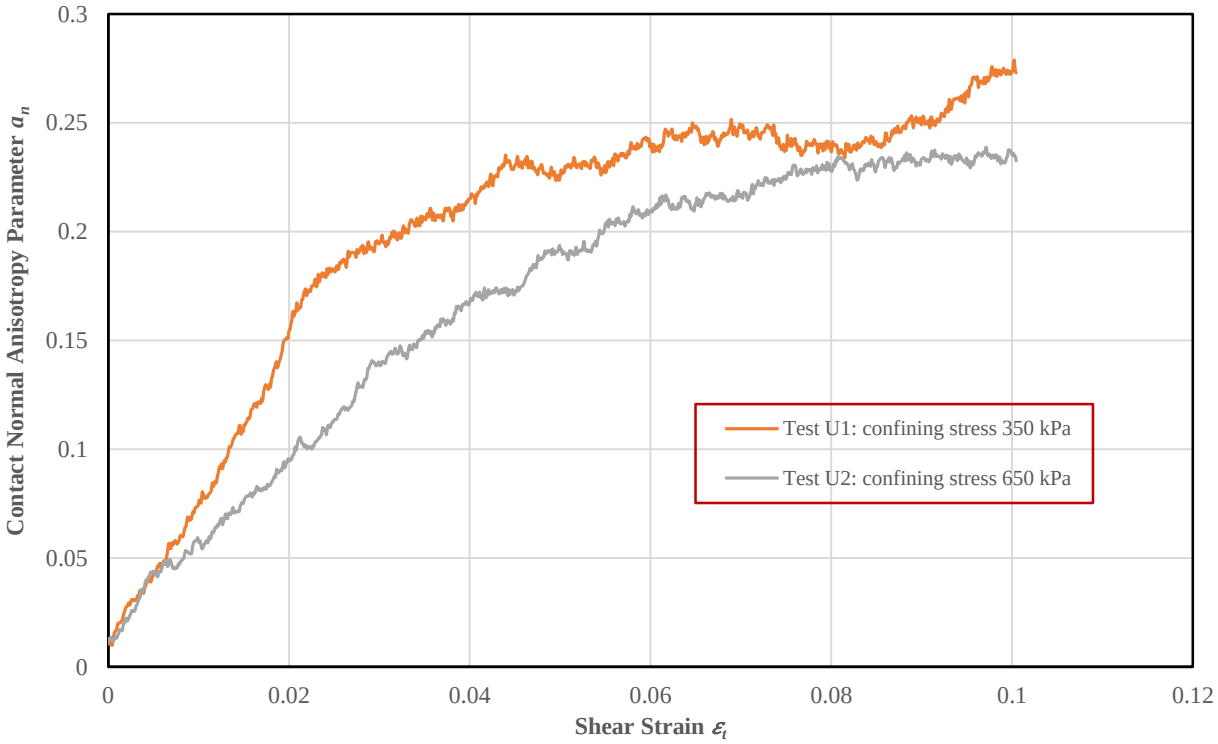

Figure B.21 Contact normal anisotropy parameter an for Tests U1 and U2

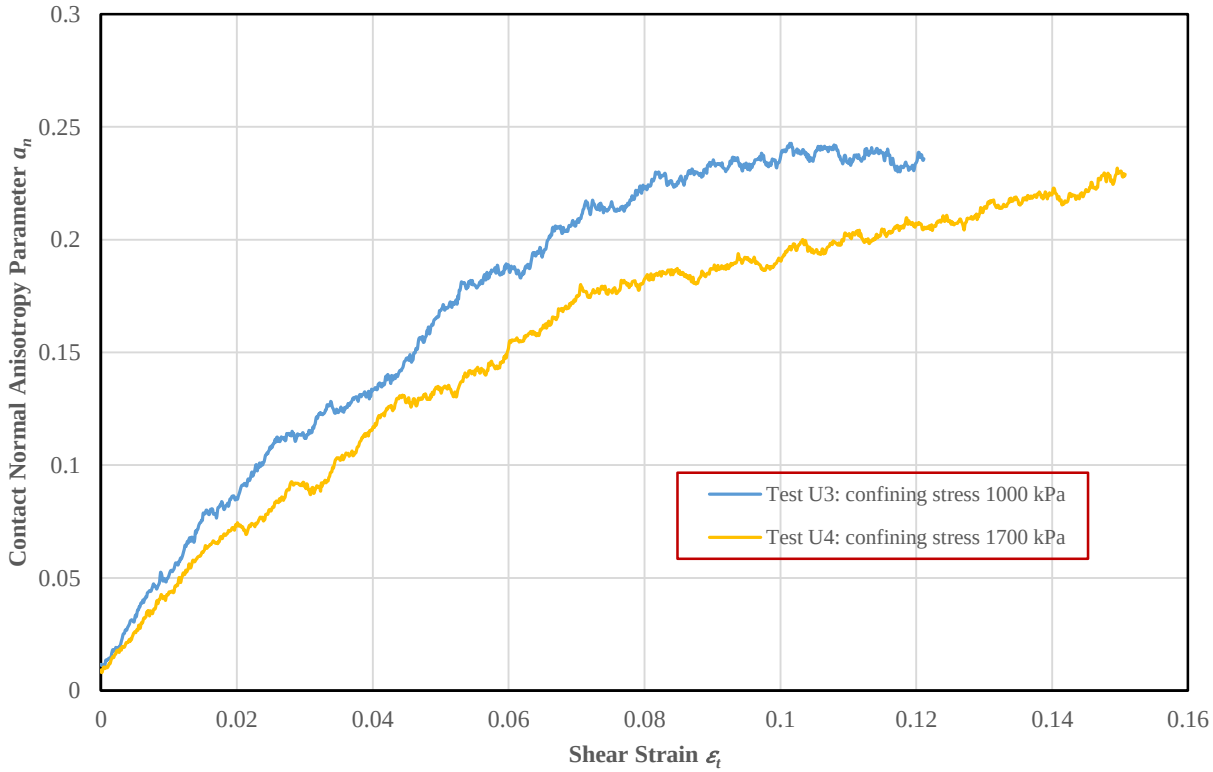

Figure B.22 Contact normal anisotropy parameter an for Tests U1 and U2

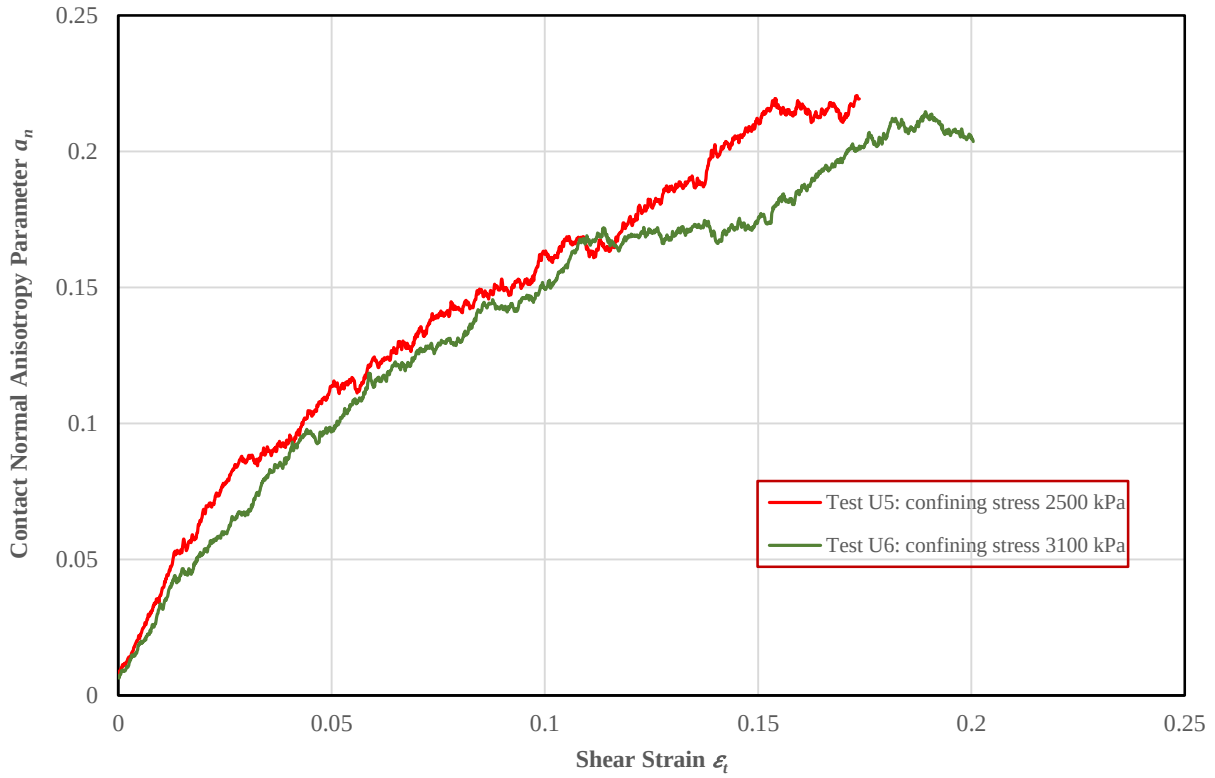

Figure B.23 Contact normal anisotropy parameter an for Tests U5 and U6

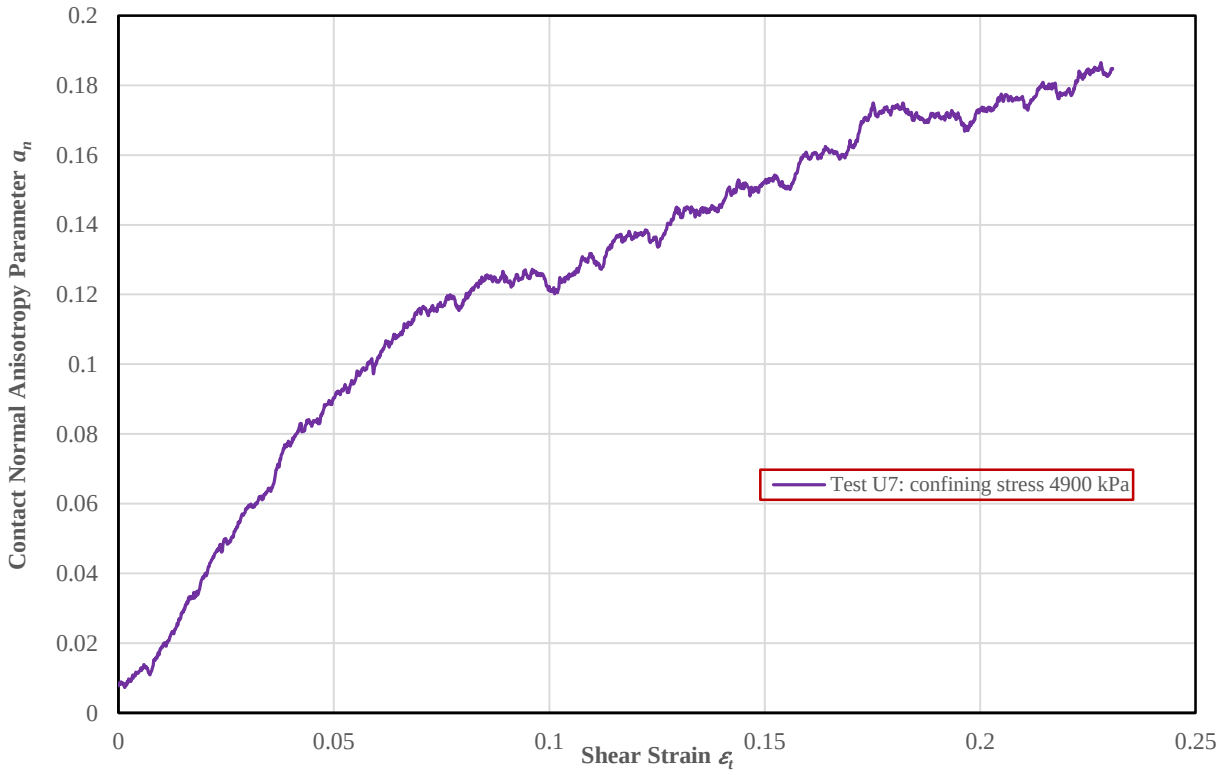

Figure B.24 Contact normal anisotropy parameter an for Tests U7 and U8

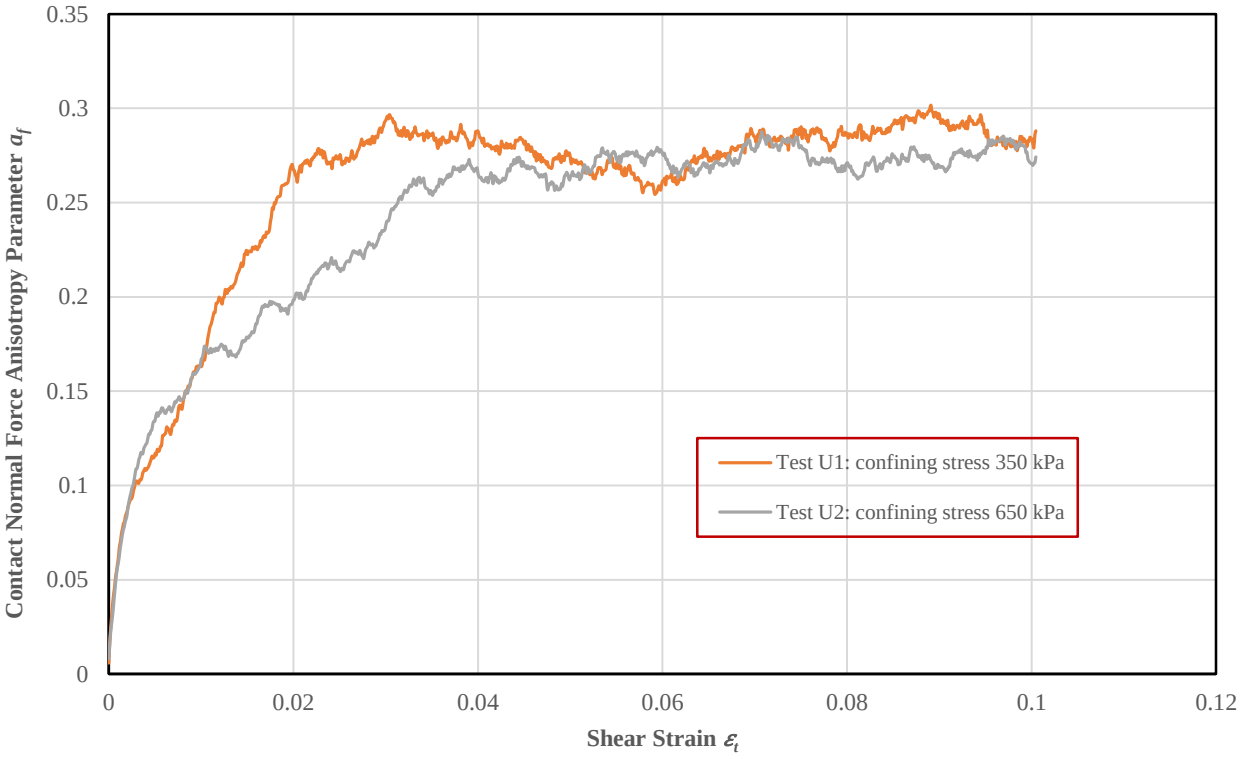

Figure B.25 Normal contact force anisotropy parameter af for Tests U1 and U2

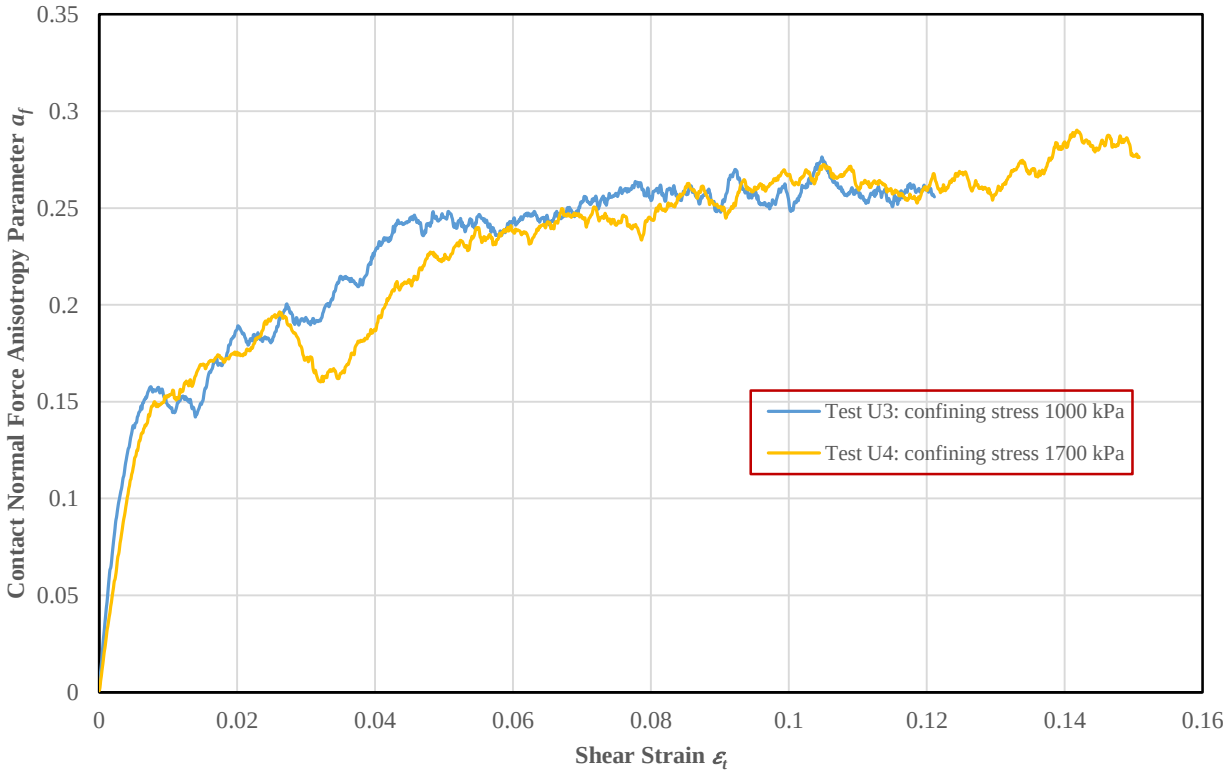

Figure B.26 Normal contact force anisotropy parameter af for Tests U3 and U4

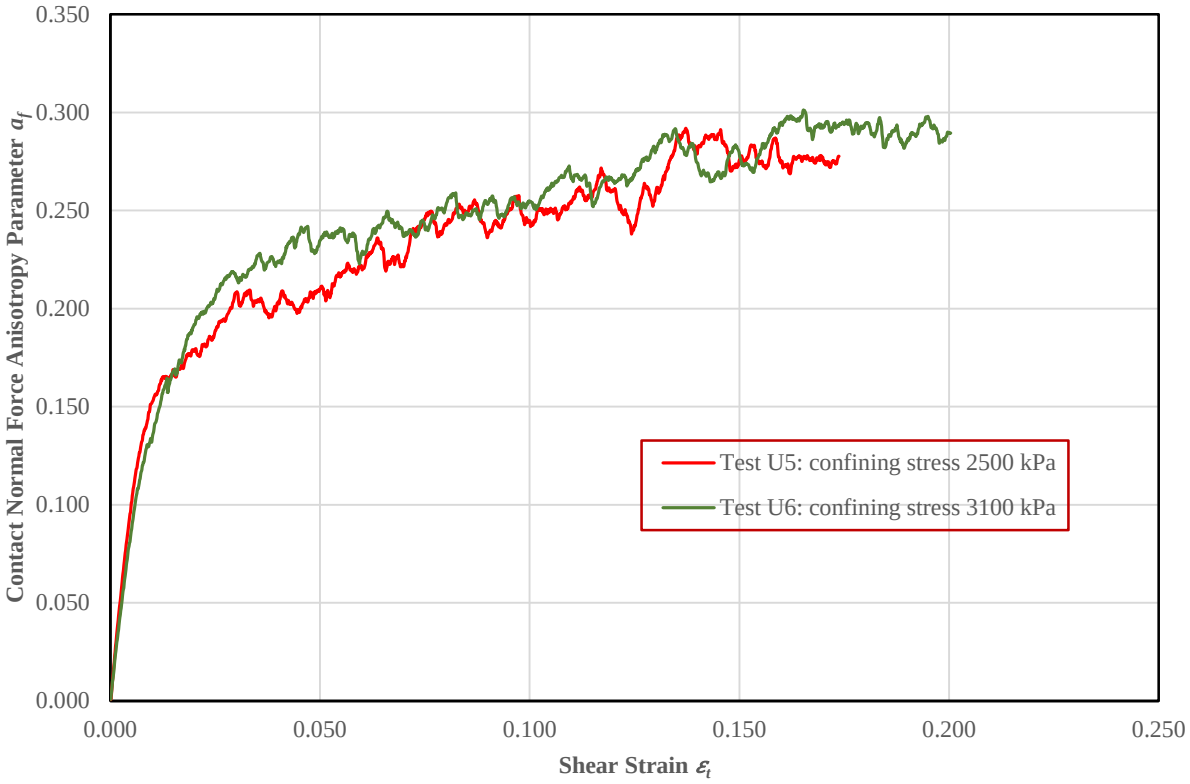

Figure B.27 Normal contact force anisotropy parameter af for Tests U5 and U6

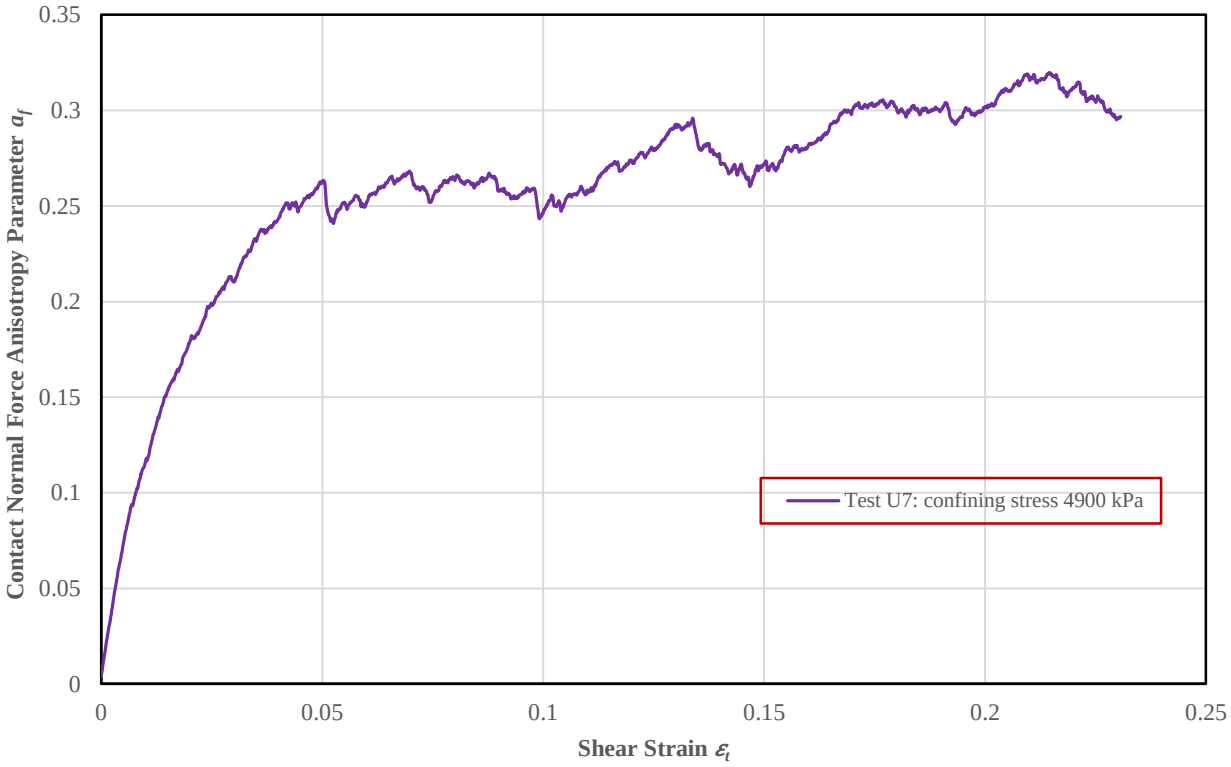

Figure B.28 Normal contact force anisotropy parameter a_f for Test U7